

PAUL SCHERRER INSTITUT



Annual Report 2011

Electrochemistry Laboratory

<http://ecl.web.psi.ch>

COVER PHOTO:

Electric Car developed by Belenos Clean Power Holding
and Paul Scherrer Institut.
Powertrain based on hydrogen and pure oxygen fuel
cell system hybridized with battery.

© Paul Scherrer Institut

DOI: 10.3929/ethz-a-007047464

PAUL SCHERRER INSTITUT



Electrochemistry Laboratory

Annual Report 2011

Hardcopies of this report are available from:
Isabella Kalt (isabella.kalt@psi.ch)
Paul Scherrer Institut
5232 Villigen PSI
Switzerland

A full version of this report is also available on the web:
<http://ecl.web.psi.ch>

Paul Scherrer Institut
Electrochemistry Laboratory
5232 Villigen PSI
Switzerland

Secretary
Phone +41 56 310 29 19
Fax +41 56 310 44 15

Publisher

Electrochemistry Laboratory
Paul Scherrer Institut
5232 Villigen PSI

Editorial Team

Isabella Kalt
Rüdiger Kötz
Günther G. Scherer
Thomas J. Schmidt

Printing

Paul Scherrer Institut

ISSN 1661-5379

DOI: 10.3929/ethz-a-007047464

PSI Electrochemistry Laboratory – Annual Report 2011

© Paul Scherrer Institut

CONTENTS

- 1 EDITORIAL**
G.G. Scherer
- 3 SCIENTIFIC CONTRIBUTIONS 2011**
- FUEL CELLS - MATERIALS**
- 5** Cost estimate of the PSI 'Generation 2' radiation grafted fuel cell membrane
- 7** Grafting of linkers onto ETFE for post-functionalization
- 9** Fuel cell characterizations of MAN containing membranes
- 11** Membranes for fuel cells: Radiation induced graft copolymerization of styrene and methacrylic acid into ETFE
- 13** Analysis of composition in radiation co-grafted films via FTIR spectroscopy
- 14** Grafting of styrene onto plasma-activated porous polypropylene
- 15** Kinetic study on the effectiveness of HO[•] scavengers in fuel cell membranes
- 17** Durability of radiation grafted membranes under dynamic operating fuel cell conditions in comparison to Nafion 212 and Nafion XL-100
- 19** Effects of synchrotron radiation on ionomer used in PEFCs
- 21 FUEL CELLS - DIAGNOSTICS**
- 23** Simultaneous testing and neutron imaging of 6 operating PEFCs: the multi-cell set-up
- 25** High resolution neutron imaging of passive fed self-breathing PEFCs
- 26** Fast *in-situ* X-ray tomographic microscopy of PEFCs
- 28** *In-situ* X-ray tomography on PEFC: The on-stage humidification concept
- 30** Factors determining the gas crossover through pinholes in PEFC membranes
- 32** Model-based transient analysis of technical sized PEFCs
- 34** Saturation dependency of effective GDL gas transport properties
- 35** Locally resolved current measurements in high temperature PEFCs
- 37** On the efficiency of H₂/air and H₂/O₂ fuel cell systems
- 39** A H₂/O₂ fuel cell system for automotive application
- 41 BATTERIES & SUPERCAPACITORS - MATERIALS**
- 43** Lithium-ion conductivity of radiation grafted membranes
- 44** Electrochemical and chemical surface modifications of carbons for Li-ion batteries
- 46** Lithium-sulphur battery development
- 48** M_{0.5}TiOPO₄ as high specific charge battery material
- 50** Lithium-bismuth alloy as a reference electrode for electrochemical impedance spectroscopy
- 52** A reference electrode for the use in ionic liquids
- 53** Graphene paper: a suitable way to utilize graphene for supercapacitor electrodes
- 55 BATTERIES & SUPERCAPACITORS - DIAGNOSTICS**
- 57** *In situ* neutron diffraction study of a graphite negative electrode
- 59** Study of oxygen loss during overcharge of Li_{1.1}(Ni_{1/3}Mn_{1/3}Co_{1/3})_{0.9}O₂ using neutron powder diffraction
- 60** *In situ* FTIR spectroscopy on glassy carbon electrodes as a model of the graphite surface for Li-ion batteries: impact of additives on the SEI film
- 62** Application of *in situ* Raman spectroscopy to understand the reaction mechanism of Li₂MnO₃-Li(Mn_xNi_yCo_z)O₂ in Li-ion batteries
- 64** *In situ* neutron diffraction applied to positive and negative electrode materials

- 65 *In situ* investigation of inhomogeneous reactions perpendicular to current collector by using two-layer electrodes
- 67 Morphological and structural changes of Mg substituted Li(Ni,Co,Al)O₂ during overcharge reaction
- 69 Aging tests of double layer capacitors - cycle vs. hold
- 70 The cathodic stability limit of the ionic liquid 1-ethyl-3-methyl imidazolium tetrafluoroborate [EMIM][BF₄] - a complementary approach
- 73 **CATALYSIS & INTERFACES**
- 75 Particle size effect on magnetron sputtered cathodes
- 77 The effect of gas front propagation on carbon corrosion during start-up and shut-down of PEFCs
- 79 Tin and tantalum oxides as supports for Pt-electrocatalysts in PEFCs
- 80 *In situ* STM study of Pt-dots on HOPG prepared by electron beam lithography
- 82 XPS analysis of activated carbon supported ionic liquids - an approach towards reliable binding energies
- 83 **THE ELECTROCHEMISTRY LABORATORY**
- 85 Impressions
- 86 Structure 2011
- 87 ECL-personnel 2011
- 88 These PhD students from ECL graduated in 2011
- 90 Exchange students, diploma theses
- 91 Seminar, invited speakers
- 91 Awards
- 92 Conferences – Symposia
- 94 Review activities of the laboratory
- 95 Industrial partners
- 96 Documentation

This is the 10th Annual Report of the Electrochemistry Laboratory, since we have started to disseminate our annual results of and information about the Laboratory in the year 2002. I had the great pleasure to accomplish this together with Isabella Kalt and Rüdiger Kötz, both of them dedicated to put a tremendous effort into this task. Over these ten years, we saw a continuous growth of the Laboratory in terms of people and projects, reflecting the increasing importance of electrochemical energy conversion and storage in both, academia and industry.

We are proud to report again about many successes during the past year. First of all, 10 of our PhD-students accomplished their PhD-thesis during 2011, the highest number ever for the Laboratory. All of them left PSI with a remarkable record in terms of education in an inspiring and challenging interdisciplinary environment, participation in projects with external partners, and finally dissemination of their results in peer reviewed publications and presentations, overall a requirement for a smooth transition to their next step in professional life. As in the past, education in the cross-cutting discipline *Electrochemistry* was and will be a major effort of our Laboratory.

The continuity and success of our activities is reflected in 48 peer reviewed publications, expressing the high standards of our work and its impact to the scientific community. Our newly obtained results are described in 40 contributions to this report, displaying again the wide spectrum of work carried out, from fundamental electrochemistry and materials science, diagnostic tools for cells, to electrochemical conversion systems. The demonstration of the fuel cell powered car (see title page), developed together with Belenos Clean Power Holding, Bienne, was certainly one of the highlights during the past twelve months.

Our annual One-Day-Symposium on topics in Electrochemistry has established itself as an international event. On May 11, the actual and well received subject "Electromobility" brought together more than 100 participants, listening to the contributions of Hubert Gasteiger (Technical University München), Janko Jamnik (Kemijski inštitut Ljubljana), Andreas Friedrich (DLR and University Stuttgart), Peter Prenninger (AVL Graz), Isotta Cerri (Toyota Europe, Brussels) and Robert Stüssi (AVERE Lisbon). Presentations and discussions emphasized the growing importance of Electromobility, with a critical view on its potential and scientific as well as engineering challenges.

On February 1st, we welcomed Thomas Justus Schmidt, formerly Director R&D of BASF Fuel Cells, as new Section Head Electrochemical Energy Conversion. At the same time he was appointed Professor for Electrochemistry in the Laboratory of Physical Chemistry of ETH Zürich, based on his excellent record of scientific contributions to electrocatalysis and fuel cell research, as well as managing experience in an industrial environment. Thomas came "home" to PSI, already having worked with us on topics of Polymer Electrolyte Fuel Cells during the years 2001 and 2002.

Starting January 1st 2012, Thomas is taking over the challenging post of Head of PSI's Electrochemistry Laboratory. Personally, I wish Thomas all the best to continue the Laboratory's success story and take the Laboratory to new grounds of *our discipline* Electrochemistry.

Finally, I want to thank all collaborators, colleagues, and friends at PSI as well as outside of PSI, with whom I had the pleasure to work and interact over the last 10 years as Head of the Laboratory and my overall 22 years at PSI, respectively, for their commitment, constructive critics, openness, and patience.

Günther G. Scherer

SCIENTIFIC CONTRIBUTIONS 2011

FUEL CELLS

MATERIALS

Cost estimate of the PSI 'Generation 2' radiation grafted fuel cell membrane

L. Bonorand, G.G. Scherer, L. Gubler

phone: +41 56 310 21 32, e-mail: lukas.bonorand@psi.ch

Fuel cells have the potential to provide a clean power source for powering automobiles of the future. While there are many technical challenges facing fuel cells, such as power density, durability, and freeze start, etc., there are also major challenges relating to the economic viability of the technologies in the market place. Fuel cells must be cost-competitive with current internal combustion engines to enter the commercial market.

Cost presents one of the most significant barriers to achieving clean, reliable, cost-effective fuel cell systems. Materials and manufacturing costs are too high for catalysts, membranes, bipolar plates and gas diffusion layers. Current pricing on state of the art PFSA materials is high, ~ \$250/m² as finished 25 μm membrane [1]. Low-cost, high-performance membranes, as well as low-cost, high-volume manufacturing process are required to make fuel cell stacks competitive.

The current cost target for a 80 kW_{net} direct hydrogen automotive PEM fuel cell system is \$30/kW_{net} by 2017. The 2011 cost status is projected to be \$49/kW, when manufactured at a volume of 500,000 units / year [2]. The fuel cell stack makes up about half of the system cost, and the membrane contributes to roughly 12% of the overall stack cost with \$20/m². At low production volumes of 1,000 units / year, membranes account for 45% of the stack cost. This is a more significant cost contribution and the membrane becomes a higher cost driver. More cost effective membranes have more impact in reducing overall stack and system costs at low volumes and can therefore act as a catalyst for early market entry and thus reduce the barrier for widespread commercialization of fuel cells.

In this context, we developed a cost model, based on our 'Generation 2' (Gen2) radiation grafted membrane. Cost outputs were categorized by materials, utilities, labor, equipment, tooling, building, general overhead, maintenance and cost of capital. We also performed sensitivity analysis to obtain an understanding of the key cost drivers and design option, as well as the critical manufacturing processes for cost-reduction initiatives.

Cost definition

The estimated cost includes factory cost, such as direct materials and labor, factory expenses and capital equipment, but excludes corporate charges for profit, sales expenses and general services and administration.

Baseline cost model description

Our membrane cost estimate is based on a manufacturing capacity appropriate for the commercialization of PEFC technology in the context of automotive markets (500,000 units / year). This would require approximately 5 M m² of membranes annually. To meet this demand, it is estimated to operate 3 production lines, which are based on a continuous reel-to-reel process. In addition, Base Cost scenarios at 1 M m², 0.1 M m² and 0.01 M m² annual production rates were also determined to obtain cost-volume relationships.

Membrane / material description

Our optimized 'Generation 2' (Gen2) radiation grafted membrane is the current standard material in our laboratory. The material has demonstrated promising performance and durability, as well as robustness and reliability compared to commercial membranes such as DuPont Nafion[®] XL-100 under application relevant conditions [3]. The membrane is composed of an ETFE base film with AMS and MAN as graft copolymer units, including DIPB as crosslinker [4].

Manufacturing process

The fabrication of the Gen2 radiation grafted membrane is assumed to be a continuous reel-to-reel process.

The base film is electron beam irradiated, followed by exposure to the monomer/crosslinker/solvent mixture at elevated temperatures. After washing and drying, the grafted film is exposed to a sulfonating agent to be functionalized, followed by a purification and drying step.

A line speed of 2.5 m/min and a working width of 2 m are assumed to obtain an annual capacity of 1.75 M m² per unit, yielding into the full 5 M m² annually, operating 3 units. The process covers 240 days/year, including 20% downtime, while operating 3 shifts / day.

Solvents are to 80% recycled, whereas monomers and crosslinker are considered to be disposables.

Membrane baseline cost

At full manufacturing scale (5 M m² / year), the estimated membrane cost is \$5.80/m², in which material cost represents about 73% of the total cost. Table 1 shows a membrane cost breakdown categorized into capital equipment, direct material and labor costs, and factory expenses.

Categories	Base Case	Lowest Case
	USD / m ²	USD / m ²
Capital Equipment	1.17	0.18
Direct Material	4.20	1.06
Direct Labor	0.30	0.08
Factory Expenses	0.10	0.02
Total (USD/m²)	5.77	1.35

Table 1. Membrane manufacturing cost at 5 M m² annual production volumes.

The 'Base Case' column represents the cost estimate based on current technologies, including high volume pricing on raw materials and no recycling of excess reactants, except solvents. The 'Lowest Case' displays the ultimate potential, which involves complete raw material recovery, aggressive raw material price projections, optimized processing yields, as well as low cost manufacturing locations.

A membrane cost breakdown pie chart at 5 M m² annual production volume (Base Case) is shown in Figure 1.

Material cost represents about 73% of the total membrane cost. Capital and labor are the second and third contributor with 20% and 5%, respectively.

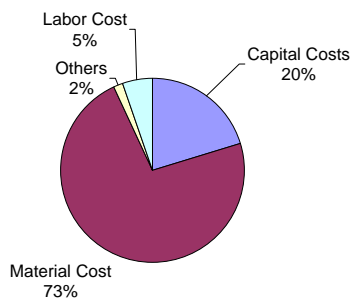


Figure 1. Membrane cost breakdown pie chart at 5 M m² annual production volumes for the Base Case scenario.

The membrane cost breakdowns for annual production volumes of 0.01, 0.1, 1 and 5 M m² demonstrate that at lower volumes, material cost contributions decrease and capital and labor portions increase.

Single variable sensitivity analysis

A parametric analysis was performed to assess the impact of processing parameters on overall membrane cost. The method tests each variable independently; it freezes the other variables at their baseline values when analyzing one variable. Figure 2 shows the sensitivities of the main processing parameters.

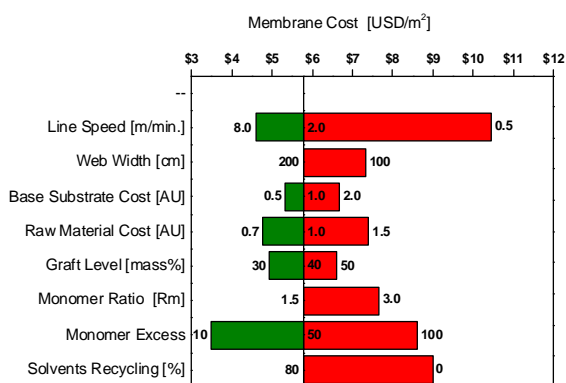


Figure 2. Membrane single variable sensitivity analysis tornado chart at 5 M m² annual production volumes.

The Tornado chart in Figure 2 shows that line speed and monomer utilization have the greatest impact on cost. Membrane cost could drop well below \$5/m², when monomer utilization and reaction rates can be increased.

The overall impact of cost factors on total membrane cost as a function of volume is shown in Figure 3. The impact factor is a relative measure of the sensitivity of cost factors impacting total membrane cost. As volumes increase, material cost and utilization have a more pronounced effect on total membrane cost. However, at high volumes (5 M m² / year), material throughput and material utilization have the highest impact. Cost reductions can be achieved by addressing these parameters, namely increasing reaction rates and minimizing monomer consumption.

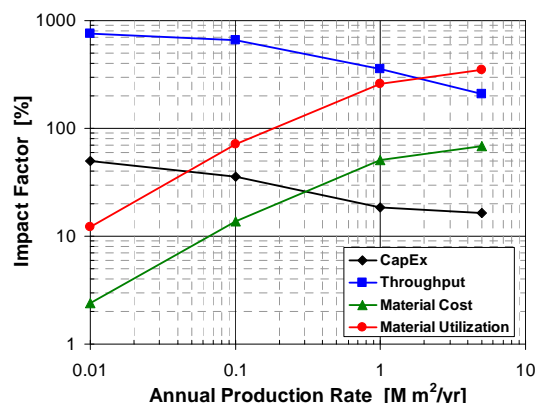


Figure 3. Impact of cost factors on total membrane cost.

Cost comparison

A comparison between a non-reinforced PFSA (DuPont) membrane cost projection [1] and our Gen2 membrane's cost estimate are shown in Figure 4.

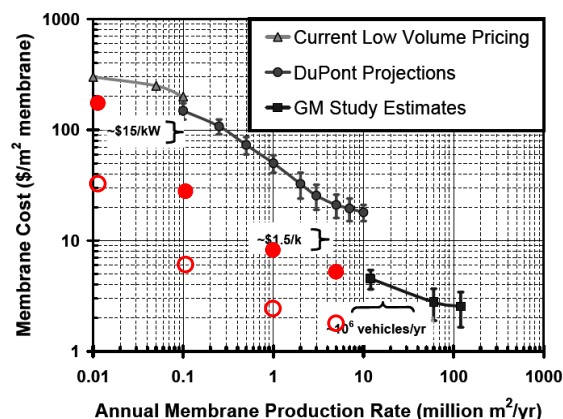


Figure 4. Price projection of PFSA membrane, adopted from Ref. [1], including PSI Gen2 membrane: Base Case (red filled circles), Lowest Case (red non-filled circles).

The discrepancy between the two PFSA projections is that the GM study assumes construction of a new high volume plant and does not account for volume ramp up.

Conclusion

The cost of our Gen2 radiation grafted membrane has the potential to be an order of magnitude lower than current PFSA type membranes, such as Nafion[®]. This is especially attractive at low production volumes, since the membranes can make up close to half the stack cost. Low-cost membranes can significantly reduce overall stack and system costs at low volumes and so act as a catalyst for early market entry. This can reduce the barrier for widespread commercialization of fuel cells.

References

- [1] M.F. Mathias et al., *Electrochem. Soc. Interface* **14**, 24-35 (2005).
- [2] U.S. Department of Energy (Hydrogen Program), Record 11012 – Fuel Cell System Cost - 2011.
- [3] L. Gubler, L. Bonorand, J. Thut, G.G. Scherer, this PSI Electrochemistry Laboratory Annual Report, 17.
- [4] L. Gubler, G.G. Scherer, in: *Handbook of Fuel Cells*, Vol. **5**, W. Vielstich, H.A. Gasteiger, H. Yokokawa (Editors), John Wiley & Sons, Chichester (UK), 313-321 (2009).

Grafting of linkers onto ETFE for post-functionalization

Y. Buchmüller, G.G. Scherer, A. Wokaun, L. Gubler

phone: +41 56 310 54 50, e-mail: yves.buchmueller@psi.ch

Radiation grafting is a versatile technique to introduce desired properties into polymers [1, 2]. Advantages are the wide range of commercially available monomers and the relatively easy control of the graft component by the appropriate choice of the irradiation dose, monomer concentration in the grafting solution, solvent and additives, the reaction time and temperature.

In this work, grafting of functionalizable monomers, so called linkers, onto poly(ethylene-*alt*-tetrafluoroethylene) (ETFE) base film is presented. Linkers can be used to post-functionalize a polymer film in bulk. They contain a functional group (electrophile) and a polymerizable double bond. Two linkers were chosen (vinylbenzyl chloride (VBC) and glycidyl methacrylate (GMA), Figure 1) and grafted onto pre-irradiated ETFE. Both monomers fulfill the requirements for linkers and are cost-effective. Functionalization of the grafted films was performed with two different nucleophiles: ETFE grafted with VBC was functionalized with tyramine to introduce a candidate of a phenol type antioxidant into the polymer film, whereas the grafted GMA was sulfonated to obtain an alternative proton exchange membrane.

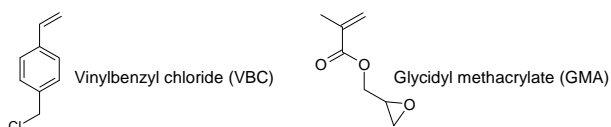


Figure 1. Monomers for grafting onto ETFE containing electrophilic groups for post-functionalization.

Experimental

GMA and VBC were grafted onto ETFE film of 25 μm thickness. The graft level (GL) is an important parameter to characterize graft copolymers:

$$GL = \frac{m_{\text{grafted}} - m_{\text{basefilm}}}{m_{\text{basefilm}}} \cdot 100\% \quad (1)$$

where m is the mass. Grafting temperature was 60°C. The ETFE base films were electron beam irradiated (Studer Leoni, Däniken) with a dose of 30 kGy, the stabilizing agent in VBC was removed by extraction and the grafting solution consisted of DMF and VBC at a volumetric ratio of 1/1. The reaction time was varied to obtain grafting kinetics. All films were characterized with FTIR and gravimetrically.

The influence of time on the amination reaction of VBC grafted onto ETFE was studied, while keeping the other parameters constant (0.25 M tyrammonium chloride in 9:1 v/v DMF/H₂O with one equivalent of NaOH, 70°C). Due to superposition of bands in the infrared spectrum it was not possible to determine the conversion via the FTIR calibration curve. Therefore, the conversion of the reaction was estimated using a gravimetric method (2):

$$\text{conversion} = \frac{(m_{\text{functionalized}} - m_{\text{basefilm}} \cdot (1 + GL)) \cdot M_{\text{VBC}} \cdot 100\%}{(M_{\text{VBT}} - M_{\text{VBC}}) \cdot GL \cdot m_{\text{basefilm}}} \quad (2)$$

where m is the mass, M the molar mass and VBT (vinylbenzyl tyramine) the aminated VBC.

For GMA, an irradiation dose of 15 kGy was used. The reaction temperature was the same (60°C). The stabilizing agent in GMA was extracted using an inhibitor remover column and the grafting solution consisted of MeOH and GMA at a volumetric ratio of 10/1.

The influence of the graft level and time on the sulfonation reaction of the epoxide group of GMA was studied. The sulfonation solution consisted of 10 m% Na₂SO₃, 3 m% Na₂S₂O₅, 10 m% ¹PrOH, and 77 m% H₂O [3]. The sulfonation was carried out at 80 °C for 8 h and 24 h, respectively. Films of graft level ranging from 10% to 300% were sulfonated.

Results

The obtained kinetics for the grafting of VBC onto ETFE is given in Figure 2. The grafting behavior is comparable to that found in the literature [3, 4]. A logarithmic dependence of the graft level on the grafting time is shown.

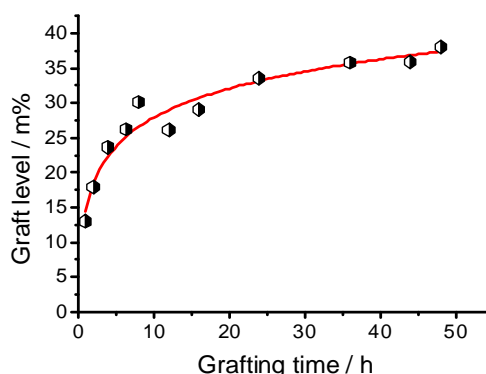


Figure 2. Grafting kinetics of VBC onto 25 μm ETFE base film.

All grafted films were characterized with FTIR. The vibrational band at 1511 cm^{-1} was used for the quantification of the VBC content in the grafted film (Figure 3).

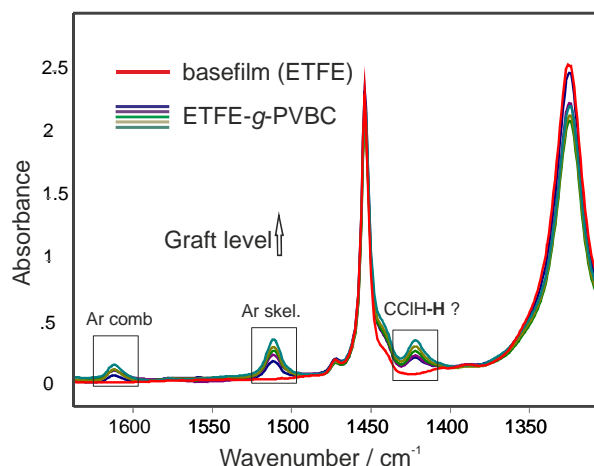


Figure 3. FTIR spectra of ETFE-g-PVBC films at different GL.

Films of different graft levels were aminated. Unfortunately, it was not possible to quantify the conversion of the amination reaction using FTIR as a broad amine band hides the VBC band at 1511 cm^{-1} . The minimum conversion, which was estimated gravimetrically (Equation 1), is relatively low: $44.5 \pm 5.0\%$. This estimation represents a minimum conversion, because HCl-elimination from the VBC units, a possible side reaction, is neglected here. There was no detectable difference in the conversion to the amine after 24 or 48 h of reaction time.

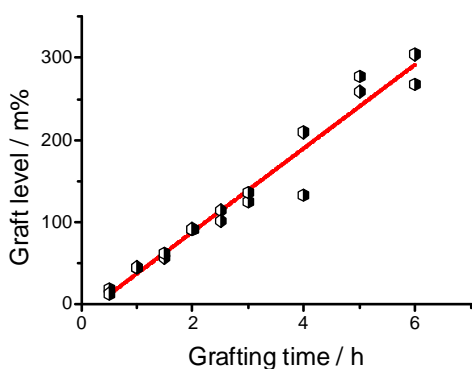


Figure 4. Grafting kinetics of GMA onto ETFE film.

The kinetics for the grafting of GMA onto ETFE is represented in Figure 4. The grafting shows a different behaviour compared to that reported by C. Schmidt et al. [5]. They found a logarithmic dependence of the graft level on the grafting time, whereas we found a linear one. They used a different solvent, thicker ETFE basefilm ($50\ \mu\text{m}$) and higher dose ($50\ \text{kGy}$). However, Saito et al. found a similar behavior for grafting of GMA at the same concentration in MeOH, yet onto polyethylene (PE) base film irradiated with a higher dose [6].

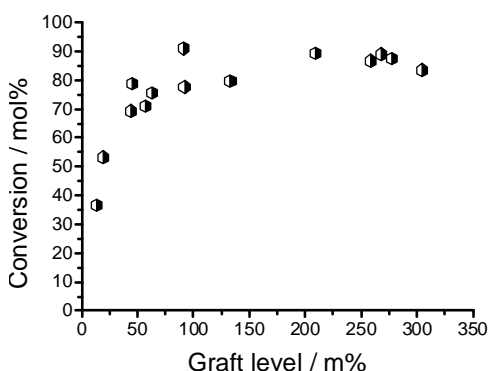


Figure 5. Conversion of the sulfonation of ETFE-g-PGMA.

All films were characterized with FTIR (spectra not shown here). The epoxide bands at 853 cm^{-1} and 902 cm^{-1} and the band of the alpha-methyl group at 1388 cm^{-1} were used for quantification of the GMA content.

Sulfonation of the epoxide group was performed to analyze the conversion of nucleophilic attack in the bulk polymer film. The number of $-\text{SO}_3\text{H}$ groups in the film was determined with acid-base titration. Additionally, the measured through-plane conductivity is an indication of base film functionalization across the entire thickness, which is a prerequisite for fuel cell application. The obtained membranes will be tested in fuel cells in forthcoming

experiments. The conversion seems to stabilize around 90% at graft levels higher than 80 m% (Figure 5). There was no detectable difference in the conversion to the sulfonic acid after 8 or 24 h of reaction time.

The substantial swelling of sulfonated ETFE-g-PGMA membranes causes a trade-off: on the one hand swelling is essential for proton conductivity (Figure 6), as proton transport takes place in the aqueous phase of the polymer. On the other hand the swelling leads to mechanical stress when the membrane is assembled into a fuel cell, which may lead to cracks and pinhole formation during cell operation.

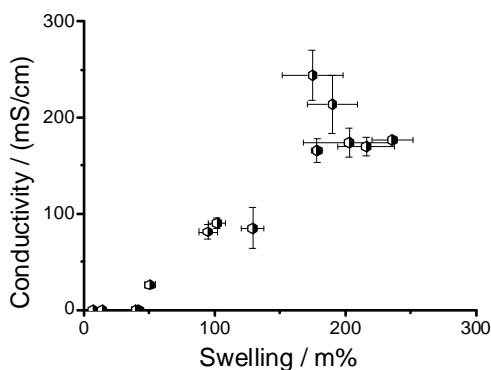


Figure 6. Proton conductivity of sulfonated ETFE-g-PGMA membranes as a function of the swelling in water.

Conclusion

VBC and GMA were grafted onto ETFE. VBC showed a logarithmic grafting behavior, whereas the grafting of GMA onto ETFE followed a linear trend. The bulk functionalization of ETFE-g-PVBC with tyramine took place with a minimum conversion of 45%. Functionalization of ETFE-g-PGMA was demonstrated using a sulfonation reaction. The conversion showed a dependence on the graft level: for films with graft levels higher than 80 m%, the conversion seems to stabilize at around 90%.

The tyramine units are thought to act as antioxidants to reduce the radical induced degradation of the polymer, which is still to be demonstrated in a fuel cell. Membranes containing sulfonated PGMA are an alternative to sulfonated styrene based membranes, since the latter ones are readily attacked by hydroxyl radicals [7]. However, hydrolytic stability under fuel cell conditions needs to be assessed.

References

- [1] S. Alkan-Gürsel, Adv. Polym. Sci. **216**, 157-217 (2008).
- [2] A. Bhattacharya, B.N. Misra, Progr. Polym. Sci. **29**, 767-814 (2004).
- [3] M. Böhme, PhD thesis, TU Clausthal (2005).
- [4] H. Herman, R.C.T. Slade, J.R. Varcoe, J. Membr. Sci. **218**, 147-163 (2003).
- [5] C. Schmidt, T. Glück, G. Schmidt-Naake, Chem. Ing. Techn. **79**, 137-145 (2007).
- [6] M. Kim, K. Saito, Rad. Phys. Chem. **57**, 167-172 (2000).
- [7] S.M. Dockheer, L. Gubler, P.L. Bounds, A.S. Domazou, G.G. Scherer, A. Wokaun, W.H. Koppenol, Phys. Chem. Chem. Phys. **12**, 11609-11616 (2010).

Fuel cell characterizations of MAN containing membranes

Z. Zhang, K. Jetsrisuparb, G.G. Scherer, A. Wokaun, L. Gubler

phone: +41 56 310 41 88, e-mail: zhuoxiang.zhang@psi.ch

To obtain tailor-made and cost-effective membranes for polymer electrolyte fuel cells (PEFCs), we are looking at utilizing radiation grafted membranes. In the development of PSI membranes of Generation 2, methacrylonitrile (MAN) was used as co-monomer to promote the grafting of α -methylstyrene (AMS), which displays poor radical homo-polymerization kinetics and a low ceiling temperature (60°C) [1]. Our further work revealed that, compared with the membrane grafted with only styrene, the incorporation of MAN improves the lifetime of the fuel cell equipped with styrene/MAN co-grafted membranes [2]. However, the stabilization mechanism is not clearly understood yet. In this study, the effect of MAN on membrane performance and durability is investigated through testing styrene/MAN co-grafted membranes in the single cell. The membranes were prepared without the addition of a crosslinker to look for intrinsic effects.

Open circuit voltage (OCV) hold tests have been widely employed as an accelerated stress test to promote membrane degradation in PEFCs due to the enhanced gas crossover [3]. The purpose of using accelerated degradation conditions is to achieve a high testing throughput.

Experimental

The membranes were prepared by co-grafting styrene and MAN into pre-irradiated poly(ethylene-alt-tetrafluoroethylene) (ETFE) (25 μm thickness) followed by sulfonation. The experimental details of the used procedures are available elsewhere [2]. Some relevant membrane properties are shown in Table 1.

#	Grafted chain composition	Graft level (%)	Styrene molar fraction in the film	Thickness (μm)
1	S-co-MAN	61.3	0.39 ± 0.02	45 ± 2
2	S-co-MAN	38.0	0.56 ± 0.02	41 ± 1
3	S-co-MAN	28.6	0.77 ± 0.04	39 ± 1
4	Styrene (S)	23.1	1	37 ± 2

Table 1. Graft level, molar fraction of styrene and thickness (water saturated state) of the used membranes.

The membranes were laminated together with gas diffusion electrodes (type ELE162, Johnson Matthey Fuel Cells) with a platinum loading of 0.4 mg/cm^2 to form membrane electrode assemblies (MEAs) in a hot-press at defined temperature, load, and duration (110°C / 40 kN / 180 s). Subsequently, the MEAs were assembled into a graphite single cell with an active area of 16 cm^2 , which comprised a straight flow field machined into graphite plates. *In situ* tests were carried out at 80 °C and 2.5 bar_a, using H₂ and O₂ as reactant gases. Fuel cell performance was recorded via online measurement of the cell voltage and high frequency resistance (HFR) at 1 kHz as a function of current density. In the durability tests, cells were held at open circuit voltage (OCV). Selective membranes with different MAN contents and a fixed ion exchange capacity (IEC) of 1.5 mmol/g were tested under OCV hold condition with online measurement of the HFR, and pre-test / post-test

determination of hydrogen permeation to assess the mechanical integrity of the membrane.

Results

Single cell polarization data of styrene based membranes showed performance comparable to that of Nafion 212 (Figure 1). In addition, similar performances were observed in both pure styrene and styrene/MAN co-grafted membranes. This implies that incorporation of MAN did not significantly affect the fuel cell performance. The *in situ* membrane resistance (HFR) displayed a slight difference for all PSI membranes: the pure styrene membrane had the lowest HFR, whereas the membrane with a styrene molar fraction of 0.39 exhibited the highest HFR. This is probably because with the increase in MAN content and graft level (Table 1), the increased thickness leads to an increase in resistance.

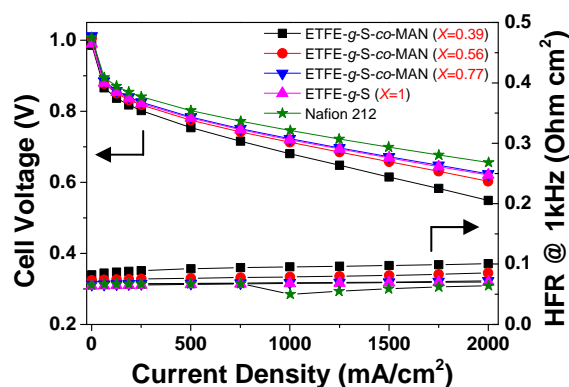


Figure 1. Single cell performance of styrene based membranes (fixed IEC = 1.5 mmol/g, X is the molar fraction of styrene), compared to Nafion 212. Fully humidified reactants (H₂ / O₂) were fed at constant flow rate of 0.6 L/min.

The single cells were operated under OCV hold condition for 100 hours (Figure 2). For the durability of the radiation grafted membranes, the effect of MAN was observed in HFR profiles, which represents the change of Ohmic resistance of the MEA. In the MEAs based on styrene/MAN grafted membranes, a pronounced reduction of the rate of HFR increase was found, in comparison to a much faster degradation in the MEA based on the pure styrene grafted membrane. This correlated well to our previous finding that the introduction of MAN improved MEA lifetime under normal fuel cell operating conditions [2]. To explain the effect of MAN in improving membrane durability, one argument is that at the high MAN content (e.g. X = 0.39), which requires high grafting level, the increased membrane thickness (Table 1) could lead to a decrease in gas crossover rate. However, when we compare the pure styrene grafted membrane with the membrane having a small amount of MAN (e.g. X=0.77), they do not show a significant difference in thickness. Yet, there is a large difference found in the HFR profile measured during the OCV hold test, where a much slower HFR increase was found in the MEA based on styrene/MAN grafted membrane (X=0.77). Actually, it has been reported that MAN is particularly effective for

conferring O₂ barrier properties to polymer materials [4]. And in the OCV hold test, the formation of hydrogen peroxide, the precursor of aggressive radicals (e.g. HO[•]), is dominated by the reaction of O₂ crossed-over from the cathode with hydrogen adsorbed on the Pt catalyst at the anode. Therefore, it could be reasonably concluded that, through reducing O₂ crossover rate, MAN can reduce the formation of H₂O₂ and improve chemical stability of styrene/MAN grafted membranes.

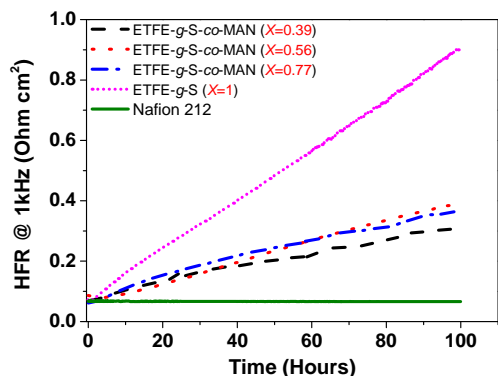


Figure 2. OCV hold test histories (HFR record) of single cells with radiation grafted membranes (fixed IEC = 1.5 mmol/g) and Nafion 212. Cell temperature 80°C, reactants H₂/O₂ at constant flow rate of 0.6 L/min, pressure 2.5 bar_a, gases fully humidified.

Degradation rates were intended to be quantified by using FTIR to determine the compositions of pristine and tested membranes, respectively. Unfortunately, the *post mortem* tests did not show any difference in the spectra of the tested membranes (Figure 3). Actually, even after 25 hours OCV hold test, the membrane with a styrene molar fraction of 0.56 did not show any characteristic peaks of styrene and MAN in its spectrum (Figure 3). It is highly possible that, without crosslinking, membrane degradation based on chain scission proceeded very quickly under the OCV hold condition. Therefore, the current durability test protocol seems to be too harsh for non-crosslinked styrene based membranes.

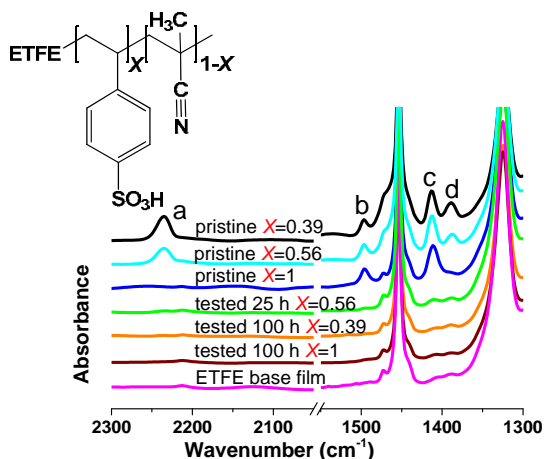


Figure 3. FTIR spectra of ETFE base film and pristine and tested membranes. The large band at 1000–1350 cm⁻¹ is an ETFE backbone signal. Graft component relevant peaks: (a) C≡N stretch vibration at 2234 cm⁻¹, (b) C=C aromatic skeleton stretch vibration at 1494 cm⁻¹ and (c) -CH₂ deformation vibration at 1411 cm⁻¹ (d) -CH₃ deformation vibration in *α*-methyl at 1388 cm⁻¹.

The continued increase in HFR could be due to the following reasons: on the one hand, the non-bonded

grafted chain fragments, which are detached from the substrate as a result of chemical degradation, are trapped by polymer matrix and catalyst layers and could continue the chain scission process; on the other hand, there are other sources of fuel cell ohmic resistance [5], which could play a part in the increase of HFR during OCV hold tests. Therefore, instead of being a direct indicator of membrane degradation, HFR is merely an indirect measure.

The reduced gas crossover owing to the incorporation of MAN can also be observed in H₂ permeation measurements (Figure 4), which were carried out by an electrochemical method. The H₂ permeation rates measured after OCV hold tests imply that no cracks or pinholes were formed in all tested membranes; meanwhile H₂ permeation of styrene/MAN co-grafted membranes was lower compared to the pure styrene grafted membrane before OCV hold tests. However, the styrene/MAN co-grafted membranes exhibited a significant increase in permeation after OCV hold tests. This is probably because the membranes with high MAN contents have higher graft level; and a more porous structure is formed in high graft level membranes as a result of the loss of grafts during OCV hold tests.

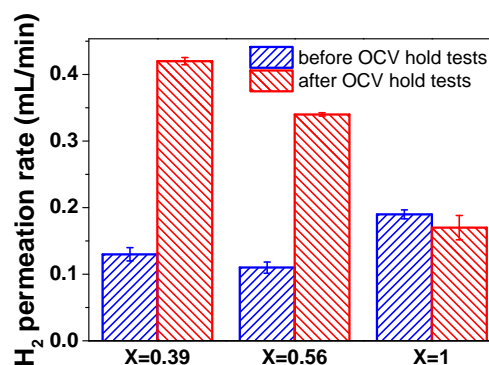


Figure 4. Hydrogen permeation rate of pristine and tested membranes after 100 hour OCV hold tests, measured electrochemically.

Durability of radiation grafted membranes can be improved by reducing gas crossover through the membrane. MAN seems to improve gas barrier properties. However, the current durability testing protocol has proven too harsh for the uncrosslinked membranes used here. Therefore, a shorter OCV hold test or altered conditions are necessary to make best use of *post mortem* tests. Since HFR is an indirect indicator of membrane degradation, other diagnostic methods (e.g. product water analysis) should be developed in the future for quantifying degradation rate.

References

- [1] L. Gubler, M. Slaski, F. Wallasch, A. Wokaun, G.G. Scherer, *J. Membr. Sci.* **339**, 68-77 (2009).
- [2] H. Ben youcef, L. Gubler, S. Alkan-Gürsel, D. Henkensmeier, A. Wokaun, G.G. Scherer, *Electrochem. Commun.* **11**, 941-444 (2009).
- [3] E. Endoh, S. Terazono, H. Widjaja, Y. Takimoto, *Electrochem. Solid-State Lett.*, **7**(7), A209-A211 (2004).
- [4] A. Barnabeo, W. Cereasy, L. Robeson, *J. Polymer Sci.* **13**, 1979-1986 (1975).
- [5] K. Cooper, M. Smith, *J. Power Sources* **160**, 1088–1095 (2006).

Membranes for fuel cells: Radiation induced graft copolymerization of styrene and methacrylic acid into ETFE

K. Jetsrisuparb, Z. Zhang, H. Ben youcef, G.G. Scherer, A. Wokaun, L. Gubler

phone: +41 56 310 21 62, e-mail: kaewta.jetsrisuparb@psi.ch

One of the attractive ways to modify the properties of a polymer used as membrane for fuel cells is through radiation induced graft copolymerization. This synthesis method allows a wide range of monomer selection as well as polymer base film. When grafting proceeds, monomers are covalently bonded to the polymer base film and favorable properties of the membrane can be obtained with a proper choice of the polymer materials. In the previous work, styrene was co-grafted with methacrylonitrile (MAN) into ETFE film and subsequently sulfonated, introducing proton conducting sites. The presence of MAN in the membrane results in reduced gas crossover compared to that without MAN and the lifetime of the membrane electrode assembly (MEA) containing MAN increased at least 5 fold in the fuel cell [1].

The MEA durability is significantly influenced by the presence of MAN. Therefore, MAN should be stable in the fuel cell environment. *Post mortem* analysis, however, showed that apart from a reduction of the content of the grafted monomers, the nitrile group of MAN undergoes partial hydrolysis during fuel cell operation, resulting in the formation of amide and carboxylic acid. This is not surprising since hydrolysis is favored by high humidity and acidity, as present in a typical fuel cell environment. We found that hydrolysis of the nitrile group is more pronounced in case of styrene / acrylonitrile membranes, implying that the alpha-methyl group may contribute to the resistance to hydrolysis [2].

In styrene / MAN co-grafted membranes, hydrolysis does not directly lead to chain scission because the nitrile group is not part of the backbone. However, it apparently reduces the number of nitrile groups and perhaps alters the properties of the membrane. For this reason, the influence of hydrolysis on membrane properties should be understood. The simplest approach is to include a co-monomer of styrene containing a carboxylic acid group, such as methacrylic acid (MAA), and investigate the resulting membrane properties. The focus of this study is the preparation of ETFE-*g*-styrene/MAA membranes including kinetics and composition analysis by FTIR.

Experimental

We modified partially fluorinated ETFE base film (25 μm , Dupont) using radiation induced graft copolymerization. The base polymer was activated through electron beam irradiation in air with a dose of 15 kGy. The pre-irradiated films were immersed into the grafting solution consisting of the monomer mixture (styrene and MAA) plus solvent (isopropanol and water). The grafting reactions were performed under nitrogen atmosphere at 60 °C. The grafted films were washed for several hours in water at 80 °C and soaked in water overnight to ensure the removal of homopolymer. Subsequently, the films were dried at 80 °C under vacuum. In a final step, sulfonic acid groups were introduced into the grafted film through sulfonation with 2 % chlorosulfonic acid in di-

chloromethane as explained elsewhere [1]. Composition analysis is done by FTIR.

Results

Several research groups have shown that copolymerization of styrene and MAA favors the formation of alternating chains under various conditions (reactivity ratios of styrene and MAA are lower than unity) [3]. Figure 1 represents the variation of graft level of styrene / MAA co-grafted into ETFE for different styrene molar fractions (X). The volumetric ratio of water to isopropanol used as solvent was kept constant at 0.14 (v/v). The graft level of the co-grafted films increases with styrene molar fraction. According to our previous findings of styrene / MAN grafted into ETFE, the grafting rate also enhances with increasing styrene molar fraction [4]. Higher graft level obtained with increasing styrene molar fraction could be attributed to the chemical compatibility of the monomer and the ETFE film. Since the apolar base film is more accessible to an apolar monomer and vice versa, diffusion of styrene into ETFE could be more favorable than that of more polar monomers such as MAN and MAA. Surprisingly, the graft level of pure MAA is higher than that of the co-grafted films with $X < 0.5$. This could be due to polymer formation in the reaction mixture, which decreases the diffusion rate of the monomers into the film, hence resulting in a decreased graft level. Polymerization of styrene / MAA in the solution was evidenced in the form of a gel-like reaction mixture at the end of the reaction.

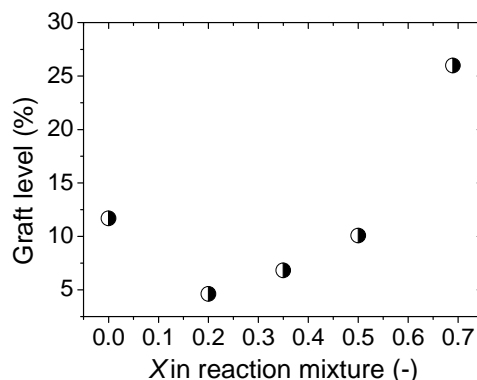


Figure 1. Effect of styrene molar fraction (X) in the reaction mixture on graft level for styrene / methacrylic acid grafting into ETFE. Reaction is carried out at 60°C for 1 hour.

In addition to the monomer composition, we can increase the graft level by using a suitable solvent. The effect of solvent was investigated by varying the volumetric ratio of water to isopropanol. Figure 2 shows that the graft level of co-grafted films increased dramatically with higher water / isopropanol ratios. A maximum graft level was reached with a water / isopropanol ratio equal to 0.33. Beyond this point the graft level of the grafted film did not change significantly. A further increase in the ratio of water to isopropanol above 0.6 leads to phase separation. While the graft level depends strongly on the water to isopropanol ratio, the styrene molar

fractions in all grafted films were comparable in spite of the graft level obtained. This implies that the change of the water to isopropanol ratio did not favor grafting of one monomer over the other, which would result in grafted films with different styrene molar fraction. On the other hand, the molar ratio of styrene to MMA exposed to the reactive sites should remain constant, independent of the water to isopropanol ratio.

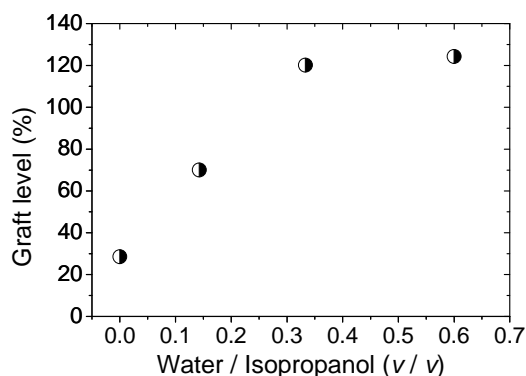


Figure 2. Variation of water to isopropanol ratio in the grafting solution. The concentration of monomers was kept constant at 20% (v/v) and $X(\text{styrene}) = 0.5$ in the reaction mixture; grafting time: 3 hours. X in the film of all grafted films is between 0.74-0.80.

A color change was observed from transparent ETFE film to milky grafted film, and to yellow after sulfonation. FTIR spectra of styrene / MAA co-grafted films and sulfonated membranes have shown the features of both styrene and MAA. A conspicuous change after sulfonation lies in the characteristic region of the carbonyl bond (Figure 3). In the co-grafted film, we found two separate characteristic peaks for the carboxyl group at 1740 and 1700 cm^{-1} , corresponding to the free carboxylic and dimeric carboxylic absorption [5]. The formation of the dimeric carboxylic acid by hydrogen bonding could take place between the grafted chains or even within the same chain. The free carboxyl group may indicate the carboxylic groups in the vicinity of styrene, which can be expected from an alternating copolymer.

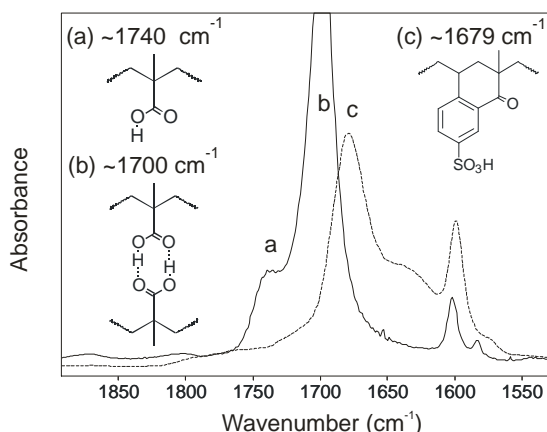


Figure 3. FTIR spectra of styrene / methacrylic acid co-grafted film (solid line) and sulfonated membrane (dashed line).

After sulfonation, no peak separation was observed and the absorption redshifted to 1679 cm^{-1} . According to the literature, this peak could be characteristic for a conjugated ketone. This observation seems reasonable, since a similar result was found for a sulfonated styrene / acrylic acid (AA) copolymer [6]. Mathew *et al* suggested

that cyclization of styrene and AA copolymer takes place during sulfonation by an internal Friedel-Crafts alkylation reaction, resulting in a cyclic ketone [6]. Concentrated sulfuric acid was used as the sulfonating agent. In case of styrene / MAA co-grafted films, the carboxyl group may be available for cyclization in the same fashion (Figure 4).

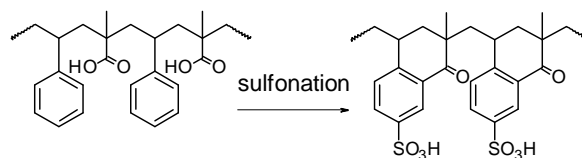


Figure 4. Possible mechanism of cyclization in styrene / methacrylic acid co-grafted film during sulfonation.

Conclusions

With the aim to understand the effect of hydrolysis on the membrane properties for fuel cell application, styrene / MAA were co-grafted into ETFE in the first step. The graft level of the co-grafted films varied with the monomer composition in the reaction mixture and the water / isopropanol ratio of the solvent. The styrene molar fraction (X) in the co-grafted film was not affected by the different water / isopropanol ratios when the concentration of the monomer mixture is kept constant.

Sulfonation of the co-grafted film was expected to give a polymer electrolyte membrane containing styrene sulfonic acid and MAA. However, this seems not to be the case as the graft copolymer possibly undergoes internal cyclization during sulfonation. Therefore, this type of membrane may not be suitable for the study of the effect of hydrolysis in membrane durability tests in the fuel cell.

References

- [1] H. Ben youcef, L. Gubler, S. Alkan-Gürsel, D. Henkensmeier, A. Wokaun, G.G. Scherer, *Electrochem. Commun.* **11**, 941-944 (2009).
- [2] H. Ben youcef, K. Jetsrisuparb, A. Waibel, L. Gubler, G.G. Scherer, A. Wokaun, *PSI Electrochemistry - Annual Report 2010*, 7-8, ISSN 1661-5379 (2011).
- [3] N. Sahloul, A. Penlidis, *Polymer. Plast. Tech. Eng.* **44**, 771-782 (2005).
- [4] K. Jetsrisuparb, H. Ben youcef, G.G. Scherer, A. Wokaun, L. Gubler, *PSI Electrochemistry - Annual Report 2009*, 9-10, ISSN 1661-5379 (2010).
- [5] J. Dong, Y. Ozaki, K. Nakashima, *Macromolecules* **30**, 1111-1117 (1997).
- [6] A. Mathew, P.C. Deb, *Macromol. Chem. Phys.* **199**, 2527-2532 (1998).

Analysis of composition in radiation co-grafted films via FTIR spectroscopy

Y. Buchmüller, K. Jetsrisuparb, L. Gubler

phone: +41 56 310 26 73, e-mail: lorenz.gubler@psi.ch

Radiation induced grafting is a useful method to synthesize proton exchange membranes (Figure 1). This method is simple, inexpensive and versatile, allowing the use of a wide range of materials and designability of membrane properties.

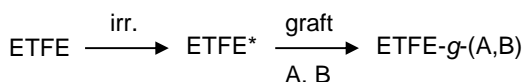


Figure 1. Schematic representation of pre-irradiation induced grafting of monomers A and B onto ETFE-base film.

Fourier transform infrared spectroscopy (FTIR) is a preferred method to quantify the composition of grafted films because of its simple and straightforward use.

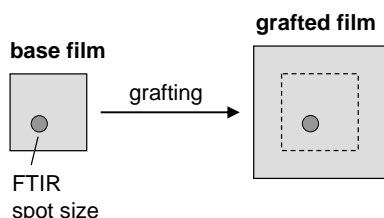


Figure 2. Schematic representation of the expansion of the film upon grafting. Since the spot size of the IR beam does not change, the dimensional change of the grafted film leads to a 'dilution' of the base polymer.

The introduction of the graft component leads to a lateral expansion and an increase in thickness of the film undergoing grafting (Figure 2). Since the transmission FTIR analysis of the polymer film probes an area of given size (spot size), the lateral expansion of the film leads effectively to a 'dilution' of the vibrational states in the probed volume. Therefore, the intensity of vibrational bands associated with the base polymer decreases with increasing graft level (Figure 3). The factor by which the intensity decreases is given by the area expansion of the film as a result of grafting, i.e., the ratio of the area of the grafted film and the area of the base film.

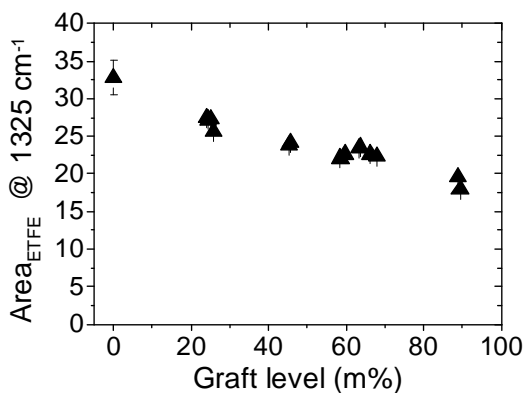


Figure 3. Decrease of ETFE-band intensity (area) at 1325 cm⁻¹ with increasing graft level.

Due to the same reason, the intensity of vibrational bands associated with the graft component will not increase in proportion to the graft level, but will be lower by the same factor related to the film expansion.

Therefore, for the determination of the fractional graft levels of different monomer units in co-grafted films, the vibrational bands associated with the monomer units need to be normalized to those associated with the base film:

$$I_{A,B} = \frac{A_{A,B}}{A_{\text{ETFE}}} \quad (1)$$

where $A_{A,B}$ is the intensity (area) of the vibrational band related to the monomer units A or B, and A_{ETFE} the intensity of a suitable ETFE base film band.

Two types of grafting reaction were carried out: grafting with a single monomer (A or B) and grafting with two monomers (A and B) onto the base film. In the first step, grafting with a single monomer was carried out to establish a calibration curve. The grafted films with different graft levels containing a single grafting monomer were subjected to FTIR analysis. The vibrational bands associated with the given monomer were normalized to the bands of the base film to obtain calibration curves for the grafted monomers (Figure 4).

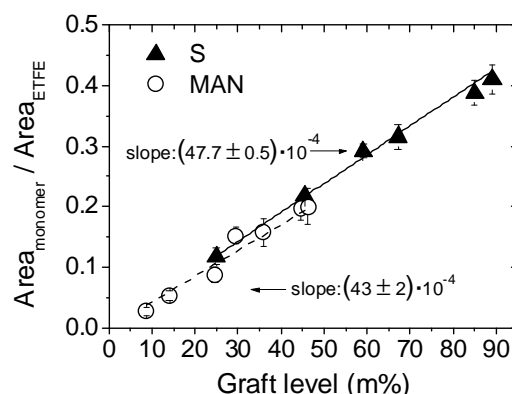


Figure 4. Calibration curves for styrene (S) and methacrylonitrile (MAN) grafted onto ETFE-base film. The vibrational bands chosen for S and MAN were at 1493 cm⁻¹ and 2235 cm⁻¹ respectively.

A cross-validation was performed, in which grafting with two monomers (S and MAN) was carried out. Using the bands associated with the two monomers in the co-grafted film and the calibration curve, the expected graft levels for A and B were calculated. The sum of the calculated graft levels have to be equal to the gravimetrically determined total graft level (Table 1).

graft level S	graft level MAN	combined graft level	measured graft level
23.3 ± 5.7	7.1 ± 1.6	30.5 ± 7.5	28.5
31.6 ± 3.5	10.8 ± 3.0	42.4 ± 6.4	40.3
34.9 ± 3.5	13.0 ± 4.9	47.9 ± 8.5	47.4

Table 1. Graft levels (calculated and measured) in mass-%.

The correlations of the values in Table 1 show the importance of this method. However, the uncertainty of the calculated values is not negligible. In conclusion, this method is useful for quantifying the content of monomer units grafted onto a base film.

Grafting of styrene onto plasma-activated porous polypropylene

L. Gubler, J.M. Conder, K. Jetsrisuparb, Y. Buchmüller, B. Deng, C. Padeste

phone: +41 56 310 26 73, e-mail: lorenz.gubler@psi.ch

The modification of porous polymer separators used in electrochemical devices by graft copolymerization could be used to impart the material with additional functionalities, for instance, to reduce the polysulfide shuttle in lithium-sulfur batteries. We have used the method of radiation grafting in the past to introduce proton conductivity into partially fluorinated films, such as FEP and ETFE, for fuel cell applications [1]. In this study, we explore the modification of a porous polypropylene (PP) substrate by plasma-activation, followed by grafting of styrene and sulfonation, as a model system to study the functionalization of porous materials. We compare the results to dense PP films grafted in bulk.

Experimental

Dense PP film (15 μm , Goodfellow) and porous PP (15 μm , Treo-Pore®) were used as the substrates. The dense PP film was electron beam pre-irradiated with a dose of 15 kGy in air. The porous PP was exposed to a low pressure Ar plasma (30 W, gas flow rate of 72 mL/min) for 5 min from both sides. The grafting reaction mixture consisted of styrene (20 v-%), isopropanol (70 v-%) and water (10 v-%). In some experiments, 0.25 wt-% of $(\text{NH}_4)_2\text{FeSO}_4$ (Mohr's salt) was added to the grafting solution to reduce the formation of homopolymer. Sulfonation was carried out in a 0.2 M solution of chlorosulfonic acid in dichloromethane at room temperature, followed by hydrolysis to yield the sulfonic acid.

Results

Both the dense and the porous PP films could be grafted with styrene successfully (Figure 1). The grafting of the dense film was slower, which could be a result of diffusion limitations associated with the transport of the monomer into the bulk of the material. For the porous substrate, grafting is probably only taking place at the surface, because the activation of the polymer via the plasma is limited to the surface [2]. Furthermore, a constant grafting rate is observed in case of the dense film, whereas in the porous substrate the grafting rate de-

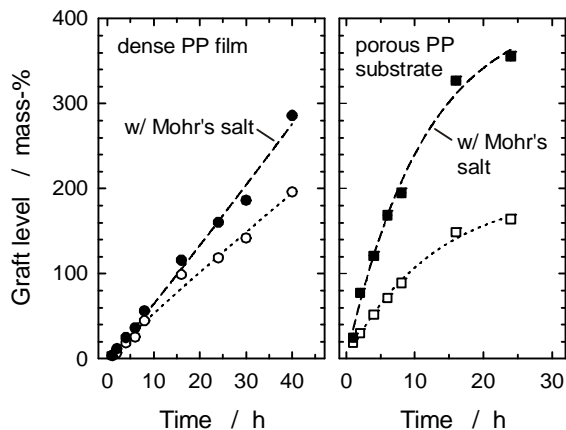


Figure 1. Comparison of grafting kinetics of styrene onto 15 μm PP dense film (pre-irradiation: 15 kGy) and PP porous substrate (plasma activation: 5 min). ●, ■: concentration of Mohr's salt $(\text{NH}_4)_2\text{FeSO}_4$ in the grafting solution: 0.25 wt-%.

creased with time. The addition of Mohr's salt, a common additive to reduce homopolymer formation [3], resulted in an increased grafting rate, in particular in case of the porous substrate.

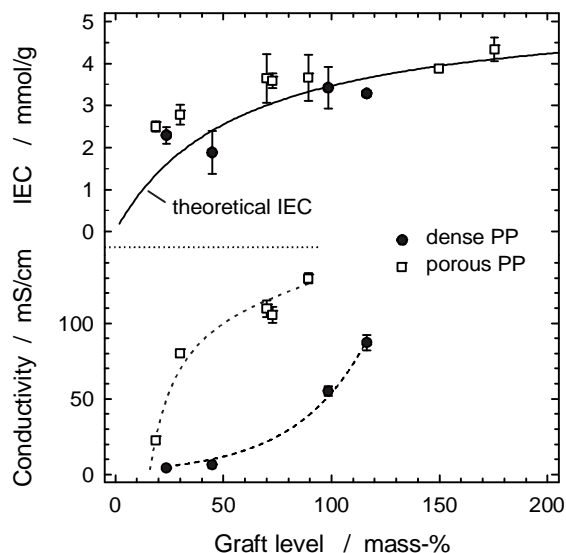


Figure 2. Ion exchange capacity (IEC) and proton conductivity in water swollen state at room temperature for sulfonated membranes.

The ion exchange capacity (IEC) is a measure of the amount of acid sites introduced upon sulfonation. The theoretical IEC corresponds to one sulfonic acid site per styrene unit. The samples based on the porous substrate show a trend of slightly higher IEC (Figure 2). Possibly, a small fraction of the PP is sulfonated as well. The much higher conductivity of the membranes based on the porous PP could be a result of facilitated proton transport in the open structure of the polymer. On the other hand, the dense PP substrate may not be well grafted in the center of the film. Detailed analysis of the polymer structure and distribution of the graft component is needed to address these questions.

Conclusion

Styrene was successfully grafted onto plasma-activated porous PP substrate to high degrees of grafting. Sulfonation yielded proton conducting membranes. This study can serve as a basis for more focused work on modifying porous separator materials to introduce specific functionalities, such as polysulfide rejection in lithium-sulfur battery electrolytes.

References

- [1] L. Gubler, G.G. Scherer, in: Handbook of Fuel Cells, Vol. 5, W. Vielstich, H.A. Gasteiger, H. Yokokawa (Editors), John Wiley & Sons, Chichester (UK), 313-321 (2009).
- [2] T. Desmet, R. Morent, N. De Geytner, C. Leys, E. Schacht, P. Dubruel, Biomacromolecules **10**, 2351-2378 (2009).
- [3] M.M. Nasef, E.S.A. Hegazy, Prog. Polym. Sci. **29**, 499-561 (2004).

Kinetic study on the effectiveness of HO• scavengers in fuel cell membranes

L. Gubler, W.H. Koppenol¹

phone: +41 56 310 26 73, e-mail: lorenz.gubler@psi.ch

The proton exchange membrane (PEM) used as polymer electrolyte in fuel cells suffers from attack by radicals created during cell operation. The hydroxyl radical (HO•) is particularly damaging due to its high oxidizing strength of $E^0(\text{HO}^*/\text{H}_2\text{O}) = 2.72 \text{ V}$ [1]. HO• and other radicals, such as the hydrogen radical (H•) and the hydroperoxyl radical (HOO•), are formed directly at the noble metal catalyst (direct mechanism) or via decomposition of H₂O₂ (indirect mechanism), which has been detected in operating fuel cells at a level of around 0.5 mM [2, 3].

It has been found that the incorporation of CeO₂ or MnO₂ particles, or the respective metal ions, into the membrane leads to a substantially lower rate of ionomer degradation, measured as fluoride released as decomposition product into the effluent water of the fuel cell. The stabilization mechanism is based on the multi-valent nature of the Mn and Ce ions: they act as HO• scavengers and thereby undergo oxidation. The reduced oxidation state is restored through the reactions with HOO• and H₂O₂ [4].

The formation of radicals from H₂O₂ as a precursor and attack of the perfluorosulfonic acid (PFSA) ionomer, e.g. Nafion®, typically used as membrane in the polymer electrolyte fuel cell has been studied in detail and serves as the basis for study reported [1]. Here, we investigate the kinetics of HO• scavenging and regeneration of the scavenger based on an extension of the established kinetic framework. Based on the findings, it is estimated whether the approach is also viable for stabilizing non-perfluorinated materials, such as radiation grafted membranes [5].

Despite the perfluorinated nature of PFSA membranes, these materials have weak points that are attacked by radical intermediates. Carboxylic end-groups, which are residues of the polymerization process, are preferred sites of attack in PFSA ionomers [6]. In addition, there is a growing body of evidence for side-chain attack mechanisms [7].

Kinetic scheme

The reactions added to the kinetic scheme reported recently [1] contain relevant reactions of Ce and Mn ions. It is important to note that a "Fenton-type reaction", i.e., $\text{M}^{2+} + \text{H}_2\text{O}_2 + \text{H}^+ \rightarrow \text{M}^{2+1} + \text{HO}^* + \text{H}_2\text{O}$ (M = Ce or

#	Reaction	Rate constant
1a	$\text{Ce}^{3+} + \text{HO}^* + \text{H}^+ \rightarrow \text{Ce}^{4+} + \text{H}_2\text{O}$	$3 \cdot 10^8 \text{ M}^{-1}\text{s}^{-1}$
2a	$\text{Ce}^{3+} + \text{HOO}^* + \text{H}^+ \rightarrow \text{Ce}^{4+} + \text{H}_2\text{O}_2$	$2.1 \cdot 10^5 \text{ M}^{-1}\text{s}^{-1}$
-2a	$\text{Ce}^{4+} + \text{H}_2\text{O}_2 \rightarrow \text{Ce}^{3+} + \text{HOO}^* + \text{H}^+$	$10^6 \text{ M}^{-1}\text{s}^{-1}$
3a	$\text{Ce}^{4+} + \text{HOO}^* \rightarrow \text{Ce}^{3+} + \text{O}_2 + \text{H}^+$	$2.7 \cdot 10^6 \text{ M}^{-1}\text{s}^{-1}$
1b	$\text{Mn}^{2+} + \text{HO}^* + \text{H}^+ \rightarrow \text{Mn}^{3+} + \text{H}_2\text{O}$	$3 \cdot 10^7 \text{ M}^{-1}\text{s}^{-1}$
2b	$\text{Mn}^{3+} + \text{HOO}^* \rightarrow \text{Mn}^{2+} + \text{O}_2 + \text{H}^+$	$10^5 \text{ M}^{-1}\text{s}^{-1}$
3b	$\text{Mn}^{3+} + \text{H}_2\text{O}_2 \rightarrow \text{Mn}^{2+} + \text{HOO}^* + \text{H}^+$	$3 \cdot 10^3 \text{ M}^{-1}\text{s}^{-1}$

Table 1. Reactions relevant to the fuel cell environment involving Ce and Mn ions. The rate constants are values at room temperature and low pH.

Mn), does not take place because it is thermodynamically not favored due to the high electrode potential of the two redox pairs, $E^0(\text{Ce}^{4+}/\text{Ce}^{3+}) = 1.44 \text{ V}$ and $E^0(\text{Mn}^{3+}/\text{Mn}^{2+}) = \sim 1.5 \text{ V}$ [9], in contrast to $E^0(\text{H}_2\text{O}_2, \text{H}^*/\text{HO}^*, \text{H}_2\text{O}) = 0.80 \text{ V}$.

In the simulation, the reactions constituting the basic kinetic framework (Table III in [1]) with the added reactions involving Ce or Mn (Table 1) are solved for steady-state of the intermediates, using a constant concentration for H₂ and O₂ of 10 and 7.5 mM, respectively, which are typical solubilities of those gases in water-swollen PFSA ionomer. We use a carboxylic end-group concentration of 18 mM, which seems to be representative for a pristine PFSA ionomer [10].

Results

Based on the rate of attack of HO• on the PFSA ionomer, the decomposition rate and corresponding fluoride emission rate (FER) can be calculated [1]. Under base case conditions in the absence of Ce or Mn scavenger, a HO• concentration of 1.9 fM and an FER of $1.3 \text{ pmol} \cdot \text{cm}^{-2} \cdot \text{h}^{-1}$ is obtained. The concentration of HOO• is on the order of 10^{-9} M . Upon doping of the membrane with Ce or Mn ions, the decomposition rate decreases (Figure 1a). Notable reduction of PFSA attack is obtained at a doping level of around 0.1 % for Ce and 1 % for Mn. Hence, Ce appears to be the more effective scavenger. The scavenging performance is mainly determined by the rate constant for the reaction with HO•, which is ten times higher for Ce (reaction 1a) vs. that of Mn (reaction 1b). At a doping level of 1 %, Ce scavenges 90 % of the HO• (Figure 1b). However, at that level, an impact on fuel cell performance is already no-

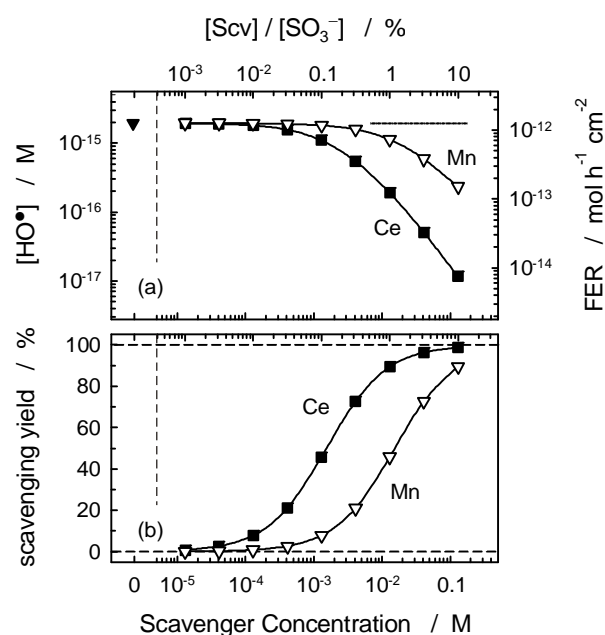


Figure 1. a) Concentration of HO• and corresponding fluoride emission rate (FER) from the ionomer; b) yield of HO• scavenging by Ce and Mn. COOH end-group concentration: 18 mM.

¹ Laboratory of Inorganic Chemistry, ETH Zürich

ticeable, because one Ce^{3+} takes the place of three protons [4].

The population of the two oxidation states of the metal ions is of paramount importance, since only the reduced metal ions (Ce^{3+} , Mn^{2+}) can scavenge HO^\bullet . The kinetic simulation shows that for both Ce and Mn the overwhelming majority of ions (>99.99 %) are in the reduced state. Therefore, almost all of the metal ions are available for HO^\bullet scavenging.

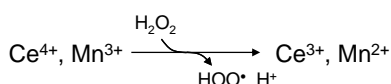
Regeneration of the scavenger

The metal ion is oxidized during the scavenging reaction. If the metal ion would be a “sacrificial” sink for HO^\bullet , the scavenging performance would gradually deteriorate as the inventory of the scavenger is slowly oxidized. It is estimated that in a stress test with accelerated chemical degradation at a cell temperature of 95 °C, Ce(III) at a doping level of 1 % would be consumed within less than a day. This, however, is not observed in the experiment. The mitigating effect of cerium can be maintained over hundreds of hours [5]. This implies that the scavenger is not consumed but instead acts in a catalytic manner. The reduction of the oxidized metal ion can take place through the reaction with H_2O_2 or HOO^\bullet . To compare the reduction reactions the effective first-order rate constants $k[\text{HOO}^\bullet]$ for reactions 3a and 2b and $k[\text{H}_2\text{O}_2]$ for reactions -2a and 3b are calculated (Table 2). The concentrations used for H_2O_2 and HOO^\bullet were $5 \cdot 10^{-4}$ M and 10^{-9} M, respectively.

Reaction	Ce^{4+}	Mn^{3+}
$\text{M}^{2+1} + \text{HOO}^\bullet \rightarrow \text{M}^2 + \text{O}_2 + \text{H}^+$	$2.7 \cdot 10^{-3} \text{ s}^{-1}$	10^{-4} s^{-1}
$\text{M}^{2+1} + \text{H}_2\text{O}_2 \rightarrow \text{M}^2 + \text{HOO}^\bullet + \text{H}^+$	500 s^{-1}	1.5 s^{-1}

Table 2. Effective first-order rate constants for the reduction of the metal ions by reaction with HOO^\bullet and H_2O_2 .

For both metals, the reaction of the oxidized ion with H_2O_2 represents the dominant mechanism for the regeneration of the HO^\bullet scavenger:



Therefore, it seems that the presence of H_2O_2 is crucial for the regenerative scavenging to be effective. The multi-valent nature of the metal ions, rapid scavenging of HO^\bullet , effective regeneration of the reduced metal, and favorable location of the redox potential well above 1 V to avoid a “Fenton-type” reaction is the basis of the stabilization mechanism (Figure 2).

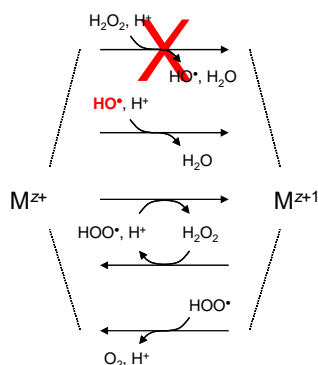


Figure 2. Mechanism of regenerative of HO^\bullet scavenging based on the multi-valent nature of a transition metal ion. At the same time, a “Fenton-type” reaction must be avoided.

Stabilization of non-perfluorinated membranes

Non-perfluorinated membranes, such as polyarylene membranes, polymer blends containing a polyelectrolyte, or radiation grafted membranes, are considered as alternative membranes due to their potential lower cost and improved particular functionalities. The stabilization of those materials against radical attack by incorporation of additives is a topic not well-explored today. An intrinsic drawback of polymers containing aromatic units is their high reactivity with HO^\bullet [11]. The rate constant for the reaction of poly(styrenesulfonic acid) (PSSA) with HO^\bullet is over two orders of magnitude higher than the rate constant for the attack of carboxylic end-groups in PFSA ionomer [1, 12]. With the high concentration of aromatic units in the membrane of around 1 M, an effective first-order rate constant for the reaction of HO^\bullet with PSSA-units of $5 \cdot 10^8 \text{ s}^{-1}$ is obtained. Any attempt at scavenging sizeable fractions of HO^\bullet with Ce is futile, as even at a doping level of 10 % the effective first-order scavenging rate constant, $4 \cdot 10^7 \text{ s}^{-1}$, is far too low. Two approaches suggest themselves to stabilize PSSA-containing or other non-perfluorinated membranes:

- Doping of membranes with phenolic compounds, which are known as antioxidants and show high rate constants for the reaction with HO^\bullet . Also, complexation with sulfonate anions is avoided.
- Devise mechanisms for repair or neutralization of formed PSSA intermediates, which have a lifetime on the order of μs [1].
- Targeting the decomposition of H_2O_2 , which is a precursor for HO^\bullet , by doping the membrane with a peroxide decomposition catalyst.

In any case, regenerative stabilization mechanisms are desired to avoid depletion of the scavenger and ensure long-term operation in the fuel cell over thousands of hours. Work in this direction is subject of current studies in the Electrochemistry Laboratory at PSI.

References

- L. Gubler, S.M. Dockheer, W.H. Koppenol, J. Electrochem. Soc. **158**, B755-B769 (2011).
- W. Liu, D. Zuckerbrod, J. Electrochem. Soc. **152**, A1165-A1170 (2005).
- C. Chen, T.F. Fuller, ECS Trans. **11**, 1127-1137 (2007).
- F.D. Coms, H. Liu, J.E. Owejan, ECS Trans. **16**, 1735-1747 (2008).
- L. Gubler, S. Alkan-Gürsel, G.G. Scherer, Fuel Cells **5**, 317-335 (2005).
- D.E. Curtin, R.D. Lousenberg, T.J. Henry, P.C. Tangeman, M.E. Tisack, J. Power Sources **131**, 41-48 (2004).
- L. Ghassamzadeh, K.D. Kreuer, J. Maier, K. Müller, J. Phys. Chem. C **114**, 14635-14645 (2010).
- A.J. Bard, R. Parsons, J. Jordan, Standard Potentials in Aqueous Solution, Marcel Dekker, New York (1985).
- S. Hommura, K. Kawahara, T. Shimohira, Y. Teraoka, J. Electrochem. Soc. **155**, A29-A33 (2008).
- G. Hübner, E. Roduner, J. Mater. Chem. **9**, 409-418 (1999).
- S.M. Dockheer, L. Gubler, P.L. Bounds, A.S. Domazou, G.G. Scherer, A. Wokaun, W.H. Koppenol, Phys. Chem. Chem. Phys. **12**, 11609-11616 (2010).

Durability of radiation grafted membranes under dynamic operating fuel cell conditions in comparison to Nafion 212 and Nafion XL-100 membranes

L. Gubler, L. Bonorand, J. Thut, G.G. Scherer

phone: +41 56 310 26 73, e-mail: lorenz.gubler@psi.ch

Partially fluorinated or non-fluorinated proton exchange membranes are developed with a view to reducing cost compared to the widely used perfluoroalkylsulfonic acid (PFSA) membranes. In addition, some of the inherent shortcomings of PFSA membranes, such as the propensity to catastrophic failure due to pinhole formation as a result of chemical degradation of the ionomer, are sought to be mitigated or eliminated.

In this context, radiation grafted membranes hold some promise, because estimated cost of production is up to an order of magnitude lower compared to PFSA membranes [1]. Furthermore, the method inherently allows to design and adjust key membrane parameters, such as ion exchange capacity and water uptake, via the choice of graft level and extent of crosslinking. Frequently, however, it is questioned whether these types of membranes can meet the performance and durability requirements under application-relevant conditions. In this study, we tested optimized 'Generation 2' (Gen2) radiation grafted membranes for performance and durability under dynamic load conditions. In Gen2 membranes, α -methylstyrene (AMS) and methacrylonitrile (MAN) are used as grafting monomers, and diisopropenylbenzene (DIPB) as crosslinker [2].

Experimental

ETFE base film from Dupont (thickness: 25 μm) and Saint-Gobain (12 μm) were electron beam irradiated in air for activation. The grafting reaction was carried out at a temperature of 55°C in a reaction mixture containing the monomers AMS, MAN and a crosslinker in proprietary ratios. Sulfonation of grafted films was carried out in a solution of chlorosulfonic acid in dichloromethane at room temperature for 5 h, followed by hydrolysis in water at 80°C for 8 h.

Membrane electrode assemblies (MEAs) were prepared through lamination of gas diffusion electrodes (Johnson Matthey ELE0162), subgaskets and membranes by hotpressing. Performance tests were carried out in water-cooled fuel cell stacks, comprising 6 cells with an active area of 30 cm^2 and a parallel flow field. Durability tests were performed in a similar hardware, yet with a cascaded serpentine flow field of 60 cm^2 active area, using a dynamic load profile (Figure 1). Electrochemical hydrogen crossover measurements were carried out intermittently around every 200 h to assess the mechanical integrity of the membranes. A crossover current density of 10 mA/cm^2 was defined as failure criterion. In all experiments, Nafion 212 and Nafion XL-100 membranes were used as benchmark.

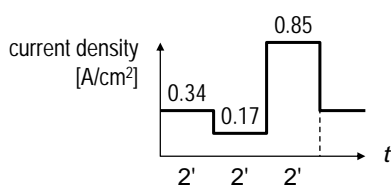


Figure 1. Dynamic operation protocol used in the durability test, using a sub-scale stack with 60 cm^2 active area, with three current levels for the simulation of a load cycle.

branes were used as benchmark.

Results

After a conditioning phase of the fuel cell stack for around 20 h at a current density of 0.5 A/cm^2 , a polarization experiment was performed to characterize performance of MEAs containing different types of membrane (Figure 1). The radiation grafted Gen2 membrane based on the 25 μm ETFE film had an ion exchange capacity of 1.7 mmol/g , whereas the membrane based on the 12 μm ETFE film had an IEC of 1.4 mmol/g . The polarization curves, averages of the cells in the stack comprising the same membrane type, show that performance approaching that of Nafion XL-100 is reached. The performance of MEAs based on Nafion 212 and Nafion XL-100 are almost identical. The difference in performance to the Nafion based MEAs is largely a result of the somewhat higher ohmic resistance of the PSI membranes.

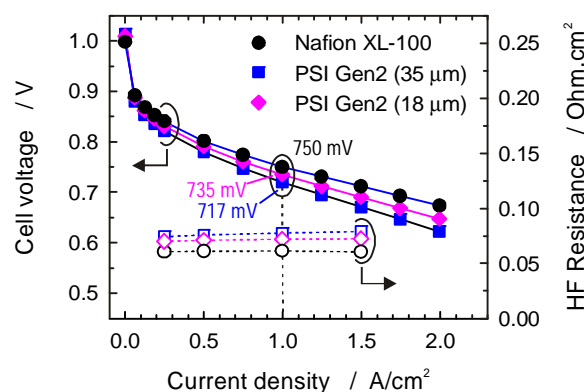


Figure 2. Polarization curves measured in a sub-scale 30 cm^2 fuel cell stack including high frequency (HF) resistance data. H_2/O_2 , cell temperature and gas dew points: 80°C, pressure: 2.5 bar_a. Commercial gas diffusion electrodes were used.

Reactant (H_2 , O_2) crossover via diffusion through the membrane is an important driving force for the formation of reactive oxygen species, which attack the membrane and cause polymer degradation. The hydrogen permeability, measured electrochemically, of the radiation grafted membranes is significantly lower compared to the Nafion membranes (Figure 3). This is a durability-relevant property, as it can be expected that fewer radical intermediates are formed.

In a first durability experiment, the stack comprising 6

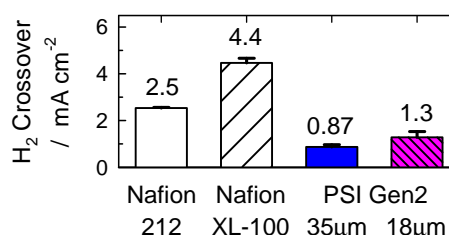


Figure 3. Hydrogen crossover measured electrochemically in H_2/N_2 mode at the beginning of test.

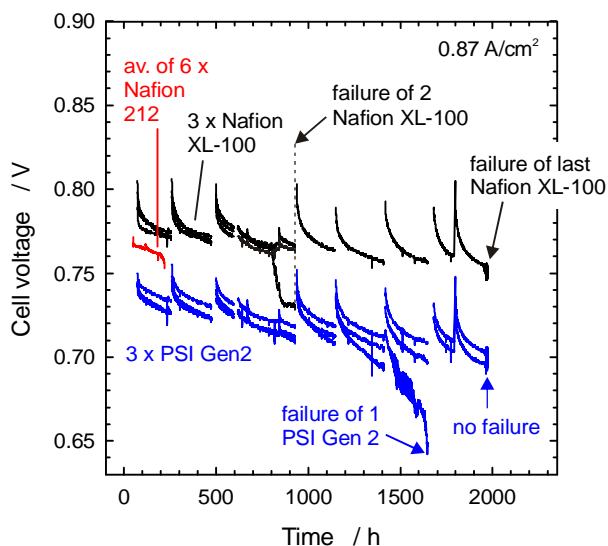


Figure 4. History of the durability test with cell voltage data extracted at the highest current setting. For the experiment using 6 Nafion 212 membranes, the average cell voltage is plotted. In the second experiment, 3 MEAs each comprising Nafion XL-100 and PSI Gen2 were tested simultaneously. H_2/O_2 , cell temperature: 80°C, gas dew points: 60°C, pressure: 2.5 bar_a.

cells with Nafion 212 was tested until failure due to excessive gas crossover occurred after around 200 h (Figure 4), with 4 of the 6 cells showing significantly higher crossover compared to typical beginning of test data.

In a second experiment, the 6-cell stack was equipped with 3 cells comprising Nafion XL-100, and 3 cells with PSI Gen2 membranes with a lower IEC of around 1.3 mmol/g, because we found that the performance at 1 A/cm² was only around 10 mV lower, yet the membranes with the significantly lower IEC are expected to show improved durability. The evolution of cell voltage for the different cells as a function of time at the highest current point (0.87 A/cm²) shows a gradual decrease in performance of 10 μV/h for Nafion XL-100 and 16 μV/h for the PSI membrane, respectively, on average. First failures were noted for 2 Nafion XL-100 cells after 927 h due to high crossover. Those cells were replaced with identical ones, yet their data is not plotted in Figure 4. The next cell to fail was a PSI membrane after 1'648 h as a result of MEA shorting. The last of the Nafion XL-100 cells failed after 2'088 h. The test was carried out for a total of 2'415 h, with the 2 remaining PSI membranes still intact at the end of test. The H₂ crossover of these PSI membranes had only increased marginally from 0.82 to 1.03 mA/cm², the high frequency resistance from 95 to 110 Ω·cm², indicating a low extent of membrane degradation.

The lifetime data of the various MEAs in this stack were subsequently collected and analyzed using Weibull statistics. The Weibull distribution is typically used in reliability engineering and failure analysis. In the context of fuel cell operation, reliability of MEA life is an essential criterion, because the life of the stack is determined by the failure of the first MEA [3]. In the Weibull plot, the percentage of failed samples is plotted against the time to failure of these units (Figure 5). The Weibull parameter m is a measure for the reliability of the components. Although there is limited life data for the two types of MEAs studied, the PSI membrane seems to offer durability superior to that of Nafion XL-100 under these test conditions.

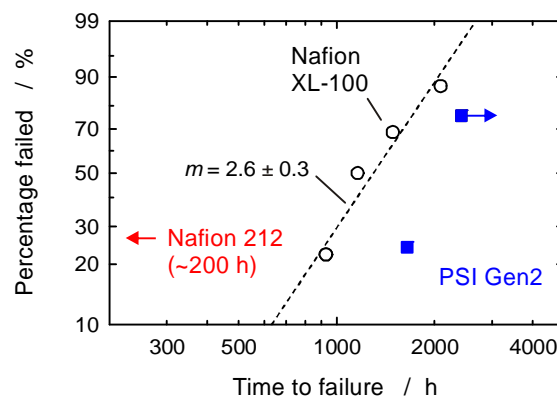


Figure 5. Analysis of MEA failure data in the fuel cell stack according to Weibull (m is the Weibull modulus).

Discussion

In addition to performance and durability, reliability is a key requirement for a fuel cell membrane, as pinhole formation and loss of mechanical integrity leads to catastrophic failure of the membrane and, with this, the stack. The degradation mechanism of Nafion membranes involves overall and local thinning, eventually leading to membrane failure. This was particularly evident for Nafion 212. Even Nafion XL-100, which is mechanically reinforced and contains additives against radical induced degradation, showed catastrophic failures after around 1'000 to 2'000 h. The PSI membrane, which does *not* contain stabilizing additives, compares very favourably with these commercial membranes, which is, on the one hand, attributed to the crosslinked nature of the ionomer. On the other hand, chemical degradation of properly designed radiation grafted membranes seldom leads to pinhole formation, because the base polymer acts, even in a degraded membrane, as an effective barrier.

Conclusion

Performance of optimized radiation grafted membranes of Generation 2 approached that of state-of-the-art Nafion membranes. The durability was assessed in a 6-cell stack at 80°C under dynamic load conditions. After a total time on test of 2'400 h, the only surviving membranes were PSI membranes. All Nafion XL-100 and one PSI membrane failed after various times. Upon exposure to a combined mechanical and chemical stress, Nafion membranes tend to develop flaws and fail, whereas the radiation grafted membranes appear to be more resilient and reliable. In forthcoming experiments, the durability of the thinner PSI membrane will be assessed.

References

- [1] L. Bonorand, G.G. Scherer, L. Gubler, this PSI Electrochemistry Laboratory Annual Report, 5.
- [2] L. Gubler, G.G. Scherer, in: Handbook of Fuel Cells, Vol. 5, W. Vielstich, H.A. Gasteiger, H. Yokokawa (Editors), John Wiley & Sons, Chichester (UK), 313-321 (2009).
- [3] M. Hicks, D. Pierpoint, in: Polymer Electrolyte Fuel Cell Durability, M. Inaba, T.J. Schmidt, F.N. Büchi (Editors), Springer Science+Business Media, New York, 385-396 (2009).

Effects of synchrotron radiation on ionomer used in PEFCs

J. Roth, J. Eller, F.N. Büchi

phone: +41 56 310 53 96, e-mail: joerg.roth@psi.ch

Synchrotron radiography and tomography are powerful diagnostic tools for studying the occurrence and characteristics of liquid water in the opaque porous structures of gas diffusion layers (GDL) in polymer electrolyte fuel cells (PEFC) [1-3]. However, it has been observed that fuel cell performance degrades rapidly under X-ray exposure [4].

The interaction of ionizing radiation of different nature with polymers like PTFE and sulfonated fluorocarbon polymers is described in the literature. Electron beams [5], soft X-rays up to 10 keV [6-8], and hard X-rays (1000 keV) [9] had been used, yet no detailed information of X-ray irradiation of all fuel cell components at energies typically used for PEFC investigations (10-20 keV) was found. It was demonstrated that the primary material damage is not caused by the X-ray photons directly but by secondary electrons released by X-ray metal interaction [10].

In order to justify the significant efforts to perform in-situ fuel cell experiments it is necessary to understand the mechanisms for the performance decay of fuel cells when exposed to synchrotron radiation (SR). Since the electrochemistry is severely affected, it is hypothesized that the damage takes place in the region of the catalyst layer and the membrane. The extent of material degradation on the membrane electrode assembly (MEA) is therefore explored.

Experimental

The materials under investigation are listed in Table 1. The parameters of exposure are similar to the XTM measurements of Eller et al. [3] The irradiation was executed at the TOMCAT beam line of the Swiss Light Source (SLS), a third generation synchrotron facility at the Paul Scherrer Institut, Switzerland [11]. The provided flux density of the source was in the order of 10^{13} photons $s^{-1} cm^{-2}$ at a beam cross section geometry of 5 mm by 25 mm. The size of the samples was 24 mm by 4 mm. Each sample type was exposed for 6 s, 60 s and 600 s. The SR dose rate is estimated based on the individual absorbance coefficients taken from [13] and a simple serial model of composite materials (Nafion, carbon and platinum in series).

Material	SR Dose rate [$mJ s^{-1} cm^{-2}$]
Nafion® 212	0.63
pMembrain™ H200	2.71

Table 1. Materials and Dose.

The fuel cell with an active area of $10 mm^2$ was designed to meet the requirements of SR-XTM imaging experiments (the details of the setup are described elsewhere [3]). The fuel cell was assembled with pMembrain™ H200 catalyst coated membrane (CCM) and corresponding pMembrain™ H200 GDL/MPL. During irradiation, the total area of the membrane was exposed to the beam at an impact angle of 90° (see also insert in Figure 1). In this configuration, the cell is exposed to the maximum possible dose. The cell was operated remotely controlled with H₂/O₂ in differential mode (stoichiometry

> 10) at $30^\circ C$ cell temperature. The gases had an inlet dew point at room temperature (unheated bubbler), the gas outlet pressure was ambient.

The equivalent weight (EW: $m [Polymer]/N[SO_3H]$) of the irradiated membrane samples was determined as follows: The dry exposed membranes were soaked in deionized water at $80^\circ C$ for 4 h. Then, the water was exchanged by 40 ml of 0.5 N KCl for replacing H⁺ by K⁺ (stirred for 48 h at room temperature). Afterwards, a titration was done with 0.05 N KOH with a Metrohm 702 SM Titrino. Finally, the membranes were dried at $80^\circ C$ in vacuum and weighed. In order to have sufficient ion exchange capacity for quantitative analysis, three stripes 20 mm by 4 mm had been processed together. Each test was done three times (9 stripes per exposure time) for statistical reasons. The mass of the polymer was obtained in the K⁺ exchanged form and corrected for the molar mass of potassium.

Results and discussion

To quantify the impact of the X-ray illumination, the PEFC was operated at a constant current density of $1.0 A cm^{-2}$. The irradiation sequence consisted of periods of 30 s X-ray exposure (with the exception of the initial exposure of 6 s), followed by stabilization periods lasting for several minutes. The plot in Figure 1 shows the average cell potential during exposure, assigned to the end-time of the individual exposures.

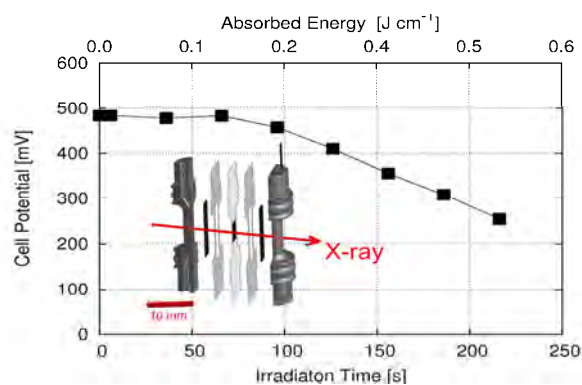


Figure 1. Irradiation effect on cell potential under operation. Conditions: 13.5 keV, X-ray energy flux: $22 mJ s^{-1}$; fuel cell: current: $1 A cm^{-2}$, $30^\circ C$. Insert: fuel cell in the orientation of exposure.

It is known that PTFE is very sensitive to irradiation thus a severe mass transport limitation in the GDL due to flooding seems possible but not very likely since previous experiments did not show unusual accumulation of liquid water. The fast degradation of the cell potential points rather to a damage mechanism acting on the catalyst layer or membrane, the most sensitive parts.

Possible changes of proton conductivity in the membrane can be detected by the characterization of the EW. The reliable determination of the EW of the membranes was possible for the irradiation up to 60 s only. For the longest exposure of 600 s, the mechanical integrity

degraded significantly and the risk of material loss during the preparation is increasing. This compromises the accuracy of the final weight in the ion-exchanged form. In addition to the mechanical disintegration, the pMembrain™ H200 material exhibited losses of the catalyst layer (colouring the water used for soaking) in dependence of exposure time (see Figure 2), also causing an increase of the experimental error for the determination of the dry weight.

The H200 membrane loses 14% of EW between a dose of 16 mJ cm^{-2} - 160 mJ cm^{-2} (6 s and 60 s exposure). The Nafion 212 samples experienced a loss in the same order of magnitude but with a less clear trend due to the experimental errors.

The results can be found in Table 2.

Exposure		0 s	6 s	60 s	600 s
Nafion® 212	Dose [mJ cm^{-2}]	-	3.8	38	380
	EW ^{sdv}	$938^{\pm 13}$	$890^{\pm 19}$	$860^{\pm 14}$	$857^{\pm 14}$
pMembrain™ H200	Dose [mJ cm^{-2}]	-	16	160	1600
	EW ^{sdv}	$1063^{\pm 45}$	$1046^{\pm 2}_5$	$894^{\pm 5}$	$919^{\pm 131}$

Table 2. Dose dependent EW.

It is obvious that the H200 experiences a more significant loss in EW but also the absorbed dose for this material is about 4 times higher due to the strong interaction of the Pt catalyst with the X-rays. This is in line with the observation of [10] who identified the secondary electrons formed on platinum as main responsible for damage.

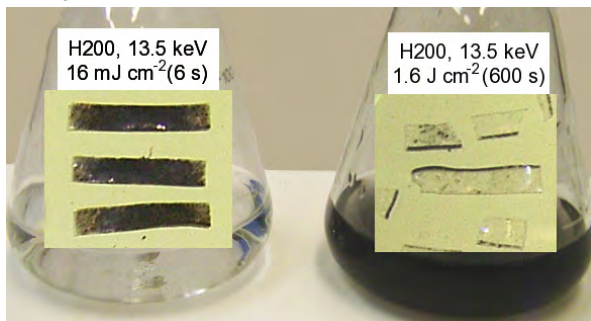


Figure 2. pMembrain™ H200 CCM and the soaking water for ion-exchange preparation. Samples: 6 s (16 mJ cm^{-2}) exposure (left) and 600 s exposure (1.6 J cm^{-2}) at 13.5-keV (right).

Conclusions

The observed decrease of the EW and the detachment of the catalyst layer from the membrane can explain the dramatic performance loss observed in fuel cell operation. The main damage mechanism seems the generation of secondary electrons emitted from the Pt in the catalyst layer contributing to the damage of the ionomer in the vicinity of the catalyst and possibly reducing the available electrochemically active catalyst surface area.

The change of EW in the membrane does probably not compromise the performance due to a loss of ionic conductivity, but, the formation of cracks and holes through the loss of mechanical integrity is one of the major failure modes caused by SR.

It may be concluded that state of the art SR-XTM based imaging of running cells strongly interferes with the fuel cell operation. When using a beam energy of 13.5 keV the dose, and thus the exposure time has to be as small as possible and for the given fuel cell setup limited to 100 s.

The recent development of high speed image capture and storage with exposures times in the order of 10 s for entire tomographic scans is promising and may be an enabler for SR-XTM studies, minimizing the radiation damage to a level below the statistical variations of in-situ fuel cell experiments for a reasonable number of scans. Shielding of the catalyst layer as a measure to reduce the primary degradation might not fully mitigating the problem since a change of the wetting properties of the GDL can also occur.

Acknowledgement

We would like to thank Fedrica Marone, Marco Stampanoni and the other members of the TOMCAT Team at the SLS for the excellent support in sample irradiation.

References

- [1] J. Eller, T. Rosén, F. Marone, M. Stampanoni, A. Wokaun, F.N. Büchi, *J. Electrochem. Soc.* **158**, B963-B970 (2011).
- [2] I. Manke, C. Hartnig, M. Grünerbel, W. Lehnert, N. Kardjilov, A. Haibel, A. Hilger, J. Banhart, H. Riesemeier, *Appl. Phys. Lett.* **90**, 174105 (2007).
- [3] R. Flückiger, F. Marone, M. Stampanoni, A. Wokaun, F.N. Büchi, *Electrochim. Acta* **56**, 2254-2262 (2011).
- [4] A. Schneider, C. Wieser, J. Roth, L. Helfen, *J. Power Sources* **195**, 6349-6355 (2010).
- [5] K. Lunkwitz, U. Lappan, U. Scheler, *J. Fluorine Chem.* **125**, 863-873 (2004).
- [6] Y. Zhang, T.K. Lippert, (Ed.), *Polymers and Light*, Springer Berlin / Heidelberg (2004).
- [7] J.A. Bearden, A.F. Burr, *Rev. Mod. Phys.* **39**, 125-142 (1967).
- [8] J. Wang, C. Morin, L. Li, A. Hitchcock, A. Scholl, A. Doran, *J. Electron Spectrosc.* **170**, 25-36 (2009).
- [9] A. Galante, O. Galante, L. Campos, *Nucl. Instrum. Methods* **619**, 177-180 (2010).
- [10] P.E. Laibins, R.L. Graham, H.A. Biebuyck, G.M. Whitesides, *Science* **254**, 981-983 (1991).
- [11] M. Stampanoni, A. Groso, A. Isenegger, G. Mikuljan, Q. Chen, A. Bertrand, S. Henein, R. Betemps, U. Frommherz, P. Böhler, D. Meister, M. Lange, R. Abela, *Developments in X-Ray Tomography* **6318**, 63180M (2006).
- [12] B. Henke, E. Gullikson, J. Davis; *Atomic Data and Nuclear Data Tables* **54**, 181-342 (1993). (<http://henke.lbl.gov/opticalconstants/filter2.html>).

FUEL CELLS

DIAGNOSTICS

Simultaneous testing and neutron imaging of 6 operating PEFCs: the multi-cell set-up

P. Oberholzer, P. Boillat, R. Siegrist, A. Kaestner, E.H. Lehmann, G.G. Scherer, A. Wokaun

phone: +41 56 310 56 37, e-mail: pierre.oberholzer@psi.ch

The PEFC technology has been attributed important research and development efforts in the last decade to gain in competitiveness for replacing internal combustion engines in cars. Beyond the cost reduction, the main technological challenges to be addressed are the improvements of performance (to reduce platinum amount), reliability and durability. The role of water in that context must be better understood.

The PEFC is a complex system and any improvement relies on the in-depth understanding acquired by modeling and experimental studies. In both cases, the use of simplified systems is of prime importance to get straightforward and reliable results. The so-called *differential cell*, meaning a single cell of reduced dimensions supplied by high stoichiometry gases, can be considered as an emulation of a small area of a cell in a stack, as the along-the-channel dimension and the stacking effects are suppressed. Such a system can be studied by the variation of the operating parameters (gas flow, gas composition, temperature) but also by the change of the design parameters (materials, geometry, compression). An efficient and reliable way to point out the influence of the design parameters is to run simultaneously different types of cells under identical operating conditions. If one single test bench is used and if some imaging aspects have to be fulfilled, then a dedicated set-up must be utilized. This was implemented by the *multi-cell* set-up, which is constituted of 6 differential cells.

Neutron imaging has proven in the last years to be a powerful visualization tool to track the spatiotemporal evolution of liquid water in the operating cell. In consequence, the increasing demand for neutron beam time is becoming a crucial reason for more efficient use. Aiming this goal, the multi-cell needed the construction of a new tilted detector based on the previous one [[1, [2], whose field of view was increased to 120 mm instead of the 25 mm in the existing one.

As an example of results delivered by the multi-cell, the influence of the MPL (microporous layer) on the water distribution and the performance will be shortly discussed hereafter.

Experimental

An overview of the multi-cell is given on the adjacent figure (Figure 1). As mentioned, the basic feature of this set-up is to provide controlled operating conditions of the cells.

For each side (anode or cathode), a common gas flow is supplied to all cells (subscript "in"). The 6 cell flows are derived from this common flow and are independently controlled (contrary to a fuel cell stack) after having flowed inside the cells (subscript "out"). So as to adjust the inlet pressure, to measure the relative humidity and to have a high gas flow (useful for gas switch techniques [[3, [4]), the main flow is supplied in excess so that part of it is returned to the test bench without flowing through the cells (subscript "by-pass").

To control the temperatures of the flowfields, the following thermal management design was realized. The main heating power is provided by a heating liquid ("Heating liquid") flowing in the aluminium housings (e.g. water). To compensate the difference of temperature that could appear due to the difference of heat losses between the cells, each flowfield of each cell (12 parts in total) can be heated by an electrical resistance ("Cell heater"). The flowfield temperature is measured via a Pt1000 resistance. In order to perform full and over-humidification conditions, a cooling gas (typically air) is flowed in a channel on the cell surfaces ("Cooling gas") so as to obtain a cell temperature colder than the housing temperature.

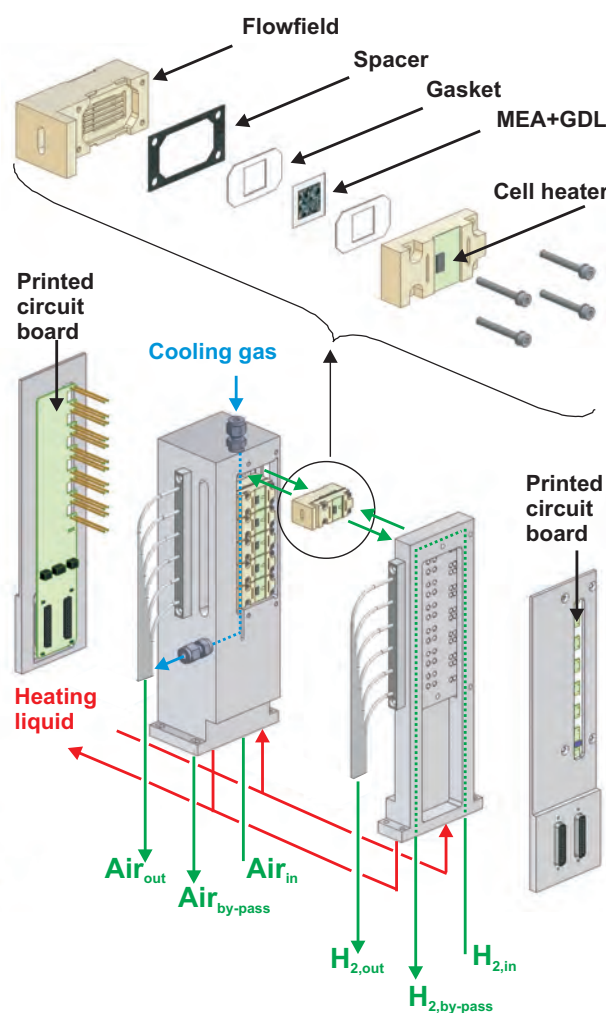


Figure 1. The multi-cell set-up.

The multi-cell is controlled in galvanostatic mode with a single load applying current on the serial connected cells. Voltages are measured independently (4 points measurement). Electrochemical impedance spectroscopy (EIS) can be performed simultaneously on the different cells.

All electrical signals are collected by printed circuit boards located in both external housings.

Given this base set-up, different kind of designs can be investigated. The flowfield geometry can be changed and the compression rate can be adjusted with the thickness of the spacer. Another option is to use different types of porous media. This is what is investigated hereafter.

Results

As an example of result provided by neutron imaging of the multi-cell, we investigated the differences of water distribution and performances induced by the presence of a MPL between the four combinations of GDL (gas diffusion layer) and MPL presented on the adjacent figure (Figure 2.a).

The voltages plotted (Figure 2.b) show that better performances are obtained when a MPL is present on the cathode side. The presence of a MPL on anode side does not significantly change the performance.

The water content profiles (Figure 2.c) reveal a maximum located for all cells in the cathode GDL. When no MPL is used, the maximum is closer to the MEA whereas it is shifted away from the MEA when a MPL is used on cathode side, as already proposed [[5]-[7]. The presence of a MPL on the anode side only seems to have an intermediary effect. The absolute quantity of water (the integral of the curves) is not much affected by the presence of a MPL, which is contrary to other suppositions [[6, [8]-[10].

Based on these observations, it can be argued that the difference of voltage are mass transport losses due to a flooding of the electrode pores and/or of a detrimental accumulation at the catalyst layer-porous media interface, as suggested in [[7]. As no major change of integral water content is observed, it can be concluded that the reduced mass transport losses observed in case a MPL is present on cathode side are not the consequence of an increased effective diffusivity due to lower water saturation in the GDL.

Conclusion

A new experimental set-up was realized to perform simultaneous testing and neutron imaging of 6 different designs of PEFCs operating at controlled conditions.

An example of application showed that the presence of a MPL does not change the average saturation level of the GDL. The water accumulation peak observed in the cathode GDL is shifted towards the MEA area when no MPL is present on cathode side. The poor performance observed in that case is probably due to flooding of the cathode electrode or to a water film formation at the electrode/GDL interface.

Acknowledgement

All people involved in the construction of the multi-cell are gratefully thanked for their contribution.

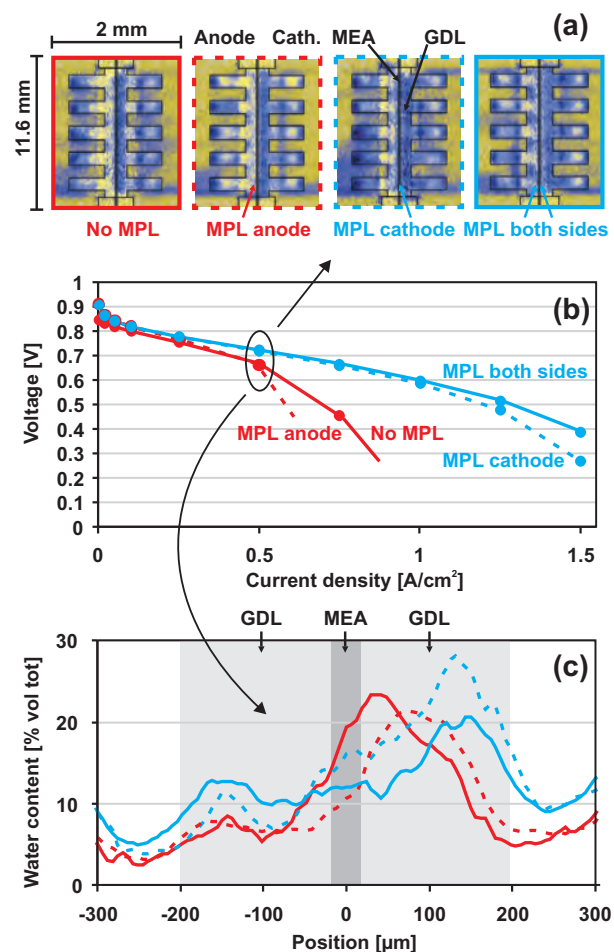


Figure 2. Effect of the MPL on the performance and water distribution.

References

- [1] P. Boillat, G. Frei, E. H. Lehmann, G.G. Scherer, A. Wokaun, *Electrochim. Solid-State Lett.* **13**, B25 (2010).
- [2] A. Kaestner, S. Hartmann, G. Kuehne, G. Frei, C. Gruenzweig, L. Josic, F. Schmid, E. Lehmann, *Nucl. Instr. Meth. A* **659**, 387 (2011).
- [3] P. Boillat, P. Oberholzer, B.C. Seyfang, A. Kaestner, R. Perego, G.G. Scherer, E.H. Lehmann, A. Wokaun, *J. Phys. Condens. Matter* **23**, 234108 (2011).
- [4] P. Boillat, P. Oberholzer, R. Perego, R. Siegrist, A. Kaestner, E. Lehmann, G.G. Scherer, A. Wokaun, *ECS Transactions* **41**, 27 (2011).
- [5] U. Pasaogullari, C.-Y. Wang, *Electrochim. Acta* **49**, 4359 (2004).
- [6] K.T. Cho, A. Turhan, M. Mench, *ECS Transactions* **41**, 513 (2011).
- [7] J.H. Nam, K.-J. Lee, G.-S. Hwang, C.-J. Kim, M. Kaviany, *Int. J. Heat and Mass Transfer* **52**, 2779 (2009).
- [8] J.S. Preston, U. Pasaogullari, D.S. Hussey, D.L. Jacobson, *ECS Transactions* **41**, 319 (2011).
- [9] A.Z. Weber, J. Newman, *J. Electrochem. Soc.* **152**, A677 (2005).
- [10] Y. Wang, P. Mukherjee, J. Mishler, R. Mukundan, R.L. Borup, *Electrochim. Acta* **55**, 2636 (2010).

High resolution neutron imaging of passive fed self-breathing PEFCs

P. Boillat, M. Weiland¹, P. Oberholzer, H. Reichl¹, E.H. Lehmann, T.J. Schmidt, G.G. Scherer, A. Wokaun

phone: +41 56 310 27 43, e-mail: pierre.boillat@psi.ch

Besides the often cited potential use in automotive applications, polymer electrolyte fuel cells (PEFCs) are an interesting alternative to batteries for small scale power supplies (e.g. for mobile applications or telemetry). In such applications, there is a dramatic need for the minimization of external components and passive, self-breathing cells (anode in dead-end mode and no forced flow on the cathode) are preferred. Such configurations imply different considerations in terms of mass and water transport than a cell with forced convective flows. In particular, the design of the openings in the current collector can have a strong impact on the water removal (see [1] for the general design approach). In this context, a neutron imaging visualization study including a current collector design variation was conducted.

Experimental

The multicell setup recently designed at PSI [2] was used for performing the simultaneous operation and imaging of 6 cells with different designs. The existing cathode flow field design with an active area of 1 cm² was modified to include an empty room. Air was flown through the bottom part of this room (Figure 1), so as to apply controlled conditions of humidity without creating a forced convection flow in the vicinity of the cell cathode.

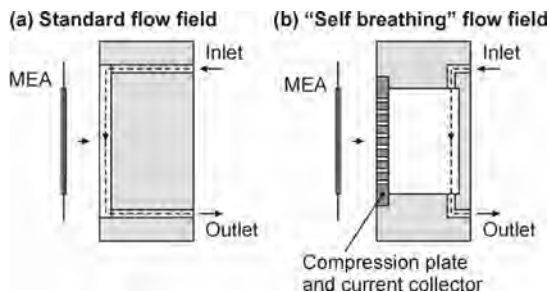


Figure 1. Modification of the standard cathode flow field to emulate a self-breathing cathode. The anode side flow field is not shown here.

On the cathode side, a gas diffusion layer was used which was compressed by a 300 µm thick gold plated aluminium current collector. The six different cell designs had different sizes (150, 300 or 600 µm) and counts (1, 3 or 5 rows) of openings in the current collector for letting the air diffuse into the cathode GDL. A gold plated compression plate with larger openings was used to allow a homogeneous compression of the GDL. On the anode side, no GDL was used and the catalyst coated membrane (CCM) was directly contacted to a flow field made of microchannels. The anode was operated in dead-end mode. In the experiment presented here, all cells were operated at a current density of 50 mA/cm², a temperature of 40°C and with a relative humidity of 20% for the air flow. Results with other operating conditions are to be presented in a forthcoming publication.

¹Technische Universität Berlin, Berlin, Germany

Results

The water distribution after 40 minutes of cell operation for six different current collector designs is shown in Figure 2. At this low humidity condition, water vapour diffusion plays an important role in the removal of water and the flow field which are more "open" (larger size or count of openings) retain less liquid water.

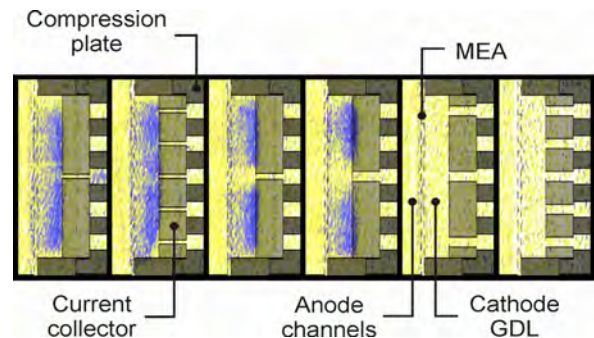


Figure 2. Observed water distribution (represented in false colour) with 6 different current collector designs.

The results clearly show that not only the number of holes (which determines the lateral diffusion paths in the GDL), but also the size of the openings has a large impact on the amount of water removed by evaporation. Another important observation is that, even in the designs with very little evaporation, no accumulation of back transported water in the anode occurs. Finally, it can also be mentioned that even in the closest designs with low removal of water by evaporation, the water amount in the GDL remains reasonable (approx. 20% of the total volume), indicating an effective lateral transport of liquid water even over distances of a few mm.

Conclusions

High resolution neutron imaging was used to study the effect of design parameters (number and size of openings in the cathode current collector) of small scale PEFCs with self-breathing cathodes. Using a newly designed multicell setup, six different designs were studied simultaneously, allowing a very effective use of beam time. An impact of the openings configuration on water removal by evaporation was clearly observed. Further observations such as the effective lateral transport of liquid water and the absence of water accumulation on the anode is of high interest for the modelling validation of such small scale passive cells.

References

- [1] M. Weiland, S. Wagner, R. Hahn, H. Reichl, Proc. Mikrosystemtechnik Kongress 2011, VDE Verlag Berlin, Offenbach, 394-397 (2011).
- [2] P. Oberholzer, P. Boillat, R. Siegrist, A. Kaestner, E.H. Lehmann, G.G. Scherer, A. Wokaun, this PSI Electrochemistry Laboratory Annual Report, 23.

Fast *in-situ* X-ray tomographic microscopy of PEFCs

J. Eller, J. Roth, F. Marone, M. Stambanoni, F.N. Büchi

phone: +41 56 310 45 80, e-mail: jens.eller@psi.ch

In 2011 the TOMCAT beamline of the Swiss Light Source (SLS) was upgraded with a new CMOS camera, enabling ultra fast *in-situ* XTM investigations of PEFC with temporal resolution of about 8 s. This acquisition speed limits irradiation of the cell, preventing radiation damage [1,2] and subsequent measurement bias. This way, PEFCs can be imaged several times before deterioration is arising. The stability of the 3D liquid water distribution in porous GDL structures was studied with a temporal resolution of 10 minutes and liquid water fraction data is presented [3].

Experimental

The new pco.Dimax camera at TOMCAT is based on CMOS technology (pco.Dimax, Germany) with 2016 × 2016 pixels on the chip and a pixel pitch of 11 μm. The exposure time ranges from 1.5 μs to 40 ms allowing ultra fast XTM scans within a few seconds or even faster than a second [4]. In combination with a continuous zoom objective microscope (ELYA solutions, Czech Republic) magnifications ranging from 2 × to 3.9 × can be achieved. At the highest magnification and for a full chip readout, this combination provides a pixel size of 2.89 × 2.89 μm², about 5.8 × 5.8 mm² field of view and 2.41E-17 m³ voxel size (2.41E-2 pL).

XTM scans in absorption contrast mode were performed at 13.5 keV beam energy. The exposure time per projection was 8 ms, so rotating the cell 180° while taking 1001 radiographic projections lead to a total SR exposure of 8 s per scan.

A specially designed single channel (0.8 mm width, 0.3 mm depth) PEFC with vertical MEA orientation [5] was used for the XTM experiments (see Figure 1). The cell was rotated during the XTM scans along its rotational symmetry axis. H200 (Umicore, Germany) catalyst coated membrane (CCM, 2-mil Nafion® membrane with Pt loading of 0.2/0.4 mg/cm² at anode/cathode) and Toray paper GDLs with MPL (Umicore) were used. In difference to the previous setup, the active area of the CCM was limited to SR beam height by laser ablation of the catalyst layer to 10 mm² (4.5 mm × 2.2 mm) by Laser Micronics GmbH (Germany).

After a drying procedure the cell was operated at 0.5 A/cm² in constant current mode at 30 °C cell tem-

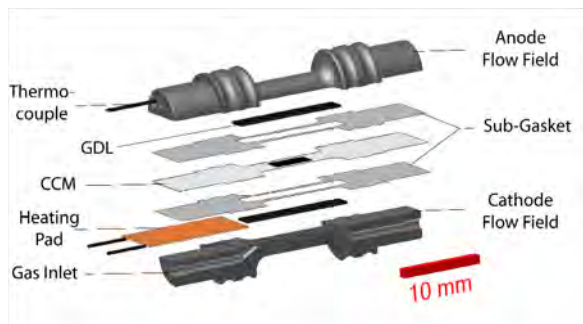


Figure 1 Components of XTM PEFC; the complete catalyst area of the laser processed CCM is exposed to the synchrotron radiation.

perature in differential mode (stoichiometries > 10) with H₂/O₂ humidified at room temperature (20 °C dew point). After 6 minutes of operation the cell was imaged for the first time and afterwards every 10 minutes until 66 minutes of operation (see Figure 2). Thereafter, the cell was dried again at 45 °C for 25 minutes and scanned once more to obtain XTM reference data of the dry GDL and flow field structures.

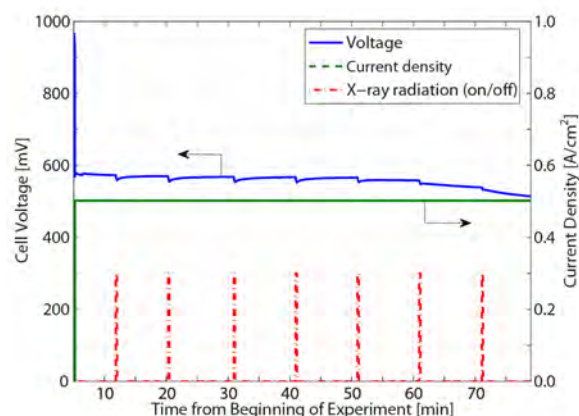


Figure 2 Cell voltage, current density and X-ray shutter state (shutter open at non-zero value) during XTM investigations of PEFC in constant current mode.

Methodology

Since the gray scale values of void, liquid and solid phases are overlapping in the raw XTM data, the liquid phase is segmented as introduced in [5] by subtracting the dry XTM data from the wet XTM data after careful alignment of the two data sets. This step is definitively necessary for cells with MPL, because there is hardly any chance to differentiate between MPL and liquid water even for trained human eyes (see Figure 3).

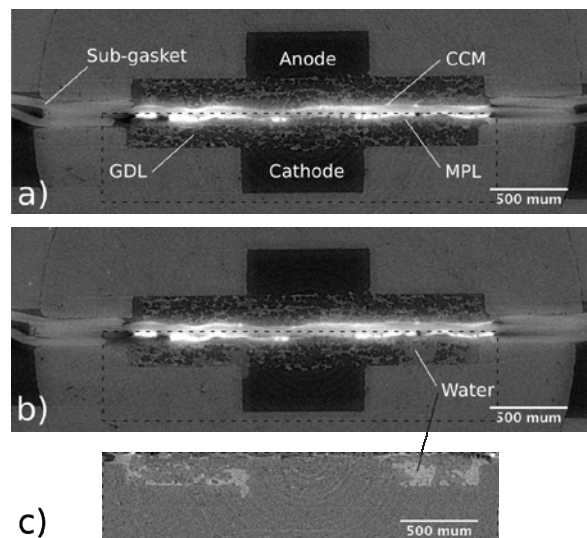


Figure 3 XTM ortho-slices in through-plane direction of a) dry XTM scan, b) wet XTM scan, and c) subtraction wet minus dry data for dashed area; in the wet scan there is no contrast between water and MPL.

Results

During the XTM experiments only minor performance losses of the PEFC were observed after a total 56 s of X-ray exposure (see Figure 2). From scan 1 to 5 the cell voltage drops typically around 15 mV during X-ray exposure, but it recovers to a stable value very close to the value before the scan. After scan 6 the cell voltage keeps decreasing slowly. This tendency is even enhanced after scan 7. A total loss of about 40 mV in cell voltage within 7 scans is considered as acceptable in terms of comparability of the PEFC operation conditions for the different scans.

The liquid water distributions in the cathode GDL domain of the consecutive XTM scans taken in 10 minutes steps were compared in terms of total water fraction as well as voxel-wise. For this a $701 \times 63 \times 1801$ voxel domain of the cathode GDL (about $2.0 \text{ mm} \times 0.18 \text{ mm} \times 5.2 \text{ mm} = 1.92 \text{ mm}^3$) was analyzed. For the chosen materials and operation conditions, it was found that, the total water fraction reached stable a value of 0.15 after 26 minutes (see Table 1).

Scan time [min]	Water Voxels [$\times 10^7$]	Water volume [mm^3]	Water fraction
6	1.11	0.268	0.140
16	1.28	0.308	0.160
26	1.22	0.294	0.153
36	1.18	0.285	0.148
46	1.20	0.288	0.150
56	1.19	0.287	0.150
66	1.17	0.284	0.148

Table 1. Water volume and water fraction of consecutive XTM scans.

The fluctuations of the water distribution of consecutive scans stabilized after 46 minutes at a value of about 10 %, both for newly filled and emptied water voxels (see Table 2).

Scan time [min]	Constant water voxels [$\times 10^6$]	Filled water voxels [$\times 10^6$]	Emptied water voxels [$\times 10^6$]
6	-	1.11 (100.0 %)	-
16	10.1 (79.0 %)	1.03 (21.0 %)	1.03 (8.1 %)
26	10.3 (84.9 %)	2.42 (15.1 %)	2.42 (19.9 %)
36	10.4 (88.1 %)	1.77 (11.9 %)	1.77 (15.0 %)
46	10.7 (89.2 %)	1.14 (10.8 %)	1.14 (9.5 %)
56	10.7 (90.2 %)	1.22 (9.8 %)	1.22 (10.2 %)
66	10.6 (90.4 %)	1.29 (9.6 %)	1.29 (10.9 %)

Table 2. Comparison of constant, new filled and emptied water voxels to previous XTM scan.

Furthermore, the similarities of the water distributions do indicate, that the water distribution approached towards the distribution measured after 66 minutes (see Table 3). This can be also seen in Figure 4, which shows development of the water distribution over time. In the GDL, the water distribution stabilizes after 26 minutes and domains with water volume fraction of up to 0.5 can be identified. Liquid water in the channel domain is found

mainly close to the outlet. Even though the water accumulation in the gas channel fluctuates over time the water distribution in the GDL does not.

Scan time [min]	Constant water voxels [$\times 10^6$]	Filled water voxels [$\times 10^6$]	Emptied water voxels [$\times 10^6$]
6	8.3 (70.6 %)	3.45 (29.3 %)	2.82 (23.9 %)
16	9.5 (80.9 %)	2.25 (19.1 %)	3.26 (27.8 %)
26	10.0 (85.1 %)	1.75 (14.9 %)	2.18 (18.5 %)
36	10.2 (86.8 %)	1.55 (13.2 %)	1.60 (13.6 %)
46	10.4 (88.7 %)	1.33 (11.3 %)	1.54 (13.1 %)
56	10.6 (90.4 %)	1.13 (9.6 %)	1.29 (10.9 %)
66	11.7 (100.0 %)		

Table 3. Comparison of the water distributions to the last XTM scan in terms of constant, new filled and emptied water voxels.

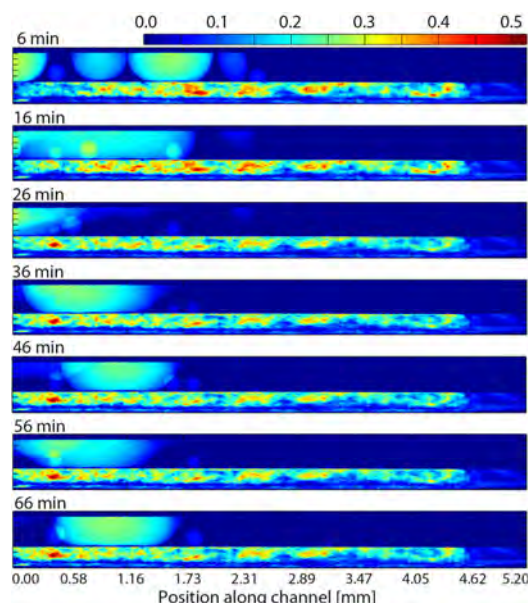


Figure 4 2D projection of the water fraction along the channel.

To derive statistical evidence it is necessary to measure and analyze an increased number of in-situ XTM fuel cell measurements. This is currently ongoing, in parallel with a revision and adaptation of the solid segmentation procedure to GDL materials with MPL.

References

- [1] A. Schneider, C. Wieser, J. Roth, L. Helfen, J. Power Sources **195**, 6349 (2010).
- [2] J. Roth, J. Eller, F.N. Büchi, ECS Trans. **41**, 371-387 (2011).
- [3] J. Eller, J. Roth, F. Marone, M. Stampanoni, A. Wokaun, F.N. Büchi, ECS Trans. **41**, 387-394 (2011).
- [4] R. Mokso, F. Marone, M. Stampanoni, AIP Conf. Proc. **87**, 1234 (2010).
- [5] J. Eller, T. Rosén, F. Marone, M. Stampanoni, A. Wokaun, F. N. Büchi, J. Electrochem. Society **158**, B963 (2011).

In-situ X-ray tomography on PEFC: The on-stage humidification concept

J. Roth, M. Citerne¹, R. Gaudenzi, J. Eller, F.N. Büchi

phone: +41 56 310 53 96, e-mail: joerg.roth@psi.ch

The investigation and optimization of the water management in PEFC has been in the focus for many years, since it strongly affects performance and durability. The progress in imaging methods based on neutrons and X-rays makes it possible to study the behaviour of liquid water and ice inside the porous opaque structures of gas diffusion layers (GDL) and flow fields. The state of the art temporal and spatial resolutions allow for 3D imaging in the GDL with time constants in the order of seconds for the X-ray tomography with synchrotron radiation (SR). The visualization of the water distribution can be used to test the hypothesis of gas/water interaction in porous structures where capillary forces dominate the physics and capillary fingering takes place [1]. One example of such a test can be found in Eller et al. [2].

The PSI has gathered experience in the field of fuel cell related ex- and in-situ synchrotron imaging experiments over the past 5 years. Mainly the high brilliance of SR at the SLS and the fast setup at the TOMCAT beamline made it possible that tomographic images of fuel cells during operation can be taken. The experimental boundary conditions are quite stringent to get the image quality that allows for quantitative segmentation. In this field PSI is among the most successful and experienced groups.

Several fuel cell setups had been evaluated in the past and are constantly under development. Recently the problem of radiation damage has been encountered and explored [3]. Based on the cognisance, the concept used in [2] is significantly modified.

Specification

The proof of concept of in-situ SR experiments was produced and so far, the experiments have been performed mainly at room temperature and ambient pressures. This is due to the fact that the existing vertical cell design gives high quality images at an increased active area, but is delicate to handle and difficult to make gas tight at elevated pressures. Furthermore, the orientation has the significant drawback of a maximum radiation damage. The new concept is a step back to the horizontal orientation with circular active area of 0.25 mm² to mitigate the radiation damage on the one hand and easier sealing on the other hand. The design is modular, meaning that flow field modifications can be implemented easily, it is shown in Figure 1. The cell design, introduced here, aims at the extension of the list of controlled variables towards pressure, humidification and sub-zero temperature operation. Here the humidification concept will be further elucidated.

For tomographic imaging, the pictures have to be taken from various angles. At synchrotron sources this is done by rotating the sample by at least 180° but up to 540° or more is possible under certain conditions. This means that the feeding tubes will wind up during the scan process and need to be sufficiently flexible (thin) and long enough (50 cm - 100 cm). The requirement of the humidification system is that hydrogen and air/oxygen will reach the active area in a condition of 100% RH at 80°C at a flow rate of 100 ml/min H₂ and 50 ml/min O₂ at ambient pressure.

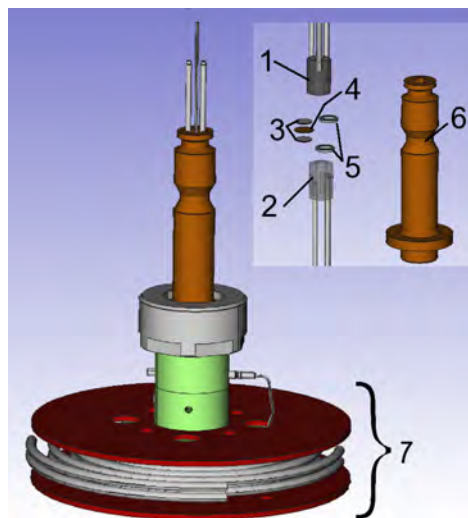


Figure 1. XTM fuel cell. 1. Anode flow field, 2. Cathode flow field, 3. GDL, 4. MEA, 5. Gaskets, 6. Outer shell, 7. Basement.

The main challenge is the absolute prevention of heat loss in the humidified gas before the active area is reached. Otherwise the dew point is incorrect, and even more severe, liquid water may enter the cell. For this reason, the gas humidification is located as close to the active area as possible.

Concept

All the parameters described previously evoke spatial constraints on the concept since the humidification shall be located on the rotation stage (see Figure 2).

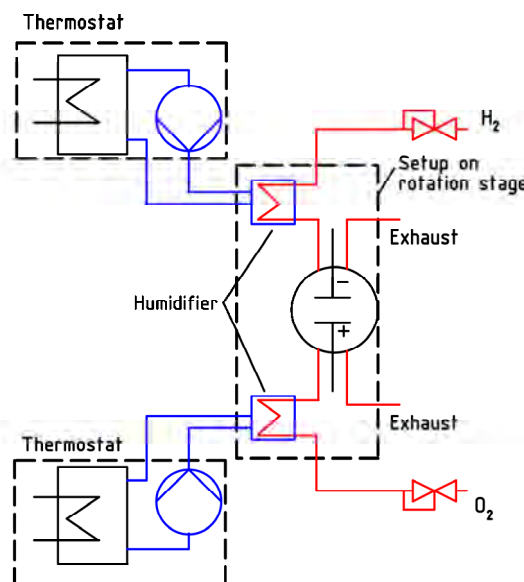


Figure 2. Fluid process flows sheet of XTM fuel cell. Red: Gas pipe. Blue: Water.

This way, the water and the gas are transported separately and condensation due to heat loss is no problem. Commercial humidification systems fail to meet these constraints and specifications, and a new design was developed. The concept of membrane humidification

¹ Università di Corsica Pasquale Paoli, Corte, France

with Nafion tubes was successfully evaluated experimentally [4]. In order to meet the spatial constraints, the length of the tube is a critical parameter and was consequently evaluated experimentally. The setup consisted of a water bath at a desired temperature. A Nafion tube with 0.63 mm inner, and 0.83 mm outer diameter ran through the bath. Similarly to a heat exchanger, the gas passing through the tube heated and humidified. Figure 3 shows the difference of the dew point of humidified oxygen from the desired set point of the bath (85°C) in dependence of gas flow rate for different tube lengths.

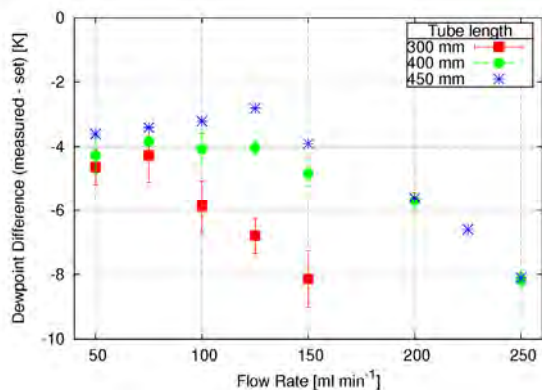


Figure 3. Humidification experiment with a Nafion tube in a water bath. The difference between water bath temperature (set-point: 85°C) and dewpoint (DP) of humidified oxygen at different gas flow rates for various tube length.

Based on the experiment it was found that a 450 mm long Nafion tube provides sufficient exchange area to meet the requirements. For this length at the required flow rate of 100 ml min⁻¹, the temperature off-set is in the order of 3 - 4 K as systematic error. Since the tube has a minimal bending diameter of about 20 mm it is reasonable to integrate such a tube into the basement of the fuel cell (Pos. 7 in Figure 1). In the chosen design the Nafion tube has the shape of a spiral winding in the location of the lower tube guiding disk (Figure 1). The tube is embedded in a groove filled with water. The water is delivered in counter flow, thus the gas leaves the humidifier with the highest possible temperature. The temperature is measured at the gas exit in the water by a Pt 100 sensor. The layout of the new basement with the integrated humidifier is presented in the cartoon of Figure 4.

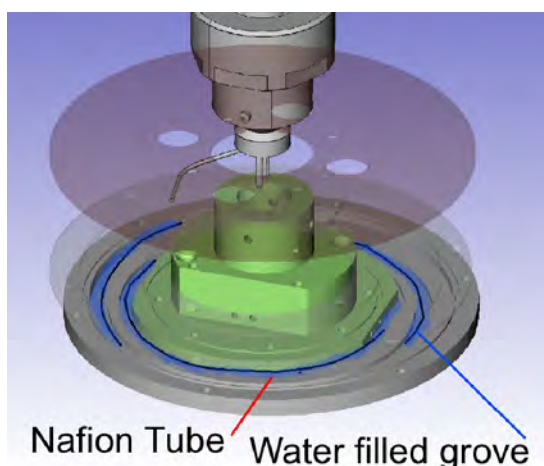


Figure 3. Basement for XTM-Fuel Cell with integrated cathode humidifier.

The evaluation of the humidifier was done at 50 ml min⁻¹ gas flow for different temperatures. It was found that an offset of about 5 K exists. This offset has to be taken into account and can be compensated.

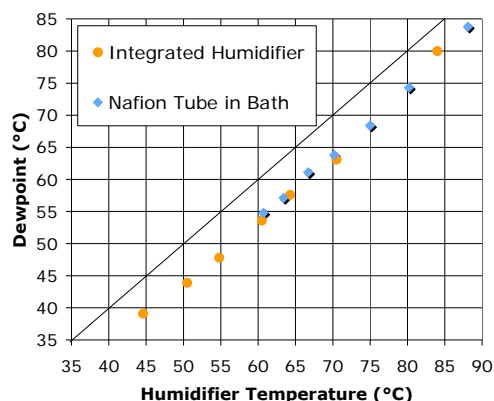


Figure 4. Humidification characteristic of the integrated humidifier at 50 ml min⁻¹ gas flow rate and of nafion tube in water.

Conclusion and Outlook

An integrated humidification system was designed for a fuel cell set-up for XTM measurements. With the humidification system, an important step towards fuel cell operating conditions of technical relevance is made. Based on the concept presented here, a humidification system for the anode can be developed. In addition to that, the cell set-up may be instrumented with a gas mixing option and outlet pressure control.

In the near future, a wide range of operating conditions become accessible for XTM investigations.

References

- [1] R. Lenormand, E. Touboul, C. Zarcone, J. Fluid Mech. **189**, 165-187 (1988).
- [2] J. Eller, T. Rosén, F. Marone, M. Stampanoni, A. Wokaun, F.N. Büchi, J. Electrochem. Soc. **158**, B963-B970 (2011).
- [3] J. Roth, J. Eller, F.N. Büchi, ECS Trans. **41**, 371-378 (2011).
- [4] M. Citerne, Master Thesis, Faculté des sciences et techniques de Corte, Università di Corsica (2011).

Factors determining the gas crossover through pinholes in PEFC membranes

S. Kreitmeier, A. Wokaun, F. N. Büchi

phone: +41 56 310 21 27, e-mail: stefan.kreitmeier@psi.ch

Cost and the durability still limit the commercial use of polymer electrolyte fuel cells (PEFC) for the application in the transport sector. The catalyst, its support and the polymer electrolyte membrane are the most susceptible components. In the past 40 years perfluorosulfonic acid (PFSA) polymers, such as Nafion, have been established as the standard material for PEFC membranes and its degradation under fuel cell conditions has been widely studied [1-3]. Besides proton transport and electric insulation, gas separation is the major function of the membrane in the PEFC. A loss of the gas separation may lead to a sudden death of the fuel cell forcing an immediate shut down of the fuel cell system [4]. In 2010 we have investigated the local gas transport characteristics of Nafion 211 membranes in different accelerated stress tests [5]. Pinhole formation is critical for the onset of enhanced membrane degradation as depicted in Figure 1. Once small pinholes are formed, the gas crossover increases, leading to enhanced chemical polymer decomposition at pinholes via radical formation and attack. The pinholes grow and the gas permeation rate is further boosted resulting in intensified chemical degradation in turns.

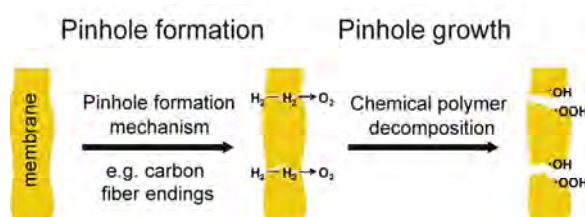


Figure 1. Mechanism for pinhole formation and pinhole growth.

As pinhole formation is an important, if not the most important initiation process for membrane degradation, their initiation and growth need to be carefully characterized. In 2010 it was found that their initiation can be reduced such as by using gas diffusion materials with proper surface morphology, reducing humidity fluctuations and operating the fuel cell at a low absolute humidity. When pinholes are formed, their growth rate may be reduced by lowering the gas crossover through pinholes. The influence of the temperature, the humidification, the gas diffusion electrode and polymer creeping on the gas crossover through pinholes is therefore investigated in 2011.

Experimental

In order to have consistent conditions, pinholes are implemented in the membrane artificially with electron beam lithography. The procedure was optimized to generate ideal cylindrically shaped pinholes as illustrated in Figure 2. A method using synchrotron based FTIR was developed to study local decomposition products next to pinholes.

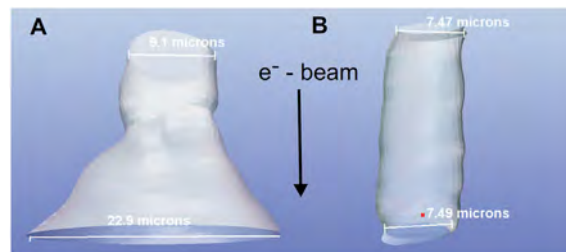


Figure 2. Electron beam lithography is optimized to produce ideal cylindrically shaped pinholes in Nafion membranes. A) 100 kV, 200 nA, 100 mC/cm²; B) 100 kV, 100 nA, 20 mC/cm².

Electron beam lithography was found to decompose the polymer partially around the pinhole by forming SOS, COOH and CO groups. The spatial absorbance of the carbonyl vibration at 1773 cm⁻¹ is shown in Figure 3 for a rectangular pinhole. Studying the effect of fuel cell operation on polymer degradation around pinholes (task in 2012) requires non destructive pinhole implementation methods. Therefore, alternative methods using focused ion beam or micro needle were successfully developed to implement pinholes without decomposing the polymer.

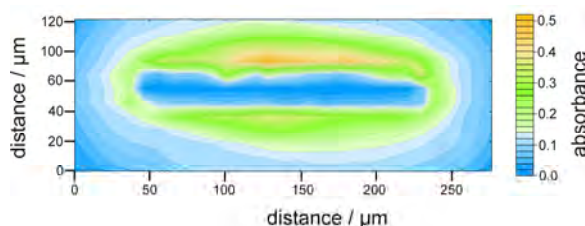


Figure 3. Spatial absorbance of the carbonyl vibration at 1773 cm⁻¹ of Nafion 211 with a rectangular pinhole (25x200 μm) in the center.

The gas crossover through pinholes is measured online with mass spectrometry by using a tracer gas concept [6]. Helium (10 Vol. %) is added as tracer to the anode stream during operation and its permeate is analyzed in the cathode stream. By varying the pressure difference between anode and cathode the pure convective gas crossover through the pinhole can be measured.

The gas crossover of perforated membranes is tested in-situ in a fuel cell with a linear flow field, an active area of 56 mm² and channel dimensions of 0.8 x 0.5 x 10 mm. Flow field plates are machined from stainless steel and coated with gold. Electrochemical components used are Nafion NR211 membranes and H400 carbon paper gas diffusion electrodes with a catalyst loading of 0.1/0.4 mg/cm² for the anode and cathode, respectively. The gas is extracted integral at the in- and outlets of the fuel cell by heated glass capillaries.

Results

The gas crossover through a pinhole is determined for different temperatures and humidities as shown in Figure 4. The gas crossover decreases with temperature, since the gas viscosity increases and the gas density decreases. However, the change in viscosity and density can not fully explain for the gas crossover decay of $0.25 \text{ pmol s}^{-1} \text{ Pa}^{-1} \text{ K}^{-1}$ for a $10 \text{ }\mu\text{m}$ pinhole.

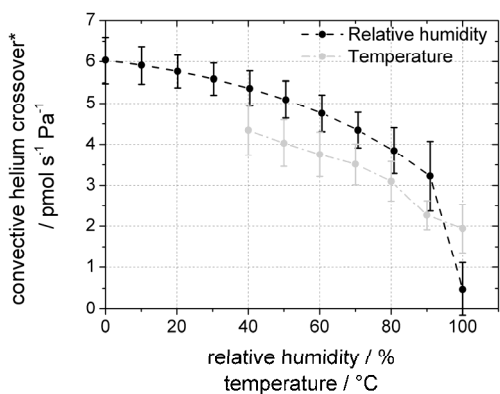


Figure 4. Gas crossover through Nafion 211 with a $10 \text{ }\mu\text{m}$ pinhole assembled with GDE H400 as function of the temperature (at 0% rH, gray) and the relative humidity (at $80 \text{ }^{\circ}\text{C}$, black).

The gas crossover through a pinhole decreases with the humidity, since membrane swelling reduces the pinhole diameter, which is verified by X-ray tomographic microscopy (XTM). At 100% relative humidity liquid water will seal the pinhole if the pressure gradient between anode and cathode is low enough. Figure 5 illustrates the blockage of pinholes by liquid water for different pinhole sizes and pressure gradients. For parameters being below the red line the pinhole is blocked by liquid water, else it is free. The pressure gradient of a fuel cell is typically in the range of 0-200 mbar, so liquid water will seal small pinholes. Since liquid water is usually not present in the inlets of a fuel cell, pinholes are free and the enhanced gas crossover will decompose the polymer close to the pinhole. This mechanism may be one reason for inhomogeneous membrane degradation, with higher degradation rates at the (drier) gas-inlets.

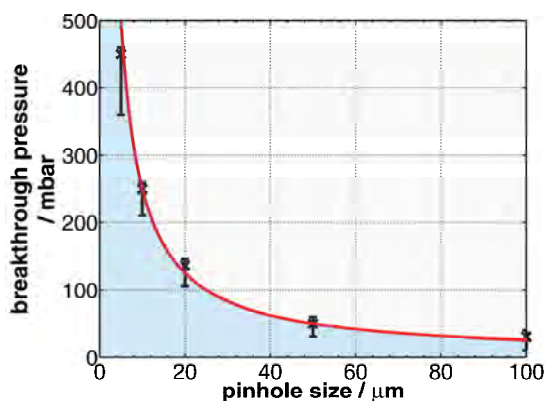


Figure 5. Breakthrough pressure for pinholes filled with liquid water. The blue area represents parameters where the pinhole is blocked by liquid water, the gray area where the pinhole is free of liquid water.

The micro porous layer of the GDE will become locally the main gas transport resistance of the MEA rather than the membrane, if the membrane has pinholes larger than about $20 \text{ }\mu\text{m}$. Figure 6 illustrates the gas crossover through a $10 \text{ }\mu\text{m}$ pinhole in Nafion 211 only and Nafion 211 assembled with the GDE H400. The bigger the pinhole, the more the GDE limits the gas crossover. Lowering the convective gas transport properties of the GDE, while maintaining the diffusive transport properties, may help to reduce the total gas crossover through degraded MEAs with pinholes in the membrane. Likewise, the gas crossover may not be an adequate indicator for the health state of highly degraded membranes with pinholes ($>20 \text{ }\mu\text{m}$). Processes degrading the gas transport properties of the GDE [7] would mimic a change in the health state of the degraded membrane with pinholes.

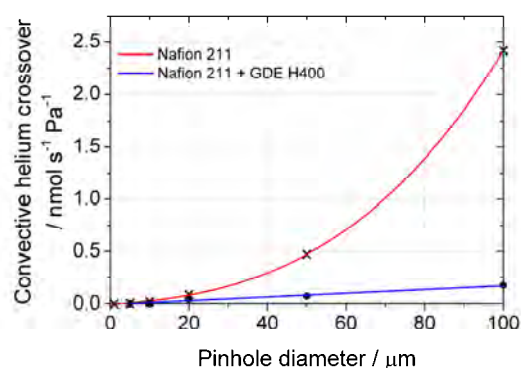


Figure 6. Gas crossover through a $10 \text{ }\mu\text{m}$ pinhole in Nafion 211 and Nafion 211 assembled with the GDE H400.

Finally, the gas crossover through a pinhole may be lowered over time due to polymer creeping. The clamping pressure leads to polymer creeping as observed by XTM. Polymer creeping may reduce the pinhole size and so will do the gas crossover. This has not been observed with the electron beam generated pinholes, because the pinhole production method may lead to a reinforcement of the polymer next to the pinhole as indicated by FTIR analysis (SOS group). So, polymer creeping may be prevented close to the pinhole.

References

- [1] A. La Conti, M. Hamdan, R. McDonald, Handbook of Fuel Cells – Fundamentals, Technology and Application, W. Vielstich, H.A. Gasteiger, A. Lamm (Editors) John Wiley & Sons, Chichester (UK) Vol. 3, 647-662 (2003).
- [2] M. Inaba, in: Polymer electrolyte fuel cell durability, M. Inaba, T.J. Schmidt, F.N. Büchi (Editors), Springer Science + Business Media, New York, 57-69 (2009).
- [3] H. Liu, H.A. Gasteiger, A. La Conti, J. Zhang, ECS Trans. 1, 283-293 (2006).
- [4] X. Huang, K. Reifsnider, Modern Aspects of Electrochemistry, Springer, 49, 1-43 (2010).
- [5] S. Kreitmeier, A. Wokaun, F.N. Büchi, PSI Electrochemistry Laboratory Annual report 2010, 41 (2011).
- [6] G.A. Schuler, Diss. ETH, No. 18883, ETH Zürich (2010).
- [7] H. Schulenburg, B. Schwanitz, N. Linse, G.G. Scherer, A. Wokaun, J. Krbanjevic, R. Grothausmann, I. Manke, J. Phys. Chem.C, 115, 14236-14243 (2011).

Model-based transient analysis of technical sized PEFCs

M. Zaglio, A. Wokaun, J. Mantzaras, F.N. Büchi

phone: +41 56 310 24 11, e-mail: felix.buechi@psi.ch

Comprehensive in-situ experimental investigation of all the processes involved in PEFCs during transient operation is currently not possible due to limited access to the core of the single cell, the membrane-electrode-assembly (MEA); therefore, modeling studies are necessary to better interpret the PEFCs behavior in dynamic operation.

In this work, a quasi two-dimensional model is developed to investigate the dynamic interactions of the fundamental processes at the cell level and the resultant loss mechanisms. Novelities of the model are the treatment of the liquid water behavior at the channel-gas diffusion layer (GDL) interface, as a function of the local humidity conditions in the channels, and the incorporation of membrane relaxation, a process occurring over hundreds of seconds after the change in operating conditions.

Aim of the work is to elucidate the influence of each transport process on the transient behavior of PEFCs, from tens of ms to hundreds of seconds time range, through an extensive comparison between experiments and simulations.

Experimental

The experimental setup consists of a linear cell with 200 cm² active surface. The MEA materials are a Nafion 212 membrane inserted between two cloth type GDLs (E-TEK ELAT V2.1) with a platinum loading of 0.5 mgcm⁻². The bipolar plates consist of 2 mm thick carbon plates (Sigracet BMA5, SGL Carbon Group), with 28 parallel 400-mm-long linear channels. To collect the current in different sections along the channels, 10 segmented current collectors are used, consisting of gold coated copper plates.

Experimental conditions in the discussed case are as follows: cell temperature 70°C, gas pressure at the channel inlets 1.5 bar, relative humidity 50% at anode and cathode inlets, stoichiometries of two (calculated at the final steady-state), and counterflow distribution of the anode and cathode gases.

Model

A 1+1-D, non-isothermal, two-phase transient model has been developed for investigating the transient behavior of the PEFC. The full set of conservation equations of multiphase, multispecies mass, momentum, species, charge, and energy for the ionomer membrane, for the GDLs, and for the solid part of the bipolar plates are solved for in the through-the-MEA direction, as described in the Appendix of [1].

Although the behavior of liquid water at the interface of GDL and distributor channels is still not clear, there is experimental evidence that liquid water can emerge and accumulate at the GDL-channel interface. Therefore, it is assumed that part of the liquid water evaporates, while the remaining part leaves the GDL in liquid phase. Therefore, the flux of liquid water N_{liq} [kgm⁻²s⁻¹] at the anode and cathode GDL-channel interfaces is determined by:

$$N_{liq} = \dot{m}_{evap} + \dot{m}_{liq} \quad (1)$$

with \dot{m}_{evap} and \dot{m}_{liq} the amount of water changing phase at the GDL interface with the channel and the amount of water leaving the GDL in liquid phase, respectively. The evaporation term is a function of the evaporation rate (fitted to be 10⁻⁴ [m³N⁻¹s⁻¹]) and of the difference between the local vapor partial pressure and the saturation pressure. The latter is assumed to increase linearly with the amount of liquid water accumulating at the interface, with a fitted slope of 5·10⁻³ [kgm⁻²s⁻¹].

A further process has been included to predict the slow transient in cell potential response to an increase in load, which occurs over hundreds of seconds as observed in the experiments. As suggested in the literature [2, 3], structural changes and polymer chain rearrangement mechanisms affect the ionomer water uptake following a change in operating conditions: initially, the water adsorption/desorption and the transport through the membrane determine the behavior of the water uptake; subsequently, the polymer relaxation determines a further uptake of water, influencing the ohmic overpotential for hundreds of seconds. In the model, a differential equation has been added simulating the increase in membrane water content, independently of the water activity at the interfaces, which can be assumed as constant at long times:

$$\frac{\partial S}{\partial t} = -\frac{1}{\tau}(S - S_{eq}) \quad (2)$$

with:

- $\tau = 300$ s the characteristic relaxation time, fitted to the experiments;
- S a parameter associated to the amount of water that the material can accommodate in the polymer, i.e. strain or volume. S affects the water content at the anode and cathode interfaces with the GDLs by:

$$\lambda = \lambda^0 + S \quad (3)$$

with λ^0 the water content at the anode and cathode interfaces obtained from the equilibrium with water activity.

- S_{eq} is determined according to λ^0 by:

$$S_{eq} = A_s \lambda^0 \quad (4)$$

with $A_s = 0.146$ a coefficient fitted to the experiments.

The 1-D through-the-MEA units are linked to the channel domains, where mass, momentum, and species transport is simulated in the perpendicular direction. Thus, local flows determine the boundary conditions to the 1-D units at each time and location, and all together are affected by the sink/source terms set by the transport processes in the 1-D models.

Results

In Figures 1a-b, the effect of the two aforementioned novel processes on the cell behavior is shown and the calculations are compared to experimental data. Figure 1a shows the calculated cell potential response to a stepwise increase in load from 0.125 to 0.5 Acm^{-2} , while Figure 1b shows the current density distribution along the channels at the final steady-state.

- Curves 1 in both figures are obtained by assuming no species transport along the channels and gas mixture compositions on both sides equal to the corresponding inlet values. The cell transient response is then of the order of seconds (99% of the final steady-state is reached in 20 s) and at least one order of magnitude shorter than the measured one (about 600 s). The current density distribution is flat due to the imposed constant properties distribution along the channels.
- Curves 2 are calculated when the transport processes in the *cathode* channel are included in the model. The cell response is fast (30 s), but the water vapor distribution increases along the cathode channel, better humidifying the cell, and the cell potential is about 40 mV higher than that of the previous case. The vapor accumulation along the cathode channel also affects the current density distribution, which increases along the channel. Toward the outlet it decreases again due to oxygen consumption.
- Curves 3 are obtained when the transport processes are included both in the anode and cathode channels, but the BC for the liquid phase at the channel-GDL interfaces is oversimplified and assumed to be zero (as in case 1 and 2).

Comparing the three cases, it is clear that the mass transport along the anode channels significantly slows down the cell transient response (steady-state is reached in about 100 s for case 3). The model predicts that the gas transport along the cathode channel has a strong influence on the cell potential by humidifying the membrane downstream, but the water production, evaporation, condensation, and finally the membrane hydration are too fast when compared to the measured cell response. At the anode side, there is no source of water except for the humidified gases at the inlet and the water transported through the membrane. Therefore, when the load is stepwise increased, the electro-osmotic drag instantaneously transports water from the anode side to the cathode side. At longer times, water diffuses back to the anode side better humidifying the membrane, the water content grows in the GDL and in the channels, and contributes to the cell potential recovery.

Even though the previous analysis has exposed the role of the transport processes in the anode and cathode channels on the cell response, the predicted transient is still about five times faster than the one observed experimentally. Therefore the two above-described processes are introduced.

- Curves 4 are obtained when the accumulation of liquid phase at the channel-GDL interfaces is added. The effect on the steady-state current density distribution is small, but the buildup of liquid water through the cathode GDL significantly affects the cell potential response, and the final steady-state is reached in about 150 s after the load change.

- Curves 5 are obtained by also including the membrane relaxation process.

The refined model predicts a transient time of 550 s to reach 99% of the final steady-state, a major improvement as compared to the other cases. Despite their large effect on the cell potential response, these processes have a minor influence on the current density distribution (curve 5 in Figure 1b). Up to 100 s, the water transient distribution is mainly determined by the electro-osmotic drag, by the water diffusion in the membrane, and by the liquid water accumulation in the GDL, and the original 1+1-D model reaches the final steady-state at this time scale. Then, the water content increases by ca. 15% in the next 500 s due to the relaxation of the polymer.

Conclusions

The developed model is a valuable tool to study the cell behavior during transient operation. When compared to experiments, the processes that have been included in previous models are not sufficient to adequately predict the cell transient response to a change in load. Herein, two novel processes are included to increase the model reliability: the liquid phase exchange at the GDL-channel interface, which determines the accumulation of liquid water through the GDL, and the relaxation of the membrane, which affects the membrane water content and its ionic resistance.

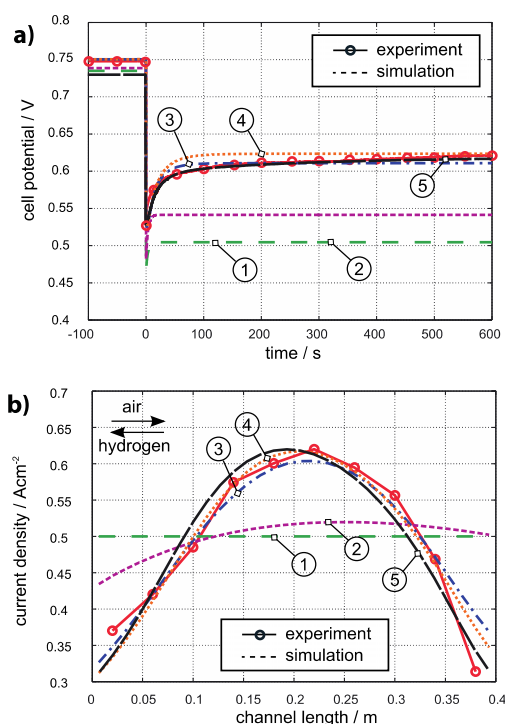


Figure 1. Comparison between experiments and simulations: a) cell potential time response to a load change at $t = 0$ s; b) current density distribution along the channels at the final steady-state. Curve numbers are discussed in the text, operation conditions are described in Experimental.

References

- [1] M. Zaglio, A. Wokaun, J. Mantzaras, F.N. Büchi, *Fuel Cells* **4**, 526-536 (2011).
- [2] M.B. Satterfield J.B. Benziger, *J. Phys. Chem. B* **112**, 3693-3704 (2008).
- [3] L.M. Onishi, J.M. Prausnitz, J. Newman, *ECS Trans.* **16**, 139-153 (2009).

Saturation dependency of effective GDL gas transport properties

J. Eller, T. Rosén, N. Prasianakis, J. Kang, I. Mantzaras, F.N. Büchi

phone: +41 56 310 45 80, e-mail: jens.eller@psi.ch

The combination of X-ray microscopic tomography (XTM) and computational fluid dynamics (CFD) is known to provide insight into the ex-situ gas transport properties of dry gas diffusion layers (GDL) [1, 2]. The availability of phase segmented *in-situ* XTM data [3] allowed deriving saturation dependent values of permeability and relative diffusivity of operating PEFCs.

Experimental

Phase segmented XTM data (solid, liquid, void) of single channel PEFCs [3] scanned at the TOMCAT beamline of the Swiss Light Source was used in conjunction with CFD calculations. The cells were equipped with Toray TGP-H-060 GDL (20% PTFE, no micro-porous layer) and operated at a current density of 0.45 A/cm² at 30 °C and gases (H₂ and O₂, stoichiometries > 10) humidified at room temperature (20 °C). The GDL domain was analyzed independently for channel and rib domains. The sample size for the channel domain was about 600 × 150 × 80 voxels (1100 × 278 × 148 μm³), while the sample size for the rib domain was slightly smaller due to GDL compression and cell geometry.

Methodology

In the calculation of the permeability values a single component three dimensional Lattice Boltzmann model (D3Q27) was used for the modeling of the gas flow. The flow driven by a uniform forcing field is shown as streamlines in Figure 1. Gas phase relative diffusivity was calculated with the DiffuDict module of the GeoDict software (Fraunhofer ITWM, Germany). The liquid water of the wet GDL was treated as immobile during the numerical calculations.

Results

The liquid saturation of the GDL, produced by the electrochemical reduction of oxygen to water was not homogeneous throughout the GDL of the operating PEFCs. This is due to local differences between the channel and rib domains and in channel direction possibly due to

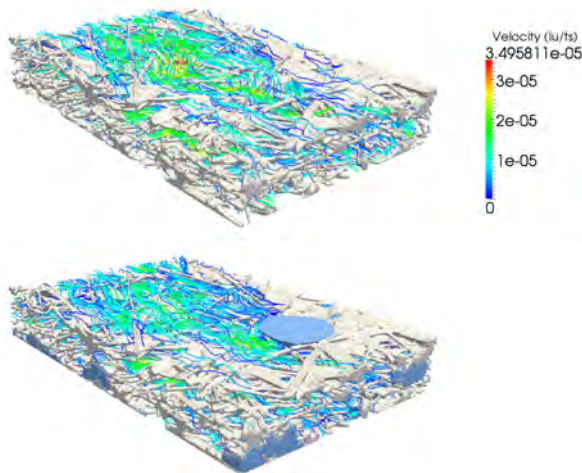


Figure 1. Visualization of streamlines of LBM permeability calculations of dry (top) and wet (bottom) GDL sample in contact with flow field channel; velocities given in lattice units.

analysing domains smaller than the representative equivalent volume of the material. Despite this, there were still similarities of the liquid water distribution between the regions. More liquid water was found under the rib sections and by pore diameter analysis it could be shown that the water resides in the larger pores. The mean pore diameter of the gas filled pore space of the channel domains reduced from 31 μm in case of dry GDL to 28.5 μm for wet GDL, and from 29 μm to 24 μm for the rib domains, respectively.

Power law relationships commonly used in PEFC modelling [5] linking the effective gas transport properties directly to the saturation of the samples could be proven (see Figure 2). For the saturation-*permeability* relation an exponent of about 3 was found for both in-plane and through-plane directions. A similar value of 3.3 was found for the through-plane direction of the saturation-*relative diffusivity* relation, while for the in-plane direction an exponent of about 2 was found.

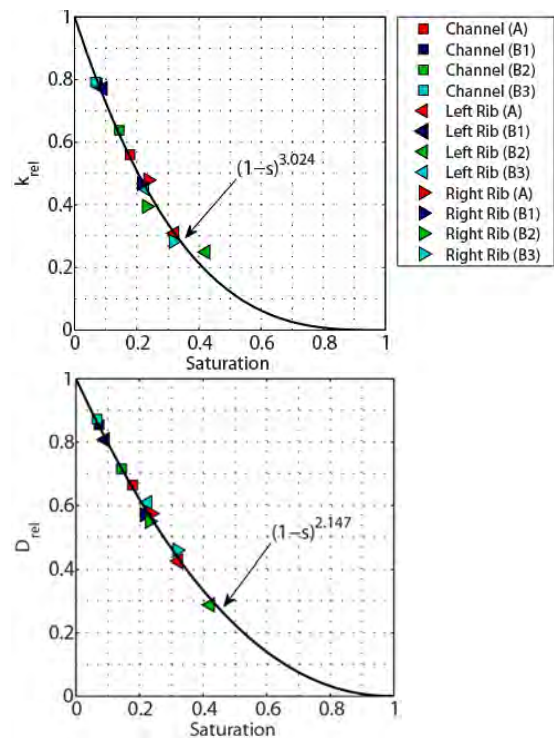


Figure 2. In-plane saturation dependence of normalized permeability ($k(wet)/k(dry)$, top) and normalized relative diffusivity ($D_{rel}(wet)/D_{rel}(dry)$, bottom).

References

- [1] J. Becker, R. Flückiger, M. Reum, F.N. Büchi, F. Marone, M. Stampanoni, J. Electrochem. Soc. **156**, B1175 (2009).
- [2] P. Rama, Y. Liu, R. Chen, H. Ostadi, K. Jiang, J. Fuel Cell Sci. Technol. **7**, 031015-1 (2010).
- [3] J. Eller, T. Rosén, F. Marone, M. Stampanoni, A. Wokaun, F. N. Büchi, J. Electrochem. Soc. **158**, B963 (2011).
- [4] S. Litster, N. Djilali, Transport Phenomena In Fuel Cells, Eds. B. Sundén, M. Faghri, WIT Press, Southampton, 175-213 (2005).

Locally resolved current measurements in high temperature PEFCs

G. Neophytides, I.A. Schneider, A. Wokaun, T.J. Schmidt

phone: +41 56 310 21 65, e-mail: george.neophytides@psi.ch

Locally resolved measurements can provide a great insight of the operation and performance behavior of a PEFC. Along the channel locally resolved measurements, have been used by Schneider et al. to investigate aspects in the impedance response of low temperature PEFCs and address, e.g., mass transport issues [2,3]. The same approach has been used in high temperature PEFCs after some modifications to the cell, leading into the locally resolved I/E measurements along the flow field channels.

Experimental

The experimental setup of the long-cell is well established and already used in numerous experiments [2,3]. The membrane electrode assemblies (MEAs) consist of a high temperature stable polymer imbibed by phosphoric acid. The operation temperature was 170°C, the cell was operated galvanostatically under steady state conditions of 0.32 A/cm² and dry gas feed with stoichiometries of 1.2 for H₂ and of 2 for O₂ in counter flow. The experiments involved both the use of pure oxygen and air as the oxidant feed during the measurement of I/E curves. Outlet and inlet are defined by the cathode side.

Discussion

Figure 1 shows the long term behavior of the cell over a period of 700 h operating on air. It can be observed that the total performance of the cell was virtually unchanged from the beginning of the experiment, regardless of the significant degradation of the outlet segments (channels 7, 8, and 9). The effect of the local degradation was balanced by the respective improvement of the inlet and mid segments (channels 2-6) of the cell. It must be noted at this point that the inlet segment's behavior can be attributed to the fact that the gas feed was not preheated which locally lowered the temperature causing the lower performance.

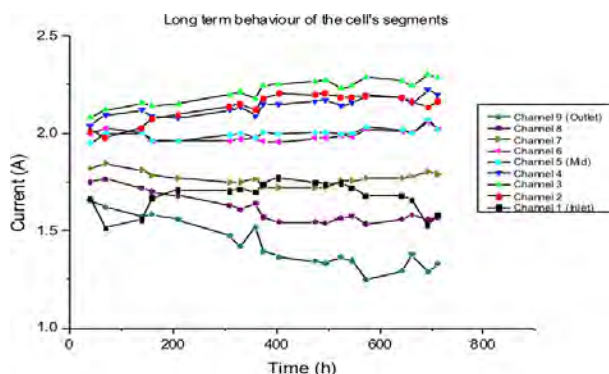


Figure 1. Time evolution of the local current density distribution.

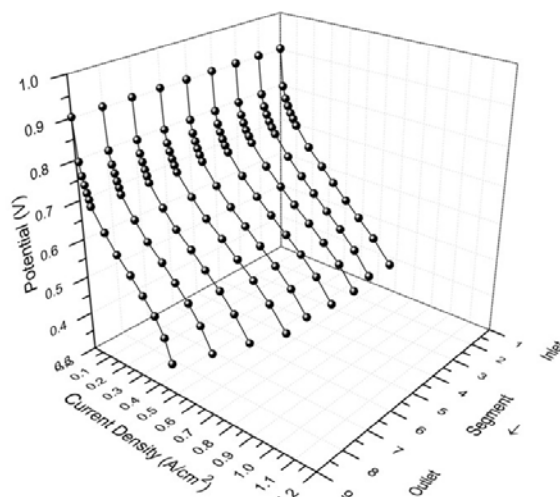


Figure 2. Beginning of life (40h) local current density distribution under H₂/Air feed with 1.2/2 stoichiometry.

It is clearly depicted that there are significant local changes although the integral performance of the cell is steady over the period of the experiment. At the beginning of the experiment, the current density distribution along the flow channel is more or less homogeneous, as shown in Figure 2, with a small decrease towards the outlet at high current densities, owing to the lowering of oxygen partial pressure.

After 712 h of operation the degradation of the outlet segments is clearly depicted, as well as the vast improvement of the inlet and mid segments (figure 3, identical conditions as figure 2). This could be an indicator of two possible phenomena taking place on the cathodic electrode. First, due to increased water vapor partial pressure towards the outlet, enhanced carbon corrosion of the catalyst support could take place. This can be rationalized by previous results in LT PEFCs, where water accumulation in the outlet regions of the cell was demonstrated. Enhanced carbon corrosion can severely alter the porous structure of the catalytic layer leading in a vast decrease of the porosity, as shown by Schulenburg et al. [4]. A second phenomenon leading to the performance decay in the outlet region of the cell is movement of phosphoric acid (from membranes and electrodes) along the channel from the inlet to the outlet region. This could explain both the degradation of the outlet and the improvement of the inlet segments. A redistribution of the phosphoric acid could free pores and make initially blocked catalyst surface area accessible for the reactants in the inlet segments. At the same time, the downstream transported phosphoric acid is leading to local acid flooding of the electrode in the outlet segments. Both phenomena can take place during the operation of the cell. A more detailed analysis of Figure 2 and 3, respectively, reveals a significant drop of the open circuit potential (by ca. 100mV) during the 700h experiment, suggesting the development of increased hydrogen crossover.

Further studies, however, are necessary in order to elaborate this degradation mode in the used experimental setup.

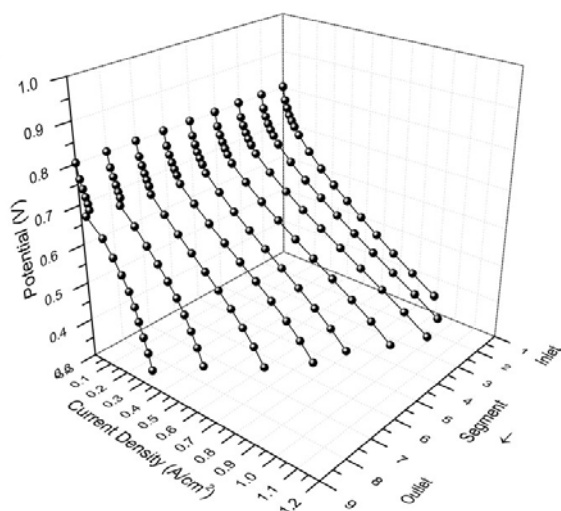


Figure 3. End of life (712h) current density distribution under H_2 /Air feed with 1.2/2 stoichiometry.

These effects can be observed even when measuring the I/E curves on pure oxygen feed as depicted by Figure 4 and 5. At the Beginning of life the performance of the different segments of the cell is quite homogeneous indicating that the binary diffusion of O_2 through N_2 , present in the case of air feed, is omitted.

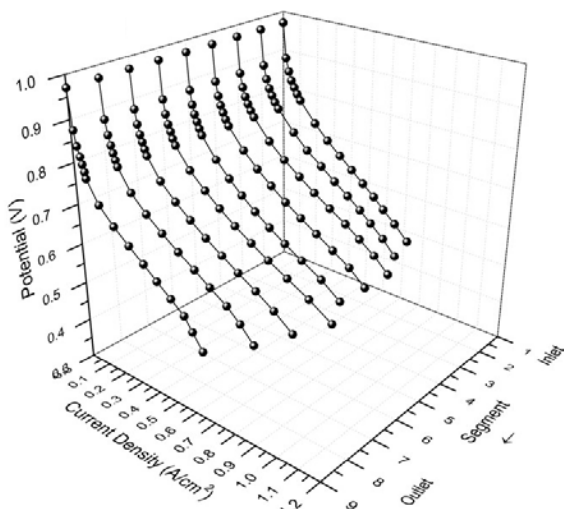


Figure 4. Beginning of life (40h) current density distribution with H_2 / O_2 feed with 1.2/2 stoichiometry.

As it can be seen in Figure 5 the degradation of the outlet segments causes mass transport limitations and a drop in performance. This fact gives further support to the possibility that one or both of the above described phenomena occur during the operation of the cell.

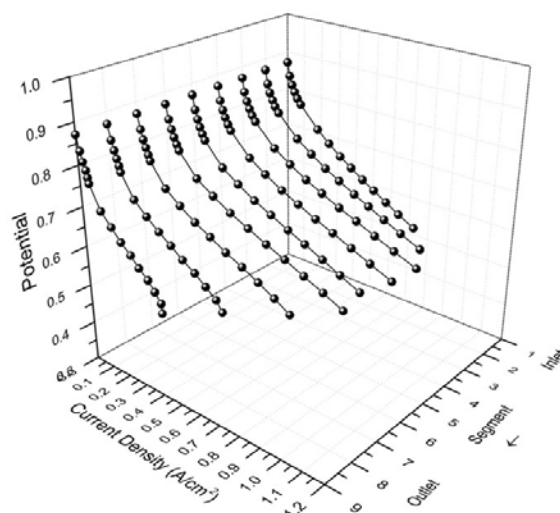


Figure 5. End of life (712h) current density distribution under H_2 / O_2 feed with 1.2/2 stoichiometry.

Conclusions and outlook

While running long term stability measurements on HT PEFCs, the overall performance of the cell remains steady when observing the integral current density and the cell voltage. By taking a closer look through locally resolved measurements along the flow channel, degradation and performance of the cell vary from inlet to outlet. Upstream there is a vast improvement in the performance compensating for the simultaneous degradation downstream. For this behavior two possible phenomena have been qualified as a cause: i) extensive carbon corrosion driven by increased water partial pressure down the channel causing changes in the porous structure of the cathode, and ii) phosphoric acid redistribution from the inlet towards the outlet region causing local flooding of the porous structure catalytic particles downstream, while freeing the respective pores upstream. For clarification of the underlying mechanisms new experiments have been designed including the measurement of the phosphoric acid distribution along the flow channel in pristine and degraded samples as well as the utilization of advanced analytical techniques like FIB-SEM (focused ion beam scanning electron microscopy) for post mortem analysis and the determination of changes in the electrode's porosity.

References

- [1] I.A. Schneider, D. Kramer, A. Wokaun, G.G. Scherer, *Electrochem. Comm.* **7**, 1393-1397 (2005).
- [2] I.A. Schneider, D. Kramer, A. Wokaun, G.G. Scherer, *J. Electrochem. Soc.* **154**, B770-B782 (2007).
- [3] I.A. Schneider, G.G. Scherer Local transient techniques in polymer electrolyte fuel cell (PEFC) diagnostics in *Handbook of Fuel Cells. From Fundamentals to Applications Vol. 6*; 673, W. Vielstich, H. Yokokawa H.A. Gasteiger (ed.) Wiley, Chichester (2009).
- [4] H. Schulenburg, B. Schwanitz, J. Krbanjevic, N. Linse, G. Scherer, A. Wokaun, R. Grothausmann, I. Manke, *J. Phys. Chem. C* **115**, 14236-14243 (2011).

On the efficiency of H₂/air and H₂/O₂ fuel cell systems

F.N. Büchi, J. Bernard, M. Hofer, U. Hannessen¹, P. Dietrich

phone: +41 56 310 24 11, e-mail: felix.buechi@psi.ch

Hydrogen, used as energy carrier in future sustainable energy systems, will be produced by splitting of water through electrochemical and/or thermochemical processes. In these processes pure oxygen incurs as an energetically cheap by-product.

When hydrogen is converted back to power in fuel cells, it is well known that the use of pure oxygen instead of diluted oxygen from air as the oxidant offers advantages for the process through the so called “oxygen gain” [1,2]. This paper aims at quantifying the difference in tank-to-DC system efficiency of the two process options for fuel cell systems.

A non-biased comparison of the system efficiency is not trivial because not all relevant boundary conditions can be kept constant for H₂/air and H₂/O₂ systems, i.e. same rated power, same power at given cell voltage or same stack size can be chosen, but the others will vary. Here it was decided to compare systems with identical active area of the stack, as with this systems of similar stack cost are compared.

As for a comparison on the system level a reasonable maturity and optimization state of the systems is required, a commercial H₂/air system HyPEM 16 (rated power 16 kW) from Hydrogenics is compared to a pre-commercial H₂/O₂ system B25 (rated power 25 kW, see Figure 1 in contribution by J. Bernard et al.) developed by Belenos Clean Power and PSI. The two systems have stacks with comparable active area.

System specifications and boundary conditions

Main properties of the two systems are listed in Table 1. It can be seen that the active area of the stacks is almost the same ($\approx 2\%$ difference). Which means that the cost of the stack is comparable. However the oxygen fuelled system is about 25% lighter, due to the much more compact system, it's rated power is more than 50% higher and consequently its power density almost doubled.

	Hydrogenics HyPEM 16	Belenos/PSI B25
fuel	H ₂ /air	H ₂ /O ₂
Cell active area [cm ²]	500	230
# cells in stack	80	178
Stack active area [m ²]	4.0	4.1
System weight [kg]	96	74
Power density [kW/kg]	0.17	0.3

Table 1. Fuel cell system data comparison.

Of course if the system boundaries include the fuel tanks then the comparative energy and power densities will depend on the size of the tanks. But because of the different efficiencies of the systems this is not a straight forward calculation and will therefore be discussed in the next section.

The system efficiencies were determined as the ratio of hydrogen consumption (LHV) and DC net power. For both systems all the parasitic loads, except for a possible cooling radiator fan (liquid/liquid heat exchangers were used) are included. For the two systems, at the same radiator size this rather adds advantage for the H₂/O₂ system because of its higher operating temperature, and thus lower coolant fan requirement.

System performances and efficiencies

In Figure 1 the characteristics of the two systems are shown as current density/voltage curves. Obviously the H₂/O₂ system achieves considerably higher current densities at the same cell voltage. At 0.8 V per cell the net current density in the oxygen system is approx. 4.5 times higher than in the air system.

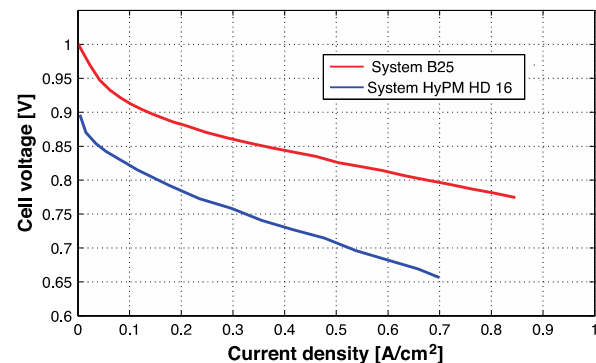


Figure 1. *i/E* characteristic of the H₂/air and H₂/O₂ fuel cell systems as function of stack current density.

The higher cell voltages in combination with a low parasitic load of the balance of plant (BoP) in the oxygen system also translates into a considerably higher system efficiency. Figure 2 shows the tank-to-DC system efficiency for both systems. The highest efficiency of the H₂/air system is 57% (LHV) at about 5 kW system power. At the same power the H₂/O₂ system efficiency is 69%. At the rated power of the air system it's efficiency is 52%, while the oxygen system returns 67%, a relative advantage of almost 30%. With the use of pure oxygen simultaneously a higher efficiency and total power are achieved with the same stack size.

To compare energy and power densities as well as the total available electric energy available from the systems, the tanks need to be considered. Independent of the size and weight of the hydrogen tank (same for both systems), with an oxygen tank weight of 22 kg the two systems will have comparable (empty) weight. For larger energy storage capabilities the energy density (not the power density however) of the air system will be higher. A 200 bar type 3 tank for oxygen weighing 22kg has a volume of about 60 L.

¹ Belenos Clean Power Holding, Bienne

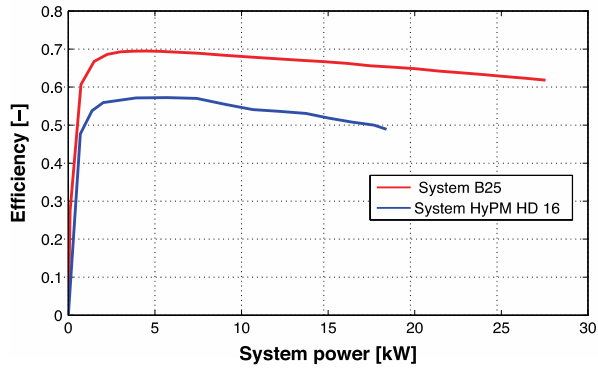


Figure 2. Efficiency of the H_2 /air and H_2 / O_2 fuel cell systems as function of system power.

Assuming a minimum pressure of the tanks of 10 bar and gas utilizations of 99% for both systems, 2.1 kg hydrogen (and in the oxygen system 17.8 kg O_2) are converted to electricity. Due to the higher average efficiency of the oxygen system about 20% more electric power will be produced as compared to the air system (80 kWh vs. 65 kWh). Table 2 lists several specifications of the systems including (empty) tanks. It can be seen that due to the higher conversion efficiency of the oxygen system its specific energy is approx. 20% higher while the power density is almost 60% higher due to the simultaneously higher efficiency and power. These values are calculated with empty tanks. If the weights with full tanks are considered in particular the values for the oxygen would be lower by about 13%.

	H_2 /air	H_2 / O_2
Avg. efficiency LHV [-]	0.55	0.67
Weight H_2 tank [kg]	40	40
Hydrogen stored [kg]	2.1	3.35
Weight O_2 tank [kg]	-	22
Oxygen stored [kg]	-	17.8
Total system weight [kg]	136	136
Stored energy [kWh]	70	70
Converted electric energy [kWh]	38	47
Energy density ¹ [Wh/kg]	280	345
Power Density ^{1,2} [W/kg]	115	180
Range of car ³ [km]	190	240

¹with empty tanks,

²at rated power

³consumption 20 kWh_{el}/100 km

Table 2. Fuel cell system comparison: Weight, and specific power and energy data only approximate (system & empty tanks only). More explanation see text.

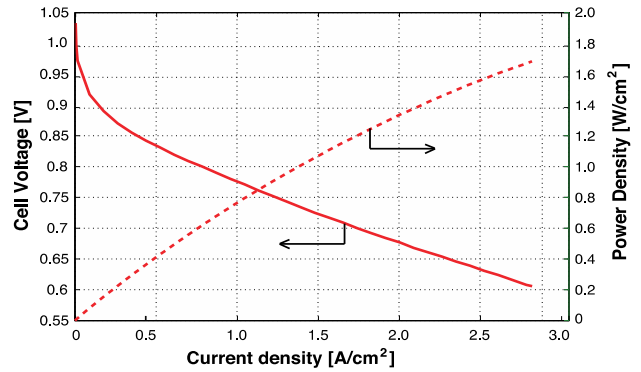


Figure 3. i/E characteristics of H_2 / O_2 230 cm² single cell.

When considering the two systems as power trains for small electric hybrid cars (see contribution by J. Bernard et al.), at the same (empty) weight the air system will at 20 kWh/100 km allow for a driving range of about 190 km while the oxygen system would produce power for 240 km increasing the range by about 25 %.

The power density of the oxygen system however could be considerably improved. As shown in Figure 3, a cell voltage close to 0.7 V/cell can be achieved at a current density of 2 A/cm². This is more than twice the value at the rated power of 25 kW of the B25 system. The resulting approx. 1.4 W/cm² are more than 30% above today's goal for automotive systems.

Conclusion

Properties of a hydrogen/air and a hydrogen/oxygen fuel cell system with comparable total active area of their stacks have been compared with and without gas tank(s) included. The higher conversion efficiency and the much higher possible current density as well as the lean balance of plant of the oxygen system translate into interesting values for the specific energy and power density of the entire system.

References

- [1] K. O'Neil, J.P. Meyers, R.M. Darling, M.L. Perry, Int. J. Hydrogen. Energ., **7**, 373-382 (2012).
- [2] F.N. Büchi, S.A. Freunberger, M. Reum, G. Paganelli, A. Tsukada, P. Dietrich, A. Delfino, Fuel Cells **7**, 159-164 (2007).

A H₂/O₂ fuel cell system for automotive application

J. Bernard, M. Hofer, U. Hannessen¹, F.N. Büchi, P. Dietrich

phone: +41 56 310 24 11, e-mail: felix.buechi@psi.ch

In collaboration with Belenos Clean Power, Paul Scherrer Institut is developing concepts for fuel cell systems (FCS) for the automotive application. Results from the latest FCS developed, based on H₂/O₂ PEFC technology, are presented.

Introduction

Polymer electrolyte fuel cell systems (PEFC) in transport applications use oxygen from air as the oxidant. However, the use of pure oxygen in mobile fuel cell systems has a number of advantages [1]: i) higher specific power (a significant cost advantage as a stack of about half the size is required for the same power); ii) higher efficiency (even if operated at the same cell voltage as the air system, with the absence of air compression in the oxygen system, the balance of plant has a lower consumption); iii) higher power dynamics (no limitations by the “slow” air path”); iv) easier water management (no nitrogen to be humidified); lower dependence on environmental conditions (altitude, humidity, air pollution). Moreover, when hydrogen is obtained from the splitting of water by electrolysis or other processes then oxygen is obtained as energetically free by-product. These advantages have to be considered when assessing the need of the required oxygen on-board storage.

Fuel Cell System description

Specific efforts were made in the integration of the system components. All actuators and sensors required for a proper fuel cell system operation have been integrated on particular plates directly assembled on the compression plates of the fuel cell stack (Figure 1). This results in a compact system, allowing better integration and management of the fluids (gases and coolant). The fuel cell system was primed by the Swiss Federal Department of Energy and received the “Watt d’or 2011” in the category “Efficient Mobility”.



Figure 1. 2011 Fuel cell system.

System efficiency

The efficiency of the stack and the system were measured on a testbench. The efficiency calculation is current based and the gas purges are neglected. The system efficiency is higher than 60% for 97% of the power range, and has a peak efficiency of 69% at 15% of nominal power. This superior system efficiency can be achieved with the high partial pressure of oxygen on the cathode side and the relatively low power consumption of the balance of plant (no air compressor is needed).

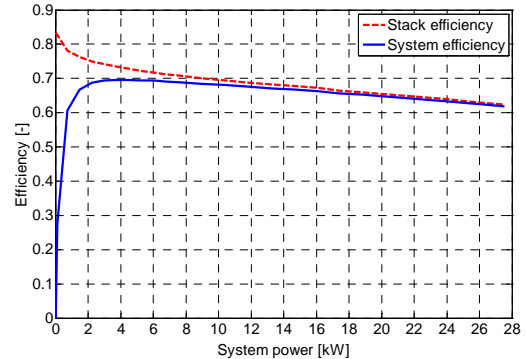


Figure 2. Efficiency of the fuel cell and the fuel cell system.

Fuel Cell System in vehicle

The fuel cell system was coupled to an 8 kWh lithium battery in an 1100 kg electric vehicle (Figure 3). The vehicle, battery and fuel cell data are recorded during drive tests. An example of test drive is given in Figure 4. It shows that the fuel cell system was able to provide more than the average power demand since the battery gains 2.5% SOC during the drive. It indicates that a fuel cell with a rated power between 25kW and 30kW is sufficient for this vehicle class.



Figure 3. Belenos-PSI vehicle for fuel cell system tests.

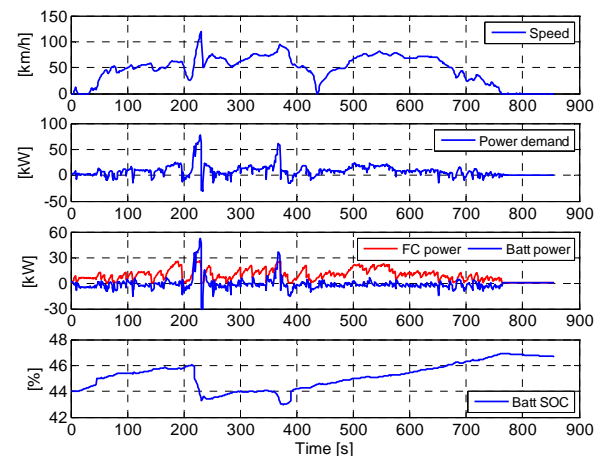


Figure 4. Drive test with the Belenos-PSI vehicle.

References

- [1] F.N. Büchi, S.A. Freunberger, M. Reum, G. Paganelli, A. Tsukada, P. Dietrich, A. Delfino, On the Efficiency of an Advanced Automotive Fuel Cell System, Fuel Cells **7**, 159-164 (2007).

¹ Belenos Clean Power Holding, Bienne

BATTERIES & SUPERCAPACITORS

MATERIALS

Lithium-ion conductivity of radiation grafted membranes

L. Gubler, M. Schreier, P. Novák

phone: +41 56 310 26 73, e-mail: lorenz.gubler@psi.ch

Lithium conducting single-ion polymer electrolytes are of interest in lithium-sulfur batteries to prevent the transport of polysulfide anions from the positive sulfur to the negative lithium electrode. In this study, we explore the Li-ion conductivity of radiation grafted membranes on the basis of an ETFE film of 25 μm thickness swollen in different solvents, and compare the results against those obtained with Nafion[®], a commercial perfluoroalkylsulfonic acid membrane.

Experimental

Cation exchange membranes were prepared by grafting styrene onto an electron beam pre-irradiated ETFE film, followed by sulfonation, yielding poly(styrenesulfonic acid) (PSSA) grafts [1]. Membranes with two different graft levels, 72 and 130 %, were selected for this study. In addition, a methacrylic acid (MAA) grafted membrane with graft level of 68 % was prepared to investigate the influence of the type of fixed anion. Membranes were exchanged into the lithium form by immersion in a saturated aqueous lithium carbonate solution overnight. The membranes swollen in organic solvents were prepared from water-swollen samples, first by drying in the vacuum oven (10 mbar, 70°C) overnight, followed by immersion in the respective solvent for at least 12 h. The conductivity of the solvent-swollen samples was measured in a modified Bekktech BT-112 in-plane conductivity cell. Solvent uptake was determined gravimetrically.

Results

The conductivity of the radiation grafted membranes in H^+ form swollen in water and in Li^+ form swollen in water, and non-aqueous solvents compatible with lithium-ion batteries is compared against the conductivity of Nafion[®] 212 and literature values [2] reported for Nafion[®] 117 (Figure 1). In general, the conductivity shows a strong decrease in going from the water swollen membrane in the proton form to the lithium form and then to non-aqueous solvents with decreasing dielectric constant (DMSO: 47, DME: 7.2, dioxolane: 7.3). The proton conductivity of the MAA grafted membrane in

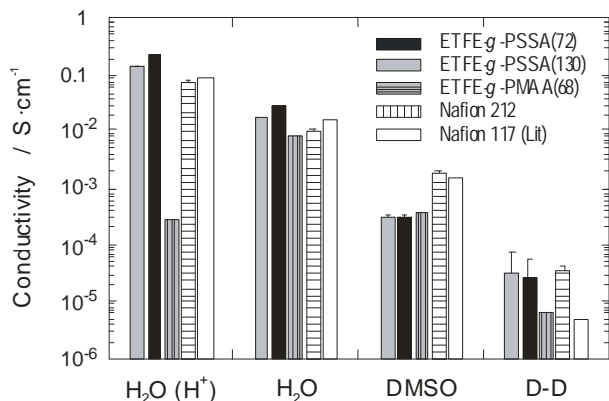


Figure 1. Proton conductivity of water swollen membranes and lithium-ion conductivity of membranes swollen in different solvents. The number in brackets for radiation grafted membrane is the graft level. D-D stands for dimethoxyethane (DME)-dioxolane (2:1 v/v).

water is very low, probably because of negligible dissociation of the carboxylic acid. The H^+ and Li^+ conductivities of the sulfonic acid membranes follow the expected trend in water according to their ion exchange capacities. However, the Li-ion conductivity of Nafion[®] is much higher than that of the grafted membranes in DMSO. This could be related to the much higher solvent uptake of Nafion[®] (Figure 2).

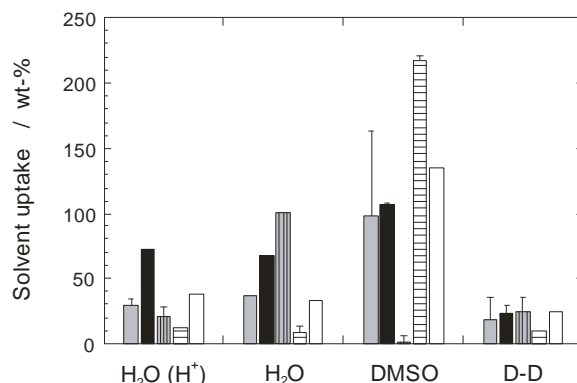


Figure 2. Solvent uptake of membranes (cf. legend of Fig.1).

DME:dioxolane is a common solvent in lithium-ion batteries. The conductivities determined in this study are encouraging and exceed the accepted minimum requirement of 10^{-5} S/cm [3]. However, we found that the Li-ion conductivity was substantially influenced by the presence of water as impurity (Figure 3).

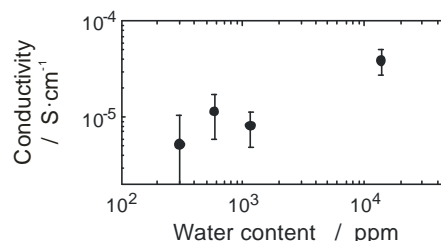


Figure 3. Li-ion conductivity of the styrene grafted and sulfonated membrane with graft level of 72 %, swollen in DME:dioxolane with different water contents.

Although encouraging, these are merely preliminary experiments to demonstrate the feasibility of the approach. Many open questions remain, such as: what is a suitable fixed anion? To minimize ion-pair formation, the use of large, delocalized anions has been suggested [4].

References

- [1] S. Alkan-Gürsel, H. Ben youcef, A. Wokaun, G.G. Scherer, Nucl. Instr. Meth. Phys. Res. B **265**, 198-203 (2007).
- [2] M. Doyle, M.E. Lewittes, M.G. Roelofs, S.A. Perusich, J. Phys. Chem. B **105**, 9387-9394 (2001).
- [3] J.B. Goodenough, Y. Kim, Chem. Mater. **22**, 587-603 (2010).
- [4] R. Meziane, J.P. Bonnet, M. Courty, K. Djellab, M. Armand, Electrochim. Acta **57**, 14-19 (2011).

Electrochemical and chemical surface modifications of carbons for Li-ion batteries

P. Verma, P. Novák

phone: +41 56 310 24 57, e-mail: petr.novak@psi.ch

A significant interfacial reaction occurring in a Li-ion battery is electrolyte reduction on the surface of the negative graphite electrode, which results in the formation of a passive layer as interphase which is called solid electrolyte interphase (SEI). SEI has been extensively studied due to its critical impact on the irreversible charge loss (ICL), self-discharge, cyclability, rate capability, and safety of the battery[1]. Once formed, the SEI electronically passivates the surface of the electrode material, and ensures cyclability by virtue of Li-ion conduction. However, there are two main limitations of SEI. Firstly the charge consumed for electrolyte reduction during the first lithiation of graphite is "lost" irreversibly and cannot be retrieved in the consecutive cycles. This charge is called ICL. Second critical issue is that the natural SEI is not able to avert endless charge of crystalline graphite in propylene carbonate (PC) electrolyte, which according to Besenhard et al. is due to solvent co-intercalation of PC in graphite[2]. This results in exfoliation of graphite, where the graphene sheets open up and continuous irreversible decomposition of the electrolyte occurs on the freshly exposed area. PC based electrolytes are very important for low temperature performance of a battery[3] as PC freezes at $-49\text{ }^{\circ}\text{C}$, compared to $+37\text{ }^{\circ}\text{C}$ for the other commonly used solvent ethylene carbonate (EC). The approach here is to modify the surface groups already existing on the surface of graphite by chemical treatment to tune reactivity of the inherent surface groups. Surface modified carbons would comprise of tuned reactivity and morphology and will play a predominant role in determining the properties of the SEI, and consequently the performance of the battery in terms of safety, ICL, exfoliation of graphite, and cyclability.

Experimental

Treatment with reducing agents: SFG6 graphite powder (from TIMCAL, Switzerland) was treated with excess reagents 1 M BH_3 in THF, 1 M BH_3 in THF followed by 1.6 M n-butyl lithium (BuLi) in hexane, 1.6 M BuLi in hexane, and 2 M LiAlH_4 in THF, individually under inert conditions. Post treatment these powders were washed with THF, hexane, hexane, and THF respectively. The powders were dried at room temperature inside an Ar filled glove box ($\text{O}_2 < 0.6\text{ ppm}$, $\text{H}_2\text{O} < 3\text{ ppm}$).

Treatment with oxidizing agents: SFG6 graphite powder was stirred in excess reagents 1 M KMnO_4 in water and 35 % H_2O_2 individually for four hours and washed copiously with water. KMnO_4 treated graphite was further reduced with aforementioned BuLi and LiAlH_4 reagents. Powders were dried overnight under vacuum at $80\text{ }^{\circ}\text{C}$.

Treatment with additive: Electrodes of SFG6BuLi using styrene butadiene rubber (SBR) binder on Ti current collector were prepared from slurry in hexane. Then $\sim 200\text{ mL}$ of neat additive was dropped on the prepared electrode. The additives were allowed to react with the electrode for ~ 10 minutes after which excess of the additive was removed. Treated electrodes were allowed to dry inside the glove box.

For battery testing, standard cells using Li metal as counter as well as reference electrode were built. Since the surface groups on graphite after various treatments were sensitive to air, the working electrodes were made using styrene-butadiene rubber (SBR) as binder (10/90 SBR/graphite w/w) and hexane as solvent inside the glove box. The slurry was applied onto Ti current collector stubs and dried. The galvanostatic cycling was done at C/10 rate in 1 M LiPF_6 in 1:1 ethylene carbonate: dimethyl carbonate. Same conditions were used for CV which was run at 0.01 mV/s . Ultra55 scanning electron microscope (SEM) was used to visualize the surface morphology of the treated samples. Pictures were taken using In Lens detector at 3 KeV accelerating voltage.

Results

SFG6 graphite treated with BuLi (SFG6BuLi) shows graphite particles covered with a ruffle on the prismatic planes. This material also shows 23% lower irreversible charge loss. However, cyclability of SFG6BuLi was poor and the practical specific charge retrieved was only 80 % of the theoretical (shown in figure 1).

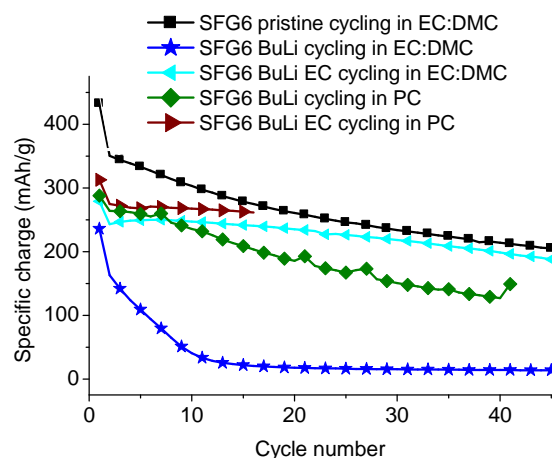


Figure 1. Cyclability of SFG6 pristine, SFG6BuLi, SFG6BuLi treated with EC, and in 1 M LiPF_6 in EC:DMC electrolyte; and that of SFG6BuLi and SFG6BuLi treated with EC in 1 M LiPF_6 in EC:PC (15:85) electrolyte.

The surface ruffle could be a result of a physical phenomenon since it is tens of nm thick. The exact nature and chemical composition of this film is unknown, but is assumed to be very nucleophilic and reactive.

One of the main possible causes for instable cycling of this material shown in figure 1 could be highly reactive surface layer. This may be reacting with the electrolyte and undergoing continued reactions during cycling. In order to stabilize the chemical composition of the surface film, some cyclic film forming additives were used on SFG6BuLi electrodes. It is observed that when cyclic carbonate additives are added to SFG6BuLi ICL is lower than that of pristine. Concomitantly, addition of these additives especially EC, improves the cyclability better than pristine (see figure 1). Good cyclability of

this sample is attributed to the stability of the resulting chemical composition of the surface film, which is expected to be alkyl carbonate.

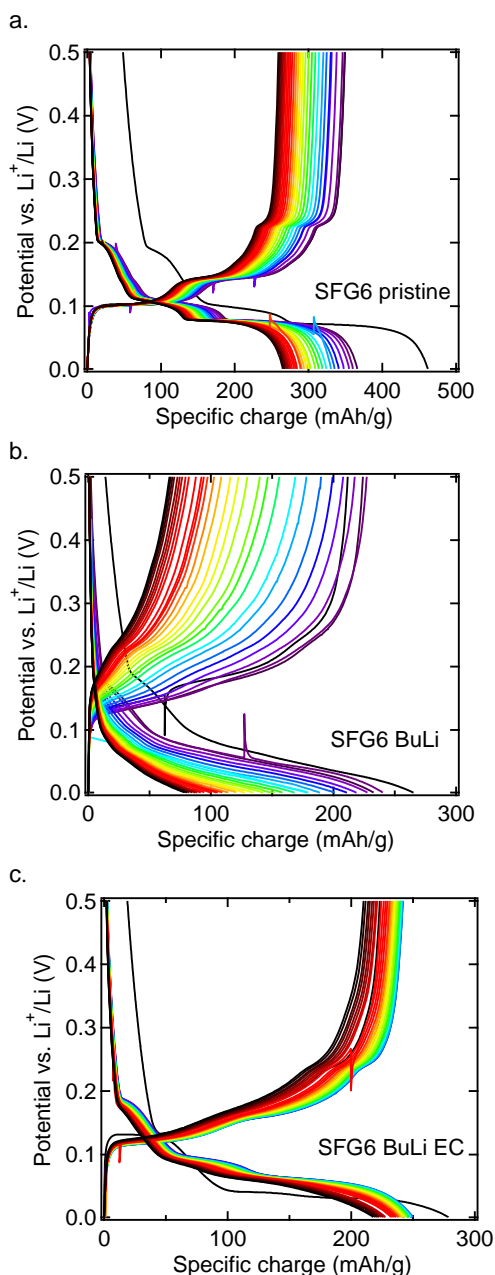


Figure 2. Cycling curves of first 30 electrochemical cycles in 1 M LiPF₆ in EC:DMC electrolyte of a. SFG6 pristine; b. SFG6 treated with BuLi; c. SFG6 treated with BuLi and using EC additive.

To prove this hypothesis evolution with cycling of charge/discharge curves of SFG6 pristine, SFG6 treated with BuLi, and SFG6 treated with BuLi and EC additive were studied (shown in figures 2.a, 2.b, and 2.c respectively). Shrinking of the curves to lower specific charge in figure 2.a showing pristine SFG6 electrode could be due to loss of active material from the electrode during cycling. This could be attributed to poor electrode engineering, which had to be with SBR binder inside the glove box so as to be comparable with other materials which are air sensitive. There is no obvious increase in polarization during cycling in this case as the shrinkage is only along horizontal and not vertical axis. On the contrary the curves shown in figure 4.b

show a shift in both specific charge (horizontal) as well as potential (vertical) axes. This implies that BuLi treated SFG6 graphite material exhibits strong polarization. Continued increase in polarization with cycling is attributed to continued reactions of the highly reactive surface layer with the electrolyte and consequently thickening of resistive passive layer. However, after treating these electrodes with EC, the increase in polarization (along potential axis) is strongly suppressed. This is shown in figure 2.c. The curves are shifted to a much smaller extent along the potential axis as compared to those in figure 2.b. This supports our argument of decreased reactivity due to stabilized chemical composition (carbonate) of the surface layer after treatment with EC, which is less reactive with the electrolyte, and hence shows lowered polarization upon cycling.

Edge coverage of graphite particles will be of utmost importance for averting exfoliation of graphite in PC based electrolyte, which occurs due to solvent co-intercalation. The first cycle of SFG6 pristine and SFG6BuLi, and SFG6BuLi EC in 1 M LiPF₆ in EC:PC (15:85) electrolyte is shown in figure 3. Pristine SFG6 undergoes endless charge due to continuous electrolyte degradation along with exfoliation, whereas the treated graphites show normal reversible behavior with low ICL.

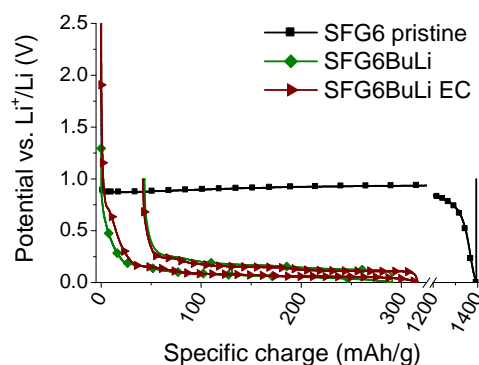


Figure 3. 1st cycle of SFG6 pristine and SFG6BuLi, and SFG6BuLi EC in 1 M LiPF₆ in EC:PC (15:85) electrolyte.

Cyclability of SFG6BuLi in PC based electrolyte is compared with that of SFG6 pristine, SFG6BuLi, SFG6BuLi treated with EC, and SFG6BuLi treated with PC in EC based electrolytes in figure 1. It is seen that fading of the specific charge SFG6BuLi in PC based electrolyte is comparable to normal cycling of SFG6 pristine in EC:DMC electrolyte. After treating SFG6BuLi electrode with EC additive, it shows reversible cycling in PC (shown in figure 1), and its cyclability in PC electrolyte is further improved (even better than that of SFG6BuLi EC in EC:DMC electrolyte) (figure 1). This implies that SFG6BuLi results in low ICL, cycles reversibly in PC based electrolyte, and shows excellent specific charge retention in PC based electrolyte.

References

- [1] P. Verma, P. Maire, P. Novák, *Electrochim. Acta* **55**, 6332-6341 (2010).
- [2] J. O. Besenhard, M. Winter, J. Yang, W. Biberacher, *J. Power Sources* **54**, 228-231 (1995).
- [3] S.S. Zhang, K. Xu, J.L. Allen, T.R. Jow, *J. Power Sources* **110**, 216-221 (2002).

Lithium–sulphur battery development

S. Urbonaite, A. Garsuch¹, P. Novák

phone: +41 56 310 57 75, e-mail: sigita.urbonaite@psi.ch

The degree to which the performance of state-of-the-art lithium-ion batteries can be improved is fundamentally limited by the lithium-ion chemistry. Therefore extensive research is now directed towards alternative chemistries, in particular those of Li–Air and Li–S systems. Li–S batteries have been studied for several decades, motivated by predictions of high specific charge of 1675 mAh/g and high specific energy of 2,500 Wh/kg [1]. Today, they are considered to provide one of the most realistic pathways to reach higher energy densities desired by new battery applications, especially in automotive industry.

However, the development of Li–S batteries faces a number of challenging problems on the way to maximum performance of these systems. One of them is the insulating nature of sulphur, necessitating the addition of conductive additives to be present in the electrode. Another is the behaviour of the lithium metal in the battery cell, in particular dendrite formation during long-term cycling and the agglomeration of insoluble non-conductive products on the lithium anode during charging leading to the formation of an insulating layer and an increase in the cell's resistance [2]. The latter is caused by a mechanism specific to the Li–S system, the so-called polysulphide shuttle, illustrated in Figure 1.

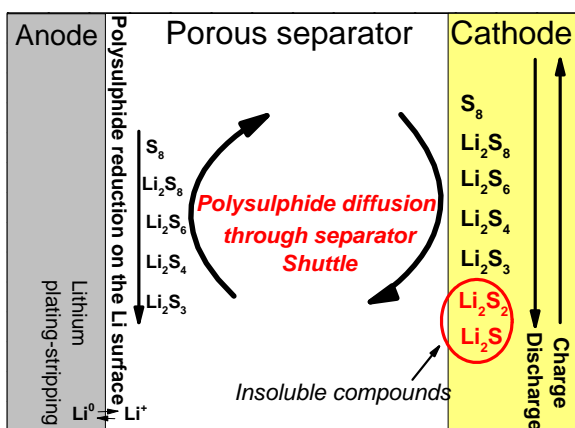


Figure 1. Schematic representation of Li–S system.

The behaviour of the Li–S system depends on a number of parameters and components, such as the composition and amount of electrolyte (including the type and amount of solvents and salts), type of binder, conductive additives, and load of active material. Recently reported capacities for Li–S systems are typically in the range of 600 mAh/g, even for advanced carbon materials, such as graphene–sulphur composites [3, 4]. The exception is highly structured mesoporous carbons, such as CMK-3, with sulphur incorporated into the pores, giving capacity of above 1000 mAh/g; however, only a few cycles have been demonstrated in these systems [1].

This project is dedicated to establishing the influence of different binders on the performance of composite electrode and the effect of different amounts of electrolyte. Results so far include the demonstration that traditional composite electrodes can exhibit capacities of 700–800

mAh/g without the use of expensive advanced carbon materials, provided that the system's parameters are well adjusted. The results of this work therefore suggest future directions for the investigation of Li–S systems.

Experimental

The sulphur–carbon composite electrodes were prepared using three different binders: CMC (carboxymethyl cellulose), Kynar flex 2801PVDF (high-molecular-weight copolymer of vinylidene fluoride and hexafluoropropylene), and PEO (polyethylene oxide).

All electrodes were prepared by doctor-blading slurries — containing 60% of sulphur, 30% of carbon black (Super P, TIMCAL), and 10% of one of above-mentioned binders — onto a carbon pre-coated aluminium-foil current collector. The slurries were mixed with a turbostirrer adding different solvents for each binder: a water-ethanol mixture for CMC, acetone for Kynar, and acetonitrile for PEO. After coating, the electrodes were dried at room temperature for at least 24 hours; where after circular electrodes were punched and assembled into test cells in an argon filled glove box.

The test cells were assembled by stacking the composite sulphur-containing cathode, a separator (Celgard) and metallic lithium into the coin-type cell with constant mechanical pressure. Before closing the cell, the electrolyte was introduced, in amounts varying from 30 to 60 μl . The electrolyte was prepared by dissolving 1M LiTFSI (Lithium Bis(Trifluoromethanesulfonyl)imide) in DME:Diox (2:1), where DME is dimethoxyethane and Diox is 1,3-dioxolane. Electrochemical testing was performed by galvanostatic cycling between 1.8 and 2.7 V vs. Li at rates C/10 and C/5, where 1C corresponds to 1675 A/kg of sulphur [1].

Results

All three binders compared in this study have different properties which influence the performance of Li–S batteries. CMC is a very stiff binder, possibly able to retain the structure of the electrode when polysulphides are bleeding from it during the reaction of lithium with sulphur. PEO is elastic and able to accommodate Li-ions in its structure, thus increasing the overall ionic conduc-

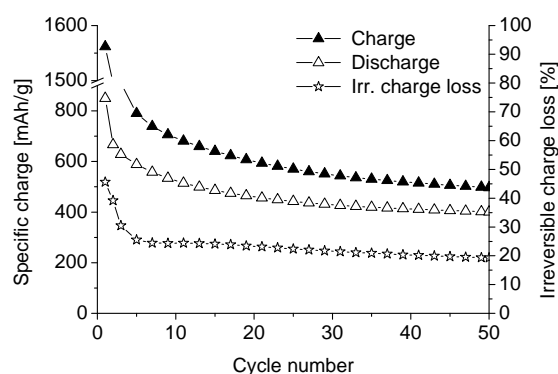


Figure 2. Li–S cell performance with CMC binder based composite electrode, C/5, 50 μl of electrolyte, Celgard 2400 separator.

¹ BASF SE, Ludwigshafen, Germany

tivity of Li in the electrode; at the same time, it might suppress polysulphide migration by allowing easier Li transport, compared to polysulphide. Kynar is very inert to any chemical reaction and should assure the stability of the electrode.

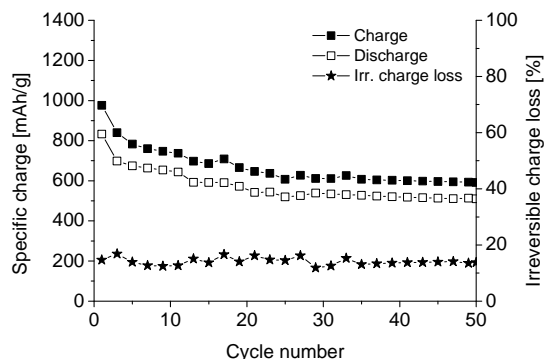


Figure 3. Li-S cell performance with PEO binder based composite electrode, C/5, 50 µl of electrolyte, Celgard 2400 separator.

The PEO and Kynar binders exhibited significantly better performances than CMC during cell cycling. Comparing the resulting capacities of cells with the same amount of electrolyte (50 µl), it is clearly higher (above 500 mAh/g) for PEO-based composites than for the electrodes containing CMC, see Figures 2 and 3. Also, the irreversibility is lower: the irreversibility of both CMC- and Kynar-based electrodes is about 20% (see Figures 2 and 4). The reason for this high value is not obvious, as both binders have different physical properties.

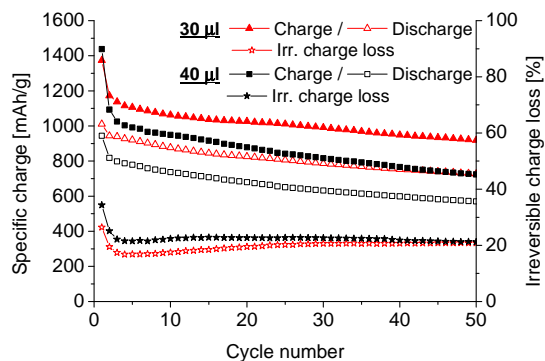


Figure 4. Li-S cell performance with Kynar binder based composite electrode, C/10, different electrolyte amounts, Celgard 2325 separator.

These findings require further investigation. The lower irreversibility of the PEO-containing electrodes might be attributed to the better conductivity of the overall composite system, as PEO might be impregnated with Li ions coming from the electrolyte. Another factor might be that PEO, in addition to incorporating Li-ions, also absorbs part of the electrolyte solution, thus reducing the free-electrolyte amount and at the same time reducing the electrolyte volume in which polysulphides can be dissolved. This leads to the next part of the investigation: the influence of electrolyte amount on the performance of the Li-S cell's performance.

As can be seen from Figures 4 and 5, in both systems — Kynar- and PEO-based — the specific charge is higher when the amount of electrolyte is smaller; a fact best observable in the case of Kynar. In the case of the

PEO composite electrodes not only the specific charge is increased, but also the irreversibility is lowered, which indicates that absorption of electrolyte and increased conductivity might be the reasons for such improved performance of the cell, as discussed above.

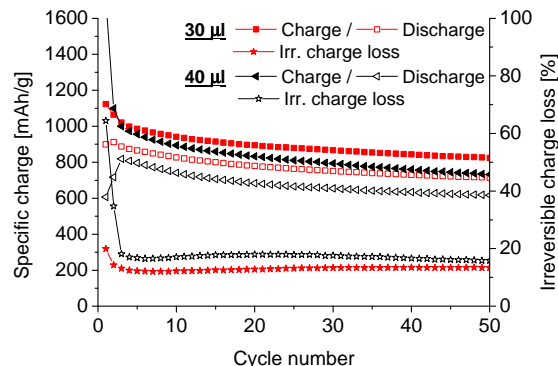


Figure 5. Li-S cell performance with PEO binder based composite electrode, C/10, different electrolyte amounts, Celgard 2325 separator.

The study of the effects of the binder type and electrolyte amount on Li-S system clearly showed that both factors have a significant impact on the performance of Li-S cells. However, as different binders affect the cell performance in different ways, with relative advantages and disadvantages, optimal mixtures of binders might be the way to proceed in order to improve the overall performance of the Li-S battery system.

References

- [1] X. Ji, K.T. Lee, L.F. Nazar, *Nature Materials* **8**, 500-506 (2009).
- [2] J.R. Akridge, Y.V. Mikhaylik, N.I White, *Solid State Ionics* **175**, 243-245 (2004).
- [3] H. Wang, Y. Yang, Y. Liang, J.T. Robinson, Y. Li, A. Jackson, Y. Cui, H. Dai, *Nano Lett.* **11** (7), 2644-2647 (2011).
- [4] Y. Yang, G. Yu, J.J. Cha, H. Wu, M. Vosgueritchian, Y. Yao, Z. Bao, Y. Cui, *Nano Lett.* **5** (11), 9187-9193 (2011).

M_{0.5}TiOPO₄ as high specific charge battery material

P. Bleith, V. Godbole, C. Villeveille, P. Novák

phone: +41 56 310 27 97, e-mail: peter.bleith@psi.ch

Nowadays, the main challenge in the battery field is the limited specific energy. This challenge can be overcome for example by increasing the specific charge of battery materials. In 2005 Belharouak and Amine found that Ni_{0.5}TiOPO₄ is a high specific charge material for lithium-ion batteries (422 Ah/kg) [1]. LiCoO₂ and graphite, both standard materials for Li ion batteries, have a specific charge of 140 Ah/kg and 372 Ah/kg, respectively. In 2009 Essehli et al. showed that the isostructural Co_{0.5}TiOPO₄ is also electrochemically active with a high specific charge (434 Ah/kg) [2]. Since other members of the M_{0.5}TiOPO₄-family (M TOP) like NiTOP, CuTOP, and FeTOP are isostructural, they are potential candidates as battery materials. Therefore it is worth to study the mechanism during lithiation and delithiation of these materials since all of them have a higher specific charge than expected and the reason for this is still unexplained.

Experimental

CuTOP was synthesized from a solution of NH₄H₂PO₄ and Cu(NO₃)₂·TiCl₄·2THF solved in ethanol was added to this solution. The precipitate from this mixture was dried and subsequently heated to 200 °C, 450 °C, 750 °C, and 950 °C. FeTOP was synthesized from CuTOP by an ion exchange with Fe powder at 900 °C in an evacuated silica tube. The Cu was removed from the FeTOP by washing with HNO₃. [3]

The resulting CuTOP was mixed in the solvent NMP (n-methyl-2-pyrrolidone) with 25 w% Super-P carbon (TIMCAL, Switzerland) and 25 w% Kynar Flex[®] 2801 as binder. For FeTOP it was 20% of Super-P carbon and 20% of binder. These slurries were doctor-bladed on Cu-foils and dried. Coin-like test cells were built with a Li counter electrode, a glass fiber separator, and 1:1 EC:DMC with 1 M LiPF₆ as electrolyte.

X-ray diffraction (XRD) analyses of powder samples were performed on a Panalytical Empyrean diffractometer with Copper K_α-radiation.

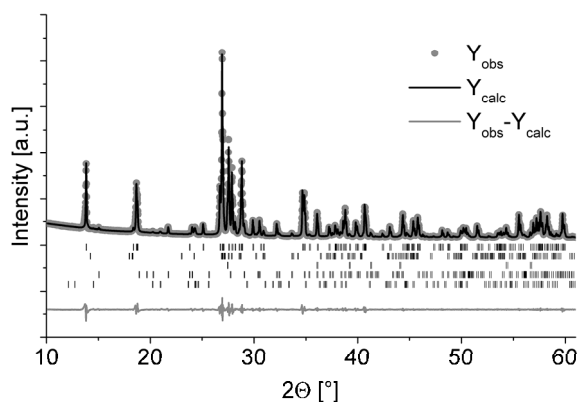


Figure 1: XRD-pattern of CuTOP (black lines indicate from top to bottom the Bragg-peaks of the following phases: α -CuTOP, β -CuTOP, rutile, Cu₃(PO₄)₂, and Cu_{0.5}Ti₂(PO₄)₃).

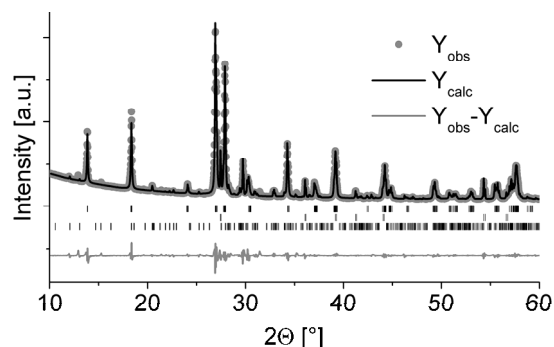


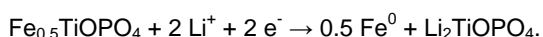
Figure 2: XRD-pattern FeTOP (black lines indicate from top to bottom the Bragg-peaks of the following phases: FeTOP, rutile, and Fe₂Fe_{1.5}(PO₄)₃).

Results

Figures 1 and 2 show the XRD-patterns of the synthesized CuTOP and FeTOP, respectively. The main phase is α -CuTOP, but there are impurities of β -CuTOP, TiO₂ (in rutile phase), Cu₃(PO₄)₂, and Cu_{0.5}Ti₂(PO₄)₃ for the CuTOP synthesis. For the FeTOP synthesis the main phase is FeTOP and TiO₂ in rutile phase as the main impurity. There is also another not completely identified phase. The best fitting phase (even with multiple phases) is Fe₂Fe_{1.5}(PO₄)₃.

Figures 3 and 4 show the galvanostatic curves for the 1st, 2nd, and 25th cycle of CuTOP and FeTOP, respectively. Both materials were cycled between 0.2-3.0 V vs. Li⁺/Li with a rate of C/10 with respect to the reported specific charge for NiTOP of 422 Ah/kg [1], which is corresponding to a reaction with 3 Li ions per formula unit. CuTOP shows in all cycles a plateau at approx. 1.7 V with these cycling conditions. In the first lithiation, the reaction at this plateau is not 100% reversible, which results in an irreversible charge loss. In the following cycles the specific charge of this plateau decreases, but the loss in the first cycle is the most drastic one. Not all stored charge is converted at 1.7 V. The charge is also partly stored and released continuously up to approx. 2.0 V. FeTOP shows a higher specific charge than CuTOP in all cycles but no plateau except in the first lithiation. So, most probably the structure changes upon lithiation irreversibly.

Table 1 gives the specific charge in the 1st, 2nd, and 25th cycle of CuTOP and FeTOP with subtracted contribution of Super-P. CuTOP shows a specific charge in the 1st lithiation that corresponds to a reaction with more than 2 Li ions per formula unit, for FeTOP it is even almost 5 Li ions. For the delithiation and the following cycles it is still more than 2 Li ions per formula unit (reaction with 1 Li ion per formula unit corresponds to \approx 140 Ah/kg) that react with the FeTOP. The most plausible reaction of the material would be



But this would only explain the reaction with 2 Li ions and not more. The reason for the extra charge is unknown yet.

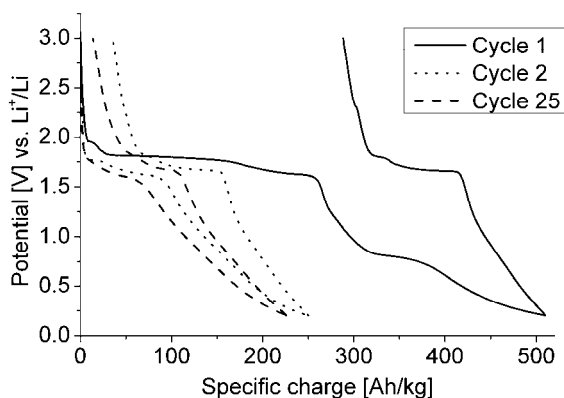


Figure 3: Galvanostatic curves of CuTOP in the 1st, 2nd, and 25th cycle, respectively.

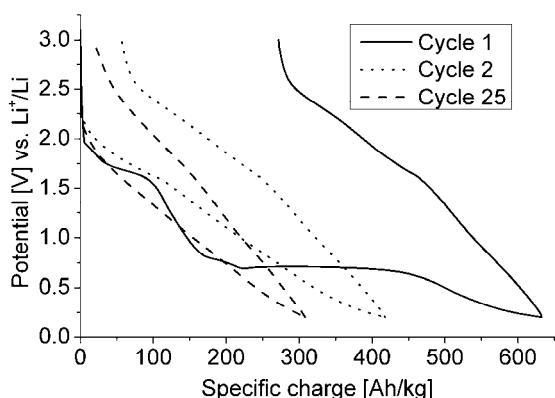


Figure 4: Galvanostatic curves of FeTOP in the 1st, 2nd, and 25th cycle, respectively.

Sample	Cycle	Specific charge [Ah/kg]		Corrected specific charge [Ah/kg]	
		lithiation	delithiation	lithiation	delithiation
CuTOP	1	510	222	370	153
CuTOP	2	250	214	171	147
CuTOP	25	226	212	160	148
FeTOP	1	632	361	539	315
FeTOP	2	418	361	365	316
FeTOP	25	308	289	264	246

Table 1: Specific charge of CuTOP and FeTOP with subtracted contribution of Super-P.

In a cyclic voltammogram of CuTOP (Figure 5) one can see that the peak at 1.7 V (corresponding to the plateau in the galvanostatic cycling) decreases with increasing cycle number. But when the electrode is cycled up to 3.6 V (above the oxidation potential of copper), the peak gets bigger again and does not get smaller as long as the electrode is cycled up to 3.5 V. When the electrode is then cycled up to 3.0 V again, the peak magnitude decreases. In a cyclic voltammogram of only CuTOP mixed with Super-P without a Cu current collector, no peak is detectable above 3 V. It seems that the reaction at 3.5 V is a side reaction that helps to stabilize the charge retention of CuTOP. For FeTOP this effect can not be observed.

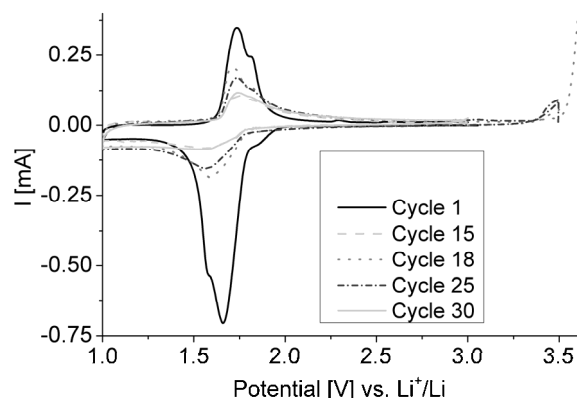


Figure 5: Cyclic voltammogram of CuTOP on a Cu current collector with a sweep rate of 0.1 mV/s. The first 15 cycles were up to 3 V, cycle 17 up to 3.6 V, cycle 18-25 it was cycled up to 3.5 V, and then up to 3.0 V.

Conclusion

CuTOP and FeTOP were synthesized and their electrochemical behavior upon lithiation and delithiation was tested. Especially FeTOP shows a high specific charge that makes it interesting as model material to study the mechanism of lithiation and delithiation. This mechanism can not directly be explained yet, so further studies are in process.

Acknowledgment

Swiss National Science Foundation is thanked for financial support (project no 200021_129508).

References

- [1] I. Belharouak, K. Amine, *Electrochem. Commun.* **7**, 648-651 (2005).
- [2] R. Essehli, B.E. Bali, H. Ehrenberg, I. Svoboda, N. Bramnik, H. Fuess, *Mater. Res. Bull.* **44**, 817-821 (2009).
- [3] S. Benmokhtar, A. El Jazouli, J.P. Chaminade, P. Grave-reau, A. Wattiaux, L. Fournes, J.C. Grenier, D. Waal, *J. Solid State Chem.* **179**, 3709-3717 (2006).

Lithium-bismuth alloy as a reference electrode for electrochemical impedance spectroscopy

J.L. Gómez-Cámer, F. Mornaghini¹, D. Cericola¹, P. Ulmann¹, T. Huckle¹, M.E. Spahr¹, P. Novák

phone: +41 56 310 57 70, e-mail: juan-luis.gomez@psi.ch

In lithium-ion batteries, the use of a sufficient amount of conductive additive (CA) in the positive electrode mixture is necessary to get a good electronic conductivity within the electrode structure, which is essential to improve the cycling stability of the cathode material. For this purpose, many kinds of graphite and carbon black are used, and the most widely used method to analyze the differences in the electrochemical behavior of the cathode mixtures is the long-term cycling. The electrochemical impedance spectroscopy (EIS) could give the necessary information to compare the performance of different CA in a standard electrode mixture. However, it is difficult to obtain this information from a single electrode due to the complexity of lithium intercalation process, i.e. into LiCoO_2 [1]. In order to simplify the impedance spectra and reduce the number of parameters measured a reference electrode (RE) is normally placed close to the studied electrode.

The literature describes the use of lithium metal as reference electrode (RE), however, lithium is strongly reducing and under certain conditions it could be poisoned [2]. Candidates for RE must have a flat potential-composition curve corresponding to a reversible two-phase equilibrium. On the substitution of lithium metal as RE, the use of a Li_xSn RE in Li-polymer cells was proposed and demonstrated [3], and a lithium-tin alloy prepared *in situ* on a tin coated copper wire was applied [4]. However, the SEI film formed at low potentials of the Li-Sn alloys can cause the same effects as with the lithium metal RE.

Lithium alloys with reaction potentials positive to the SEI formation like lithium-antimony (ca. 0.95 V vs. Li^+/Li) or lithium-bismuth (ca. 0.82 V vs. Li^+/Li) [5] are good candidates. We selected bismuth in order to avoid the high toxicity of antimony. This study is focused on the preparation of a stable reference electrode, necessary to obtain accurate impedance spectra, and this will be the starting point to develop a method to analyze the performance of different graphites as conductive additives in positive electrodes through electrochemical impedance spectroscopy.

Experimental

Bismuth pieces (Bi rods, ABCR) were used as working electrode against a lithium foil as counter electrode. Standard two electrode laboratory cells, described elsewhere [6], were used to prepare and study the Li-Bi alloy. Glass fiber separator soaked with electrolyte (500 μL ethylene carbonate/dimethyl carbonate 1:1 by weight, 1M LiPF_6 , Ferro) was used. Galvanostatic charge steps at different C rates with time limitation were applied in order to lithiate the bismuth to a desired composition.

LiCoO_2 was used as active material in the current study. Super P carbon black and KS6L graphite additive (both from TIMCAL), with Kureha PVDF binder, were used in the positive electrode. The slurry was prepared by dispersing 90% LiCoO_2 , 1.5% Super P, 1.5% KS6L, and

7% binder in N-methylpyrrolidone (NMP, Fluka). After homogenization with a turbo stirrer (Ultra Turrax), the slurry was casted onto an aluminum foil and dried at 80 °C in vacuum. Electrode rings with 15 mm \varnothing_{ext} and 7.5 mm \varnothing_{int} were punched out and dried for 12h at 120 °C in vacuum. Three-electrode cells, with the RE placed in the empty space in the middle of the WE, were assembled for the experiments. Lithium foil was placed as counter electrode and *in situ* prepared Li_xBi alloy as reference electrode.

Results

The study of Li_xBi alloy was carried out by charging (lithiating) a bismuth electrode at a current density corresponding to C/5 for a limited period of time in a two electrode cell. Figure 1 shows the galvanostatic curves corresponding to the preparation of a Li_xBi alloy. By changing the lithiation time it was possible to achieve different compositions for the alloy, i.e., $\text{Li}_{0.75}\text{Bi}$ and $\text{Li}_{0.25}\text{Bi}$. According to the literature [5], the Li_xBi alloy shows a potential of ca. 0.8 V vs. Li^+/Li for a lithium content of $x < 1$, which is stable over 72 h (Figure 1).

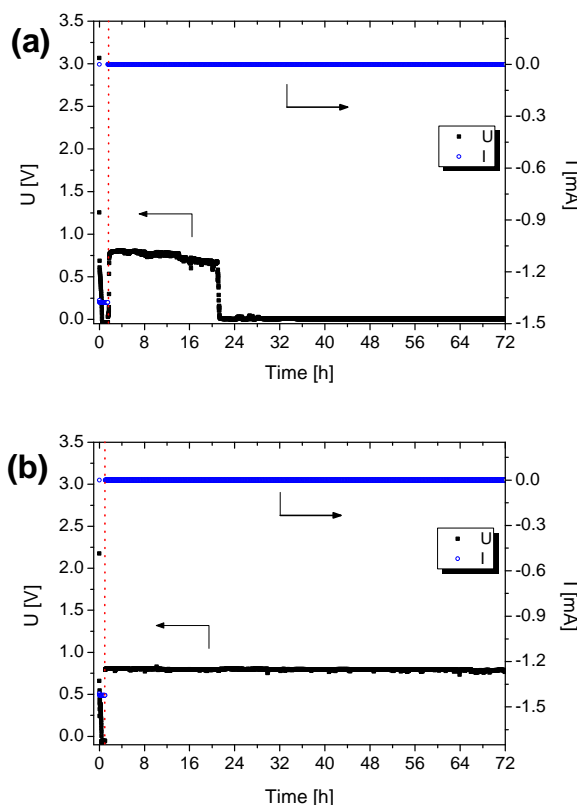


Figure 1. Charge curves followed by open circuit conditions corresponding to (a) $\text{Li}_{0.75}\text{Bi}$, top, and (b) $\text{Li}_{0.25}\text{Bi}$, bottom, alloy preparation.

The first alloy prepared was charged (Figure 1a) until the composition $\text{Li}_{0.75}\text{Bi}$ was achieved, but the cell voltage was not stable after 20h, showing a short-circuit. During charge the Bi piece expanded, breaking the separator

¹ TIMCAL SA, Bodio

and touching the lithium counter electrode (CE), causing the short-circuit. In order to avoid such a large expansion, the amount of Li in the alloy was reduced to 0.25 mol. As shown in Figure 1b, the voltage for $\text{Li}_{0.25}\text{Bi}$ is stable up to 72h.

The suitability of this alloy as a RE lies not only in its voltage stability with time, but also in its relative position with respect to the SEI formation. At this potential no surface film is formed, which means that fewer distortions in the EIS spectra will occur. Figure 2 shows the EIS spectra obtained with two electrode and three electrode configurations in the frequency range from 100 kHz to 10 mHz, of the LiCoO_2 cathode in the second charge, at a voltage of 3 V (Figure 2a) and at 4 V (Figure 2b) vs. the Li CE. Two distinct RE were used in the case of three electrode configuration; a piece of metallic lithium (empty circles in Figure 2) and an *in situ* prepared Li_xBi alloy (triangles in Figure 2). The Li-Bi alloy was prepared *in situ* by placing a piece of metallic bismuth in the RE position in the three electrode cell and charging it against the lithium counter electrode before the impedance measurements. As can be seen in Figure 2, there is a big difference in the impedance spectra depending on whether a 2 electrode or a 3 electrode configuration is used. It is clear from Figure 2 that the impedance spectrum with the Li-Bi RE is simpler and has fewer overlapped processes, since there is no contribution from the anode or any surface film over the RE.

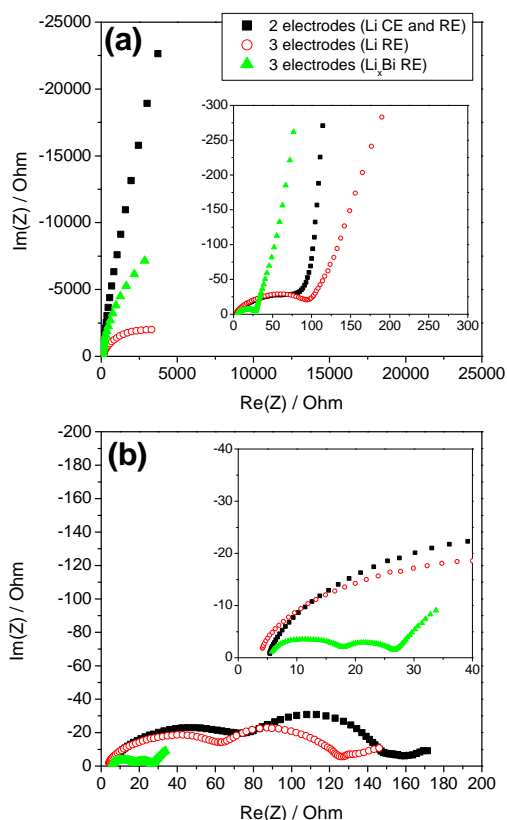


Figure 2. EIS spectra obtained from a LiCoO_2 electrode at (a) OCV voltage (3 V) and (b) 4 V with two electrode configuration and three electrode configuration with lithium metal and lithium-bismuth alloy as reference electrode. Insets with enlarged high frequency region are shown.

In order to determine which elements in the impedance spectra are related to the active material and to the properties of the conductive network or the contact resistances, we performed a study on the state of charge

(SOC) dependency of the impedance spectra during the second cycle, using the three electrode configuration and Li_xBi alloy as RE (Figure 3). The EIS spectra were recorded at 0, 25, 50, 75, and 100% SOC, corresponding to 3.00, 3.95, 3.96, 4.02, and 4.30 V, respectively. From the spectra at 0% SOC of LiCoO_2 , at the beginning of the second charge, two overlapping semicircles appeared in the high frequency region, followed by a capacitor like behavior in the medium and low frequency region. As the SOC increases (delithiation of LiCoO_2) the second semicircle, in the middle frequency region, shrank drastically, due to the creation of lithium ion vacancies in LiCoO_2 and the reduction of charge transfer resistance [1]. We suggest that the first semicircle in the high frequency region is related to the conductive network, since its SOC dependency seems to be negligible. Further experiments will be performed to investigate the influence of CA on this element.

Conclusion

The lithium-bismuth alloy is well suitable to serve as a reference electrode for electrochemical impedance spectroscopy of lithium-ion batteries. With this reference electrode a semicircle in the EIS spectrum related to the conductive additive was identified.

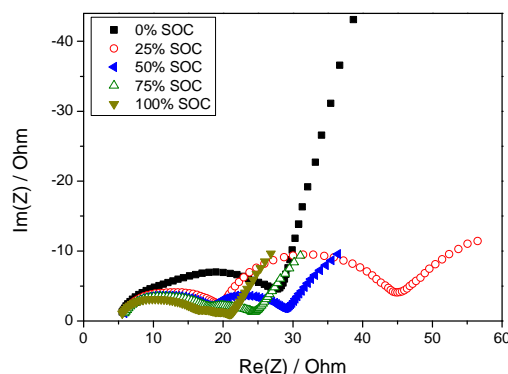


Figure 3. State of charge dependency of the impedance response of a LiCoO_2 positive electrode.

Acknowledgments

The authors are very grateful for the technical support from Hermann Kaiser (PSI).

References

- [1] M.D. Levi, G. Salitra, H. Teller, D. Aurbach, U. Heider, L. Heider, *J. Electrochem. Soc.*, **146**, 1279-1289 (1999).
- [2] A. Blair, C. Sigala, G. Amatucci, D. Guyomard, Y. Chabre, J.M. Tarascon, *J. Electrochem. Soc.*, **145**, 194-209 (1998).
- [3] C.S. Johnson, D.W. Dees, in: *Lithium Batteries Symposium Proceedings*, Fall meeting of the Electrochemical Society, New Orleans, LA, October 10-15 (1993).
- [4] D.P. Abraham, S.D. Poppen, A.N. Jansen, J. Liu, D.W. Dees, *Electrochim. Acta* **49**, 4763-4775 (2004).
- [5] J. Wang, I.D. Raistrick, R.A. Huggins, *J. Electrochem. Soc.*, **133**, 457-460 (1986).
- [6] P. Novák, W. Scheifele, F. Joho, O. Haas, *J. Electrochem. Soc.*, **142**, 2540-2544 (1995).

A reference electrode for the use in ionic liquids

D. Weingarth, A. Foelske-Schmitz, R. Kötzer, A. Wokaun

phone: +41 56 310 41 31, e-mail: daniel.weingarth@psi.ch

The utilization of Ionic Liquids (IL) in electrochemistry increased very rapidly in the last years. For example, IL as electrolytes in electrochemical energy storage devices are becoming more and more important [1]. Additionally fundamental studies of these molten salts on model electrodes are carried out [2]. Many of these measurements require a common electrochemical three electrode system, consisting of a working electrode (WE), counter electrode (CE) as well as a suitable reference electrode (RE). In 2009 we reported on the use of activated carbon (AC) as reference electrodes in organic electrolytes, where we pointed out that AC is reasonably stable in acetonitrile and propylene carbonate based electrolytes [3]. In the present study $[\text{Fe}(\text{cp})_2]$ was added to several IL in order to determine the half wave potential of the first oxidation/reduction of $[\text{Fe}(\text{cp})_2]^{0/+}$.

Experimental

Before use $[\text{EMIM}][\text{BF}_4]$ (99%, Merck KGaA), $[\text{EMIM}][\text{TFSI}]$ (99%, Iolitec Technologies), $[\text{EMIM}][\text{FAP}]$ (98%, Merck KGaA), $[\text{Pyr}_{13}][\text{TFSI}]$ (99%, Iolitec Technologies) and the $[\text{Fe}(\text{cp})_2]$ (Aldrich) were dried at 100°C and a vacuum better than $1 \cdot 10^{-2}$ mbar for at least 8 hours. All substances were transferred into a glove box where 50 mM mixtures of $[\text{Fe}(\text{cp})_2]$ in the respective IL were prepared. The activated carbon (AC, YP17 Kuraray Chemical Japan) electrodes as well as the electrochemical cell were prepared as already described elsewhere [3].

Results

Typical cyclic voltammograms (CVs) showing the oxidation and reduction of $[\text{Fe}(\text{cp})_2]^{0/+}$ in $[\text{Pyr}_{13}][\text{TFSI}]$ are presented in Figure 1. Five CVs in the range of -200 mV to 500 mV vs. the AC quasi reference electrode were recorded every 5 h and the average value of E_{half} was determined. The shown CVs are representative for all

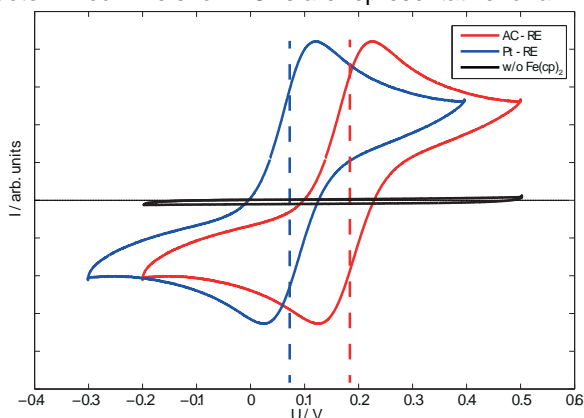


Figure 1. Cyclic voltammograms of 50mM $[\text{Fe}(\text{cp})_2]$ in $[\text{Pyr}_{13}][\text{TFSI}]$ using AC and Pt REs. Vertical lines indicate E_{half} ; Black curve: w/o $[\text{Fe}(\text{cp})_2]$; scan rate: 50mVs^{-1} .

investigated IL / $[\text{Fe}(\text{cp})_2]$ mixtures. Two different REs were attached to the cell, one being a Pt wire and one being AC. The CVs clearly show different half wave potentials in $[\text{Pyr}_{13}][\text{TFSI}]$ for the AC RE (195 mV) and for the Pt RE (80 mV) as indicated with dashed lines. It

is important to note that the recorded oxidation/reduction current decreased with increasing number of CV. However, the current was always several orders of magnitude higher than the double layer charging current measured in that potential region with no $[\text{Fe}(\text{cp})_2]$ present in the system (c.f. black curve Figure 1).

Figure 2 represents the data obtained over several hours of measurements for the IL $[\text{EMIM}][\text{BF}_4]$ as well as $[\text{Pyr}_{13}][\text{TFSI}]$ with the two different REs as already mentioned above. The half-wave potential of the redox couple in the two liquids vs. the AC RE is very well in the range of 0.19 ± 0.01 V, whereas the potential discrepancy is very large (>300 mV) in the case of the Pt wire as RE. Since metal wire pseudo-reference electrodes are very sensitive towards any kind of impurity and easily chargeable, a stable reference potential might only be established after several hours (see $[\text{Pyr}_{13}][\text{TFSI}]$). In addition different liquids exhibit completely different E_{half} . A Pt wire is therefore not at all universal for the use in different IL.

In the case of the AC RE the half-wave potentials of $[\text{Fe}(\text{cp})_2]$ in all investigated IL were in the range of the grey area in Figure 2 indicating that a special mechanism determines the reference potentials in the case of a high surface area carbon electrode. As already discussed in [3] AC is an ideally polarisable electrode. The very high surface area with the resulting large double layer capacitance makes AC less sensitive to impurities and charging. In addition no redox system is needed to establish a stable reference system over many hours, in particular no foreign ions have to be introduced to the system.

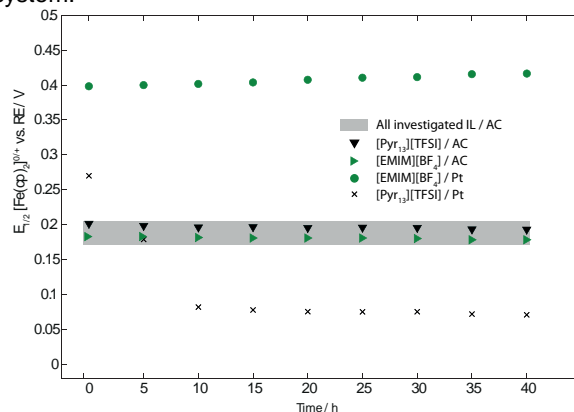


Figure 2. Overview of E_{half} over time for $[\text{EMIM}][\text{BF}_4]$ and $[\text{Pyr}_{13}][\text{TFSI}]$ with AC and Pt REs. Grey area: Potential region for all liquids against AC RE.

References

- [1] M. Galinski, A. Lewandowski, I. Stepniak, *Electrochim. Acta* **51**, 5567–5580 (2006).
- [2] M. Gnahm, T. Pajkossy, D. Kolb, *Electrochim. Acta* **55**, 6212–6217 (2010).
- [3] P. Ruch, D. Cericola, M. Hahn, R. Kötzer, A. Wokaun, *J. Electroanal. Chem.* **636**, 128–131 (2009).

Graphene paper: a suitable way to utilize graphene for supercapacitor electrodes

M.M. Hantel, T. Kaspar¹, R. Nesper¹, A. Wokaun, R. Kötz

phone: +41 56 310 41 89, e-mail: moritz.hantel@psi.ch

Graphene with a theoretical specific surface area of $2630 \text{ m}^2\text{g}^{-1}$ [1] is a promising starting material for applications requiring high surface areas, like supercapacitor electrodes. One way to utilize graphene in an electrode structure is by preparing a so called free-standing graphene paper. Such a paper could be produced by a flow-directed filtration of a graphene dispersion [2], where the thickness of the paper could easily be tuned by the amount of graphene in the solution or by the filtration time. Another approach is to start from a graphene oxide dispersion instead of a graphene one [3]. The resolved graphene oxide paper shows similar morphology like the graphene paper, but with an increased interlayer distance of 6-8 Å which is approximately twice that of graphite [4]. As a drawback such papers are not conductive and hence need to be further treated to regain conductivity. A former study in our group on partially reduced graphite oxide showed that a thermal reduction treatment is a viable technique to restore the conductivity within graphite oxide even by keeping an increased interlayer distance [5]. Applying this thermal reduction treatment on a self-standing graphene oxide paper leads to a partially reduced graphene oxide paper which is characterized in the present work.

Experimental

Starting from graphite oxide made from synthetic graphite (TIMREX SFG44, Timcal, Switzerland) a graphene oxide dispersion in water was prepared by sonication. A flow-directed filtration of the dispersion was used to prepare the self-standing paper like graphite oxide film. After thermal reduction of the graphene oxide paper at 200°C the resulting partially reduced graphene oxide paper was attached to carbon coated aluminium.

Cyclic voltammetry was performed using these electrodes with 1 M TEABF_4 in acetonitrile at a scan rate of 1 mVs^{-1} utilising a VMP3 potentiostat (BioLogic, France). In addition, galvanostatic charge / discharge cycles were performed to characterize the rate capability of the electrodes.

The interlayer distance of the electrodes were characterized by XRD (D8 system, Bruker, Germany) measurements using a Bragg-Brentano diffraction mode. The morphology of the electrodes was investigated by SEM (FE-SEM Ultra55, Carl Zeiss, Germany)

Results and Discussion

The morphology of the partially reduced graphene oxide paper (GOpr-P) and its precursor the graphene oxide paper (GO-P) was investigated first. The XRD characterization of the GO-P (Figure 1) reveals a layered structure of the graphene oxide sheets with an interlayer distance d_{001} of 7.11 \AA , but no features of d_{100} and d_{110} . After the thermal treatment the interlayer distance is decreased to 4.35 \AA and part of the stacking order is lost, indicated by the decrease in intensity for the d_{001} reflex. The SEM micrographs for the partially reduced paper (Figure 2a and b) verify the paper like structure. Figure 2a shows the edge of the paper structure in a low

magnification without any obvious indication that this structure is based on layered graphene sheets with a diameter smaller than $40 \mu\text{m}$. However, at high magnification (Figure 2b) a stacking of partially reduced graphene oxide blocks is evident.

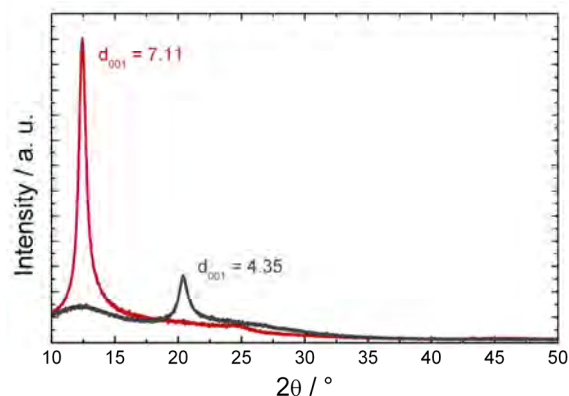


Figure 1. XRD spectra of the GO-P with interlayer distance of 7.11 \AA and the GOpr-P with a reduced interlayer distance of 4.35 \AA .

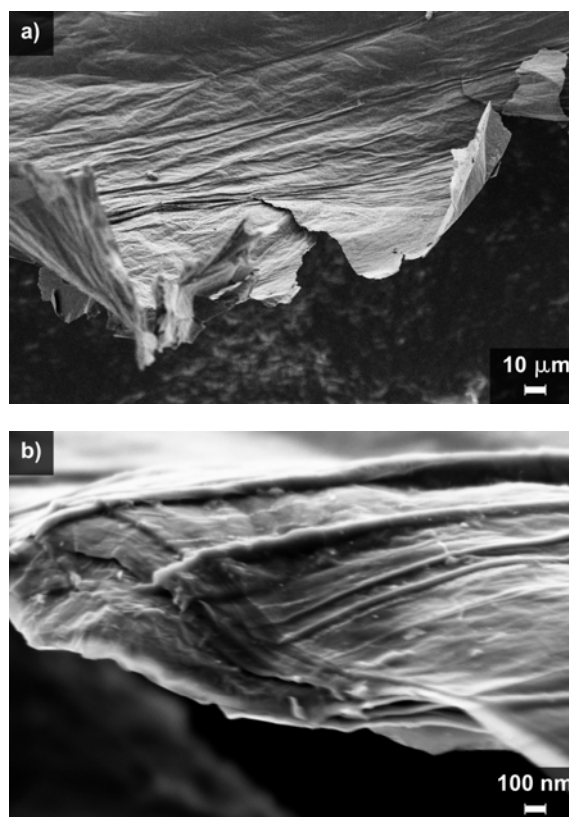


Figure 2. SEM micrographs of GOpr-P showing a) the paper like structure in low magnification and b) the layered graphene agglomerates at a higher magnification.

¹ Laboratory of Inorganic Chemistry, ETH Zürich

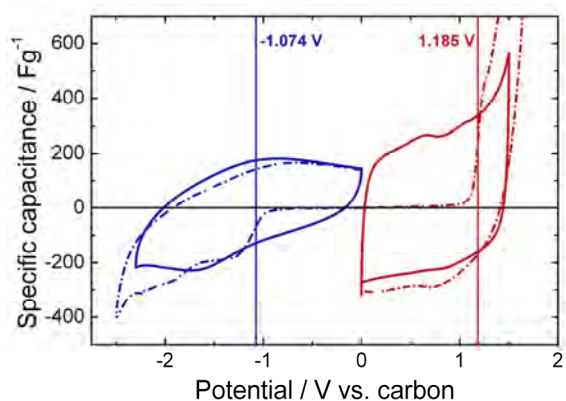


Figure 3. Cyclic voltammograms of GOpr-P showing the first two cycles of the positive and the negative electrode. The dashed line shows the first cycle and the continuous line the second cycle. The CVs were recorded separately for each electrode using 1 M Et_4NBF_4 in acetonitrile with a scan rate of 1 mVs^{-1} .

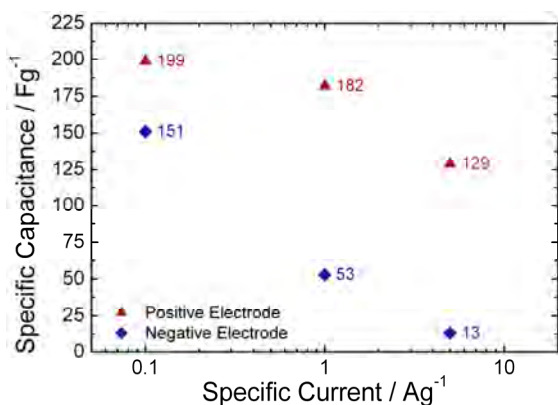


Figure 4. Rate capability of the positive and negative electrode of GOpr-P, calculated from the discharge of galvanostatic charge discharge cycles.

Figure 3 shows the first two cycles for a positively and negatively polarized paper electrode. Both polarizations show an electrochemical activation reaction within the first sweep. The activation potentials, 1.185 V vs. carbon for the positive and -1.074 V vs. carbon for the negative activation, are comparable to those of partially reduced graphite oxide with an interlayer distance of 4.43 Å [5]. A closer look on the activation behaviour reveals an intense activation reaction for the positive polarization with activation currents exceeding the scale of Figure 3. On the contrary the activation of the negative electrode seems to be somehow hindered and the stepwise increase in activation current might indicate some kind of staging during the activation process. The activated electrodes show on one hand a nice rectangular shaped CV for the positive electrode and on the other hand a distorted rectangular shaped CV for the negative electrode indicating a slow charge reversal.

The calculated specific capacitance for the negative and positive electrode for specific currents of 0.1, 1.0 and 5.0 Ag^{-1} are plotted in Figure 4. In each case the discharge current was used for the calculation. For the positive electrode the achieved values are 199, 182 and 129 Fg^{-1} and for the negative electrode 151, 53 and 13 Fg^{-1} .

The electrochemical characterization shows that GOpr-P could be either activated by a negative or a positive potential sweep modifying the properties of GOpr-P to show capacitor like behavior. This characteristic of gra-

phene paper like electrodes was never described before in literature. It also implies that the internal surface of the pristine graphene paper electrode is not accessible for ions at first contact with electrolyte. Therefore the observed electrochemical activation somehow modifies the stacking of the graphene sheets to allow ion transport within this network.

The comparison between the activated positive and negative electrode reveals a huge difference in the performance. On one hand the positive electrode shows a steep current peak during activation which results in large specific capacitance. On the other hand the negative electrode exhibits a somehow staged activation resulting in a relatively small specific capacitance. This discrepancy may not be only related to the different type of intercalated ions, TEA^+ and BF_4^- , but might be the result of different activation reaction mechanisms.

Conclusions

GOpr-P was proven to be a viable electrode material for supercapacitor electrodes utilizing organic electrolytes. The achieved specific capacitance of 199 Fg^{-1} for the positively activated electrode containing neither a conductive agent nor any polymer binder is among the largest electrode capacitance reported in literature for organic electrolytes.

Acknowledgement

The authors would like to thank Swiss National Science Foundation (SNSF) for financial support (project # 200021_126855/1).

References

- [1] A.K. Geim, K.S. Novoselov, *Nat. Mater.* **6**, 183–191 (2007).
- [2] D. Li, M.B. Muller, S. Gilje, R.B. Kaner, G.G. Wallace, *Nat. Nanotechnol.* **3**, 101–105 (2008).
- [3] D.A. Dikin, S. Stankovich, E.J. Zimney, R.D. Piner, G.H.B. Dommett, G. Evmenenko, S.T. Nguyen, R. S. Ruoff, *Nature*, **448**, 457–460 (2007).
- [4] O.C. Compton, S.T. Nguyen, *Small* **6**, 711–723 (2010).
- [5] M.M. Hantel, T. Kaspar, R. Nesper, A. Wokaun, R. Kötz, *Electrochem. Commun.* **13**, 90–92 (2011).

BATTERIES & SUPERCAPACITORS

DIAGNOSTICS

In situ neutron diffraction study of a graphite negative electrode

M. Hess, C. Villevieille, P. Novák

phone: +41 56 310 21 76, e-mail: michael.hess@psi.ch

Graphite is the most common negative electrode material in today's lithium-ion batteries. Its lithium-ion intercalation thermodynamics have been investigated intensively for many years [1-3], but some reactions can still not be fully explained. One of these is the transition at low state-of-charge (SOC). Therefore, we conducted *in situ* neutron diffraction experiments to investigate the lithium-ion intercalation between 7-30 % lithiation ($100\% = \text{LiC}_6$).

Neutron powder diffraction was conducted at D20 beamline at Institut-Laue-Langevin (ILL) in Grenoble, France. It has been reported previously [2,4] that the lithiation proceeds starting from stage 1L, where every interslab is lithiated with 7 % lithium, followed by stage 4L, where every fourth layer is filled. The next proposed transitions include stage 3L, with every third layer is filled with lithium, to stage 2L with every other layer filled. The letter L means no in-plane order. The transition proceeds with stage 2, filled with LiC_6 in-plane order every second interslab. The end structure, stage 1, has LiC_6 in-plane order in every layer.

Experimental

Nine *ex situ* samples in a vanadium container and one *in situ* cell were measured during lithiation. We describe the *in situ* approach in detail because this experiment is very difficult to perform, but gives the only true insight into the material during cycling. For the *in situ* neutron diffraction experiment no changes have to be taken into account which could happen during the relaxation between cycling and *ex situ* powder diffraction. But there is a trade-off between neutron diffraction and electrochemistry. For electrochemical cycling one prefers an electrode thickness of 50-100 μm with a material content of 5-10 mg/cm^2 . In contrast, for neutron diffraction one needs a mass of at least 200-300 mg and an increased cross section due to the beam thickness.

Therefore, we used 200 mg of graphite powder, SFG44 (TIMCAL), with an electrode thickness of approximately 2 mm for the *in situ* experiment. Deuterated electrolyte EC: DMC 1:1 (wt) with 1M LiPF_6 containing 6.8 ppm of water was used to avoid diffuse neutron scattering from hydrogen. The temperature of the cell was set to 50 °C to increase kinetics in the porous electrode and allow stage 2L to appear [3]. A glass fiber separator and a lithium metal counter electrode were used. The first lithiation was investigated. During this so-called formation cycle a solid electrolyte interphase is formed consuming some lithium and electrolyte. The formation was done starting from 3 V and inserting lithium until the potential decreased to 0.22 V vs. Li/Li^+ . During the formation 80 mAh/g were consumed from which 25 mAh/g are reversible [4]. The neutron diffraction was done at the D20 beamline with a wavelength of 1.3594 Å with a configuration of high resolution and a collimator. The electrochemical cycling was continued with a C/300 rate for 40 h at ILL during which patterns have been taken for 10 min between 10-150°.

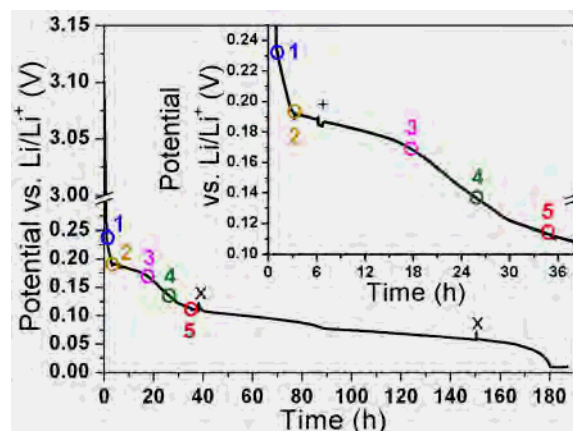


Figure 1. Electrochemical lithiation of graphite powder during *in situ* measurement from point 1-5. The following cycling is a continuation of the cycling of this cell without neutron diffraction where each restart of a cell is indicated by x and a stop by +.

Results

Figure 1 shows the electrochemical cycling of graphite vs. Li/Li^+ with deuterated electrolyte. Point 1 is the start at ILL in stage 1L after SEI formation. Point 2 refers to a full lithiation of stage 1L with 7 % lithium. Point 3 indicates the stage 4, point 4 depicts stage 3, and finally point 5 indicates stage 2L. The cycling rate was C/300 which corresponds to a full electrochemically lithiation in 300 hours. This rate was chosen to avoid phase mixing. After the measurement at ILL from point 1-5 in Figure 1, we continued lithiating the graphite to stage 2 and stage 1, which are well known from previous experiments [1]. This was done to proof the proper cycling of the *in situ* cell. The two x in Figure 1 correspond to the relaxation times when transferring the cycling system back from ILL (after ≈ 40 h) and one current shut-off (after ≈ 150 h). One can see the low potentials during the lithiation confirming the good electrochemical cycling of the cell.

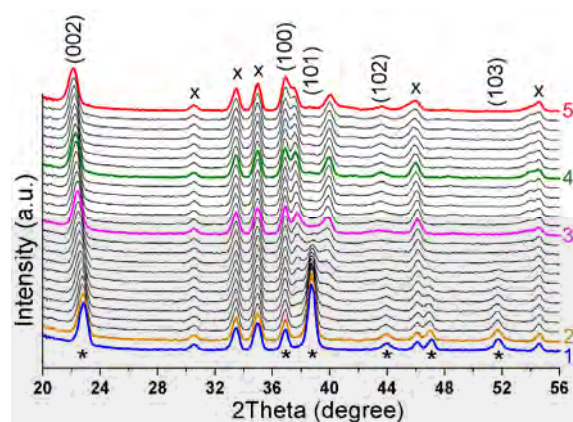


Figure 2a. Evolution of neutron diffraction reflexes during electrochemical lithiation.

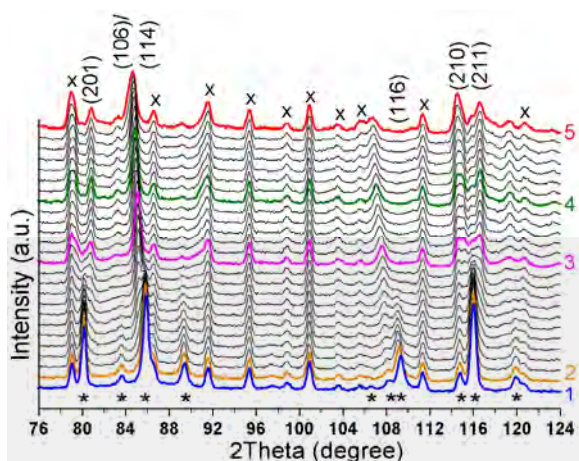


Figure 2b. Evolution of neutron diffraction reflexes during electrochemical lithiation.

In Figure 2, we show the *in situ* Bragg peak evolution where the points 1-5 from Figure 1 are also marked in the same color. In these waterfall diagrams the reflexes originating from graphite are marked with a star "*" and the reflexes originating from the used titanium container with "x". The signal to noise ratio is excellent. The Rietveld refinement of the reflexes in point 1 using Fullprof software is depicted in Figure 3. Table 1 presents all refined phases. The starting material SFG44 has AB and ABC stacking, as presented in Table 1. The 7 % lithiated graphite is the starting point for the *in situ* experiment. The refined parameters correspond to a C-C in-plane distance of 1.422 Å and a graphene interlayer distance of 3.384 Å. Due to the 7 % lithium insertion these distances are changed compared to the starting material SFG44 by -0.006 and +0.81 %, respectively. The second phase in Figure 3 corresponds to the titanium container in which the graphite was cycled. No rhombohedral structure could be found at 7 % lithium insertion.

Figure 4 depicts the Rietveld refinement of the fully lithiated sample LiC_6 during the *ex situ* measurements. Two phases could be assigned, mainly stage 1 with small contributions from stage 2. The refined parameters of stage 1 in Table 1 correspond to a C-C in-plane distance of 1.439 Å. The refined parameters of stage 2 are equivalent to a C-C in-plane distance of 1.430 Å. These values are close to the ones reported by Billaud et al. [2] using X-ray diffraction. They reported 4.286 Å and 7.025 Å for stage 2 and 4.305 Å and 3.706 Å for stage 1, respectively.

Graphite sample	space group	a	c	R_{wp}
graphite AB stacking	$P6_3/mmc$	2.4635	6.7162	9.8
graphite ABC stacking	R-3m	2.4636	10.0734	
7 % lithiated, stage 1L	$P6_3/mmc$	2.4623	6.7674	13.7
Stage 2	$P6/mmm$	4.2906	7.0379	10.4
Stage 1	$P6/mmm$	4.3172	3.70294	

Table 1. Rietveld refined parameters of graphite samples.

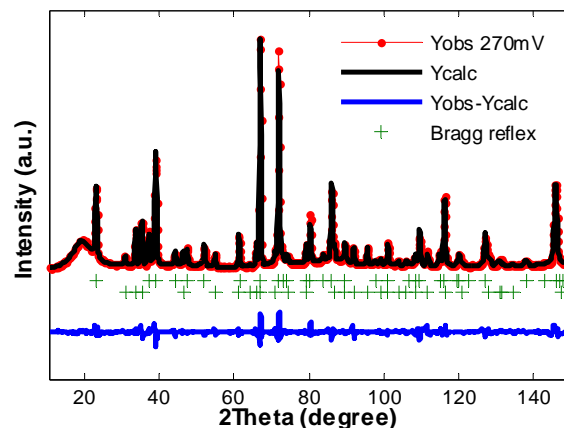


Figure 3. Rietveld refinement of starting material, 7 % lithiated graphite in an *in situ* neutron diffraction cell, second phase is the titanium container.

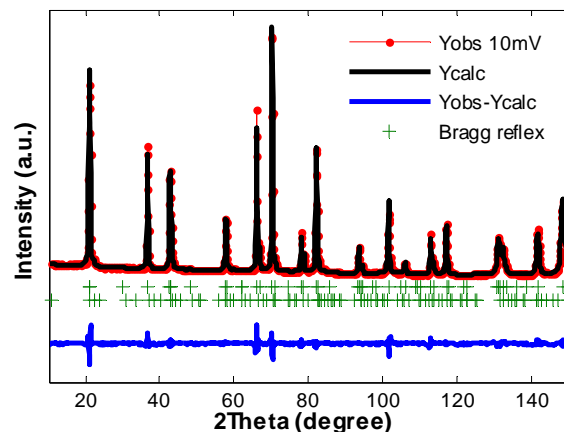


Figure 4. Rietveld refinement of fully lithiated graphite, LiC_6 , from *ex situ* neutron diffraction, second phase are small contributions from stage 2.

Conclusion

Due to the high signal to noise ratio of the *in situ* neutron diffraction experiments on graphite, we could refine the patterns. The evaluated parameters of the stages correspond to those found by XRD [1,2,4]. Now, it should be possible to identify the transitions between stages 4, 3, and 2L which were not possible to elucidate by XRD completely. Further, refinement on these transitions is needed.

References

- [1] D. Guerard, A. Herold, Carbon **13**, 337-345 (1975).
- [2] D. Billaud, F.X. Henry, M. Lelaurain, P. Willmann, J. Phys. Chem. Solids **57**, 775-781 (1996).
- [3] K.C. Woo, W.A. Kamitakahara, D.P. DiVincenzo, D.S. Robinson, H. Mertwoy, D.J. Milliken, J.E. Fischer, Phys. Rev. Lett. **50**, 182-185 (1983).
- [4] J.R. Dahn, Phys. Rev. B **44**, 9170-1977 (1991).

Study of oxygen loss during overcharge of $\text{Li}_{1.1}(\text{Ni}_{1/3}\text{Mn}_{1/3}\text{Co}_{1/3})_{0.9}\text{O}_2$ using neutron powder diffraction

V. Godbole, C. Villevieille, T. Sasaki, P. Novák

phone: +41 56 310 24 57, e-mail: petr.novak@psi.ch

Previous study on NMC [$\text{Li}_{1+x}(\text{Ni}_{1/3}\text{Mn}_{1/3}\text{Co}_{1/3})_{1-x}\text{O}_2$, $x \geq 0$] reported that the overlithiated NMC ($x=0.1$) has better cycling stability as compared to the stoichiometric ($x=0$) one when cycled between 2.5-5.0 V vs. Li/Li^+ [1]. Differential Electrochemical Mass Spectrometry (DEMS) measurements on $\text{Li}_{1.1}(\text{Ni}_{1/3}\text{Mn}_{1/3}\text{Co}_{1/3})_{0.9}\text{O}_2$ have revealed that there occurs an O_2 release for the overlithiated NMC during its first charge till 5.0 V vs. Li/Li^+ [1]. This study uses neutron powder diffraction as a tool to confirm if the O_2 released is lost from the structure of the overlithiated NMC and correlates changes in unit cell parameters, oxygen content, and Li-Ni exchange with the specific charge of the material.

Experimental

Five different coin-like test cells were built using $\text{Li}_{1.1}(\text{Ni}_{1/3}\text{Mn}_{1/3}\text{Co}_{1/3})_{0.9}\text{O}_2$ (NMC-10) and Super-P carbon (TIMCAL, Switzerland) as the electrode mixture. A Celgard® 2400 (Celgard, USA) was used as the separator and was soaked in ethylene carbonate (EC): dimethyl carbonate (DMC) 1M LiPF_6 (Ferro, USA) electrolyte. The cells were assembled inside an Ar-filled glove box using lithium as the counter electrode. The cells containing 0.12-0.15 g of electrode material were cycled at C/20 rate with respect to 322.5 mAh/g, stopped at different stages of cycling; the electrode mass removed, washed with DMC, dried, and then used for *ex situ* neutron powder diffraction (NPD) measurements. The NPD measurements were performed at the D20 beamline of ILL, Grenoble, France. For the measurements, the dry powder samples were held in vanadium tubes sealed under Ar and the measurements were performed at a wavelength of 1.36 Å for 20 min each.

Results

Figure 1(A) shows the first electrochemical cycle of NMC-10 and marks the points where the *ex situ* NPD patterns were recorded. Profile matching was performed on these NPD patterns giving the data for evolution of unit cell parameters on cycling, shown in Figure 1(B). During the first charge, the total unit cell volume change was only 2%, indicating the structural stability of NMC-10. The results in Figure 1(C) show the evolution of Li and O content and Li-Ni exchange as a function of specific charge, obtained via Rietveld refinement of the NPD patterns. As the Li is removed from the material during its first charge, the oxygen content remains unchanged until 100 mAh/g. However on further charging, the oxygen content drops down for the point 3 at a potential around 4.5 V vs. Li/Li^+ . This potential is close to the potential for O_2 release observed from the DEMS measurements [1]. On further charging the oxygen content falls down even further. During the first discharge, i.e., lithiation, no change in oxygen content was observed.

Thus it could be seen from the NPD data that the O_2 release seen from the DEMS measurements is indeed due to extraction of O^{2-} from the structure of NMC-10. The Li-Ni exchange also shows interesting variation

during the first cycle. During the course of first charge, the Li-Ni exchange increases, while after the first discharge its value drops down slightly. However the total percentage of Li-Ni exchange after first cycle is eventually higher than that in the starting compound. Increased Li-Ni exchange is known to induce structural stability in the layered oxides, presumably resulting in the lower volumic expansion seen for NMC-10 and hence its better cyclability.

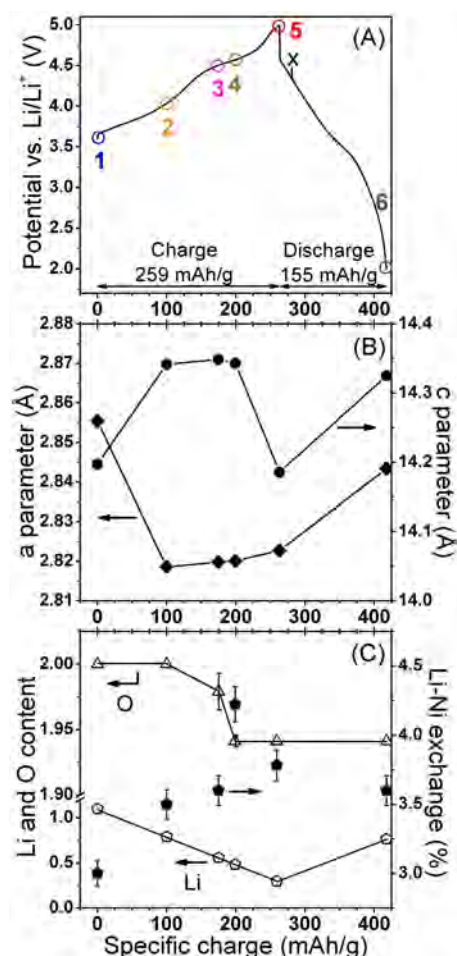


Figure 1. (A) First electrochemical cycle of NMC-10 between 2.0-5.0 V vs. Li/Li^+ , (B) evolution of unit cell parameters, and of (C) Li and oxygen content and Li-Ni exchange as a function of specific charge. X is voltage fluctuation due to rest period.

Thus using the high intensity NPD beamline, it has been shown for the first time for NMC-10 that O^{2-} is indeed removed from the structure during its first overcharge. Moreover increased Li-Ni exchange suggests stabilization of the NMC-10 structure for further cycling via the pillaring effect.

References

- [1] F. La Mantia, F. Rosciano, N. Tran, P. Novák, J. Appl. Electrochem. **38**, 893–896 (2008).

In situ FTIR spectroscopy on glassy carbon electrodes as a model of the graphite surface for Li-ion batteries: impact of additives on the SEI film

S. Pérez-Villar, H. Schneider, P. Novák

phone: +41 56 310 24 57, e-mail: petr.novak@psi.ch

FTIR spectroscopy is a surface sensitive analytical method suitable to gain insight into interfacial phenomena. Here, the focus is on the analysis of the solid electrolyte interphase (SEI) film formed on the surface of graphite electrodes during the first reduction (lithium intercalation), which has been widely investigated by both *ex situ* [1] and *in situ* infrared spectroscopy [2]. Our goal was to establish this method as a first step to the development of *in situ* infrared microscopy on the same system.

Three major challenges have been faced in the method development. Firstly, there is the strong absorption of the infrared (IR) radiation by the electrolyte. It was mitigated by adjusting the working electrode to a position very close to the IR window, thereby allowing only a very thin layer (ca. 10 μm) of electrolyte solution between the electrode and the window [3]. Secondly, it is difficult to identify the IR signature of the species adsorbed on the electrode surface as the magnitude of the relevant IR bands is extremely weak due to the species' low concentration. Therefore, subtraction of the IR spectra recorded at different potentials had to be performed and differential spectra were evaluated. Thirdly, the weak and diffuse infrared reflection of standard battery grade graphite powder makes the application of a reflection technique very challenging. Therefore, for the development of the method glassy carbon (GC) was used to model the surface of graphite, as GC offers a flat surface with a high reflectivity in the infrared region. Indeed, despite of its retarded lithium insertion behavior GC is a useful model substitute for an electrode made from graphite, when surface reactions only are studied [4]. In order to enhance the protective SEI layer on the surface of the carbon, additives are typically used. Such additives make the SEI normally thicker, and stronger infrared signals from SEI are therefore expected. Thus, the addition to a standard battery electrolyte of vinylene carbonate (VC) and ethylene sulfite (ES) in small quantities has been investigated here as a model case.

Experimental

For electrochemical characterization, composite electrodes of 80 wt.% of synthetic graphite SFG44 (TIMCAL) and 20 wt.% PVDF binder were cycled in a 1M LiClO₄ in EC/DMC (1:1 v/v) electrolyte solution. Vinylene carbonate (VC) and ethylene sulfite (ES) were used as respective additives in the electrolyte (5 % v/v). Lithium foil served as both counter and reference electrode. The galvanostatic tests were performed at a C/20 rate in the first cycle and a C/5 rate in the next cycles.

The spectroelectrochemical experiments were carried out in a Fourier transform infrared spectrometer Perkin Elmer System 2000 equipped with a DTGS detector. The *in situ* spectroelectrochemical cell for the external reflectance and the optical system for *in situ* FTIR spectroscopy are depicted in Figure 1. A 12 mm diameter GC disc was used as received and served as a working electrode. A Li strip served as both, the counter and reference electrode, and the electrolytes were the same as above. The cell was assembled and hermetically

sealed in a glove box with water and oxygen content <1 ppm. A single beam reference spectrum R_0 was recorded at 3.0 V vs. Li/Li⁺ after stabilization of the cell at this potential for 60 min. The potential was then successively decreased in steps to 1.5, 1.0, 0.7, 0.4, and 0.2 V, respectively, with an equilibration time of 60 min at each potential. After 55 min of equilibration time, a single beam spectrum R_E was recorded at the given potential E . The potential-dependent changes at the electrode/electrolyte interface were visualized by plotting R_E/R_0 . IR spectra were accumulated over 500 scans with a resolution of 4 cm^{-1} .

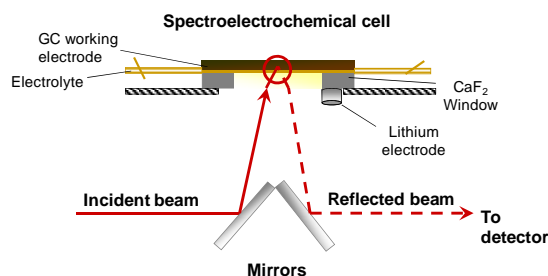


Figure 1. Sketch of the IR path and the spectroelectrochemical cell in the setup used.

Results

The first cycle of test electrodes based on SFG44 graphite in the LiClO₄, EC/DMC electrolyte without and with VC and ES additive is shown in Figure 2. The charge consumption, respectively, is 415, 439, and 1026 (in Ah/kg) and the respective irreversible capacity "loss" is 13%, 16%, and 72%. The galvanostatic curve of the graphite electrode in the LiClO₄, EC/DMC electrolyte exhibits a reductive shoulder at ca. 0.7 V vs. Li/Li⁺ due to the reduction of the EC component. By adding VC to the electrolyte, the reductive shoulder is less visible. The reason is that the SEI formed with VC is formed in part chemically, without charge consumption. Further, the cell containing ES as an additive shows two reduction processes around 1.9 V and 1.4 V, respectively. – The cycling stability was also tested and no significant capacity fade was observed for all systems during 25 cycles.

In the next step the spectroscopical setup was developed. Prior to the *in situ* FTIR experiments, a background spectrum at 3.0 V is recorded after the system stabilization. One of the main challenges in reflectance spectroscopy is the strong absorbance of the electrolyte in the infrared region, making it difficult to observe spectral features of products formed at the electrolyte/electrode interface during cycling. To minimize this effect the spectroscopy has to be performed in a thin layer configuration with the electrolyte layer having a thickness of less than ca. 10 μm [3]. This is illustrated in Figure 3 showing the improvement of the single beam spectra of the system GC in LiClO₄, EC/DMC when the electrode is pushed against the optical window. The strong downward going bands correspond to the electrolyte absorption in the spectroelectrochemical cell.

A good compromise between the spectroscopy and electrochemistry was found by adjusting the strongest absorption band to about 75 % with respect to the relative energy absorption measured [4].

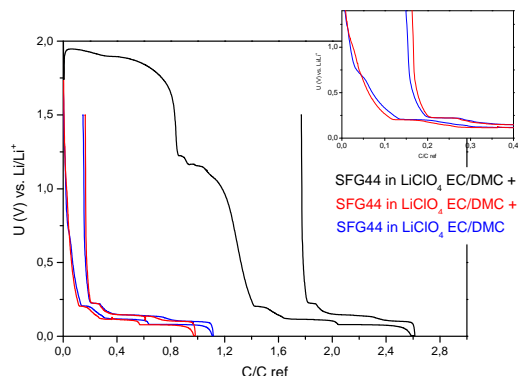


Figure 2. First cycle of a test cell made of SFG44 in LiClO_4 , EC/DMC with and without VC and ES additive, respectively. The inset shows an enlarged view of the potential curve for the electrolyte without additive and with 5 % of VC.

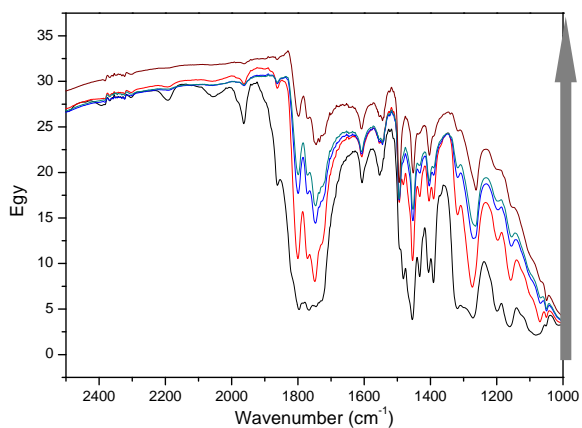


Figure 3. Single beam spectra recorded when pushing the working electrode towards the IR window by increasing the mechanical pressure.

Figure 4 displays the *in situ* FTIR spectra of GC in the investigated electrolytes. These spectra show a clear potential-dependent evolution demonstrating changes of related species in the thin layer between electrode and IR window. Several upward and downward going bands are observed negative to 1.0 V vs. Li/Li^+ . Similar behavior is noticed for each spectrum at the same wavenumber but with an increase in the intensity of the bands with the decreasing potential. When the additives are present, the most significant difference is the downward going band at 1850 cm^{-1} for 5 % VC. Moreover, with the ES additive, the intensity of the bands is stronger. The IR bands between $1700\text{--}1850\text{ cm}^{-1}$, 1300 cm^{-1} , and $1200\text{--}1100\text{ cm}^{-1}$ may be assigned to the IR absorption of species containing C=O, CH_2 , and C-O functional groups, respectively. The interpretation of these spectra is ambiguous as many explanations are suggested in the literature. Matsui et al. [5] support the standard interpretation that the upward bands correspond to a disappearance of a chemical bond (and, consequently, the amount of the respective species is decreasing), while the downward bands correspond to a formation of new chemical bonds and, thus, to an increase in the amount of species. However, in their work Ikezawa et al. [2] established the idea of a reversible equilibrium between

PC solvated species and free PC. (Note that PC and EC behave very similarly.) Thus, the upward bands would correspond to the vibrational modes of solvent molecules solvated to lithium anions while the downward bands would correspond to free PC. Therefore, a final interpretation of our spectra is not elaborated yet and further experiments are needed to understand the processes that occur at the electrolyte/electrode interface. Nonetheless, we demonstrated the viability of the approach and made the first step towards *in situ* infrared microscopy in battery relevant systems.

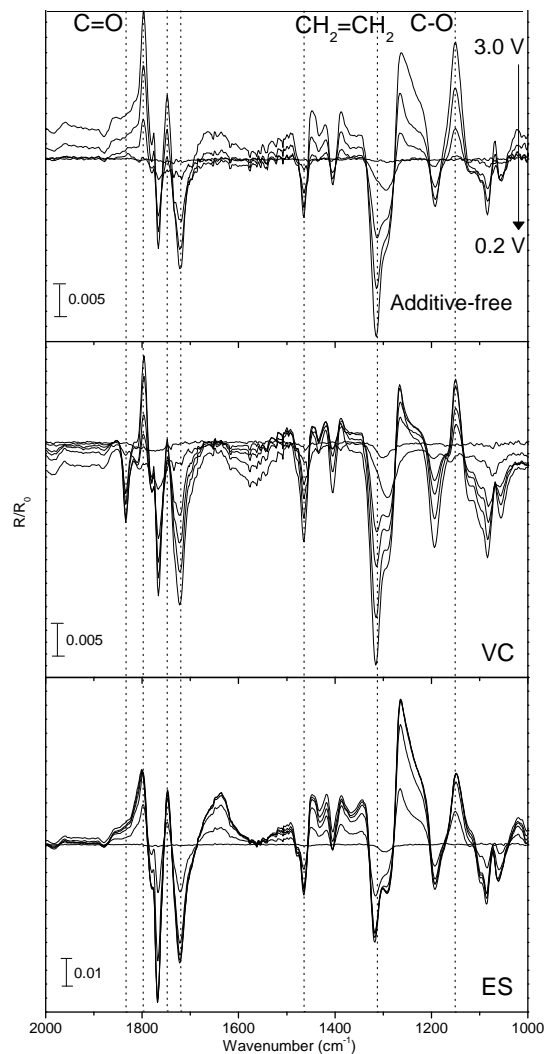


Figure 4. *In situ* FTIR spectra of GC in LiClO_4 , EC/DMC without additive (top) and with 5 % VC and ES (middle, bottom) recorded at 3.0, 1.5, 1.0, 0.7, 0.4, and 0.2 V vs. Li/Li^+ .

References

- [1] D. Aurbach, Y. Ein-Eli, O. Chusid, Y. Carmeli, M. Babi, H. Yamin, *J. Electrochem. Soc.* **141**, 603-611 (1994).
- [2] Y. Ikezawa, H. Nishi, *Electrochim. Acta* **53**, 3663-3669 (2008).
- [3] A. Bewick, K. Kunimatsu, B.S. Pons, *Electrochim. Acta* **25**, 465-468 (1980).
- [4] F. Joho, P. Novák, *Electrochim. Acta* **45**, 3589-3599 (2000).
- [5] M. Matsui, K. Dokko, K. Kanamura, *J. Electrochem. Soc.* **157**, A121-A129 (2010).

Application of *in situ* Raman spectroscopy to understand the reaction mechanism of $\text{Li}_2\text{MnO}_3\cdot\text{Li}(\text{Mn}_x\text{Ni}_y\text{Co}_z)\text{O}_2$ in Li-ion batteries

C. Villevieille, S. Pérez-Villar, P. Lanz, P. Novák

phone: +41 56 310 24 10, e-mail: claire.villevieille@psi.ch

Since the introduction of LiCoO_2 in Li-ion batteries by Sony, layered metal oxides have drawn a lot of interest. Because of the high toxicity of cobalt, current research focuses on replacing cobalt and building new, safer batteries with higher power and energy densities. Numerous groups have investigated layered materials such as Li_2MnO_3 and $\text{LiNi}_{1/3}\text{Mn}_{1/3}\text{Co}_{1/3}\text{O}_2$ (NMC). Li_2MnO_3 positive electrode material has been shown to have very poor cyclability. However, it can be activated when charged to 4.5 V vs. Li/Li^+ , resulting in a loss of Li_2O and the formation of MnO_2 [1]. Stoichiometric NMC is one of the most interesting families of layered oxides [2]. NMC materials combine three different transition metals in a certain ratio, which decreases the amount of cobalt. Unfortunately, when lithium is extracted from their structure, several phase transitions occur, which affects long-term cyclability. Recently, several groups have investigated the stabilization of NMC by formally adding Li_2MnO_3 , creating what is commonly known as overlithiated NMC [3]. Despite the different space groups of NMC and Li_2MnO_3 , $R\bar{3}m$ and $C2/m$, respectively, the close-packing structures of oxygen in these two compounds are almost identical. This results in Li_2MnO_3 -like domains within the NMC structure. In comparison with stoichiometric NMC, the overlithiated compounds contain extra lithium in the transition metal slabs. This presence of ions with different radii and charges in the slabs leads to ordering of Mn^{4+} and $\text{Ni}^{2+/3+}$ around Li^+ .

Before performing the Raman experiments, we characterized Li_2MnO_3 -stabilized $\text{Li}(\text{Mn}_x\text{Ni}_y\text{Co}_z)\text{O}_2$ electrochemically. Cyclic voltammetry studies revealed that an irreversible reaction occurs at a potential of 4.5 V vs. Li/Li^+ during the first delithiation step. Differential electrochemical mass spectrometry (DEMS) showed the release of oxygen at the same potential. An *in situ* neutron diffraction study was also performed on the Li_2MnO_3 -stabilized $\text{Li}(\text{Mn}_x\text{Ni}_y\text{Co}_z)\text{O}_2$, showing the course of the oxygen occupancy inside the structure during the first delithiation.

The aim of this study is to follow the reaction mechanism of Li_2MnO_3 -stabilised $\text{Li}(\text{Mn}_x\text{Ni}_y\text{Co}_z)\text{O}_2$ during electrochemical cycling using Raman spectroscopy as a local characterisation method, in order to obtain information on the NMC and Li_2MnO_3 structural ordering.

Experimental

Electrodes were prepared by casting a mixture of 80% $\text{Li}_2\text{MnO}_3\cdot\text{Li}(\text{Mn}_x\text{Ni}_y\text{Co}_z)\text{O}_2$ (henceforth called Li-NMC) (BASF), 10% PVDF (binder) and 10% carbon black Super-P (TIMCAL), all suspended in N-methyl-2-pyrrolidone (Fluka) onto a nickel mesh. After drying, the electrodes were punched out and assembled in a spectroelectrochemical cell as described elsewhere [4]. The *in situ* Raman spectroscopy was performed in a cell that allows the recording of Raman spectra from the back of the working electrode.

Raman spectroscopy of the starting material

In order to optimize the performance of Li-NMC materials it is important to have knowledge of the structure of the material and the ratio between the $\text{Li}(\text{Mn}_x\text{Ni}_y\text{Co}_z)\text{O}_2$ and Li_2MnO_3 components. Therefore, we investigated the electrodes using Raman spectroscopy. Figure 1 presents three different Raman spectra belonging to NMC ($a = b = 2.865(2) \text{ \AA}$, $c = 14.248(1) \text{ \AA}$, $R\bar{3}m$ space group and $V = 99.97(1) \text{ \AA}^3$), Li_2MnO_3 ($a = 4.940(2) \text{ \AA}$, $b = 8.556(2) \text{ \AA}$, $c = 5.025(2) \text{ \AA}$, $\beta = 109.28^\circ$, $C2/m$ space group and a cell $V = 200.5 \text{ \AA}^3$) and Li-NMC ($a = b = 2.852(1) \text{ \AA}$, $c = 14.235(2) \text{ \AA}$, $R\bar{3}m$ space group and $V = 100.34(2) \text{ \AA}^3$), respectively. [5]

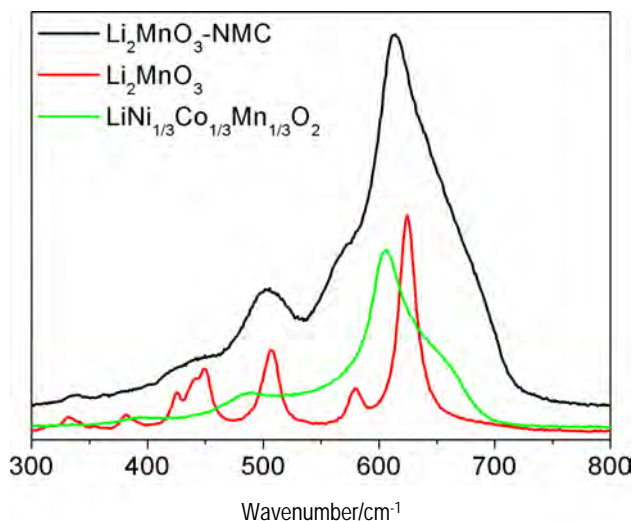


Figure 1. Raman spectra of stoichiometric NMC ($\text{LiNi}_{1/3}\text{Mn}_{1/3}\text{Co}_{1/3}\text{O}_2$), Li_2MnO_3 , and $\text{Li}_2\text{MnO}_3\cdot\text{Li}(\text{Mn}_x\text{Ni}_y\text{Co}_z)\text{O}_2$ electrodes.

As we can see in figure 1, the Raman spectrum of Li-NMC seems to be a linear combination of the peaks of stoichiometric NMC and Li_2MnO_3 . The fact that the two contributions cannot be separated complicates the spectral interpretation of Li-NMC electrode materials. According to the standard Raman spectroscopic treatment, NMC materials have D_{3d} symmetry. In this symmetry group there are only two Raman-active modes, A_{1g} and E_g , belonging to M-O symmetrical stretching and O-M-O bending vibration, respectively. Because of the similarity of each transition metal and because of the layered structure, it is easy to understand that we expect six bands for NMC (since there are three metals). But the NMC spectrum shows only three bands, leading us to conclude that overlapping occurs. Thus, we attempted to deconvolute the NMC and the Li-NMC spectra. As presented in figure 2, it was possible to deconvolute the spectra into six different contributions. Table 1 summarizes the position of the deconvoluted Raman bands of NMC and Li-NMC, as well as the full width at half maximum (FWHM) of both materials for peak number 5 (corresponding also to the most intense band

of Li_2MnO_3 , which gives a probability of overlapping in the case of Li-NMC).

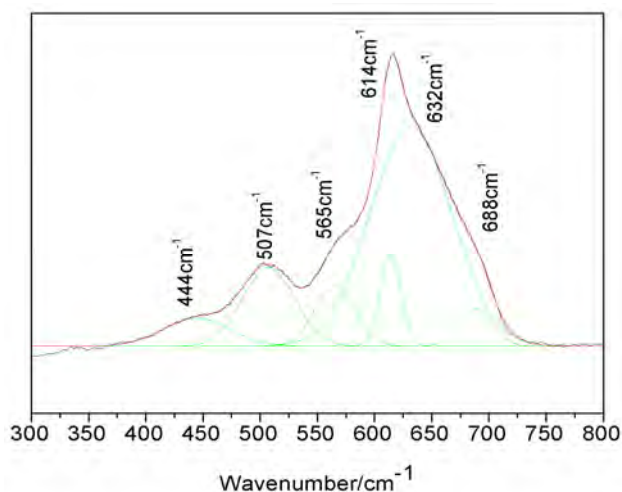


Figure 2. Deconvolution of the Raman spectra for the starting material $\text{Li}_2\text{MnO}_3\text{-Li}(\text{Mn}_x\text{Ni}_y\text{Co}_z)\text{O}_2$.

Looking at table 1, one notices that the bands of Li-NMC are shifted to higher frequencies. This shift could be explained by the stress created within the layered structure due to the Li_2MnO_3 ordering. As we have already discussed elsewhere [5], the ordering inside the Li-NMC layer leads to two exchange processes, namely Li/Ni and Li/Mn, causing stress inside the structure (smaller volume). The second striking feature is the huge increase in the FWHM for band number 5. As we already mentioned, that peak has the largest overlap with Li_2MnO_3 .

peak	1	2	3	4	5	6	FWHM
NMC	405	486	572	581	605	637	23
Li-NMC	444	507	565	614	632	688	55

Table 1: Band position (in cm^{-1}) after deconvolution for the NMC and the Li-NMC. The FWHM is for band n°5.

In situ Raman spectroscopy during the first delithiation of the Li-NMC

An *in situ* Raman spectroscopic study was performed on Li-NMC during the first delithiation process. The electrochemical result is presented in figure 3 (top). The first delithiation curve exhibits two main phenomena; the first one between 3.3 V and 4.3 V vs. Li/Li^+ and the second one between 4.4 V and 4.8 V vs. Li/Li^+ . The bottom of figure 3 shows the evolution of the *in situ* Raman spectra.

Just like the galvanostatic curve, the *in situ* Raman spectra can also be separated into two processes. The first one corresponds to the first phenomenon on the galvanostatic curve, which is ascribable to the delithiation of the NMC component. The second one corresponds to the second plateau of the galvanostatic curve and is ascribable to the delithiation of the Li_2MnO_3 component. While the processes are quite easy to understand from an electrochemical point of view, it is more complicated to understand the *in situ* Raman spectra.

Along the time axis of the first process we can clearly see a decrease in the intensity of the bands, which is

probably due to the amorphization of the material or an increase in electrical conductivity at a higher state of charge, leading to a decrease in optical skin depth. For the second process, the new set of peaks cannot yet be ascribed to a phase and two hypotheses are under investigation:

- NMC layer without lithium
- MnO_2 created by Li_2MnO_3 activation.

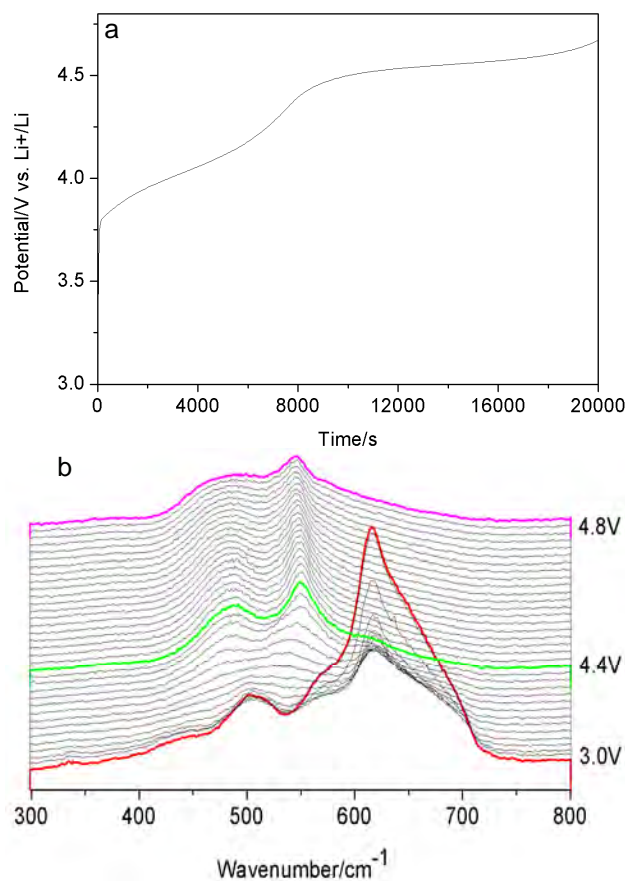


Figure 3. a) Galvanostatic curve for the first delithiation of the Li-NMC and b) evolution of the *in situ* Raman spectra of Li-NMC electrode.

Conclusion

In situ Raman spectroscopy has proved to be a useful tool to follow structural changes occurring during electrochemical cycling of NMC type materials.

Acknowledgments

The authors are very grateful for the financial support from BASF SE.

References

- [1] A.D. Robertson, P.G. Bruce, *Chem. Mat.*, **15**, 1984 (2003).
- [2] A. Manthiram, J. Choi, W. Choi, *Solid State Ionics*, **177**, 2629 (2006).
- [3] N. Tran, L. Croguennec, C. Jordy, P. Biensan, C. Delmas, *Solid State Ionics*, **176**, 1539, (2005).
- [4] H. Schneider, A. Hintennach, P. Maire, P. Novák, *PSI Electrochemistry Laboratory Annual Report*, 2010, 67 (2011).
- [5] C. Villevieille, H. Sommer, H. Schneider, P. Novák, *PSI Electrochemistry Laboratory Annual Report*, 2010, 65-66 (2011).

In situ neutron diffraction applied to positive and negative electrode materials

V. Godbole, C. Villevieille, M. Hess, P. Novák

phone: +41 56 310 24 10, e-mail: claire.villevieille@psi.ch

One of the most important issues for the lithium-ion battery is its safety. During the cycling of a material changes occur inside its structure leading to stable or metastable phases which can be potentially dangerous and/or toxic. In order to identify these different phases, structural information recorded during the cycling or *in operando* is needed. Then X-ray and neutron diffraction are the best techniques for this purpose. The problem is to measure all these structural changes during the cycling that means *in situ*, in which case we can avoid the problem of air exposure and relaxation of some materials. A new *in situ* cell for neutron diffraction (ND) was built in our group for this purpose and can be used at the D20 beamline (ILL, Grenoble, France). The design of the cell is described elsewhere [1].

The cell was electrochemically tested to work with various electrode (negative or positive) materials as seen in figure 1.

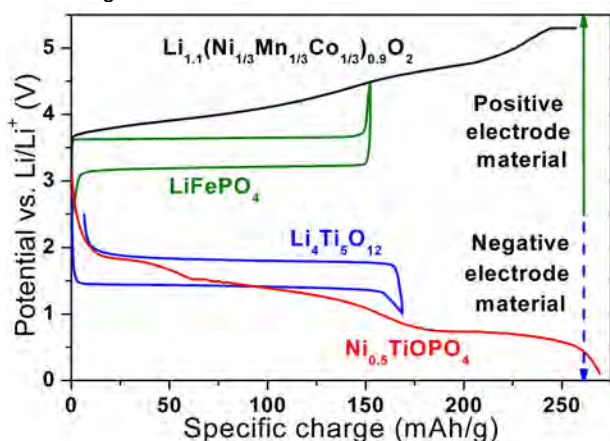


Figure 1. Electrochemical cycling of various electroactive materials in the *in situ* ND cell.

Results

Two different examples (LiFePO_4 for positive and graphite for negative electrode) are shown in figure 2 and 3 to demonstrate the feasibility of the method. In figure 2, we can see that during the course of first charge, the peaks corresponding to LiFePO_4 phase disappear, while those from FePO_4 emerge. At 50% specific charge both phases coexist. The second example presents the result of the *in situ* cycling of a graphite electrode (Figure 3). The neutron diffraction patterns recorded during lithiation of graphite show lot of changes. As an example, the peak (002) is seen to shift to lower 2θ values, i.e., higher c unit cell parameter, which is expected. Other peaks are also shifting or subject to evolve during the course of lithiation. The detailed results are presented also in this annual report (contribution M. Hess et al.)

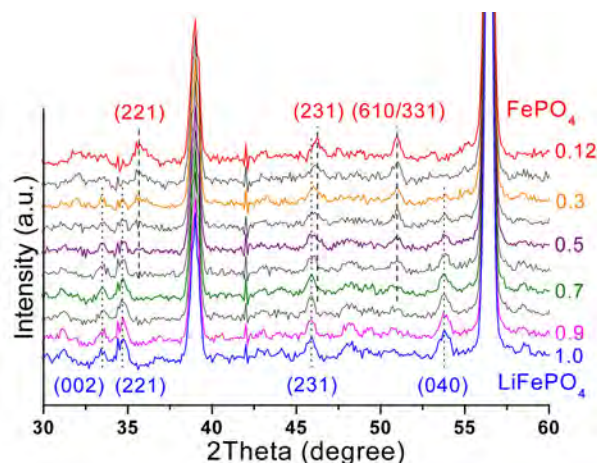


Figure 2. *In situ* ND patterns ($\lambda=1.36\text{\AA}$) recorded during the 1st charge of LiFePO_4 .

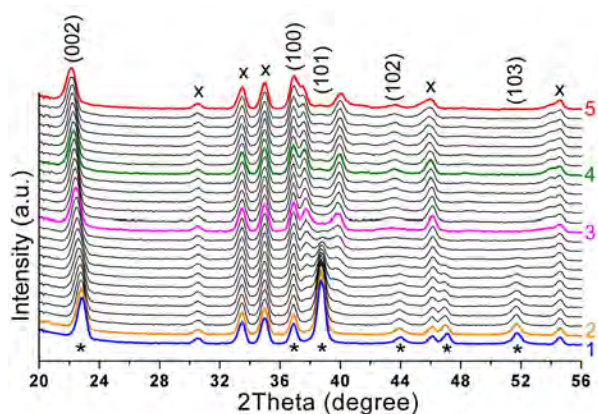


Figure 3. *In situ* ND patterns ($\lambda=1.36\text{\AA}$) recorded during the 1st lithiation of graphite. (*) and (x) mark peaks from graphite and titanium, respectively.

Conclusion

The *in situ* experiments performed using both graphite and LiFePO_4 showed very good electrochemical performance and high peak/noise ratio for the ND patterns. Thus, with this new ND cell we proved the feasibility of the concept. Now it is possible to follow the structural evolution in electroactive materials for lithium-ion batteries in real time.

References

- [1] J.-F. Colin, V. Godbole, H. Kaiser, P. Novák, PSI Electrochemistry Laboratory Annual Report 2009, 64-65 (2010).

In situ investigation of inhomogeneous reactions perpendicular to current collector by using two-layer electrodes

T. Sasaki, V. Godbole, C. Villevieille, Y. Ukyo¹, P. Novák

phone: +41 56 310 43 96, e-mail: tsuyoshi.sasaki@psi.ch

The homogeneity of reactions in electrodes has a tremendous impact on the safety and the durability of Li-ion batteries. An inhomogeneous reaction should lead to a concentration of current flow into a part of the electrode which then suffers from overcharge and overuse. Several investigations have been conducted on inhomogeneous reactions in the lateral direction in electrodes [1, 2]. However, few studies have been made at inhomogeneous reactions in the direction perpendicular to the current collector. Our objective in this study is to investigate the inhomogeneous reactions in the perpendicular direction by *in situ* measurements. For the direct detection of inhomogeneous reactions, we applied *in situ* synchrotron X-ray diffraction (XRD) measurements in transmission mode using “two-layer” electrodes.

Experimental

The two-layer electrodes were built of two self-standing sheets with different active materials. The self-standing sheets were prepared by mixing 70 wt. % of active materials, 10 wt. % of conductive carbon (TIMCAL SuperP), and 20 wt. % of polyvinyl difluoride-hexafluoropropylene copolymer binder (KYNAR FLEX 2801). In this study, two-layer electrodes with LiMn_2O_4 (LMO) and $\text{LiNi}_{0.80}\text{Co}_{0.15}\text{Al}_{0.05}\text{O}_2$ (NCA) were used as the working electrodes. The crystal structure changes of LMO and NCA during the charge/discharge process have been reported both by our group [3] and other researchers [4-5]. We can thus detect which active material is reacting during the *in situ* measurement by tracing each XRD pattern. The sandwiched structure of the two-layer electrode was confirmed with Scanning Electron Micrographs and Energy Dispersive X-ray Spectroscopy. Three kinds of the two-layer electrodes were made using different order of the layers or different overall density, i.e., porosity. The weight of each active material is the same in all two-layer electrodes. The schematic diagrams of the three two-layer electrodes are shown in Figure 3.

- Sample H1: Upper side: LMO, Lower side: NCA High density (Packing density: 2.9 g/cm^3)
- Sample H2: Upper side: NCA, Lower side: LMO High density (Packing density: 2.9 g/cm^3)
- Sample L1: Upper side: LMO, Lower side: NCA Low density (Packing density: 2.4 g/cm^3)

“Coffee-bag” cells were used for the *in situ* XRD measurements [6]. Li metal was used as a counter electrode and 1 M LiPF_6 in ethylene carbonate (EC) / dimethyl carbonate (DMC) was applied as an electrolyte solution. Using the assembled “coffee-bag” cells and an auto sample changer [7], *in situ* XRD patterns were collected at the MS-powder beamline at Swiss Light Source (SLS) at PSI. The XRD patterns are collected in transmission mode using a 17.5 keV X-ray beam. The electrochemical operation was carried out galvanostatically between 2.8 V and 5.0 V vs. Li metal.

Results

All the two-layer electrodes showed identical XRD patterns before the first charge, as shown in Figure 1.

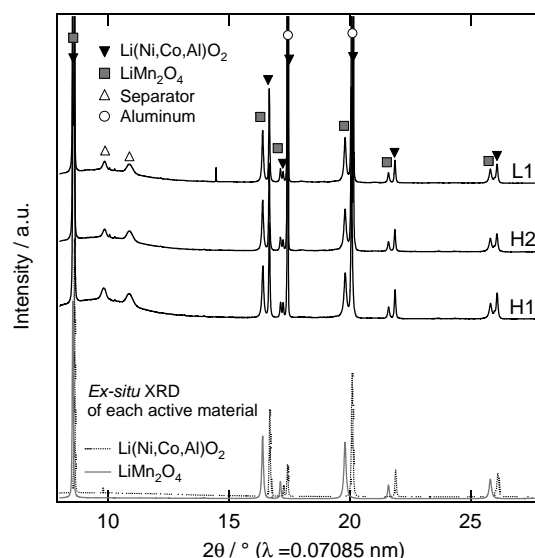


Figure 1. XRD patterns of the H1, H2, and L1 cells collected before the first charge and powder diffraction patterns of LMO and NCA.

However, the electrochemical behaviour and crystal structure change was completely different depending on the density and the order of the two layers, as shown in Figure 2 and 3. Figure 2 shows the first charge and discharge curves of these “coffee-bag” cells operated at voltages between 2.8 and 5.0 V during the *in situ* XRD measurements. The electrodes with the higher density showed better electrochemical performance. However, strangely enough, the charge and discharge profiles of H2 and L1 cells seemed to be similar in spite of the difference in the density and the order.

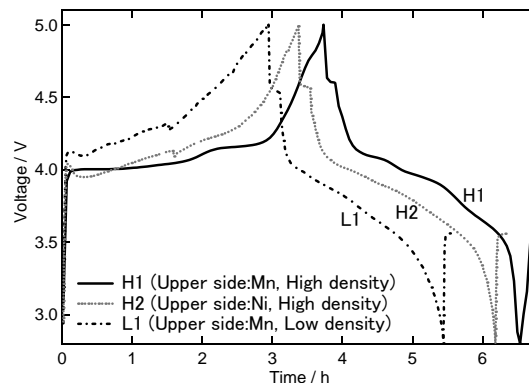


Figure 2. Charge/discharge curves of the H1, H2, and L1 cells during the *in situ* XRD measurements.

¹ Toyota Central R&D Labs., Inc., Nagakute, Japan

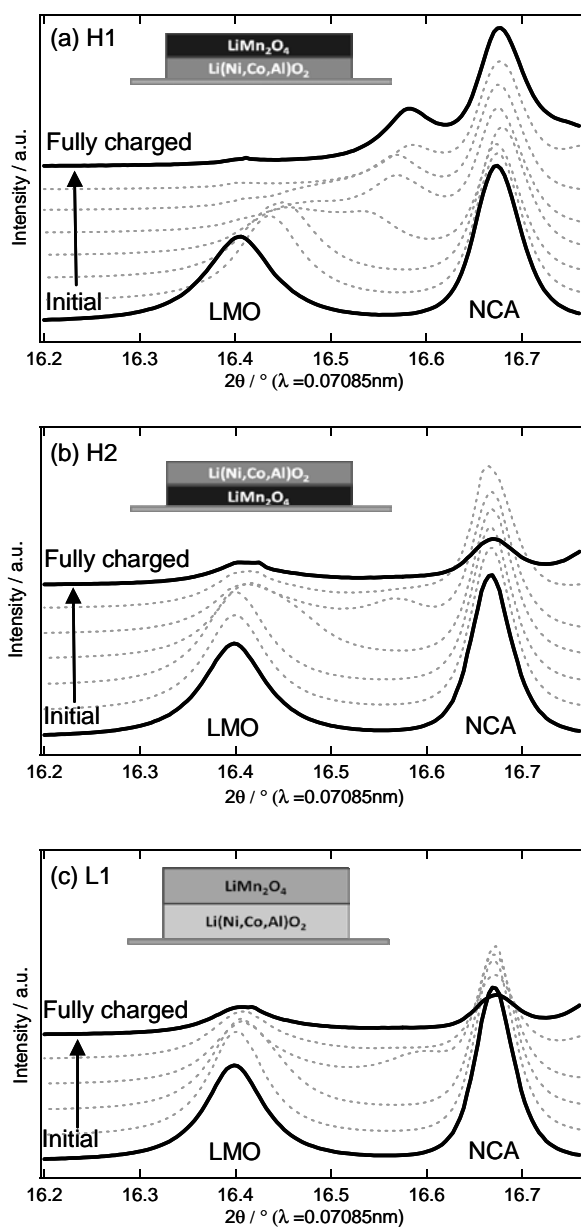


Figure 3. *In situ* XRD patterns ($2\theta=16.2\text{--}16.8^\circ$) collected during the first charge up to 5.0 V vs. Li metal.

Figure 3 shows *in situ* XRD patterns collected during the first charge up to 5.0 V. In this diffraction angle range, $2\theta=16.2\text{--}16.8^\circ$, one peak from LMO and one peak from NCA can be detected in initial stage. The changes of these peak intensities are good indicators to detect which active material is reacting. From the comparison between H1 (Figure 3 (a)) and H2 (Figure 3 (b)) cells, the active material in the upper side was obviously more active than that in the lower side in the case of the high-density electrodes. This difference between H1 and H2 cells showed clear evidence of the inhomogeneous reaction in the perpendicular direction. Additionally, this inhomogeneity in H1 and H2 cells should be due to the rate-limitation of ionic conductivity because the current rushed into the upper side of the electrodes.

Figure 3 (c) shows the other inhomogeneous reaction in the perpendicular direction. In contrast with H1 cell, L1 cell showed the active material in the lower side was more active. This means that the rate-limiting process should be electronic conductivity in the case of the low-density electrode. This result also suggested that the current distribution perpendicular to the current collector can be controlled by the adjustment of the electrode density (i.e., electrode porosity). The behavior of inhomogeneous reactions as shown in Figure 3 is consistent with the electrochemical behavior as shown in Figure 2. In other words, H2 and L1 cells show similar XRD change and charge/discharge curve because these electrodes have the active NCA layers in common.

These studies on the inhomogeneous reactions gave us a starting point for improving the stability against overcharge and overuse. These results also suggested that we have to be careful about this inhomogeneity when we conduct degradation analyses after overcharge or overuse because the degradation would be localized in perpendicular to current collector.

Acknowledgments

The authors would like to express gratitude to all-round technical assistance from Mr. Hermann Kaiser and Mr. Christoph Junker, and experimental support and advice from members of the Battery group at PSI. We also thank the MS beamline team at the SLS for their help during these experiments.

References

- [1] M. Kerlau, M. Marcinek, V. Srinivasan, R.M. Kostecki, *Electrochim. Acta*, **52**, 5422–5429 (2007).
- [2] P. Maire, A. Evans, H. Kaiser, W. Scheifele, P. Novák, *J. Electrochem. Soc.* **155**, A862–A865 (2008).
- [3] T. Sasaki, V. Godbole, Y. Takeuchi, Y. Ukyo, P. Novák, *J. Electrochem. Soc.* **158**, A1214–A1219 (2011).
- [4] H. Berg, J.O. Thomas, *Solid State Ionics*, **126**, 227–234 (1999).
- [5] W.-S. Yoon, K.Y. Chung, J. McBreen, X.-Q. Yang, *Electrochem. Commun.*, **8**, 1257–1262 (2006).
- [6] F. Rosciano, J.-F. Colin, F. La Mantia, N. Tran, P. Novák, *Electrochem. Solid-State Lett.* **12**, A140–A144 (2009).
- [7] F. Rosciano, M. Holzapfel, H. Kaiser, W. Scheifele, P. Ruch, M. Hahn, R. Kötz, P. Novák, *J. Synchrotron Radiat.*, **14**, 487–491 (2007).

Morphological and structural changes of Mg substituted Li(Ni,Co,Al)O₂ during overcharge reaction

T. Sasaki, V. Godbole, Y. Takeuchi¹, Y. Ukyo¹, P. Novák

phone: +41 56 310 43 96, e-mail: tsuyoshi.sasaki@psi.ch

The safety and durability of lithium-ion batteries when exposed to overcharge is a major concern of battery developers and users. Over the past decades, a considerable number of studies have been conducted on this issue. Most researchers seem to agree that the stability of overcharged positive electrode materials is one of the key factors for the safety of lithium-ion batteries [1]. LiNiO₂-based materials such as Li(Ni,Co,Al)O₂ have been widely studied because they have a large charge capacity when used as a positive electrode material. However, the processes in batteries utilizing Li(Ni,Co,Al)O₂ during abuse conditions, such as overcharge cycling up to 5.0 V, are not clear in detail. Besides, some research has shown that a small amount of Mg substitution in Li(Ni,Co,Al)O₂ has much impact on the electrochemical behavior [2]. However, detailed information about overcharge behavior of the material is also still lacking. Our objectives in this study are to investigate overcharge behavior of Mg-substituted Li(Ni,Co,Al)O₂ and to clarify the effect of Mg substitution on the same. To explore the behavior under such abusive conditions, analyses “after” overcharge would be not enough; analyses “during” overcharge are necessary because the active materials are obviously unstable and in a non-equilibrium state at high potentials. From these viewpoints, *in situ* synchrotron XRD is the method of choice to investigate the overcharge behavior. Additionally, we have previously reported that some cracks were observed at grain boundaries in secondary particles of LiNi_{0.80}Co_{0.15}Al_{0.05}O₂ after standard cycles [3]. This morphological behavior deserves careful attention when investigating the overcharge reaction. We thus decided to determine the structural and morphological changes occurring in Mg-substituted Li(Ni,Co,Al)O₂ during the overcharge reaction by *in situ* synchrotron XRD and SEM combined with electrochemical analyses.

Experimental

The following electrochemical measurements were performed in standard two electrode coin-type cells. The positive electrodes were prepared from the LiNi_{0.80-x}Co_{0.15}Al_{0.05}Mg_xO₂ (x = 0, 0.05) powders [2], conductive carbon, and polyvinyl difluoride (PVdF) binder and coated on an Al current collector. Li metal was used as a counter electrode and 1 M LiPF₆ in ethylene carbonate (EC)/ dimethyl carbonate (DMC) was applied as an electrolyte solution. Coin-type test cells were electrochemically cycled three times between 3.0 V and 4.3 V prior to overcharge tests. Overcharge tests were conducted using constant current charging up to 5.1 V. Scanning electron micrographs (SEM) were recorded after disassembling discharged cells in an argon-filled glove box and washing the electrodes with DMC.

“Coffee-bag” cells [4] were used for the *in situ* synchrotron XRD measurements. The working electrode consisted of a self-standing active layer pressed onto an Al mesh that acts as the current collector. The active layer is prepared by LiNi_{0.80-x}Co_{0.15}Al_{0.05}Mg_xO₂ (x=0, 0.05) powder, conductive carbon, and PVdF-hexafluoropropylene copolymer binder. Li metal was used as a

counter electrode and 1 M LiPF₆ in propylene carbonate (PC) / DMC was applied as an electrolyte. Using the assembled “coffee-bag” cells and an auto sample changer, *in situ* XRD patterns were collected at the MS-powder beamline at Swiss Light Source (SLS) in the PSI. The XRD patterns were collected in transmission mode using a 17.5 keV X-ray beam, during the first cycle of the “coffee-bag” cells at a C/10 rate between 3.0 V and 5.1 V vs. Li counter electrode.

Results

Figure 1 shows post mortem SEM images of the electrodes after overcharge. The non Mg-substituted electrode after overcharge features many cracks and some fragments, whereas Mg-substituted electrodes exhibit fewer cracks and fragments. This morphological change is assumed to have a deep relationship with Mg-substitution.

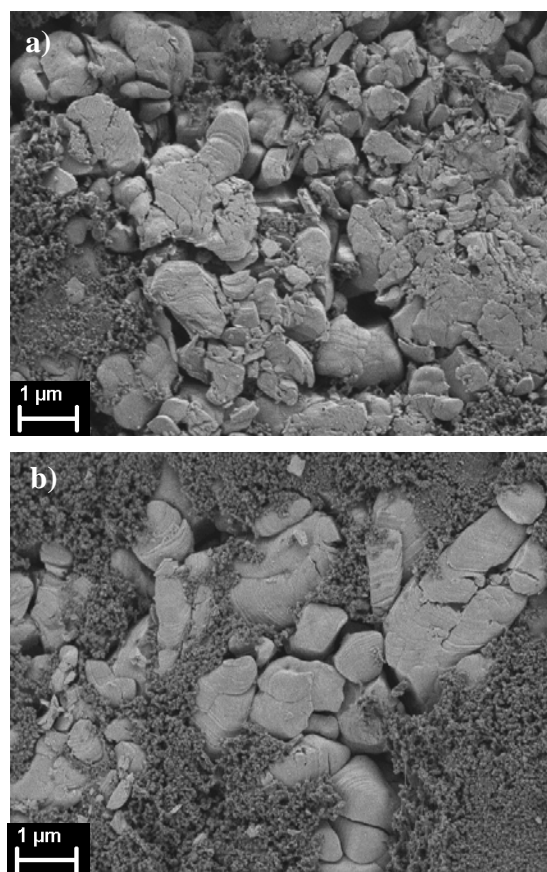


Figure 1. Typical SEM images of a) LiNi_{0.8}Co_{0.15}Al_{0.05}O₂ and b) LiNi_{0.75}Co_{0.15}Al_{0.05}Mg_{0.05}O₂ electrodes, both after overcharge (up to 5.1 V) and discharge.

Figure 2 a) shows the charge and discharge curve of a LiNi_{0.8}Co_{0.15}Al_{0.05}O₂ “coffee-bag” (Mg0) cell operated in a voltage window between 3.0 and 5.1 V during the *in situ* measurement. A pair of redox reactions appeared in the overcharge region around 4.6 V indicated by the two

¹ Toyota Central R&D Labs., Inc., Nagakute, Japan

arrows. Figure 2 b) shows the corresponding *in situ* XRD patterns in the 003 reflection region for hexagonal structure as collected during the first cycle of the Mg0 cell. The color of each XRD pattern corresponds to the color of the charge and discharge curve in Figure 2 a). The c-axis in the hexagonal unit cell is normal to the set of planes that contribute to the 003 reflection. Therefore, changes in the length of c-axis can be monitored by the changes of the 2θ angle of 003 reflections. The non Mg-substituted sample showed a drastic c-axis shrinking during overcharge from 4.5 V to 5.1 V. The shrinking ratio of c-axis was calculated to be about 8.3%. During the subsequent discharge, the c-axis expanded and returned to the former state reversibly. The potential at which the shrinking and expanding occurred corresponds to the pair of redox reactions.

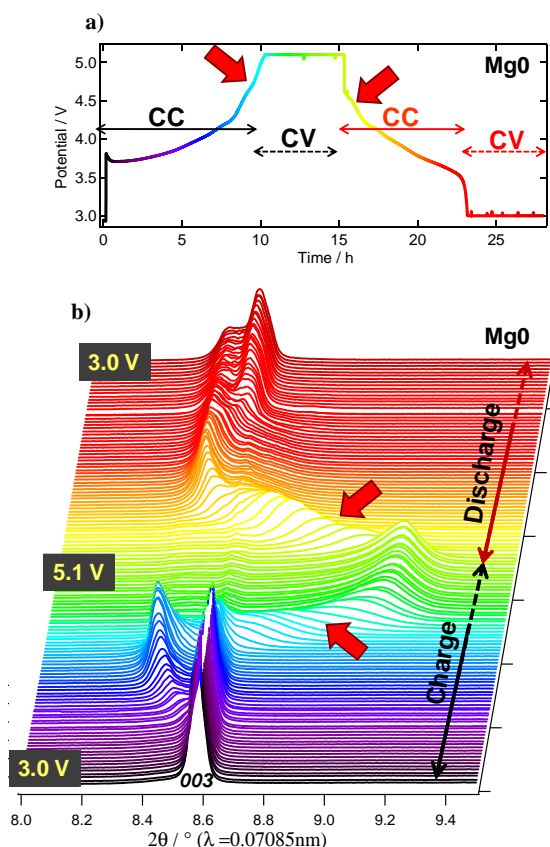


Figure 2. a) The charge and discharge curve of a Mg0 “coffee-bag cell” between 3.0 and 5.1 V at a C/10 rate and b) *in situ* XRD patterns in the 003 reflection region ($2\theta=8.0-9.5^\circ$) collected during the charge and discharge of the Mg0 cell. The color of each XRD pattern corresponds to the color of the charge and discharge curve.

Figure 3 a) shows the respective charge and discharge curve of a $\text{LiNi}_{0.75}\text{Co}_{0.15}\text{Al}_{0.05}\text{Mg}_{0.05}\text{O}_2$ “coffee-bag” (Mg5) cell, operated in the voltage window between 3.0 and 5.1 V during the *in situ* measurement. In contrast to the Mg0 cell, the Mg-substituted samples show no noticeable redox reactions in the overcharge region but an irreversible reaction at around 4.8 V during the overcharge. Figure 3 b) shows the *in situ* XRD patterns in the 003 reflection region collected during the first cycle of the Mg5 cell. The c-axis changes of the Mg-substituted samples in the overcharge region were much less than that of the non Mg-substituted sample, as indicated by the arrows in Figure 3 b). This finding leads to a straightforward conclusion that the Mg-substitution strongly

suppressed the drastic c-axis shrinking during overcharge up to 5.1 V. Finally, the relationship between the crystal structural change and the morphological change during the abusive overcharge needs to be discussed here. From the result of the *in situ* XRD measurements, the non Mg-substituted sample showed a drastic c-axis shrinking during overcharge. This structural change could be responsible for the observed numerous cracks of the cycled materials as shown in Figure 1 b). On the other hand, the Mg-substitution had the positive effect of suppressing the c-axis shrinking. The suppression of the shrinking could lead to the suppression of cracks during the overcharge.

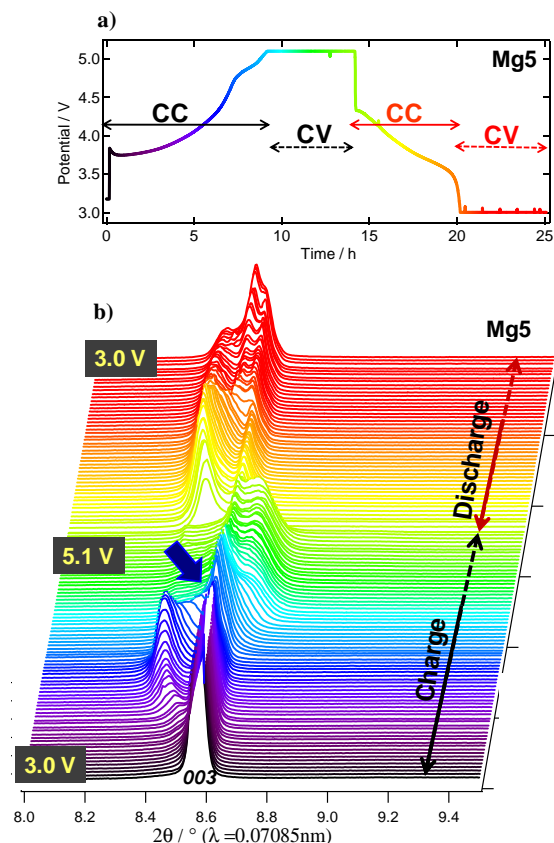


Figure 3. a) The charge and discharge curve of a Mg5 “coffee-bag” cell between 3.0 and 5.1 V at a C/10 rate and b) *in situ* XRD patterns in the 003 reflection region ($2\theta=8.0-9.5^\circ$) collected during the charge and discharge of the Mg5 cell.

Acknowledgments

The authors would like to express gratitude to all-round technical assistance from Mr. Hermann Kaiser. We also thank the MS beamline team at the SLS for their help.

References

- [1] R. A. Leising, M. J. Palazzo, E. S. Takeuchi, K. J. Takeuchi, *J. Electrochem. Soc.*, **148**, A838-A844 (2001).
- [2] H. Kondo, Y. Takeuchi, T. Sasaki, S. Kawauchi, Y. Itou, O. Hiruta, C. Okuda, M. Yonemura, T. Kamiyama, Y. Ukyo, *J. Power Sources*, **174**, 1131-1138 (2007).
- [3] Y. Itou, Y. Ukyo, *J. Power Sources*, **146**, 39-44 (2005).
- [4] F. Rosciano, J.-F. Colin, F. La Mantia, N. Tran, P. Novák, *Electrochem. Solid-State Lett.* **12**, A140-A144 (2009).

Aging tests of double layer capacitors - cycle vs. hold

R. Kötzt, D. Weingarth, A. Foelke-Schmitz, M.M. Hantel

phone: +41 56 310 20 57, e-mail: ruediger.koetz@psi.ch

Electrochemical Double Layer Capacitors (EDLC) are characterized by high power density and an unsurpassed cycle stability. However, EDLCs suffer from a relatively low energy density, which is at least 10 to 20 times smaller than today's Li-ion batteries.

As a consequence many research groups worked on the increase of the energy density by either increasing the voltage window of the capacitor or by increasing the specific capacitance of the active electrode material. In both directions significant progress has been reported in the past.

One typical approach towards higher cell voltage of EDLC is the use of an ionic liquid (IL) as electrolyte [1]. IL are so-called room temperature melts, which do not need any solvent, which otherwise limits the electrochemical stability window of the EDLC. Another approach towards higher stability is the utilization of special carbons such as carbon nano tubes (CNT). The high surface area of CNT is mainly provided by the basal plane like walls of the tube, which are assumed to be rather inert [2]. A combination of both, ionic liquids and single walled carbon nanotubes was proposed in [3] and allowed for an EDLC with a cell voltage of 4 V.

An attempt to increase EDLC energy density, however, can only be called successful if other parameters like stability and lifetime are not diminished.

There are two ways to prove the stability and longevity of the capacitor electrode or capacitor cell. Firstly by cycling the EDLC between the new extended cell voltage and zero and secondly by constant load tests at the increased maximum cell voltage. While in the literature EDLC stability is often demonstrated by cycling experiments lasting over several ten thousand cycles at PSI we prefer the constant voltage hold tests [4].

Experimental

Electrodes were prepared from a mesoporous carbon MM192 using PTFE as a binder. The electrolyte used was a typical ionic liquid EMIMBF₄. During constant voltage hold tests the after every 10 hours the cell was cycled between 2.5 V and 0 V in order to control the capacitance [4]. During cycling at a constant current of mA/g the capacitance could continuously be determined from each cycle.

Results

Aging tests of the capacitor cells using EMIMBF₄ and mesoporous carbon was tested by constant voltage hold experiments at a cell voltage of 3.75 V and by cycling experiments between 3.75 V and 0.0 V. The results of the cyclic experiment are reproduced in Figure 1a. The cell appears to be stable over more than 12000 cycles, which was equivalent to a test period of 50 days. The initial increase in capacitance can be ascribed to some kind of a formation period during which the wetting of the pores is completed. The capacitance loss during 12000 cycles is in the order of 10%.

The results of the constant load tests are shown in Figure 1b over a time period of 500 hours. While an increase of the capacitance during the first 100 h is in good agreement with the results of the cycling test the

decrease in capacitance for times above 200 h is significant and leads to the conclusion that the system is not stable under the applied conditions.

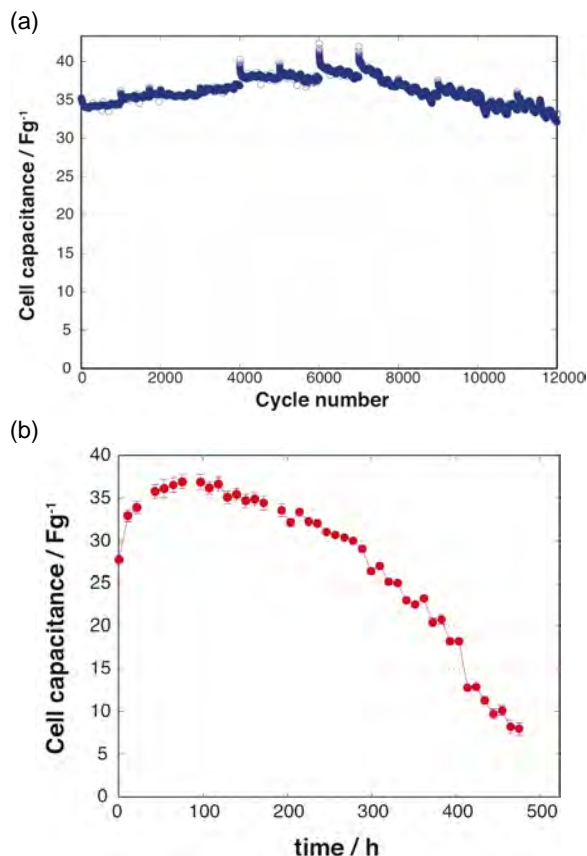


Figure 1. Accelerated stability test of an EDLC by (a) constant current cycling and (b) by constant voltage hold.

With the assumption that only the cell voltages above 3.25 V are harmful to the system one can calculate the time the cell was exposed during cycling to cell voltages between 3.25 and 3.75 V. This is about 166 h. Figure 1b clearly shows that a test period of 166 h is not enough to decide whether the system is stable or not. Only after about 300 h severe performance loss is obvious.

From the above results one can conclude that constant voltage hold tests are the more demanding, and less time consuming accelerated aging tests than cycling tests with the same maximum cell voltage.

References

- [1] C. Arbizzani, M. Bisio, D. Cericola, M. Lazzari, F. Soavi, M. Mastragostino, J. Power Sources **185**, 1575–1579 (2008).
- [2] A. Izadi-Najafabadi, S. Yasuda, K. Kobashi, T. Yamada, Don N. Futaba, H. Hatori, M. Yumura, S. Iijima, K. Hata, Adv. Mater. **22**, E235–E241 (2010).
- [3] H. Zhanga, G. Cao, Y. Yang, Z. Gu, Carbon **46**, 30–34 (2008).
- [4] P.W. Ruch, D. Cericola, A. Foelske-Schmitz, R. Kötzt, A. Wokaun, Electrochim. Acta **55**, 4412–4420 (2010).

The cathodic stability limit of the ionic liquid 1-ethyl-3-methyl imidazolium tetrafluoroborate [EMIM][BF₄] - a complementary approach

D. Weingarth, A. Foelske-Schmitz, R. Kötzt, A. Wokaun

phone: +41 56 310 41 31, e-mail: daniel.weingarth@psi.ch

Ionic Liquids (IL) as electrolytes in electrochemical energy storage devices are becoming more and more important and an increasing number of research groups investigate this special type of electrolytes exhibiting unusually large stability windows [1-3]. However, the reported electrochemical stability windows differ to a great extent and a method allowing for reliable determination of the usable electrochemical potential window is needed.

Within the present contribution four methods for the determination of the cathodic potential limits of [EMIM][BF₄] on different electrode materials will be described and compared. At first cyclic voltammetry measurements on glassy carbon model electrodes and defined current cut-off criteria will be presented. Further developments lead to *in situ* XPS measurements enabling the online detection of decomposition products in dependence of the applied potential. The transfer of these potential limits to high surface area carbon (HSAC) electrodes used in supercapacitors will be elucidated. As a result it can be stated that cyclic voltammetry on model electrodes even with low current cut-off criteria overestimates by far the usable voltage window in cathodic direction, whereas in combination with XPS the results are in good agreement with the applicable voltage window on HSAC electrodes.

Experimental

Before use the [EMIM][BF₄] was dried at 100°C and a vacuum better than $1 \cdot 10^{-2}$ mbar for at least 8 hours. *In situ* XPS measurements were performed using a VG ESCALAB 220iXL spectrometer equipped with an Al K_α mono-source (power: 150 Watt; spot diameter: 500 μm) and a magnetic lens system. The spectra are recorded in constant analyzer energy mode at a pass energy of 20 eV. The setup of the *in situ* cell can be found elsewhere [4, 5]. In short, the cell is positioned in the analyzer chamber of the XP spectrometer where it can be used in three electrode arrangement. A polycrystalline Pt foil served as working electrode, reference and counter electrode were prepared from activated carbon (AC, YP17, Kuraray Chemical Co., Japan).

The single electrode electrochemical measurements were performed in our standard cells used for capacitor application. An experimental carbon black named MM192 (Timcal) was used as working and counter electrode. The counter electrode was largely oversized in charge capacity. YP17 served as reference electrode [6]. A glassfiber separator was used for electrical insulation between the working and counter electrode. The electrode/separator/electrode sandwich was placed between two spring loaded (50 Ncm⁻²) Ti pistons, the reference was attached through a peripheral hole at the side of the cell. Cyclic voltammetry measurements were carried out with a VMP 3 (Biologic, France) potentiostat/galvanostat.

Results

Cyclic voltammetry on GC. Cyclic voltammetry experiments on glassy carbon (Figure 1) with a cut-off current of 100 μAcm⁻² indicate a cathodic stability potential of -2.3 V.

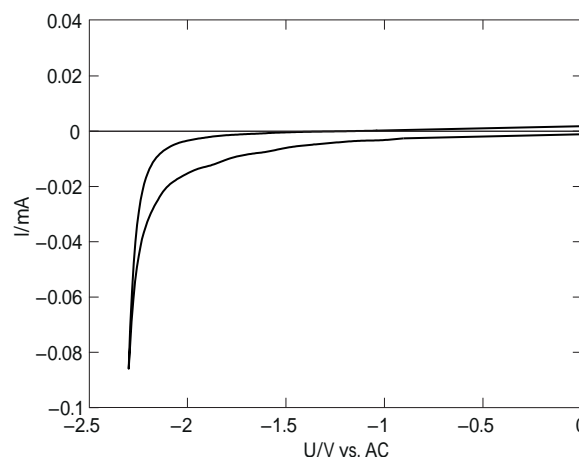


Figure 1. Cathodic potential window of [EMIM][BF₄] on a glassy carbon electrode. Cut-off current: 100 μA cm⁻². Scan rate: 10 mV s⁻¹.

The potential cut-off current, however, appears to be rather arbitrary. In order to observe the onset potential, we have set up an *in situ* XPS cell [4] where chemical changes can be monitored online while applying an electrochemical potential.

***In situ* XPS approach on Pt.** Figure 2 shows *in situ* XPS measurements as a function of the applied potential (right). The potential dependent N1s spectra clearly show that at potentials below -1.9 V an additional species appears in the XPS spectrum. Compared to the cyclic voltammogram (Figure 2 left) this is exactly where the onset of a large current increase is observed (but well below 100 μA (cf. Figure 1)). A further decrease in potential increases the current in the CV as well as the size of the additional peak in the N1s spectrum.

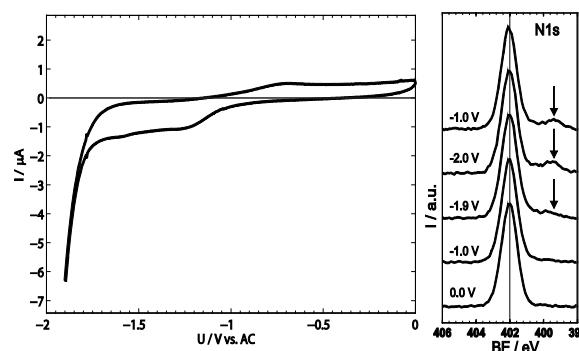


Figure 2. *In situ* XPS measurements on a Pt working electrode. Electrolyte: [EMIM][BF₄]. Left CV: Scan rate: 10 mVs⁻¹; right: potential dependent N1s spectra.

Although now there is experimental proof for the cathodic decomposition, the earlier current onset might also be due to the different working electrode. Pt might catalyse the cathodic decomposition of the IL.

Considering HSAC as electrode material for supercapacitors, distinct differences in the determination of the potential limits as compared to model electrodes such as glassy carbon or Pt have to be taken into account. Due to the high surface area and therewith high double layer capacitance, specific current cut-off criteria cannot be applied for HSAC. As a first step single electrode window opening experiments are carried out.

Window opening on AC electrodes. Figure 3 shows cathodic window opening experiments in a half-cell arrangement at room temperature. The sweep rate was set to 1 mVs^{-1} . As soon as faradaic currents occur (e.g. at -2.0 V), a positive reoxidation current is measured at -1.4 V (figure 3), indicating a reversible redox process and, therefore, the start of electrolyte degradation.

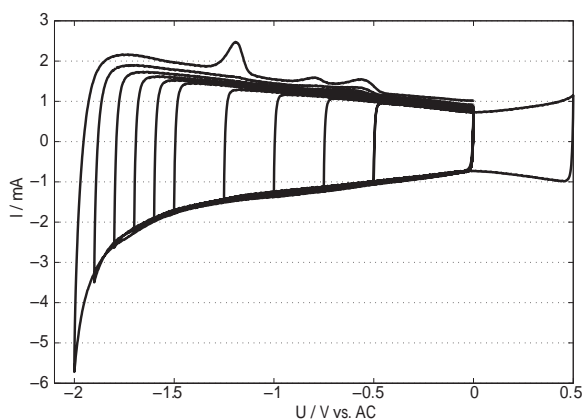


Figure 3. Cathodic half cell window opening experiments. Electrolyte: $[\text{EMIM}][\text{BF}_4]$. Scan rate: 1 mVs^{-1} .

However, during cycling the electrode has to withstand the maximum potential for a very short time and there are no considerable changes in the double layer capacitance even after several sweeps. Hence, an additional way to confirm the potential limit at -1.9 V with more demanding boundary conditions was developed.

Single electrode aging experiments (Figure 4). In a three electrode arrangement at first galvanostatic characterization cycles up to -1 V with 280 mA g^{-1} were performed and afterwards the potential was held for one hour at the desired value. This procedure was repeated 10 times (though 10 h altogether) before the potential was decreased further.

As it can clearly be seen in Figure 4, the charge/discharge cycles down to -1.9 V show very nice capacitor like behaviour. As soon as a potential of -2.0 V is reached, an additional plateau is visible in the discharge scan indicated by the circle. This plateau corresponds to the before mentioned reoxidation current (Figure 3). However, since the electrode has to withstand the potential for a much longer time than in cyclic voltammetry experiments, the potential hold measurements are much more demanding. A capacitance decrease in the charge/discharge cycles after the potential excursion to -2.0 V is measured, showing that the electrode cannot withstand potentials below -1.9 V .

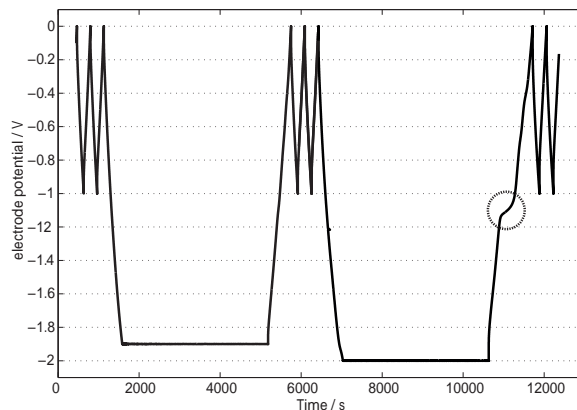


Figure 4. Cathodic single electrode aging experiments. Electrolyte: $[\text{EMIM}][\text{BF}_4]$. Charge/discharge current 280 mA g^{-1} .

Conclusion

In conclusion, cyclic voltammetry measurements on model electrodes such as glassy carbon or Pt are not good indicators for the electrochemical stability as the potential cut-off criterion is arbitrary. The determination of the onset potential of electrochemical degradation or the discrimination between adsorption and impurity peaks is a challenging task. Transferring the potential limits measured on model electrodes to HSAC electrodes is not straightforward. Reliable potential limits, however, may be obtained when combining CV measurements with a method to follow changes in the electrolyte *in situ* as for instance *in situ* XPS. The potential limit for Pt of -1.9 V vs. AC seems to be in good agreement with the measurements on HSAC electrodes indicating a negligible electro-catalytic effect of Pt on the degradation of the $[\text{EMIM}]^+$ cation.

Single electrode aging experiments, where the electrode has to withstand the vertex potential for at least one hour, provide more information for EDLC application. Clear indications for aging phenomena can be taken from the discharge after the holding period and from the detailed evaluation of the capacitance fading. The cathodic potential limiting reaction in this particular ionic liquid $[\text{EMIM}][\text{BF}_4]$ seems to be at least partially reversible, which in contrast to non reversible processes, leads to a slightly increased lifetime of the electrode (slower capacitance fading over time).

References

- [1] A. Balducci, U. Bardi, S. Caporali, M. Mastragostino, F. Soavi, *Electrochem. Commun.* **6**, 566–570 (2004).
- [2] M. Ue, M. Takeda, A. Toriumi, A. Kominato, R. Hagiwara, Y. Ito, *J. Electrochem. Soc.* **150**, A499–A502 (2003).
- [3] K. Denshchikov, M. Izmaylova, A. Zhuk, Y. Vygodskii, V. Novikov, A. Gerasimov, *Electrochim. Acta* **55** 7506–7510 (2010).
- [4] D. Weingarth, A. Foelske-Schmitz, A. Wokaun, R. Kötz, *Electrochem. Commun.* **13**, 619–622 (2011).
- [5] D. Weingarth, A. Foelske-Schmitz, R. Koetz, A. Wokaun, *PSI Electrochemistry Laboratory Annual Report 2010*, 89–90 (2011).
- [6] P. Ruch, D. Cericola, M. Hahn, R. Kötz, A. Wokaun, *J. Electroanal. Chem.* **636**, 128–131 (2009).

CATALYSIS & INTERFACES

Particle size effect on magnetron sputtered cathodes

B. Schwanitz, A. Rabis, M. Horisberger, G.G. Scherer, T.J. Schmidt

phone: +41 56 310 51 72, e-mail: annett.rabis@psi.ch

High Pt catalyst loadings and limited stability are still strong impediments for a broader commercialization of polymer electrolyte fuel cells (PEFCs). While lowering the Pt anode loading down to $50 \mu\text{g}/\text{cm}^2$ is straightforward [1, 2], a lowering of today's cathode loadings of ca. $400 \mu\text{g}/\text{cm}^2$ is difficult due to the sluggish oxygen reduction reaction (ORR) kinetics. It is discussed in the literature that only a thin layer within the cathode is participating in the ORR [1]. Thus, producing thin catalyst layers by using the sputtering thin Pt films can be a promising approach to raise the Pt utilization. As was demonstrated previously, different sputtered Pt catalyst loadings lead to different Pt morphologies ranging from discrete nanoparticles at low to extended Pt films at high loadings, respectively [3]. The impact of this effect on the area and mass specific catalyst activity is studied in defined experiments using model electrodes in liquid electrolyte and in gas diffusion electrodes in PEFCs.

Experimental

The model electrodes were prepared by DC magnetron sputtering of Pt onto a Vulcan XC72 layer on a glassy carbon electrode (2, 10, 20, 100 and $200 \mu\text{g}_{\text{Pt}}/\text{cm}^2$). The ORR and cyclic voltammetry measurements were conducted at 20°C and ambient pressure in 0.1M HClO_4 . Tafel plots were obtained from the $i\text{R}$ corrected polarization curves.

For PEFC measurements cathodes were obtained by DC magnetron sputtering of Pt onto a micro porous layer of Vulcan XC72 supported on Carbon Cloth (GDL LT1410W E-TEK, 25, 50, 100 and $500 \mu\text{g}_{\text{Pt}}/\text{cm}^2$) [3]. A commercial electrode (E-TEK LT140EW; $0.5 \text{ mg}_{\text{Pt}}/\text{cm}^2$) was used as anode in the hot-pressed membrane electrode assembly (MEA, Nafion 212, sputtered electrodes do not contain ionomer). The experiments were carried out in a 30 cm^2 single cell at 80°C , 1 bar_a , using fully humidified H_2 and O_2 ($\lambda_{\text{H}_2/\text{O}_2} = 6/12$ for $0.1\text{A}/\text{cm}^2$), respectively. After conditioning, $i\text{E}$ -curves were taken. Ohmic cell resistance is measured by electrochemical impedance spectroscopy (EIS).

Results and Discussion

In Figure 1 the resulting electrochemical surface areas (ECSAs) of the model and the PEFC electrodes, respectively are summarized. The ideal linear correlation between loading and surface area for monodispersed homogeneous systems is given as reference. As depicted from these data, the ECSA drops with decreasing loading logarithmically due to agglomeration of single Pt nanoparticles to form thin Pt films upon increase of the Pt loading. The differences between model and PEFC electrodes, respectively, is a result of lower Pt utilization at the Pt-Nafion vs. Pt-liquid electrolyte interface.

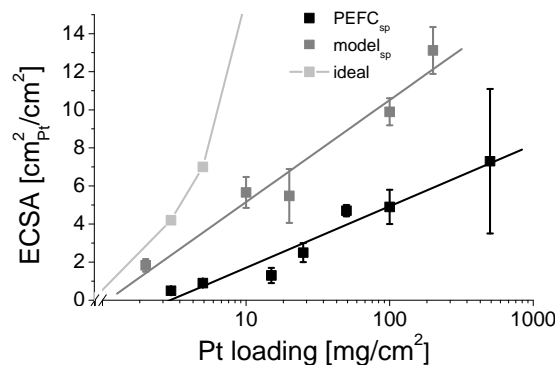


Figure 1. Plot of ECSA vs. the Pt loading, virtually shown for a linear growth of an ideal, model and PEFC electrode, measured by H_{UPD} for the sputtered model and CO-stripping for the sputtered PEFC electrode, respectively.

After performing RDE measurements, the ORR surface specific activity at 0.9V as function of Pt loading was extracted from the ORR current densities and is illustrated in Figure 2. With increasing loading (decreasing specific surface area), the specific activity of the Pt electrodes are increasing, an effect described in the literature for Pt/C and Pt-black catalysts [1]. This increase in specific activity for Pt from the same source (same particle size) is surprising. However, detailed analysis of the recorded double-layer corrected cyclic voltammograms (not shown) reveals that depending on the Pt loading the surface coverage of oxygenated species on the Pt surface is affected.

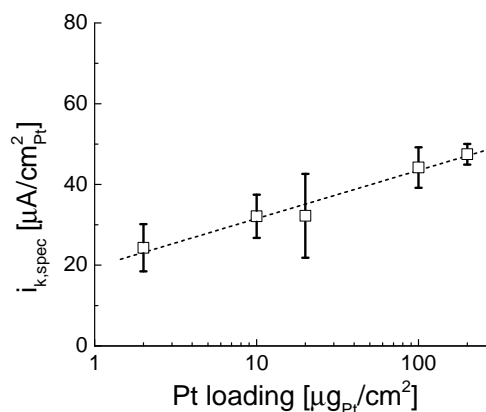


Figure 2. Surface specific activities for the ORR using model rotating disk electrodes with different Pt-loadings taken from $i\text{R}$ - and mass transport corrected polarization curves at $E=0.9 \text{ V}$, 20°C , ambient pressure in 0.1M HClO_4 .

Note: while electrodes with low Pt loadings of around $3 \mu\text{g}_{\text{Pt}}/\text{cm}^2$ mainly exhibit Pt-nanoparticles ($\sim 2\text{nm}$), an increase in Pt loading results in Pt-agglomeration and finally formation of thin Pt films for loadings $>100 \mu\text{g}_{\text{Pt}}/\text{cm}^2$ [2].

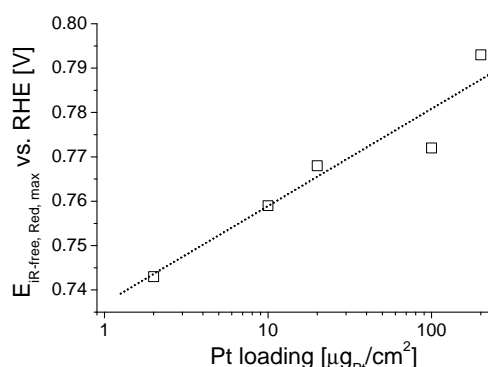


Figure 3. Peak maxima of the OH_{ad} reduction peaks taken from CVs of model electrodes.

With increasing Pt particle size the OH_{ad} surface coverage decreases. Due to the lower OH_{ad} surface coverage of the Pt film, more active sites are available for the ORR. Thus, the surface specific activity is increased compared to the Pt-nanoparticle.

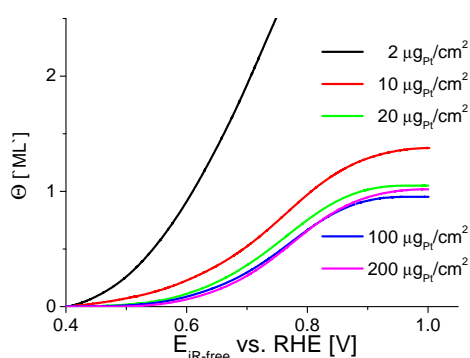


Figure 4. OH coverage of the sputtered catalyst surface for various loadings.

As shown in Figure 3, the position of the Pt-OH reduction peak is shifted to more negative potentials with decreasing Pt loading, i.e., when going to electrodes with isolated Pt nanoparticles (ca. $30\text{mV}/\text{dec}$ shift). Integration of the reduction peak can reveal an estimate of the surface coverage of oxygenated species. The resulting values are plotted as function of potential in Figure 4. An increase of OH_{ad} species is seen going from 200 to $10 \mu\text{g}_{\text{Pt}}/\text{cm}^2$. Due to the larger error bar in determination of the double-layer correction for ultra-small loadings, the adsorption isotherm for the $2 \mu\text{g}_{\text{Pt}}/\text{cm}^2$ sample may be slightly overestimated (without hampering the general trend). The different surface coverages of oxygenated species as function of Pt loading (which represents in our case different Pt morphology) can be rationalized by the decrease of the potential of total zero charge on nanoparticles vs. Pt-black type extended surfaces (like Pt-films) due to the presence of more under-coordinated surface Pt sites. This in turns makes nanoparticles more oxophilic as compared to Pt-films, leading to higher coverages of oxygenated species and reduced specific Pt activity [4].

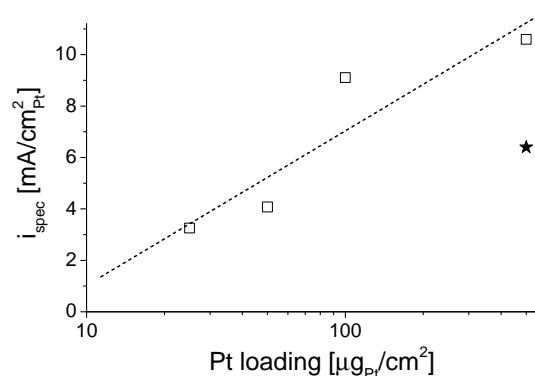


Figure 5. Surface specific activity of sputtered PEFC cathodes with different Pt loadings (squares) compared to ETEK cathode (star), measured for H_2/O_2 at $T = 80^\circ\text{C}$, 1 bar, 100% R.H., constant gas flow of $600 \text{ mL}/\text{min}$ and 0.75V . The dotted line serves as guide to the eye.

Similar experiments were carried out for sputtered cathodes in a PEFC. The resulting surface specific activities for various Pt loadings (open squares) and for a commercial electrode (star) are shown in Figure 5 confirming the observed effect from the model electrode experiments. Interestingly, the specific Pt activity of the commercial electrode with $0.5\text{mg}_{\text{Pt}}/\text{cm}^2$ would match the specific activity of a sputtered sample below $0.1\text{mg}_{\text{Pt}}/\text{cm}^2$.

Summary

The effect of Pt loading concomitant with the change of Pt morphology (nanoparticles vs. extended Pt black type film surfaces) on the kinetics of the ORR in both model electrodes and PEFCs was studied. The specific Pt activity was found to be clearly a function of the Pt loading due to intrinsic changes of the Pt morphology going from nanoparticles (low loading) to extended Pt films (high loadings).

References

- [1] H.A. Gasteiger, S.S. Kocha, B. Sompalli, F.T. Wagner, *Appl. Catal. B: Environmental* **56**, 9-35 (2005).
- [2] B. Schwanitz, PhD thesis, ETH Zürich Nr. 20142, 2012.
- [3] B. Schwanitz, H. Schulenburg, M. Horisberger, A. Wokaun, G.G. Scherer, *Electrocatal.* **2**, 35-41 (2011).
- [4] K.J.J. Mayrhofer, B.B. Blizanac, M. Arenz, V. Stamenkovic, P.N. Ross, N.M. Markovic; *J. Phys. Chem. B* **109**, 14433-14440 (2005).

The effect of gas front propagation on carbon corrosion during start-up and shut-down of PEFCs

N. Linse, G.G. Scherer, A. Wokaun, L. Gubler

phone: +41 56 310 26 73, e-mail: lorenz.gubler@psi.ch

The elevated potentials occurring at the positive electrode during fuel cell start-up and shut-down by purging of the anode compartment with hydrogen and air, respectively, can cause severe corrosion of the carbon catalyst support material. Since the duration of the detrimental potential conditions is controlled by the coexistence of hydrogen and oxygen at the negative electrode [1], the exchange of the anode gas is a crucial process influencing start/stop induced fuel cell degradation. In several studies, the propagation of the hydrogen/air front through the anode compartment has been investigated by measuring local current densities both along the direction of the flow field and on the channel and land scale [2-5]. This approach offers the advantage of monitoring the front propagation with a good spatial and temporal resolution. Yet, since the discrimination between the different sources of current generation is not possible, the determination of local current densities can only provide rough estimations about the influence of different parameters on the carbon corrosion behaviour. To obtain further information about the effects related to the propagation of the hydrogen/air front, the influence of reactant gas composition and anode gas flow rate on the corrosion of the catalyst support material was therefore systematically investigated by monitoring the CO₂ concentration in the exhaust gas of the positive electrode.

Experimental

All experiments were performed using 16 cm² cells with parallel flow fields and MEAs fabricated by hot pressing of a Nafion 212 membrane with electrodes supplied by Johnson Matthey Fuel Cells (60% Pt/C, 0.4 mg_{Pt}/cm²). Start-up and shut-down of the fuel cell was performed by purging the anode compartment with hydrogen and air, respectively. The theoretical residence time of the hydrogen/air front was calculated by dividing the total volume of the channels in the anode flow field by the respective gas flow rates. During all measurements, the cathode was continuously fed with air (600 ml_n/min). Carbon corrosion rates were determined by integration of the CO₂ concentration peaks in the exhaust gas of the positive electrode [6]. All measurements were carried out at a temperature of 50°C, 70% r.h. and ambient pressure.

Results and Discussion

The amount of CO₂ evolved during start-up and shut-down of the fuel cell strongly depends on the duration of the purging process and the concentration of the reactant gases. In Figure 1, carbon corrosion rates are shown as a function of the anode gas flow rate for measurements carried out with hydrogen concentrations of 5%, 21% and 100%. Due to the increasing duration of the gas exchange process, corrosion rates generally become higher if the gas flow rate at the negative electrode is decreased. Thereby, both the absolute amount of evolved CO₂ as well as the ratio between corrosion rates obtained in response to start-up and shut-down

processes strongly depends on the hydrogen concentration. The most pronounced effect of hydrogen content was found for shut-down processes. Depending on the gas flow rate, an increase in hydrogen concentration from 5% to 100% leads to an increase in the carbon corrosion rates by more than a factor of 20. In case of fuel cell start-up, however, CO₂ evolution shows a completely different behaviour. While a change in hydrogen concentration from 5% to 21% does not significantly influence the carbon corrosion rates, a further increase to 100% results in a considerable decrease in the amount of evolved CO₂. At low gas flow rates, however, the corrosion rates approach the values obtained in measurements carried out with diluted hydrogen. As a consequence of this strong influence of gas flow rate, the ratio between corrosion rates determined for start-up and shut-down processes changes by a factor of three if the cell is operated with pure hydrogen. For measurements carried out with hydrogen concentrations of 5% and 21%, however, this ratio is independent of the gas flow rate.

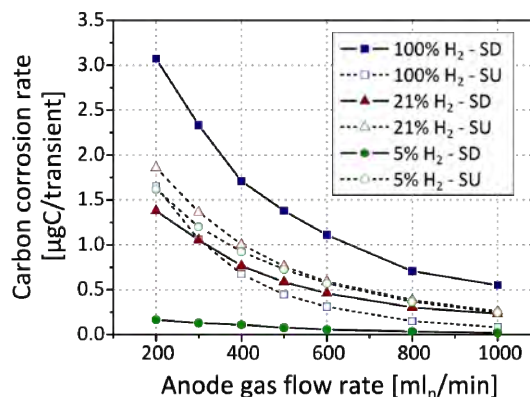


Figure 1. Carbon corrosion rates determined for single start-up (SU) and shut-down (SD) transients as a function of the anode gas flow rate for measurements with different hydrogen concentrations.

This strong influence of hydrogen concentration on the carbon corrosion behaviour can be explained by the processes occurring during the exchange of the anode gas. In case of fuel cell shut-down, the hydrogen-filled anode compartment is purged with air. During the resulting gas replacement process, the potential at the negative electrode is dominated by the presence of hydrogen. The duration of the detrimental potential conditions leading to carbon corrosion at the positive electrode is therefore determined by the time necessary to completely remove the hydrogen from the anode compartment. Since this process strongly depends on the initial amount of hydrogen, carbon corrosion rates become significantly lower if the hydrogen concentration is decreased. During start-up of the fuel cell, the air in the anode compartment is replaced by hydrogen. Thereby, catalyst support corrosion is limited to areas with oxygen present at the negative electrode. Thus, since the removal of oxygen does not significantly depend on the

hydrogen concentration of the purging gas, the difference between carbon corrosion rates is substantially lower than in case of shut-down processes. As another effect, the influence of residual gas in the catalyst layer significantly differs for start-up and shut-down processes. While small amounts of remaining hydrogen during fuel cell shut-down lead to carbon corrosion in large areas of the positive electrode, the effect of trapped air during start-up is much less severe.

To obtain a comprehensive overview about the influence of reactant gas composition, similar experiments were carried out with varied oxygen concentrations. As shown in Figure 2, an increase in oxygen content strongly increases CO₂ evolution both during start-up and shut-down of the fuel cell. Compared to the influence of hydrogen concentration, oxygen content has a significantly more pronounced effect on start-up induced carbon corrosion. In contrast, the differences in CO₂ evolution during fuel cell shut-down are considerably smaller. The ratios between the carbon corrosion rates determined for fuel cell shut-down and start-up were found to be independent of both gas flow rate and reactant gas composition. Both processes can thus be assumed to be equally influenced by the oxygen concentration. Furthermore, the constant ratios indicate that the mechanisms determining the gas exchange process do not change in the investigated gas flow range.

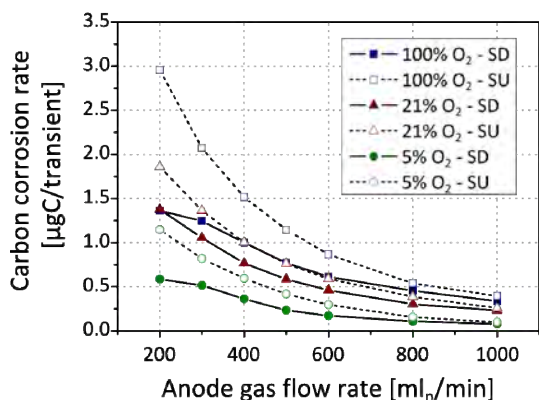


Figure 2. Carbon corrosion rates determined for single start-up (SU) and shut-down (SD) transients as a function of the anode gas flow rate for measurements with different oxygen concentrations.

The observed correlation between oxygen concentration and carbon corrosion behaviour confirms the processes discussed above. Since the duration of the detrimental potential conditions during fuel cell shut-down is mainly controlled by the time necessary to completely remove the hydrogen from the anode compartment, the influence of reactant gas composition is less pronounced than in case of measurements carried out with varied hydrogen concentrations. However, although the constant start-up/shut-down ratios indicate that the removal of hydrogen is not significantly influenced by the direct recombination with oxygen, an increase in oxygen content from 5% to 100% increases the carbon corrosion rates by a factor of up to three. This comparatively strong increase in CO₂ evolution might be explained by the influence of oxygen concentration on the polarisation of the negative electrode in the air/air sections of the fuel cell. Due to the strong effect on the kinetics of the oxygen reduction reaction, an increase in oxygen concentration significantly decreases the potential drop at the fuel cell anode. As a consequence, the potential developing at the positive electrode increases, thus leading to

an increase in CO₂ evolution rates. Since this process equally influences fuel cell start-up and shut-down, the ratio between the respective corrosion rates is not affected. In case of fuel cell start-up, carbon corrosion behaviour is assumed to be primarily controlled by the residual amount of oxygen at the negative electrode. Accordingly, an increase in oxygen concentration significantly increases the CO₂ evolution rate.

Besides the identification of processes influencing the amount of CO₂ generated during start-up and shut-down of the fuel cell, the obtained results allow conclusions about the propagation of the gas front. Under all investigated conditions, the corrosion rates were found to increase linearly with the theoretical front residence time, indicating that the hydrogen/air front propagates almost ideally through the anode compartment. This behaviour is highly contradictory to studies which reported that the duration of the gas exchange process is mainly controlled by electrochemical reactions and diffusion processes both along the direction of the flow field [7] and on the channel and land scale [4]. Since both mechanisms are largely independent of the gas flow rate, a significant contribution of these processes would be expected to result in strong deviations from the linear correlation. Due to the same reason, pseudo-capacitive effects, which were suggested to influence corrosion behaviour in case of short gas front residence times [8], can be assumed to be negligible under the investigated conditions.

Conclusions

The results obtained in measurements with different reactant concentrations show that CO₂ evolution during fuel cell start-up is mainly controlled by the oxygen concentration while the effect of hydrogen concentration is more pronounced in case of fuel cell shut-down. The ratio between the corrosion rates obtained in response to fuel cell start-up and shut-down was found to be solely determined by the hydrogen concentration. In case of measurements carried out under the most application relevant conditions (operation with pure hydrogen and air), fuel cell shut-down leads to significantly higher carbon corrosion rates.

References

- [1] C.A. Reiser, L. Bregoli, T. Patterson, J.S. Yi, J.D. Yang, M.L. Perry, T.D. Jarvi, *Electrochem. Solid-State Lett.* **8(6)**, A273-A276 (2005).
- [2] G. Maranzana, O. Lottin, T. Colinart, S. Chupin, S. Didierjean, *J. Power Sources* **180(2)**, 748-754 (2008).
- [3] H. Fukumoto, S. Yoshioka, S. Matsumoto, *ECS Trans.* **16**, 841-847 (2008).
- [4] I.A. Schneider, S. von Dahlen, *Electrochem. Solid-State Lett.* **14(2)**, B30-B33 (2011).
- [5] Z. Siroma, N. Fujiwara, T. Ioroi, S. Yamazaki, H. Senoh, K. Yasuda, K. Tanimoto, *J. Power Sources* **172**, 155-162 (2007).
- [5] N. Linse, L. Gubler, G.G. Scherer, A. Wokaun, *Electrochim. Acta* **56**, 7541-7549 (2011).
- [7] Y. Ishigami, K. Takada, H. Yano, J. Inukai, M. Uchida, Y. Nagumo, T. Hyakutake, H. Nishide, M. Watanabe, *J. Power Sources* **196**, 3003-3008 (2011).
- [8] W. Gu, R.N. Carter, P.T. Yu, H.A. Gasteiger, *ECS Trans.* **11**, 963-973 (2007).

Tin and tantalum oxides as supports for Pt-electrocatalysts in PEFCs

A. Rabis, M. Horisberger, R. Kötzt, T.J Schmidt

phone: +41 56 310 51 72, e-mail: annett.rabis@psi.ch

Pt electrocatalysts supported on carbon are widely used in polymer electrolyte fuel cells (PEFCs). Corrosion of the carbon-based catalyst support [1] is one of the important technological issues that need to be solved to improve the long-term durability of the PEFC system. Because carbon is thermodynamically unstable under high potentials, strong oxidizing conditions [2], alternative carbon-free electrocatalyst support materials are desired for PEFCs. As alternatives to the conventional carbon support conductive metal oxides are interesting candidates. Among various oxides, which are stable under PEFC relevant conditions, SnO_2 and Ta_2O_5 as host materials and Nb and N as dopands, respectively, have been selected for investigation of the suitability as support materials for Pt-based electrocatalysts. For the evaluation of the electrocatalytic activity we will prepare thin oxide film electrodes for rotating ring disk electrode (RRDE) measurements. The thin films will be deposited by reactive sputtering on glassy carbon disks. Prior to this we performed some experiments on the discharge behavior of the metal targets, to be able to deposit Sn and Ta oxides with a certain dopand concentration.

Experimental

Ta oxynitride and Nb-doped Sn oxide films were deposited on glass, Si and glassy carbon substrates by reactive magnetron sputtering. For the deposition metallic targets (Ta, Sn and Nb; purity 99.99%), with a fixed target-to-substrate distance were used. The oxygen content in the sputtering gas is characterized by the ratio of oxygen flow to the total gas flow $\text{Ar}+\text{O}_2$ (+ N_2 for oxynitride). The deposition was performed without any additional heating of the substrates. Chemical analysis of the sputtered films was performed using X-ray photoelectron spectroscopy (XPS, ESCALAB 220iXL, Thermo Scientific) and X-ray diffraction (Bruker D8). Prior to oxide film deposition, experiments to monitor the discharge behavior of the metal targets have been carried out. The relation between the power input and the resulting cathodic voltage was analyzed. To realize this, we varied the discharge power at different oxygen contents (30-45%) of the gas mixture while scanning the cathodic voltage and partial pressures of oxygen and argon.

Results

Figure 1 shows the "phase"- or power-voltage diagram of the tin target in $\text{Ar}-\text{O}_2$ plasma. Depending on the discharge power and oxygen content in the plasma three regions can be identified: in the first region (Sn^{4+} -zone) the cathodic voltage increase very slowly; in the second region (transition zone) a voltage jump occurs over a small power range of 2-4 W, and in the third one (Sn^{2+} -zone) the voltage also rises, but with a steeper slope than in the first region [3]. A fourth region (Sn^0 or metallic zone) could not be observed. These results were proofed by XRD measurements of oxide films deposited under conditions to yield SnO_2 and SnO . Figure 2 shows the XRD spectra of tin oxide films deposited under a discharge voltages of 330 V (80 W), 340 V (120 W) and 430 V (180 W). Samples deposited at discharge voltages up to 340 V show a polycrystalline like nature and (110), (211) and (200) cassiterite (SnO_2) characteristic

peaks [3]. With increasing discharge power the peaks become more intensive. Further increase, beyond 340 V leads to an amorphous film with SnO chemical composition, which was analyzed by XPS and observed by a change in optical properties from a transparent colourless to an orange oxide layer.

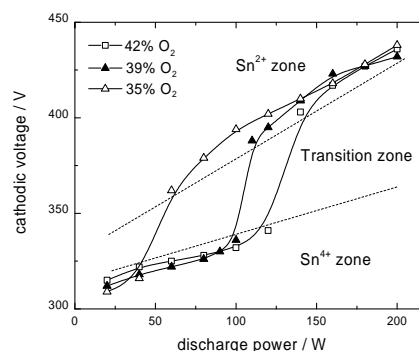


Figure 1. "Phase" or discharge power-voltage diagram of the Sn target for different percentages of oxygen in $\text{Ar}-\text{O}_2$ plasma.

Similar experiments were carried out for the deposition of TaO_xN_y films. However, the Ta target does not show such a switch in the oxidation state in the analysed range like the tin target. Therefore, we suggest that the Ta remains in its pentavalent state and only the O-to-N ratio in the film varies by changing the composition of the reactive gas.

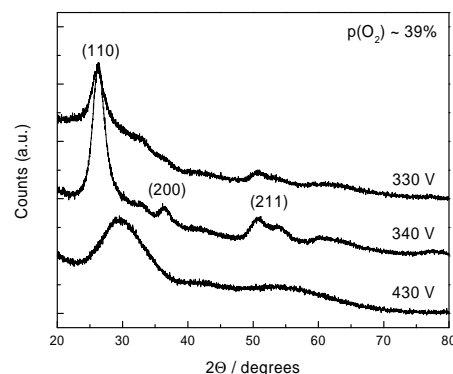


Figure 2. XRD pattern of Sn oxide films reactively sputtered at different discharge voltages without intentional heating.

These experiments were carried out to relate the chemical composition of the films with the discharge parameters. Next steps in this project will be the electrical and electrochemical characterization of the prepared oxide films.

References

- [1] M.F. Mathias, et al., *Interface* **14**, 24 (2005).
- [2] M. Pourbaix, *Atlas of Electrochemical Equilibria in Aqueous Solutions*, 2nd ed. National Association of Corrosion Engineers, Houston, TX (1974).
- [3] A. Martel, *Surf. Coat. Technol.* **122**, 136-142 (1999).

In situ STM study of Pt-dots on HOPG prepared by electron beam lithography

A. Peitz, A. Foelske-Schmitz, D. Weingarh, V. Guzenko, G.G. Scherer, A. Wokaun, R. Kötz

phone: +41 56 310 41 93, e-mail: annette.foelske@psi.ch

A possible approach towards better understanding of fundamental Pt and carbon corrosion processes is preparation of model systems, which can be investigated via e.g. *in situ* methods, thus enabling records of changes in morphology and/or composition of the electrode materials during degradation. A method to prepare monodisperse, well-separated Pt particles on a flat carbon substrate was described recently in [1]. This previous work showed that an area of one square centimetre on glassy carbon (GC) could be homogeneously patterned with Pt dots by electron beam lithography (EBL) [1]. EBL could be likewise successfully implemented to a different flat carbon support such as highly oriented pyrolytic graphite (HOPG) [2]. In [2], such Pt/HOPG model electrodes were used to monitor carbon, Pt and Pt-induced carbon oxidation and/or corrosion as a function of the electrochemical reaction conditions. It was shown that the dot pattern was stable during scanning tunnelling microscopy (STM) measurements in air, indicating immobilisation of the Pt dots, which are otherwise mobile on the untreated HOPG surface [3, 4]. Upon application of anodic potentials in the electrolyte, 0.5 M sulphuric acid, the dots gradually disappeared and a hole pattern, corresponding to the original dot pattern appeared on the HOPG surface. The possible origin of the holes was discussed, but not completely elucidated. Herein, the origin of the holes will be further elaborated. The stepwise oxidation process was visualised *ex situ* by Scanning Electron Microscopy (SEM) and *in situ* by electrochemical scanning tunnelling microscopy (EC-STM).

Experimental

The exposures of the dot arrays HOPG were performed according to [1]. Rectangular dot arrays on an area of one square centimeter were generated by setting the beam step size equal to the dot pitch of 100 or 200 nm, so that the exposure of each dot was performed within a single "beam shot" with a dose of 105, 75 and 14 $\mu\text{C cm}^{-2}$, respectively. As photoresist, two-layers of a poly(methyl-methacrylic acid) (PMMA) / ethyl lactate solution, an 2% solution of PMMA with the molecular weight of 50k (lower layer) and 1% solution of PMMA with the molecular weight of 950k (upper layer), was used. Deposition of a Pt layer on the developed samples was performed with a DC magnetron-sputtering device TIPS1 with an Ar pressure of 10^{-3} mbar and a power of 30 W. Alternatively, vapour deposition of Pt was performed in a Balzers BAK 600 (Oerlikon Balzers, Liechtenstein) evaporator. The surface of the obtained samples was investigated by SEM (ZEISS SUPRA 55 VP). The STM measurements were conducted in an electrochemical STM cell with a three electrode arrangement where the sample acted as working electrode (WE) and two annealed high purity Pt wires with a diameter of 0.5 mm (FG 999.5, Carl Schaefer AG) as quasi-reference (RE) and counter (CE) electrodes, respectively. *In situ* STM images were recorded in an electrochemical cell, exposing 0.7 cm^2 of the working electrode to the electrolyte (0.5 M H_2SO_4 , diluted from sulphuric acid 95-97%, pa, Merck). The solution was prepared using UHQ (ultra high quality, Millipore) water ($> 18 \text{ M}\Omega \text{ cm}$). Tip etching

was done according to [2]. After etching, the tips were immersed into UHQ water and partially coated with apiezon wax (B7276, Plano GmbH, Germany). STM measurements were conducted using an Agilent PicoLe microscope with a 10 μm STM scanner in constant current mode with the set point current of 1 nA. The STM images were processed using WSxM 5.0 Develop 3.1. software [5].

The oxidation of Pt/HOPG model electrodes was performed in 0.5 M sulphuric acid by the means of stepwise potential increase. For these measurements, the STM tip was under potential control at 0.4 V. Starting from 0.7 V, the potential of the model electrode was increased by 100 mV steps at a scan-rate of 5 mV s^{-1} and kept constant for the time of image acquisition (approximately 6-7 min). The procedure was repeated up to the potential of 1.9 V. After reaching 1.9 V, the potential was scanned back to 0.7 V with a scan-rate of 5 mV s^{-1} and again images were recorded at 0.7 V. All potentials are cited versus standard hydrogen electrode (SHE).

Results

The current response recorded during the 100 mV scans to higher potentials, is shown in Figure 1 for a sample with a pitch of 200 nm. The current measured upon immersion at 0.7 V was typically between -0.5 and -2.0 μA , which may be ascribed to oxygen reduction as the measurements were performed under ambient conditions. Upon potential increase the current increases and zero crossing occurs at a potential of 0.89 V \pm 0.03 V. The oxidation current further increases with further potential increase due to Pt oxide formation and oxygen evolution, and, finally, rapidly increases for the last two investigated potentials, i.e. 1.8 and 1.9 V.

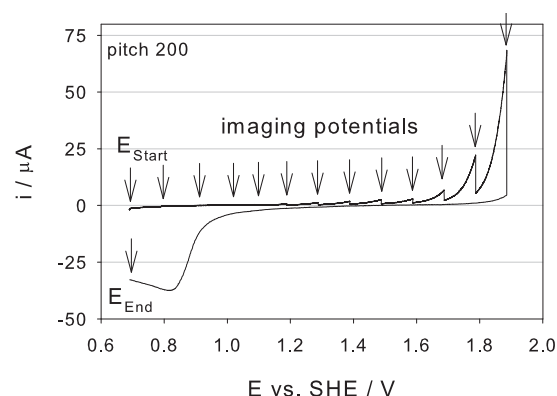


Figure 1. IV curve for an EBL Pt/HOPG model electrode, recorded during an *in situ* STM experiment, pitch 200 nm.

The current at the latter potentials is due to mixed contributions of the oxygen evolution and carbon corrosion. Oxidised Pt and oxygen in the solution are subsequently reduced during the backscan, resulting in a current peak at 0.85 V.

The STM images reproducibly showed that the dot pattern is stable in the electrolyte up to a potential of 1.4 V (Figure 2). At potentials of and above 1.5 V (Figure 2 b)

the dots starts to disappear (black circles), and the dot pattern is replaced by a corresponding hole pattern (Figure 2 c-d and insets Figure 3). Also, corrosion of HOPG, starting at the step edges, can be observed at potentials above 1.5 V (see markers).

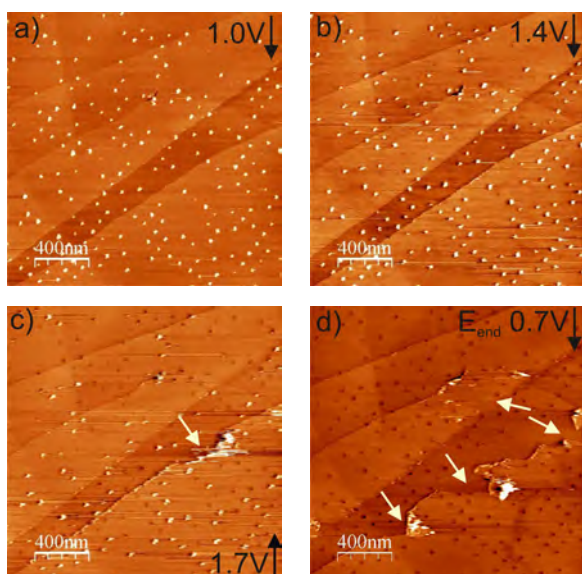


Figure 2. EC-STM image of a Pt/HOPG model electrode (pitch 100 nm) in 0.5 M sulphuric acid at a) 0.9 V, b) 1.6 V, c) 1.7 V and d) 0.7 V upon return. Tip potential is 0.4 V vs. SHE, tip bias: - 0.5 V, - 1.1 V, - 1.3 V and -0.3 V, respectively. The Δz -range is 7 nm for a-c and 5 nm for d.

The results of the experiments performed by stepwise potential increase are presented in Figure 3. Herein, the potential is plotted against the abundance of dots on the surface (Figure 3). The plot shows that a few dots start to leave the surface in the potential range of 0.9 V – 1.4 V. The majority of dots starts to disappear above 1.4 V. The onset of HOPG corrosion is observed at > 1.5 V. HOPG corrosion progresses with increasing anodic potentials, leading to complete disappearance of the dot pattern.

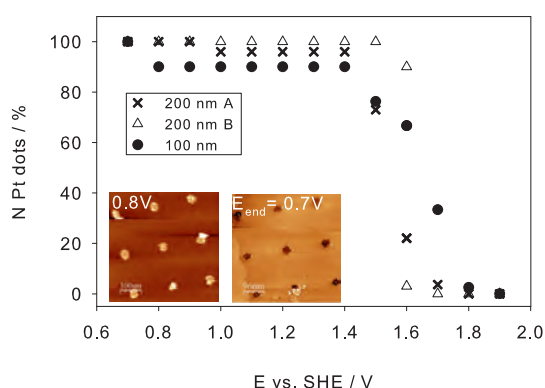


Figure 3. Amount of particles (in %) still present on the sample at a given potential.

The comparison of Figures 1 and 3 reveals that the slight current increase for potentials > 1.4 V roughly corresponds to the values at which the dots start to disappear and the holes to appear.

During the back-scan (Figure 1) a clear reduction peak is observed at about 0.85 V, which indicates that Pt is still present on the model electrode, probably accumu-

lated at HOPG edges, in areas with insufficient lift-off or remaining in the holes.

In order to understand the unusual stability of the Pt dot pattern on HOPG in air and in the electrolyte as well as the appearance of holes upon application of anodic potentials, the origin of the holes has to be examined. Either the holes are generated during the lithographic process by e.g. Pt sputtering or they are a consequence of Pt induced preferential carbon corrosion during electrochemical oxidation. Therefore, the sputtering step during the lithographic process was replaced by a Pt evaporation step.

SEM images after the lift-off of vapor deposited samples (Figure 4a), showed a high amount of Pt dots, which arrangement, however, was not according to the pattern written by the e-beam (Figure 4b). Some of the dots were still part of a square pattern with a pitch of 200 nm, but most were loosely distributed on the HOPG surface or clustered into long strings, probably decorating the steps and the edges of the HOPG substrate [3]. Consequently, the immobilization of Pt on HOPG is most likely induced by the sputtering process.

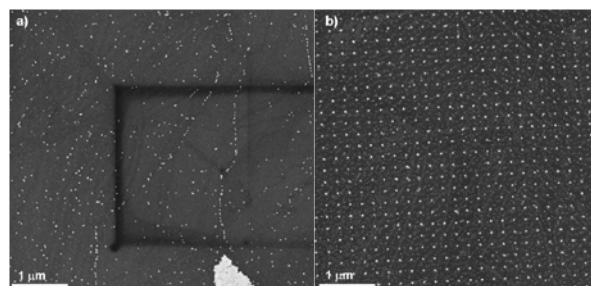


Figure 4. SEM images of EBL Pt/HOPG model electrodes prepared by a) vapour-deposition and b) sputtering of Pt.

In conclusion, stability of Pt dots generated by e-beam lithography on HOPG and corrosion of HOPG could be successfully imaged with STM *in situ* in sulphuric acid. Further studies to investigate the origin of defects led to the assumption that the latter are created during the sputtering step.

Acknowledgement

The authors would like to thank Michael Horisberger (LDM, PSI) for Pt sputtering, Arnold Lücke (LMN, PSI) for Pt vapour deposition and Swiss National Science Foundation (SNSF) for financing the project 200021_121719/1.

References

- [1] V.A. Guzenko, J. Ziegler, A. Savouchkina, C. Padeste, C. David, *Microelectron. Eng.* **88**, 1972-1974 (2011).
- [2] A. Savouchkina, A. Foelske-Schmitz, V.A. Guzenko, D. Weingarh, G.G. Scherer, A. Wokaun, R. Kötz, *Electrochem. Commun.* **13**, 484-487 (2011).
- [3] F. Atamny, O. Spillecke, R. Schlogl, *Phys. Chem. Chem. Phys.* **1**, 4113-4118 (1999).
- [4] J. Chen, K.-Y. Chan, *Mol. Simul.* **31**, 527-533 (2005).
- [5] I. Horcas, R. Fernandez, J.M. Gomez-Rodriguez, J. Colchero, J. Colchero, J. Gomez-Herrero, A.M. Baro, *Rev. Sci. Instrum.* **78**, 013705 (2007).
- [6] M. Peuckert, F.P. Coenen, H.P. Boenzel, *Electrochim. Acta* **29**, 1305-1314 (1984).

XPS analysis of activated carbon supported ionic liquids - an approach towards reliable binding energies

A. Foelske-Schmitz, D. Weingarth, R. Kötzt

phone: +41 56 310 41 93, e-mail: annette.foelske@psi.ch

Sample charging is known to be a challenging issue for fundamental XPS analysis of IL [1]. As a consequence, Villar Garcia et al. [1] devoted strong efforts towards the measurement of absolute binding energies of IL. These authors chose the binding energy of aliphatic carbon appearing in the C 1s spectra of cations having long alkyl chains ($n \geq 8$) as an internal reference and set the binding energy of this species to 285.0 eV. For charge correction of spectra recorded from IL having cations with short alkyl chains, such as [EMIM], these authors used the BE of the N 1s line determined from the corresponding imidazolium cation with long alkyl chain as reference. The use of an internal reference, however, may also comprise disadvantages. Charge correction cannot be performed if a compound having a long alkyl chain ($n \geq 8$) is not available and it would be more straightforward if the binding energies were obtained directly from the XPS measurement.

Herein, we report on XPS analysis of four different 1-Ethyl-3-methylimidazolium [EMIM] based ionic liquids with varying anions (Table 1) prepared on an activated carbon (AC) and on an aluminium (Al) support. The results indicate that preparation on AC may allow for the determination of reliable binding energies (BE) of IL without charging.

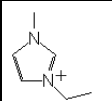
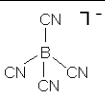
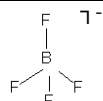
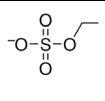
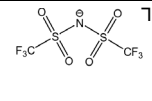
[EMIM]	[B(CN) ₄]	[BF ₄]	[ES]	[TFSI]
				

Table 1. Chemical structures of the investigated ionic liquids

Experimental

For analysis a droplet of each liquid was deposited on a sample holder made from aluminium (Al) and for comparison on Teflon bound activated carbon (AC). XPS measurements were performed with an ESCALAB 220iXL spectrometer using monochromatic Al K α radiation for excitation.

Results

The charging issue is exemplarily shown for the N 1s line of [EMIM][TFSI] in Figure 1. The grey spectrum was recorded from a droplet prepared on Al, the black one from a droplet of the same liquid prepared on AC. Both spectra feature the two different carbon species present in the liquid, i.e. the imidazolium nitrogen of the cation at a BE around 402.0 eV and the sulfonyl imide nitrogen of the anion at a BE around 399.5 eV. The N 1s spectrum of the droplet prepared on Al is shifted by 0.3 eV if compared to the one prepared on AC indicating charging on the Al support. Further measurements showed that the data obtained from the AC support shows consistently lower binding energies if compared to data obtained from the liquids prepared on the Al support (compare BE values of the imidazolium nitrogen obtained from AC and Al in Table 2).

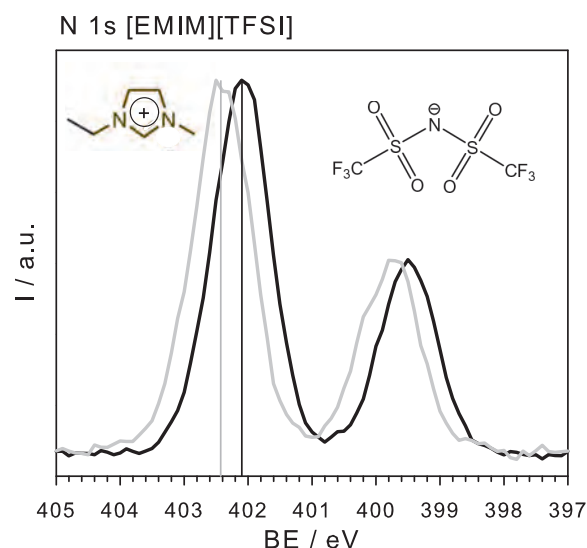


Figure 1: N 1s spectra of [EMIM][TFSI] recorded on Al (grey line) and on AC (black line) support.

Comparison of the determined BE with published data [1, 2] further suggests that sample charging does not occur when IL samples are prepared on the AC support (compare determined BE values of the imidazolium nitrogen species from AC and Ref. listed in Table 2).

	[B(CN) ₄]	[BF ₄]	[ES]	[TFSI]
Ref.	n.a.	402.0 [1]	401.8 [2]	402.1 [1]
AC	402.1	402.0	401.8	402.1
Al	402.5	402.2	401.7	402.4

Table 2. Binding energies of the N 1s line of the nitrogen species of the [EMIM] cation recorded from the different IL on the different substrates.

This observation may be explained by the high surface area, and, therefore, extremely huge solid/liquid interface with correspondingly high double layer capacitance of the AC support when compared to common substrates such as metal foils.

In conclusion this preparation method may provide a straightforward opportunity for the determination of reliable binding energies in this research field (see also [3]).

References

- [1] I.J. Villar-Garcia, E.F. Smith, A.W. Taylor, F. Qiu, K.R.J. Lovelock, R.G. Jones P. Licence, Phys. Chem. Chem. Phys. **13**, 2797 (2011).
- [2] J.M. Gottfried, F. Maier, J. Rossa, D. Gerhard, P.S. Schulz, P. Wasserscheid, H.P. Steinrück, Z. Phys. Chem. **220**, 1439 (2006).
- [3] A. Foelske-Schmitz, D. Weingarth, R. Kötzt, Surf. Sci. **605**, 1979 (2011).

THE ELECTROCHEMISTRY LABORATORY

IMPRESSIONS

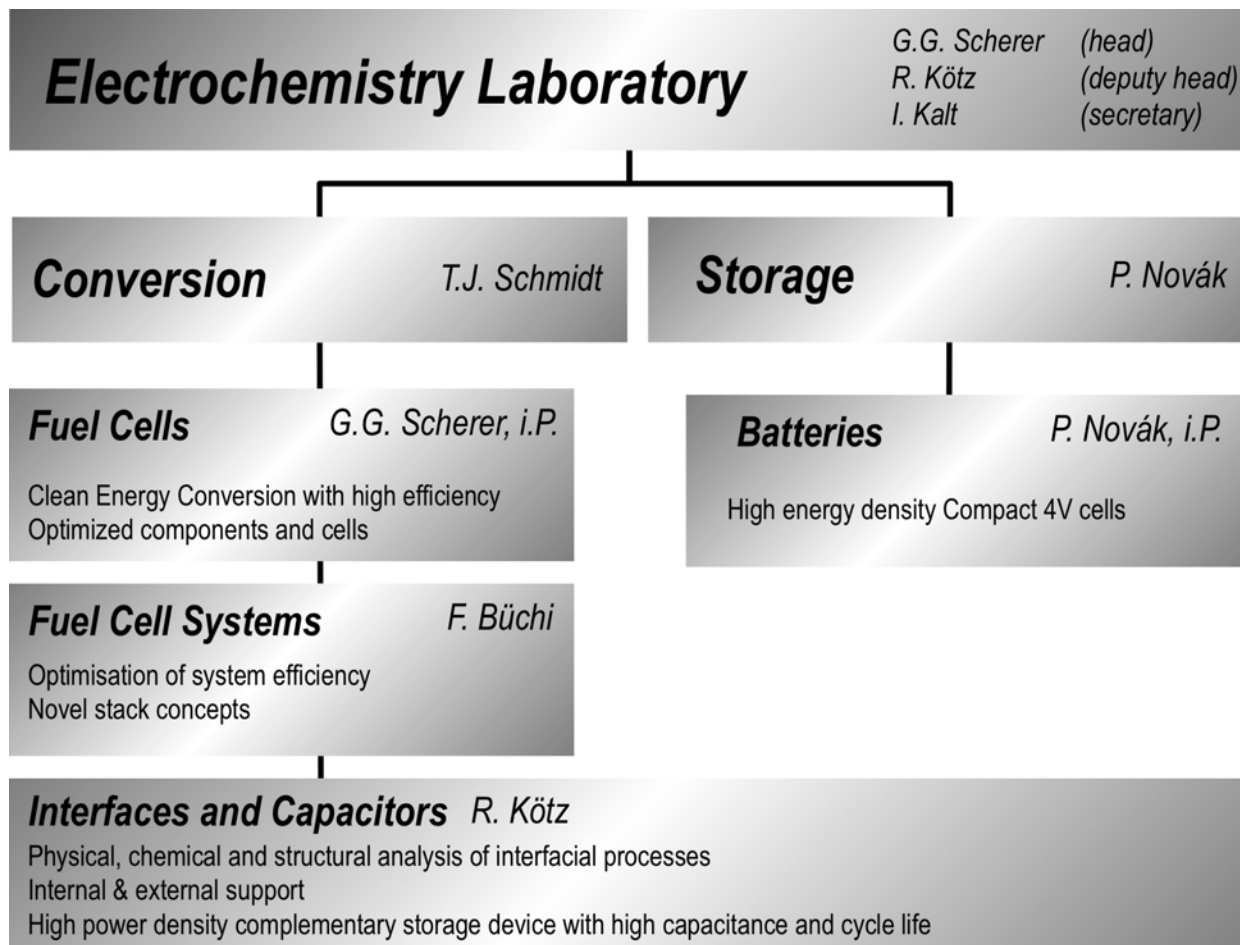


The fuel cell system of the car (see also the title page) developed together with Belenos Clean Power Holding (top left) and the fuel cell driven coffee machine (left) received a lot of attention during the "Tag der offenen Türe" at PSI in October 2011.



Watching posters during the 27th One-Day-Symposium on May 11, 2011 at PSI.

STRUCTURE 2011



ECL-PERSONNEL 2011

Staff

Ben youcef Hicham (until February), Dr. ♦ Bernard Jérôme, Dr. ♦ Boillat Pierre, Dr. ♦
Bonorand Lukas, ♦ Büchi Felix, Dr.

Foelske Annette, Dr.

Garcia-Araez Nuria, Dr. (since November) ♦ Gloor Thomas ♦ Gómez Juan Luis, Dr. (since March) ♦
Gubler Lorenz, Dr.

Hofer Marcel

Jämstorp-Berg Erik, Dr. (since November) ♦ Junker Christoph

Kaiser Hermann ♦ Kalt Isabella ♦ Kötz Rüdiger, Dr.

Lüscher Sandro (until Mai)

Märkle Wolfgang, Dr. (until April) ♦ Marmy Christian

Novák Petr, Prof. Dr.

Perez Sofia, Dr. (until December)

Rodriguez-Perez Paramaconi, Dr. (since November) ♦ Roth Jörg, Dr.

Sallard Sebastien, Dr. (since May) ♦ Sasaki Tsuyoshi, Dr. ♦ Sasaki Yuri, Dr. (until December) ♦
Scherer Günther G., Dr. (until December) ♦ Schmidt Thomas Justus, Prof. Dr. (since February) ♦
Schneider Holger, Dr. (until July) ♦ Schneider Ingo, Dr. (until November) ♦ Schulenburg Hendrik, Dr.
(until March) ♦ Siegrist Raphael (until May)

Thut Jürg

Urbonaite Sigita, Dr. (since April)

Villevieille Claire, Dr.

PhD Students

Bayer Michael (until May) ♦ Bernardo Philippe (until February) ♦ Bleith Peter (since March) ♦
Buchmüller Yves

Cericola Dario (until May)

Eller Jens

Godbole Vikram (until October)

Hantel Moritz ♦ Hess Michael

Jetsrisuparb Kaewta

Kreitmeier Stefan

Lanz Patrick (since June) ♦ Linse Nicolas (until December)

Neophytides George

Oberholzer Pierre

Peitz-Savouchkina Anastasia (until November)

Rabis Annett (since June)

Schwanitz Bernhard (until December)

Verma Pallavi (until October) ♦ Von Dahlen Steffen (until December)

Weingarth Daniel

Zaglio Maurizio (until December) ♦ Zhang Zhuoxiang (since March) ♦ Zurbrügg Mark (since August)

THESE PHD STUDENTS FROM ECL GRADUATED IN 2011

Dr. Michael Bayer



Ein mehrdimensionales Impedanzmodell für Polymerelektrolyt-Brennstoffzellen

Ph.D. Thesis, No. 19746, ETH Zürich, May 2011.

Examiners Prof. Dr. A. Wokaun, PSI/ETH Zürich
Dr. G.G. Scherer, PSI Villigen
Dr. I. Schneider, PSI Villigen
Prof. M. Quack, ETH Zürich

Dr. Dario Cericola



Towards the reliable hybridization of electrochemical capacitors and rechargeable batteries

Ph.D. Thesis, No. 19744, ETH Zürich, May 2011.

Examiners Prof. Dr. A. Wokaun, PSI/ETH Zürich
Prof. Dr. T.J. Schmidt, PSI/ETH Zürich
Prof. Dr. P. Novák, PSI/ETH Zürich
Dr. R. Kötz, PSI Villigen

**Dr. Philippe
Bernardo**



Influence des propriétés du graphite sur le premier cycle d'intercalation du lithium

Ph.D. Thesis, No. 16620, University of Mulhouse, July 2011.

Examiners Dr. C. Delmas, ICMCM Bordeaux, France
Prof. Dr. P. Novák, PSI/ETH Zürich
Dr. M.E. Spahr, Timcal, Bodio
Prof. Dr. R. Gadiou, IS2M, Mulhouse, France
Dr. C. Vix, IS2M, Mulhouse, France

Dr. Maurizio Zaglio



Model based transient analysis of polymer electrolyte fuel cells

Ph.D. Thesis, No. 19992, ETH Zürich, September 2011.

Examiners Prof. Dr. A. Wokaun, PSI/ETH Zürich
Prof. Dr. M. Morbidelli, ETH Zürich
PD Dr. I. Mantzaras, PSI Villigen
Dr. F.N. Büchi, PSI Villigen

Dr. Pallavi Verma



Electrochemical and chemical surface modifications of carbons for Li-ion batteries

Ph.D. Thesis, No. 20006, ETH Zürich, October 2011.

Examiners Prof. D. A. Wokaun, PSI/ETH Zürich
Prof. Dr. P. Novák, PSI/ETH Zürich
Prof. Dr. T.J. Schmidt, PSI/ETH Zürich

Dr. Vikram Godbole



Elucidating the reaction mechanism of electrode materials for Li-ion batteries using in situ structural characterization

Ph.D. Thesis, No. 20007, ETH Zürich, October 2011.

Examiners Prof. Dr. A. Wokaun, PSI/ETH Zürich
Prof. Dr. P. Novák, PSI/ETH Zürich
Prof. Dr. R. Nesper, ETH Zürich

Dr. Nicolas Linse



Start/stop phenomena in polymer electrolyte fuel cells

Ph.D. Thesis, No. 20132, ETH Zürich, December 2011.

Examiners Prof. Dr. A. Wokaun, PSI/ETH Zürich
Prof. Dr. T.J. Schmidt, PSI/ETH Zürich
Dr. G.G. Scherer, PSI Villigen
Dr. L. Gubler, PSI Villigen

Dr. Anastasia Peitz



Degradation mechanisms of electro-catalysts used in polymer electrolyte fuel cells

Ph.D. Thesis, No. 20133, ETH Zürich, December 2011.

Examiners Prof. Dr. A. Wokaun, PSI/ETH Zürich
Prof. Dr. T.J. Schmidt, PSI/ETH Zürich
Dr. G.G. Scherer, PSI Villigen
Dr. A. Foelske-Schmitz, PSI Villigen

Dr. Bernhard Schwanitz



Reduzierung der Platinbeladung und Imaging von Alterungsphänomenen in der Polymerelektrolyt-Brennstoffzelle

Ph.D. Thesis, Nr. 20142, ETH Zürich, December 2011.

Examiners Prof. Dr. A. Wokaun, PSI/ETH Zürich
Prof. Dr. T.J. Schmidt, PSI/ETH Zürich
Dr. G.G. Scherer, PSI Villigen
Dr. H. Schulenburg, Metroglas AG, Affoltern a.A.

Dr. S. von Dahlen



Ortsaufgelöste in situ Charakterisierung von Polymerelektrolyt-Brennstoffzellen in Kanal- und Stegregionen

Dissertation Nr. 20131, ETH Zürich, December 2011.

Examiners Prof. Dr. A. Wokaun, PSI/ETH Zürich
Prof. Dr. M. Quack, ETH Zürich
Dr. G.G. Scherer, PSI Villigen
Dr. I. Schneider, PSI Villigen

EXCHANGE STUDENTS, DIPLOMA THESES, SUMMER STUDENTS

Friederike Lindner	<i>Untersuchungen zur chemischen Alterung von Membranen für Niedertemperatur-PEM-Brennstoffzellen</i> Technische Universität Bergakademie Freiberg, Deutschland November 2010 – March 2011.
Thomas Rosen	<i>Determination of water saturation dependent gas transport properties of PEFC gas diffusion layers via the Lattice Boltzmann method</i> Kungliga Tekniska Högskolan (KTH), Stockholm, Sweden, January - May 2011.
Urs Siegenthaler	<i>Studies of lithium batteries at extreme conditions</i> Universität Basel, February - May 2011.
Sarah Hodel	<i>Herstellung und Charakterisierung von strahlengefropften Membranen für die Brennstoffzelle</i> Kantonsschule Wettingen, February – March 2011.
Matteo Michiardi	<i>Characterization of the gas transport through pinholes in PEFC membranes</i> Université de Rennes I, France, April – July 2011.
Matthias Weiland	<i>Watermanagement for passive self-breathing micro fuel cells and visualisation through neutron radiography</i> TU Berlin, Germany, March – August 2011.
Mylène Citerne	<i>Developpement d'un humidificateur pour une micro pile à combustible</i> PSI Villigen and Università di Corsica, France, April - September 2011.
Marcel Schreier	<i>Exploration von strahlengefropften Membranen für Lithium-Schwefel-Batterien</i> ETH Zürich, May 2011.
Baptise Verdin	<i>Development of a new recirculation system for a fuel cell system</i> Grenoble INP-Phelma, France, May – August 2011.
Johanna Conder	<i>Radiation grafted polymer electrolytes for the lithium-sulfur battery</i> Warsaw University of Technology, Poland, July – September 2011.
Yan Yan	<i>Simulation of a fuel cell/battery hybrid system for automotive application</i> ETH Zürich, September – December 2011.
Rocco Gaudenzi	<i>Assembling and testing of two nafion-based humification systems for in-situ XTM measurement of PEFC</i> ETH Zürich, October – December 2011.
Patrick Pietsch	<i>Development of a new in situ lithium battery for X-ray diffraction application</i> ETH Zürich, October – December 2011.

SEMINAR, INVITED SPEAKERS

Dr. Pascal Häring, Renata SA, Itingen	<i>Spezialitäten bei Knopfzellen (Entwicklung und spezielle Anwendungsbeispiele, Hg-freie Silberoxidbatterie, Designaspekte)</i> January 24, 2011.
Prof. Dr. Brian C. Benicewicz University of South Carolina, Columbia, USA	<i>Advances in PBI-PA membranes for high temperature PEM devices</i> March 14, 2011.
Dr. Arnd Garsuch, BASF SE, Ludwigshafen, Germany	<i>Lithium-air batteries – current research at BASF SE</i> May 30, 2011.
Prof. Dr. Yong Yang, Xiamen University, Xiamen, China	<i>Polyanion compounds as positive electrode materials for Li-ion batteries</i> June 20, 2011.
Prof. Bhuvanesh Gupta, Indian Institute of Technology, New-Delhi, India	<i>Polymers as biocompatible materials and artificial organs</i> October 10, 2011.

AWARDS

J. Bernard, M. Hofer, U. Hannesen¹, N. Hayek¹, P. Dietrich, F.N. Büchi	Watt d'Or 2011 <i>Potenzial einer kostengünstigen Brennstoffzelle für Autos aufgezeigt</i> Swiss Federal Office of Energy, Bern January 6, 2011. ¹ Belenos Clean Power Holding, Biel/Bienne
P. Boillat	PSI-Impuls-Prize for the best PhD thesis in the year 2010 <i>Advanced characterization of polymer electrolyte fuel cells using high resolution neutron imaging</i> September 30, 2011.
M. Hantel	ISE Young researcher award for the best oral presentation <i>Partially reduced graphite oxide: A graphene like material for supercapacitor electrodes</i> ISEE'Cap, Poznan, Poland, June 12-16, 2011.

CONFERENCES – SYMPOSIA

27th One-Day-Symposium
May 11, 2011.

Electromobility

Organizers: Günther G. Scherer, Rüdiger Kötz, Petr Novák

Contributions from:

Hubert Gasteiger, Technische Universität München, Germany

Janko Jamnik, Kemijski Institut Ljubljana, Slovenia

Andreas Friedrich, Deutsches Zentrum für Luft-Raumfahrt (DLR)
Stuttgart, Germany

Peter Prenninger, AVL List GmbH, Graz, Austria

Isotta Cerri, Toyota Europe, Brussels, Belgium

Robert Stüssi, Avere, Lisbon, Portugal



Lecturers and organizers of the 27th One-Day-Symposium of the Electrochemistry Laboratory on 'Electromobility'.

From left to right: Rüdiger Kötz, Janko Jamnik, Peter Prenninger, Günther G. Scherer (front), Isotta Cerri, Thomas J. Schmidt, Andreas Friederich, Robert Stüssi, Petr Novák, Hubert Gasteiger, Felix Büchi.

**22 Jahre Brennstoffzellenforschung am
PSI, December 15, 2011.**

This special symposium has been organized on the occasion of the retirement of the head of the laboratory, Dr. Günther G. Scherer.

Contributions from:

Alexander Wokaun, Paul Scherrer Institut, Villigen

Frank Willig, Fritz Haber Institut der MPG Berlin

Bernhard Andreaus, Inficon AG, Balzers

Thomas J. Schmidt, Paul Scherrer Institut, Villigen



Günther G. Scherer during his farewell address and receiving flowers from Isabella Kalt and Thomas J. Schmidt.



REVIEW ACTIVITIES OF THE LABORATORY

Journals

Angewandte Chemie International Edition

Carbon ♦ Chemical Communications

Electrochimica Acta ♦ Electrochemistry Communications ♦ Energy & Environmental Science

Fuel Cells

International Journal of Hydrogen Energy

Journal of the American Chemical Society ♦ Journal of Applied Electrochemistry ♦ Journal of Catalysis ♦ Journal of the Electrochemical Society ♦ Journal of Materials Chemistry of RSC ♦ Journal of Membrane Science ♦ Journal of Physical Chemistry ♦ Journal of Power Sources ♦ Journal of Solid State Electrochemistry

Physical Chemistry Chemical Physics

Science ♦ Solid State Ionics

Nature Materials

Organisations

Alexander von Humboldt-Stiftung, Germany ♦ ANR (Agence Nationale de Recherche), France

CCEM-CH

ETH Zürich Research Commission

SNF (Schweizerischer Nationalfond)

Co-Referee's Report for Dissertations

M.H. Bayer, PSI/ETH Zürich ♦ Ph. Bernardo; PSI/University of Mulhouse, FR

D. Cericola PSI/ETH

V. Godbole PSI/ETH

N. Linse PSI/ETH

A. Peitz PSI/ETH

B. Schwanitz PSI/ETH

P. Verma PSI/ETH ♦ S. von Dahlen PSI/ETH

M. Zaglio PSI/ETH

INDUSTRIAL PARTNERS

The Laboratory had the pleasure to collaborate with the following industrial partners during the year 2011:

CEKAtec, Wattwil

BASF SE, Ludwigshafen, Germany ♦ **Belenos Clean Power Holding**, Biel/Bienne

Daimler AG, Stuttgart, Germany

Fiat, Centro Ricerche (CRF), Torino, Italy ♦ **Freudenberg Fuel Cell Component Technology KG (FFCCT)** Weinheim, Germany

Heraeus Quarzglas GmbH & Co. KG, Kleinostheim, Germany

IBM Zürich Research Laboratory, Rüschlikon

Liebherr-Aerospace Lindenberg GmbH, Lindenberg, Germany

MES SA, Stabio

PowerCell (Volvo), Göteborg, Sweden

SolviCore GmbH & Co. KG, Hanau, Germany

TIMCAL SA, Bodio

Umicore AG & Co. KG, Brussels, Belgium

Volkswagen, Wolfsburg, Germany

DOCUMENTATION

PROJECT COLLABORATIONS WITH EXTERNAL PARTNERS

CCEM

F.N. Büchi
Projektleiter *hy.muve: Development of hydrogen powered municipal vehicle with EMPA Dübendorf and Industrial Partners*

BFE

F.N. Büchi
Projektleiter *X-ray micro-tomography of polymer electrolyte fuel cells*

F.N. Büchi
Projektleiter *Gasanalysis in polymer electrolyte fuel cells*

L. Gubler
Projektleiter *Lebensdauer-Limitierungen von Brennstoffzellen-Membranen: Mechanismen, Methoden und Innovationen*

L. Gubler, I.A. Schneider
Projektleiter *go.PEF-CH: Enhancing PEFC durability and reliability under application-relevant conditions*
Partner: Berner Fachhochschule Technik und Informatik (BFH-TI, Biel BE), CEKAtec Elektrowerkzeuge AG & Co. KG (Wattwil SG), MES-DEA SA. (Stabio TI)

J. Roth
Projektleiter *S_Chain fundamentals*
with ZHAW Winterthur and Belenos Clean Power AG

EU

F.N. Büchi
Projektleiter *JTI FCH: Auto-Stack: Automotive fuel cell stack cluster initiative for Europe*
with auto-stack consortium

R. Kötz
Member of MC *COST Action MP1004 Hybrid energy storage devices and systems for mobile and stationary applications*

P. Novák
Projektleiter *MAHEATT Materials for high energy accumulators in traction and tools*

I.A. Schneider, T.J. Schmidt
Projektleiter *DEMMEA Understanding the degradation mechanisms of membrane-electrode-assembly for high temperature PEMFCs and optimization of individual component)*

Industry

P. Boillat
Projektleiter *Diagnostics of polymer electrolyte fuel cells*
Automotive Industry

F.N. Büchi
Projektleiter *Developments for mobile fuel cell systems*
S_Chain project

J.L. Gómez-Cámer
Projektleiter *Graphite für Lithiumionen-Batterien*
TIMCAL SA, Bodio

L. Gubler
Projektleiter *Development of components for fuel cells*
S_Chain project

P. Novák
Projektleiter *Forschungsnetzwerk „Elektrochemie und Batterien“*
BASF SE, Ludwigshafen, Germany

P. Novák Projektleiter	<i>Projekt HE-Lion (Hochenergie-Lithiumionenbatterien für die Zukunft)</i> BASF SE, Ludwigshafen
T.J. Schmidt Projektleiter	<i>Electrochemical energy conversion for high-power densities in microfluidic cells</i> IBM Zürich Research Laboratory, Rüschlikon
I.A. Schneider Projektleiter	<i>Diagnostics of polymer electrolyte fuel cells</i> Automotive industry
S. Urbonaite Projektleiterin	<i>Kohlenstoffe</i> Heraeus Quarzglas GmbH & Co. KG, Kleinostheim

Nationalfonds

A. Foelske-Schmitz Projektleiterin	<i>Degradation mechanisms of electro-catalysts used in polymer electrolyte fuel cells</i>
L. Gubler Projektleiter	<i>Antioxidant strategies for the stabilization of fuel cell membranes against oxidative stress</i>
R. Kötz Projektleiter	<i>Graphite oxides and graphene for electrochemical energy storage</i>
P. Novák Projektleiter	<i>Synthetic solid electrolyte interphase on carbon electrodes for lithium-ion batteries</i>
P. Novák Projektleiter	<i>New oxyphosphates as high specific charge electrode materials for lithium-ion batteries</i>

TEACHING ACTIVITIES

University Level Teaching

Prof. Dr. P. Novák,	<i>Elektrochemie</i> ETH Zürich, HS 2011
Prof. Dr. A. Wokaun, Dr. G.G. Scherer, Prof. Dr. K. Boulouchos	<i>Renewable Energy Technologies II</i> ETH Zürich, FS 2011

Contributions to Courses at Universities, FHL, and other Institutes

Prof. T.J. Schmidt	<i>Renewable energy technologies II</i> ETH Zürich, March 29, 2011
Prof. T.J. Schmidt	<i>Strategische Übungen in analytischer Chemie</i> ETH Zürich, December 6, 2011
Dr. I.A. Schneider	<i>Renewable energy technologies II</i> ETH Zürich, April 12/19, 2011

PUBLICATIONS

Books and Reviewed Book Chapters

P. Boillat, G.G. Scherer	<i>Neutron imaging</i> PEM Fuel Cell Durability Handbook – Vol. II: PEM Diagnostic Tools, Chapter 12, edited by H. Wang, H. Li, X.T. Yuan ISBN: 9781439839218, ISBN 10: 1439839212, CRC Press - Taylor & Francis Group (2011).
--------------------------	--

H. Gasteiger¹, F.N. Büchi,
V. Ramani¹, A. Weber¹,
P. Shirvanian¹, T. Fuller¹,
S. Narayanan¹, A. Davenport¹,
H. Nakagawa¹,
M. Edmundson¹, D. Jones¹,
H. Uchida¹, C. Lamy¹,
P. Strasser¹, S. Mukerjee¹,
R. Mantz, K. Swider-Lyons¹,
T.J. Schmidt (Editors)

Polymer electrolyte fuel cells 11
ECS Transactions **41** (2011) 220th ECS Meeting, Boston, USA,
Oct. 9–14 (2011) ISBN: 978-1-60768-255-4.
¹ external editors

I. Kalt, R. Kötz, G.G. Scherer

PSI Electrochemistry Laboratory Annual Report 2010
ISSN 1661-5379 (2011).

Peer Reviewed Papers

S. Balog, U. Gasser,
K. Mortensen¹, H. Ben youcef,
L. Gubler, G.G. Scherer

Nano-scale morphology in graft copolymer proton-exchange membranes cross-linked with DIPB
doi: 10.1016/j.memsci.2011.08.031, J. Membr. Sci. **383**, 50-59 (2011).
¹ University of Copenhagen, Denmark

H. Ben youcef, L. Gubler,
A. Foelske-Schmitz,
G.G. Scherer

Improvement of homogeneity and interfacial properties of radiation grafted membranes for fuel cells using diisopropenylbenzene crosslinker
doi: 10.1016/j.memsci.2011.07.021, J. Membr. Sci. **381**, 102-109 (2011).

J. Bernard, M. Hofer,
U. Hannesen¹, A. Toth²,
A. Tsukada, F.N. Büchi,
P. Dietrich

Fuel cell/battery passive hybrid power source for electric powertrains
doi:10.1016/j.jpowsour.2011.03.015, J. Power Sources **196**, 5867-5872 (2011).
¹ Belenos Clean Power Holding, Biel/Bienne
² Swatch Group, Biel/Bienne

Ph. Bernardo, J. Dentzer¹,
R. Gadiou¹, W. Märkle,
D. Goers², P. Novák,
M.E. Spahr², C. Vix-Guterl¹

Influence of graphite surface properties on the first electrochemical lithium intercalation
doi:10.1016/j.carbon.2011.07.007, Carbon **49**, 4867-4876 (2011).
¹ Institute for Material Science of Mulhouse, Mulhouse, France
² TIMCAL SA, Bodio

I. Bilecka¹, A. Hintennach,
M.D. Rossell¹, D. Xie¹,
P. Novák, M. Niederberger¹

Microwave-assisted solution synthesis of doped LiFePO₄ with high specific charge and outstanding cycling performance
doi:10.1039/c0jm03476b, J. Mater. Chem. **21**, 5881-5890 (2011).
¹ ETH Zürich

P. Boillat, P. Oberholzer,
B.C. Seyfang, A. Kaestner,
R. Perego, G.G. Scherer,
E.H. Lehmann, A. Wokaun

Using ²H labeling with neutron radiography for the study of solid polymer electrolyte water transport properties
doi:10.1088/0953-8984/23/23/234108, J. Phys.: Condens. Matter **23**, 234108 (2011).

D. Cericola, P. Novák,
A. Wokaun, R. Kötz

Hybridization of electrochemical capacitors and rechargeable batteries: an experimental analysis of the different possible approaches utilizing activated carbon, Li₄Ti₅O₁₂ and LiMn₂O₄
doi: 10.1016/j.jpowsour.2011.07.032, J. Power Sources **196**, 10305-10313 (2011).

D. Cericola, P. Novák,
A. Wokaun, R. Kötz

Mixed bi-material electrodes based on LiMn₂O₄ and activated carbon for hybrid electrochemical energy storage devices
doi: 10.1016/j.electacta.2011.07.029, Electrochim. Acta **56**, 8403-8411 (2011).

D. Cericola, P.W. Ruch,
A. Foelske-Schmitz,
D. Weingarh, R. Kötz

Effect of water on the aging of activated carbon based electrochemical double layer capacitors during constant voltage load tests
Int. J. Electrochem. Sci. **6**, 988-996 (2011).

D. Cericola, R. Kötz,
A. Wokaun

Effect of electrode mass ratio on aging of activated carbon based supercapacitors utilizing organic electrolytes
doi: 10.1016/j.jpowsour.2010.11.157, J. Power Sources **196**, 3114-3118 (2011).

- D. Cericola, P. Novák,
A. Wokaun, R. Kötz
- Segmented bi-material electrodes of activated carbon and LiMn_2O_4 for electrochemical hybrid storage devices: effect of mass ratio and C-rate on current sharing*
doi: 10.1016/j.electacta.2010.10.016, *Electrochim. Acta* **56**, 1288-1293 (2011).
- S.M. Dockheer¹, L. Gubler,
A. Wokaun, W.H. Koppenol¹
- Damage to fuel cell membranes: reaction of SO_4^{\ominus} with an oligomer of poly(sodium styrene sulfonate)*
doi: 10.1039/c1cp20499h, *Phys. Chem. Chem. Phys.* **13**, 12429-12434 (2011).
¹ ETH Zürich
- J. Eller, T. Rosén, F. Marone,
M. Stampanoni¹, A. Wokaun,
F.N. Büchi
- Progress in in situ X-ray tomographic microscopy of liquid water in gas diffusion layers of PEFC*
doi: 10.1149/1.3596556, *J. Electrochem. Soc.* **158**, B963-B970 (2011).
¹ Institute for Biomedical Engineering, University and ETH Zürich
- R. Flückiger, F. Marone,
M. Stampanoni¹, A. Wokaun,
F.N. Büchi
- Investigation of liquid water in gas diffusion layers of polymer electrolyte fuel cells using X-ray tomographic microscopy*
doi:10.1016/j.electacta.2010.12.016, *Electrochim. Acta* **56**, 2254-2262 (2011).
¹ Institute for Biomedical Engineering, University and ETH Zürich
- A. Foelske-Schmitz ,
D. Weingarh, R. Kötz
- XPS analysis of activated carbon supported ionic liquids: Enhanced purity and reduced charging*
doi: 10.1016/j.susc.2011.07.016, *Surf. Sci.* **605**, 1979-1985 (2011).
- A. Foelske-Schmitz,
D. Weingarh, R. Kötz
- Quasi in situ XPS study of electrochemical oxidation and reduction of HOPG in $[\text{EMIM}][\text{BF}_4]$ electrolytes*
doi: 10.1016/j.electacta.2011.03.064, *Electrochim. Acta* **56**, 10321-10331 (2011).
- R. Francke¹, D. Cericola,
R. Kötz, G. Schnakenburg²,
S.R. Waldvogel¹
- Bis(2,2'-biphenoxy)borates for electrochemical double-layer capacitor electrolytes*
doi: 10.1002/chem.201003449, *Chem. Eur. J.* **17**, 3082–3085 (2011).
¹ Mainz University, Mainz, Germany
² Bonn University, Bonn, Germany
- S.A. Freunberger¹, Y. Chen¹,
Z. Peng¹, J.M. Griffin¹,
L.J. Hardwick¹, F. Bardé²,
P. Novák, P.G. Bruce¹
- Reactions in the rechargeable lithium- O_2 battery with alkyl carbonate electrolytes*
doi:10.1021/ja2021747, *J. Am. Chem. Soc.* **133**, 8040-8047 (2011).
¹ University of St. Andrews, Scotland
² Toyota Motor Europe, Zaventem, Belgium
- V. A. Godbole, J.-F. Colin,
P. Novák
- Study of overcharge behavior of $\text{Li}_{1+x}(\text{Ni}_{1/3}\text{Mn}_{1/3}\text{Co}_{1/3})_{1-x}\text{O}_2$ using in situ and ex situ X-ray synchrotron diffraction*
doi:10.1149/1.3607982, *J. Electrochem. Soc.* **158**, A1005-A1010 (2011).
- D. Goers¹, M.E. Spahr¹,
A. Leone¹, W. Märkle, P. Novák
- The influence of the local current density on the electrochemical exfoliation of graphite in lithium-ion battery negative electrodes*
doi:10.1016/j.electacta.2011.02.046, *Electrochim. Acta* **56**, 3799-3808 (2011).
¹ TIMCAL SA, Bodio
- L. Gubler, S.M. Dockheer¹,
W.H. Koppenol¹
- Radical (HO^\bullet , H^\bullet and HOO^\bullet) formation and ionomer degradation in polymer electrolyte fuel cells*
doi: 10.1149/1.3581040, *J. Electrochem. Soc.* **158**, B755-B769 (2011).
¹ ETH Zürich
- V.A. Guzenko, J. Ziegler,
A. Savouchkina, C. Padeste,
Ch. David
- Fabrication of large scale arrays of metallic nanodots by means of high resolution e-beam lithography*
doi: 10.1016/j.mee.2011.02.042, *Microelectron. Eng.* **88**, 1972-1974 (2011).

- M.M. Hantel, V. Presser¹,
R. Kötz, Y. Gogotsi¹ *In situ electrochemical dilatometry of carbide-derived carbons*
doi:10.1016/j.elecom.2011.08.039, *Electrochem. Commun.* **13**,
1221–1224 (2011).
¹ Drexel University, PA 19104, USA
- M.M. Hantel, T. Kaspar¹,
R. Nesper¹, A. Wokaun,
R. Kötz *Partially reduced graphite oxide for supercapacitor electrodes: Effect of
graphene layer spacing and huge specific capacitance*
doi: 10.1016/j.elecom.2010.11.021, *Electrochem. Commun.* **13**, 90-92
(2011).
¹ ETH Zürich
- A. Hintennach, P. Novák *A novel combinative Raman and SEM mapping method for the
detection of exfoliation of graphite in electrodes at very positive
potentials*
doi:10.1002/jrs.2930, *J. Raman Spectrosc.* **42**, 1754-1760 (2011).
- D. Koziej¹, M.D. Rossell¹,
B. Ludi¹, A. Hintennach,
P. Novák, J.-D. Grunwaldt²,
M. Niederberger¹ *Interplay between size and crystal structure of molybdenum dioxide
nanoparticles – synthesis, growth mechanism, and electrochemical
performance*
doi:10.1002/sml.201001606, *Small* **7**, 377-387 (2011).
¹ ETH Zürich
² Karlsruhe Institute of Technology, Karlsruhe, Germany
- N. Linse, G.G. Scherer,
A. Wokaun, L. Gubler *The effect of platinum on carbon corrosion behavior in polymer
electrolyte fuel cells*
doi: 10.1016/j.electacta.2011.06.093, *Electrochim. Acta* **56**, 7541-7549
(2011).
- W. Märkle, Ch.-Y. Lu, P. Novák *Morphology of the solid electrolyte interphase on graphite in
dependency on the formation current*
doi: 10.1149/2.077112jes, *J. Electrochem. Soc.* **158**, A1478-A1482
(2011).
- P. Nesvadba¹, L. Bugnon
Folger¹, P. Maire, P. Novák *Synthesis of a polymeric 2,5-di-*t*-butyl-1,4-dialkoxybenzene and its
evaluation as a novel cathode material*
doi:10.1016/j.synthmet.2010.11.030, *Synthetic Metals* **161**, 259-262
(2011).
¹ BASF SE, Basel
- Z. Peng¹, S.A. Freunberger¹,
L.J. Hardwick¹, Y. Chen¹,
V. Giordani¹, F. Bardé²,
P. Novák, D. Graham¹,
J.-M. Tarascon³, P.G. Bruce¹ *Oxygen reactions in a non-aqueous Li⁺ electrolyte*
doi:10.1002/anie.201100879, *Angew. Chem. Int. Ed.* **50**, 6351-6355
(2011).
¹ University of St. Andrews, St. Andrews, Scotland
² Toyota Motor Europe, Zaventem, Belgium
³ Université de Picardie Jules Verne, Amiens, France
- T. Sasaki, V. Godbole,
Y. Takeuchi¹, Y. Ukyo¹,
P. Novák *Morphological and structural changes of Mg-substituted Li(Ni,Co,Al)O₂
during overcharge reaction*
doi:10.1149/2.025111jes, *J. Electrochem. Soc.* **158**, A1214-A1219
(2011).
¹ Toyota Central R&D Labs., Nagakute, Japan
- A. Savouchkina, A. Foelske-
Schmitz, G.G. Scherer,
A. Wokaun, R. Kötz *Study of platinum deposition on untreated and thermally modified
glassy carbon*
doi: 10.1149/1.3589915, *J. Electrochem. Soc.* **158**, D420-D425 (2011).
- A. Savouchkina, A. Foelske-
Schmitz, V.A. Guzenko,
D. Weingarh, G.G. Scherer,
A. Wokaun, R. Kötz *In situ STM study of Pt-nanodot arrays on HOPG prepared by electron-
beam lithography*
doi: 10.1016/j.elecom.2011.02.027, *Electrochem. Commun.* **13**,
484-487 (2011).
- H. Schneider, P. Maire,
P. Novák *Electrochemical and spectroscopic characterization of lithium titanate
spinel Li₄Ti₅O₁₂*
doi:10.1016/j.electacta.2011.08.008, *Electrochim. Acta* **56**, 9324-9328
(2011).

- I.A. Schneider, S. von Dahlen *Start-stop phenomena in channel and land areas of a polymer electrolyte fuel cell*
doi: 10.1149/1.3518520, *Electrochem. Solid State Lett.* **14**, B30-B33 (2011).
- I.A. Schneider, M.H. Bayer, S. von Dahlen *Locally resolved electrochemical impedance spectroscopy in channel and land areas of a differential polymer electrolyte fuel cell*
doi: 10.1149/1.3536498, *J. Electrochem. Soc.* **158**, B343-B348 (2011).
- H. Schulenburg, B. Schwanitz, J. Krbanjevic¹, N. Linse, G.G. Scherer, A. Wokaun *Quantification of platinum deposition in polymer electrolyte fuel cell membranes*
doi: *Electrochem. Commun.*, **13**, 921–923 (2011).
¹ EPFL Lausanne
- H. Schulenburg, B. Schwanitz, N. Linse, G.G. Scherer, A. Wokaun, J. Krbanjevic¹, R. Grothausmann², I. Manke² *3D imaging of catalyst support corrosion in polymer electrolyte fuel cells*
doi.org/10.1021/jp203016u, *J. Phys. Chem. C* **115**, 14236–14243 (2011).
¹ EPFL Lausanne
² Helmholtz Zentrum für Materialien und Energie, Berlin, Germany
- B. Schwanitz, H. Schulenburg, M. Horisberger, A. Wokaun, G.G. Scherer *Stability of ultra low Pt anodes for polymer electrolyte fuel cells - prepared by magnetron sputtering*
doi: 10.1007/s12678-010-0032-z, *Electrocatal.* **2**, 35-40 (2011).
- F. Simmen, A. Foelske-Schmitz, P. Verma, M. Horisberger, Th. Lippert, P. Novák, C.W. Schneider, A. Wokaun *Surface layer formation on $Li_{1+x}Mn_2O_{4-\delta}$ thin film electrodes during electrochemical cycling*
doi:10.1016/j.electacta.2011.07.046, *Electrochim. Acta* **56**, 8539- 8544 (2011).
- F. Simmen, M. Horisberger, B. Seyfang, T. Lippert, P. Novák, M. Döbeli¹, M. Mallepell, C.W. Schneider, A. Wokaun *Glassy carbon – a promising substrate material for pulsed laser deposition of thin $Li_{1+x}Mn_2O_{4-\delta}$ electrodes*
doi:10.1016/j.apsusc.2010.11.176, *Appl. Surf. Sci.* **257**, 5347-5353 (2011).
¹ ETH Zürich
- P. Verma, P. Maire, P. Novák *Concatenation of electrochemical grafting with chemical or electrochemical modification for preparing electrodes with specific surface functionality*
doi:10.1016/j.electacta.2010.11.055, *Electrochim. Acta* **56**, 3555-3561 (2011).
- O. Waser¹, R. Büchel¹, A. Hintennach, P. Novák, S.E. Pratsinis¹ *Continuous flame aerosol synthesis of carbon-coated nano- $LiFePO_4$ for Li-Ion batteries*
doi:10.1016/j.jaerosci.2011.06.003, *J. Aerosol Sci.* **42**, 657-667 (2011).
¹ ETH Zürich
- D. Weingarh, A. Foelske-Schmitz, A. Wokaun, R. Kötz *In situ electrochemical XPS study of the Pt / [EMIM][BF₄] system*
doi: 10.1016/j.elecom.2011.03.027, *Electrochem. Commun.* **13**, 619-622 (2011).
- M. Zaglio, G. Schuler, A. Wokaun, J. Mantzaras, F.N. Büchi *Parameter extraction from experimental PEFC data using an evolutionary optimization algorithm*
doi:10.1051/epjap/2011100190, *Eur. Phys. J. Appl. Phys.* **54**, 23409 (2011).
- M. Zaglio, A. Wokaun, J. Mantzaras, F.N. Büchi *1d-modeling and experimental study of the PEFC dynamic behavior at load increase*
doi: 10.1002/fuce.201000127, *Fuel Cells* **11**, 526-536 (2011).

Conference Proceedings / Other Papers

- J. Bernard, M. Hofer,
U. Hannesen¹, A. Toth²,
A. Tsukada, F.N. Büchi,
P. Dietrich
Direct electrical coupling of fuel cell and battery for electric powertrains
Proc. International Advanced Mobility Forum (IAMF), Geneva, March
8-9, (2011).
¹ Belenos Clean Power Holding, Biel/Bienne
² Swatch Group, Biel/Bienne
- J. Bernard, M. Hofer,
U. Hannesen¹, F.N. Büchi
H₂/O₂ fuel cell system for automotive application
Proc. of European Fuel Cell Forum 2011, contribution # A0402,
Lucerne, June 28 – July 1 (2011).
¹ Belenos Clean Power Holding, Biel/Bienne
- P. Boillat, P. Oberholzer,
R. Perego, R. Siegrist,
A. Kaestner, E.H. Lehmann,
G.G. Scherer, A. Wokaun
Application of neutron imaging in PEFC research
doi: 10.1149/1.3635541, ECS Trans. **41**, 27 (2011).
- J. Eller, J. Roth, F. Marone,
M. Stambanoni¹, A. Wokaun,
F.N. Büchi
*Towards ultra-fast X-ray tomographic microscopy of liquid water in
PEFC*
doi: 10.1149/1.3635572, ECS Trans. **41**, 387-394 (2011).
¹ Institute for Biomedical Engineering, University and ETH Zürich
- L. Gubler, S.M. Dockheer¹,
W.H. Koppenol¹
Radicals in fuel cell membranes: mechanisms of formation and
ionomer attack
doi: 10.1149/1.3635674, ECS Trans. **41**, 1, 1431-1439 (2011).
¹ ETH Zürich
- L. Gubler, H. Ben youcef,
S. Lüscher, J. Thut,
L. Bonorand, G.G. Scherer
*Development of high performance and durable fuel cell membranes
based on radiation grafting*
Proc. European Fuel Cell Forum 2011, contribution #A1008, Luzern,
June 28 - July 1 (2011).
- M. Havenith¹, W. Märkle
THz-Spektroskopie und Solvatationsdynamik
GDCh Nachrichten aus der Chemie **03**, 291-296 (2011).
¹ Ruhr-Universität, Bochum, Germany
- R. Kötz, D. Cericola,
A. Foelske, M. Hantel,
D. Weingarh
How to increase specific energy of electrochemical capacitors
Proc. 2nd European Advanced Automotive Battery Conference, ECCAP
Symposium - Large EC Capacitor Technology and Application,
103-107, Mainz, Germany, June 6-10 (2011).
- E.H. Lehmann, A. Tremsin,
C. Grünzweig, I. Johnson,
P. Boillat, L. Josic
Neutron imaging - detector options in progress
doi:10.1088/1748-0221/6/01/C01050, J. Instr. **6**, C01050 (2011).
- P. Oberholzer, P. Boillat,
R.I. Siegrist, R. Perego,
A. Kaestner, E.H. Lehmann,
G.G. Scherer, A. Wokaun
*Neutron imaging of isothermal sub-zero degree celsius cold-starts of a
polymer electrolyte fuel cell (PEFC)*
doi: 10.1149/1.3635569, ECS Trans. **41**, 363 (2011).
- B. Perucco¹,
J.O. Schumacher¹,
J. Roth, F.N. Büchi
*Two-phase modelling of the membrane electrode assembly of proton
exchange membrane fuel cells*
Proc. EFC 2011, European Fuel Cell - Piero Lunghi Conference,
contribution EFC11126, Rome, Italy, December 14-16 (2011).
¹ Zürich University of Applied Sciences, Winterthur
- Th. Priem¹, I. Noirot¹,
P. Mukish¹, A. Martin²,
L. Jörisen², F.N. Büchi,
S. Kreitmeier, F. Finsterwalder³
*Could a generic european fuel cell stack be competitive during early
market introduction phase and medium term horizon?*
Proc. EFC 2011, European Fuel Cell - Piero Lunghi Conference,
contribution EFC11024, Rome, Italy, December 14-16 (2011).
¹ CEA/LITEN, Grenoble, France
² Zentrum für Solarenergie- und Wasserstoff Forschung (ZSW), Ulm,
Germany
³ Daimler AG, Stuttgart, Germany

TALKS

Invited Talks

- F.N. Büchi *Brennstoffzellen - Prinzip, Eigenschaften und Anwendungen*
Naturwissenschaften und Unterricht, Zürcher Hochschulinstitut für
Lehrerbildung, ETH Zürich, March 26, 2011.
- P. Boillat *Application of neutron imaging in PEFC research*
220th ECS Meeting, Boston, USA, October 9-14, 2011.
- A. Foelske-Schmitz *XPS studies of ionic liquids for electrochemical energy storage - closing
the pressure gap in electrochemistry research*
Mitarbeiterseminar, Lehrstuhl E19, Technische Physik, TU München,
Munich, Germany, July 1, 2011.
- L. Gubler *Polymerelektrolyt Brennstoffzellen: Entwicklungsstand und
materialwissenschaftliche Herausforderungen*
9. Riesaer Brennstoffzellen – Workshop, Riesa, Germany, June 22,
2011.
- R. Kötz *How to increase specific energy of electrochemical capacitors*
2nd European Advanced Automotive Battery Conference, Mainz,
Germany, June 6-10, 2011.
- R. Kötz *Carbon nanomaterials for electrochemical capacitors*
EICOON Summer School, Nanomaterial Issues in Electrochemical
Energy Conversion: Fuel Cells, Batteries, Supercapacitors, Technology
Centre Innopoli 1, Espoo, Finland, June 15-17, 2011.
- R. Kötz *Roads to high energy electrochemical capacitors*
62nd ISE Annual Meeting of the ISE, Niigata, Japan, September 11-16,
2011.
- R. Kötz *Potential and limits of electrochemical double layer capacitors*
GDCh Wissenschaftsforum, Bremen, Germany, September 4-7, 2011.
- R. Kötz *Batterietechnologie – Bewertung im Licht von drei Fragen: Reichweite,
Kosten, Umweltverträglichkeit*
2nd Novatlantis Mobilitätsforum, Elektromobilität - Vom Konzept in die
Praxis, Basel, November 16, 2011.
- P. Novák *Oxygen, nano & Co.: Future or buzzwords of lithium batteries?*
Seminar at Toyota Central R&D Labs., Inc., Nagoya, Japan, September
19, 2011.
- P. Novák *Re-visiting the SEI: Everything is much more complex than believed in
the past*
62nd ISE Annual Meeting, Niigata, Japan, September 12, 2011.
- P. Novák *Was kommt nach der Lithiumionen-Batterie?*
Universität Münster, Münster, Germany, September 6, 2011.
- P. Novák *State-of-the-Art der Lithium-Ion Technologie*
5. DFG Statusmeeting, Münster, Germany, September 5, 2011.
- P. Novák *Nanomaterials for battery electrodes: The characterization challenge*
International Conference on Materials for Advanced Technologies
ICMAT 2011, Singapore, June 30, 2011.
- P. Novák *Li-S and Li-Air systems: The characterization challenge*
Symposium "Beyond Lithium IV", Pacific Northwest National
Laboratory, Richland, USA, June 9, 2011.

- P. Novák *Battery research: A wedding of surface electrochemistry with solid state electrochemistry*
SAOG 2011 - 27th Annual Meeting of the Swiss Working Group on Surface and Interface Science, Université de Fribourg, Fribourg, January 28, 2011.
- G.G. Scherer *Degradation of solid polymer electrolytes in electrochemical cells - some considerations*
First International LoLiPEM Workshop. Long life membranes based on PFSA & SAPs: Preparation and characterization, Grottaferrata, Italia, March 17-18, 2011.
- G.G. Scherer *Some aspects of aging, degradation, and failure modes in polymer electrolyte fuel cells*
PEM fuel cell catalyst and MEA preparation and characterization, HySA Catalysis, Hydrogen South Africa, Capetown, South Africa, March 28-29, 2011.
- G.G. Scherer *General introduction to fuel cells*
Joint ICTP-IAEA Advanced School on the Role of Nuclear Technology in Hydrogen-Based Energy Systems, Trieste, Italy, June 17, 2011.
- G.G. Scherer *Neutron imaging of liquid water in polymer electrolyte fuel cells*
Joint ICTP-IAEA Advanced School on the Role of Nuclear Technology in Hydrogen-Based Energy Systems, Trieste, Italy, June 17, 2011.
- G.G. Scherer *Proton-conducting membranes as solid electrolytes prepared by radiation grafting*
Joint ICTP-IAEA Advanced School on the Role of Nuclear Technology in Hydrogen-Based Energy Systems, Trieste, Italy, June 17, 2011.
- G.G. Scherer *Part 1: Introduction to fuel cells*
Part 2: Types of fuel cells
Part 3: PEFC applications
Tutorials on the occasion of the European Fuel Cell Forum 2011, Lucerne, June 28, 2011.
- G.G. Scherer *Protonen-leitende polymere Festelektrolyte für Brennstoffzellen*
Leibnitz-Institut für Oberflächenmodifizierung e.V., Leipzig, Germany, Juli 7, 2011.
- G.G. Scherer *The Electrochemistry Laboratory of Paul Scherrer Institut*
Yamanashi University, Kofu, Japan, September 8, 2011.
- G.G. Scherer *Water management of polymer electrolyte fuel cells studied by neutron imaging*
Electrochemical Society of Japan, Niigata, Japan, September 9-10, 2011.
- G.G. Scherer *Polymer electrolyte fuel cells materials research aspects studied at Paul Scherrer Institut*
62nd ISE Annual Meeting, Niigata, Japan, September 11-15, 2011.
- G.G. Scherer *Aspects of electromobility – today and tomorrow*
Nissan Research Center, Nissan Motor Co. Ltd., Kanagawa, Japan. September 17, 2011.
- G.G. Scherer *Fuel cell technology for automotive applications*
Chemistry Department, University of Fribourg, October 11, 2011.
- G.G. Scherer *Individual electromobility based on electrochemical devices – an overview*
Centre for Bioprocess Engineering Research, University of Cape Town, South Africa, November 18, 2011.
- G.G. Scherer *Fundamentals and some practical aspects of electrocatalysis for energy conversion and storage processes*
CATSA 2011, Gauteng, South Africa, November 13-16, 2011.

- G.G. Scherer *Nanostructures in polymer electrolyte fuel cells*
Winterschool "Nanomaterials for Energy Applications", University
Duisburg, Germany, December 9, 2011.
- T.J. Schmidt *Durability and diagnostics of membrane electrode assemblies: Can
lifetime be predicted?*
ETH Zürich, Februar 22, 2011.
- T.J. Schmidt *Electrocatalysis for electrochemical energy conversion*
1st CEA-ETH Zürich Workshop, June 8, 2011.
- T.J. Schmidt *Catalyst research for polymer electrolyte fuel cells*
Institute of Electrochemistry, Ulm University, Germany, July 14, 2011.
- T.J. Schmidt, H.A. Gasteiger¹ *Polymer electrolyte fuel cells*
Short Course at the ECS Meeting, October 9, 2011, Boston, USA
¹ TU Munich, Germany
- T.J. Schmidt *Electrocatalysts for polymer electrolyte fuel cells: From fundamentals to
applications*
Departement of Chemistry and Biochemistry, Bern University,
November 10, 2011.

Other Talks

- J. Bernard, M. Hofer, U. Hannesen¹, A. Toth², A. Tsukada, F.N. Büchi, P. Dietrich *Direct electrical coupling of fuel cell and battery for electric powertrains*
International Advanced Mobility Forum (IAMF), Geneva, March 8-9, 2011.
¹ Belenos Clean Power Holding, Biel/Bienne
² Swatch Group, Biel/Bienne
- P. Bleith, V. Godbole, C. Viellevieille, P. Novák *M_{0.5}TiOPO₄ as high specific charge battery material*
LAC Christmas Symposium, ETH Zürich, December 21, 2011.
- P. Boillat, P. Oberholzer, R. Siegrist, A. Kästner, E.H. Lehmann, G.G. Scherer, A. Wokaun *Assessing the effect of liquid water on PEFC performance by the
combined use of transient helox operation and neutron imaging*
8th Symposium on Fuel Cell Modeling and Experimental Validation (MODVAL8), Bonn, Germany, March 8-9, 2011.
- C.N. Borca, A. Uldry, A. Idhil, N. Zema¹, S. Turchini¹, D. Catone¹, A. Foelske, D. Grolimund, M. Samaras² *The influence of Cr-composition on the local magnetic structure of FeCr
alloys*
E-MRS ICAM IUMRS 2011 Spring Meeting, Nice, France, May 9-13, 2011.
¹ CNR, Roma, Italy
² University of Applied Science, Rapperswil
- F.N. Büchi, J. Eller, J. Roth, F. Marone, M. Stampanoni¹, A. Wokaun, *Progress in insitu X-ray tomography of in PEFC*
8th Symposium on Fuel Cell Modelling and Experimental Validation (MODVAL 8), Bonn, Germany, March 8-9, 2011.
¹ Institute for Biomedical Engineering, University and ETH Zürich
- F.N. Büchi, J. Bernard, M. Hofer, U. Hannesen¹ *H₂/O₂ fuel cell system for automotive application*
European Fuel Cell Forum 2011, Lucerne, June 28 –July 1, 2011.
¹ Belenos Clean Power Holding, Biel/Bienne
- F.N. Büchi, J. Eller, J. Roth, F. Marone, M. Stampanoni¹, A. Wokaun *Towards ultra-fast X-ray tomographic microscopy of liquid water in
PEFC*
220th ECS Meeting, Boston, MA, USA, October 9-14, 2011.
¹ Institute for Biomedical Engineering, University and ETH Zürich
- J. Eller, J. Roth, M. Stampanoni¹, A. Wokaun, F.N. Büchi *XTM visualization of water condensation and evaporation in porous gas
diffusion layers of polymer electrolyte fuel cell*
MUSIS Workshop, Bad Lauterbad, Germany, February 2-4, 2011.
¹ Institute for Biomedical Engineering, University and ETH Zürich

- J. Eller, J. Roth, F. Marone, M. Stambanoni¹, A. Wokaun, F.N. Büchi
In situ X-ray tomographic microscopy of polymer electrolyte fuel cells: Analysis of 3D water distribution
3rd Interpore Conference, Bordeaux, France, March 29-31, 2011.
¹ Institute for Biomedical Engineering, University and ETH Zürich
- A. Foelske-Schmitz, D. Weingarh, A. Wokaun, R. Kötz
XPS analysis of electrochemical processes at the ionic liquid/electrode and the ionic liquid/ultra high vacuum interface
220th ECS Meeting, Boston, USA, October 9-14, 2011.
- A. Foelske-Schmitz, D. Weingarh, A. Wokaun, R. Kötz
Quasi in situ XPS study of electrochemical oxidation/reduction of HOPG in the ionic liquid [EMIM][BF₄]
SAOG, Fribourg, January 28, 2011.
- V. Godbole, C. Villeveille, H.-H. Sommer, S. Indris¹, P. Novák
Structural and electrochemical studies of M_{0.5}TiOPO₄ (M=Ni, Cu, Mg) synthesized using modified solution route
Lithium Batteries Discussion 2011, Arcachon, France, June 12-17, 2011.
¹ Karlsruhe Institute of Technology, Karlsruhe, Germany
- L. Gubler, S.M. Dockheer¹, G.G. Scherer, W.H. Koppenol¹
Radicals in fuel cell membranes: concentration, reaction kinetics and lifetime
Fundamentals and Developments of Fuel Cell Conference 2011, Grenoble, France, January 19-21, 2011.
¹ ETH Zürich
- M.M. Hantel, T. Kaspar¹, R. Nesper¹, A. Wokaun, R. Kötz
Partially reduced graphite oxide: A graphene like material for supercapacitor electrodes
ISEE'Cap, Poznan, Poland, June 12-16, 2011.
¹ ETH Zürich
- M.M. Hantel, T. Kaspar¹, R. Nesper¹, A. Wokaun, R. Kötz
A comprehensive study on partially reduced graphite oxide for supercapacitor electrodes
CESEP, Vichy, France, September 25-29, 2011.
¹ ETH Zürich
- M. Heß, W. Märkle, P. Novák
Intercalation kinetics of lithium in graphite
The 16th International Symposium on Intercalation Compounds ISIC-16, Seč-Ústupy, Czech Republic, May 22-27 2011.
- S. Kreitmeier, A. Wokaun, F.N. Büchi
Characterization of the gas separation in PEFC membranes
8th Symposium on Fuel Cell Modeling and Experimental Validation (MODVAL8), Bonn, Germany, March 8-9, 2011.
- S. Kreitmeier, A. Wokaun, F.N. Büchi
Local degradation of the gas separation in PFSA membranes
2nd International Workshop on Degradation Issues of Fuel Cells, Thessaloniki, Greece, September 21-23, 2011.
- P. Novák
Fährt das Auto der Zukunft mit Batterien?
Touring Club Schweiz, PSI Villigen, August 5, 2011.
BMW Schweiz, Schloss Böttstein, Böttstein, March 31, 2011.
Tag der offenen Türe, PSI Villigen, October 16, 2011.
- P. Oberholzer, P. Boillat, R. Siegrist, A. Kästner, E.H. Lehmann, G.G. Scherer, A. Wokaun
Sub-zero isothermal start-up of PEFC visualized with neutron imaging
8th Symposium on Fuel Cell Modeling and Experimental Validation (MODVAL8), Bonn, Germany, March 8-9, 2011.
- P. Oberholzer, P. Boillat, R. Siegrist, A. Kästner, E.H. Lehmann, G.G. Scherer, A. Wokaun
Neutron imaging of isothermal sub-zero degree celsius cold-starts of a polymer electrolyte fuel cell (PEFC)
220th ECS Meeting, Boston, USA, October 9-14, 2011.
- J. Roth, J. Eller, F.N. Büchi
Effects of synchrotron radiation on polymer electrolyte fuel cell materials
220th ECS Meeting, Boston, USA, October 9-14, 2011.

- T. Sasaki, V. Godbole,
C. Villevieille, Y. Ukyo¹,
P. Novák
Direct detection of inhomogeneous reactions perpendicular to current collector by using in situ XRD
Lithium Batteries Discussion 2011, Arcachon, France, June 12-17, 2011.
¹ Toyota Central R&D Labs., Japan
- T. Sasaki, V. Godbole,
C. Villevieille, Y. Ukyo¹,
P. Novák
In situ investigation of inhomogeneous reactions perpendicular to current collector by using two-layer electrodes
62nd ISE Annual Meeting, Niigata, Japan, September 11-16, 2011.
¹ Toyota Central R&D Labs., Japan
- A. Savouchkina, A. Foelske-Schmitz, V.A. Guzenko,
D. Weingarh, R. Kötz,
G.G. Scherer, A. Wokaun
In situ STM study of Pt-nanodot arrays on HOPG prepared by electron beam lithography
ECASIA, Cardiff, United Kingdom, September 4-9, 2011.
- M.E. Spahr¹, T. Huckle¹,
F. Mornaghini¹, W. Märkle,
P. Novák
The influence of carbon additives on the engineering and performance of lithium-ion battery electrodes
International Battery Association 2011 Meeting, Cape Town, South Africa, April 11-15, 2011.
¹ TIMCAL SA, Bodio
- P. Verma, P. Novák
Grafting as novel approach to obtain surface modified carbons for tuning Li⁺ intercalation kinetics and SEI morphology
Lithium Batteries Discussion 2011, Arcachon, France, June 12-17, 2011.
- C. Villevieille, H. Sommer,
H. Schneider, S. Pérez-Villar,
P. Novák
Structural investigations of Li₂MnO₃:Li(Mn_xNi_yCo_z)O₂ - neutron diffraction, in situ X-ray diffraction, and in situ Raman spectroscopy
220th ECS Meeting, Boston, USA, October 9-14, 2011.
- D. Weingarh, A. Foelske-Schmitz, A. Wokaun, R. Kötz
Electrochemistry combined with XPS: In situ study of the Pt / [EMIM][BF₄] system
ECASIA, Cardiff, United Kingdom, September 4-9, 2011.

POSTERS

- P. Bleith, V. Godbole,
C. Villevieille, P. Novák
Fe_{0.5}TiOPO₄ as battery material with high specific charge
Empa-Doktoranden-Symposium, St. Gallen, October 18, 2011.
- Y. Buchmüller, G.G. Scherer,
A. Wokaun, L. Gubler
Introduction of functionalizable groups via radiation grafting into polymer electrolyte membranes for fuel cells
12th Tihany Symposium on Radiation Chemistry, Zalakaros, Hungary, August 27 - September 1, 2011.
- J. Eller, J. Roth, F. Marone,
M. Stampanoni, A. Wokaun,
F.N. Büchi
Insight into the 3D water distribution in PEFC gas diffusion layer by in-situ X-ray tomographic microscopy
JUM@P '11 Joint Users' Meeting at PSI, Villigen PSI, September 15-16, 2011.
- A. Foelske-Schmitz,
A. Savouchkina,
V.A. Guzenko, D. Weingarh,
A. Wokaun, G.G. Scherer,
R. Kötz
In situ STM study of Pt-nanodot arrays on HOPG prepared by electron beam lithography
220th ECS Meeting, Boston, USA, October 9-14, 2011.
- A. Foelske-Schmitz,
D. Weingarh, R. Kötz,
A. Wokaun
XPS study of electrochemical processes at the ionic liquid/electrode and ionic liquid/ultra high vacuum interface
Ionic Liquids: Faraday Discussion 154, Belfast, UK, August 22-24, 2011.
- L. Gubler, W.H. Koppenol¹
Mechanism of the chemical stabilization in fuel cell membranes using the Ce³⁺/Ce⁴⁺ redox couple
220th ECS Meeting, Boston, USA, Abstract #908, October 9-14, 2011.
¹ ETH Zürich

- K. Jetsrisuparb, F. Lindner,
H. Ben youcef,
G.G. Scherer, A. Wokaun,
L. Gubler
Modification of proton exchange membranes for fuel cells by radiation induced grafting
PolyColl 2011, Geneva, April 29, 2011.
- K. Jetsrisuparb, Z. Zhang,
H. Ben youcef,
G.G. Scherer, A. Wokaun,
L. Gubler
Influence of functional groups on membrane durability
2nd International Workshop on Degradation Issues of Fuel Cells,
Thessaloniki, Greece, September 21-23, 2011.
- T. Rosén, N. Prasianakis,
J. Kang, J. Eller,
J. Mantzaras, F.N. Büchi
In-situ measurements of gas transport properties in gas diffusion layers of PEFCs
Tagung Verbrennungsforschung in der Schweiz, ETH Zürich, October 28, 2011.
- A. Savouchkina, A. Foelske-Schmitz, R. Kötz,
G.G. Scherer, A. Wokaun
Oxidation of Pt/glassy carbon model electrodes: effect of heat-treatment of glassy carbon
SAOG, Fribourg, January 28, 2011.
- A. Savouchkina,
V.A. Guzenko, A. Foelske-Schmitz, D. Weingarh,
R. Kötz, A. Wokaun,
G.G. Scherer
Model electrodes prepared by electron beam lithography: Pt (im)mobility on HOPG
27th One-Day-Symposium of the Electrochemistry Laboratory, PSI Villigen, May 11, 2011.
- P. Verma, P. Novák
Surface modified carbons for Li-ion batteries
27th One-Day-Symposium of the Electrochemistry Laboratory, PSI Villigen, May 11, 2011.
- M. Zaglio, J. Roth,
J. Mantzaras, F.N. Büchi
Transient Bi-domain 1D PEFC model
8th Symposium on Fuel Cell Modelling and Experimental Validation (MODVAL 8), Bonn, Germany, March 8-9, 2011.
- Z. Zhang, K. Jetsrisuparb,
L. Gubler, G.G. Scherer,
A. Wokaun
Proton conductivity studies on radiation-grafted membranes
Fall Meeting of the Swiss Chemical Society 2011, Lausanne, September 09, 2011.
- Z. Zhang, K. Jetsrisuparb,
G.G. Scherer, A. Wokaun,
L. Gubler
A study on the effects of methacrylonitrile as co-monomer in radiation grafted membranes
2nd International Workshop on Degradation Issues of Fuel Cells, Thessaloniki, September 21-23, 2011.

CONFERENCES, WORKSHOPS & EXHIBITIONS

- M. Hofer, M. Frei-Hardt
Swiss Innovation Forum - Presentation of S-Chain Project
Basel, November 3, 2011.
Presenters
- R. Kötz
2nd European Advanced Automotive Battery Conference, , ECCAP Symposium - Large EC Capacitor Technology and Application
Mainz, Germany, June 6-10, 2011.
Chair of Session 1
- R. Kötz
The 2nd International Symposium on Enhanced Electrochemical Capacitors ISEE'Cap 2011
Poznan, Poland, June 12-16, 2011.
Member of International Advisory Board
- P. Novák
62nd Annual Meeting of the International Society of Electrochemistry
Niigata, Japan, September 11-16, 2011.
Organizing Committee
- T.J. Schmidt, F.N. Büchi
Polymer Electrolyte Fuel Cells 11, 220th ECS Meeting
Boston, USA, October 9-14, 2011.
Co-Organizer

G.G. Scherer, R. Kötz,
P. Novák

Electromobility
27th One-Day-Symposium of the Electrochemistry Laboratory, PSI
Villigen, May 11, 2011.
Organizers

MEMBERSHIPS IN EXTERNAL COMMITTEES

F.N. Büchi	<i>Prüfungskommission Physiklaboranten, Kanton Zürich</i> Experte
L. Gubler	<i>Prüfungskommission Physiklaboranten, Kanton Zürich</i> Experte
R. Kötz	<i>Electrochimica Acta</i> Associate Editor
P. Novák	<i>Materials</i> Editorial Board
P. Novák	<i>The Northeastern Center for Chemical Energy Storage (NECCES)</i> Scientific Advisory Board
G.G. Scherer	<i>Advisory Board European Fuel Cell Forum</i> Member
G.G. Scherer	<i>Asian Polymer Association, New Delhi, India</i> Honorary Member
G.G. Scherer	<i>Kantonsschule Wohlen</i> Maturitätsprüfungsexperte Biologie/Chemie
G.G. Scherer	<i>Advisory Board Electrocatalysis, Springer</i> Member
T.J. Schmidt	<i>HySA/Catalysis Competence Centre, University of Cape Town, South Africa</i> Technical Steering Committee

PAUL SCHERRER INSTITUT



Paul Scherrer Institut, 5232 Villigen PSI, Switzerland
Tel. +41 56 310 21 11, Fax +41 56 310 21 99
www.psi.ch